System Design and Elastic Stability Modeling of Transendoscopic Continuum Robots

By

Richard J. Hendrick

Dissertation

Submitted to the Faculty of the

Graduate School of Vanderbilt University

in partial fulfillment of the requirements

for the degree of

DOCTOR OF PHILOSOPHY

in

Mechanical Engineering

August 11, 2017

Nashville, Tennessee

Approved:

Nilanjan Sarkar Ph.D.

Robert J. Webster III Ph.D.

S. Duke Herrell M.D.

Benoit M. Dawant Ph.D.

Karl E. Zelik Ph.D.

W. David Merryman Ph.D.

To Renee:

My best friend, wife,

& constant source of encouragement

ACKNOWLEDGMENTS

The work compiled in this dissertation would absolutely not have been possible without the guidance, teaching, collaboration, and support from many sources.

First and foremost, I would like to thank my wife Renee for providing me with constant support over the past five years as I worked towards this goal. Renee's constant encouragement, empathy, and support made this work possible, and her humor, love, and perspective kept me grounded.

I would like to particularly thank my advisor, Dr. Robert Webster III. Throughout the past five years, it has been abundantly clear that he has had the best interest of me, and all of his other students, completely prioritized. I specifically appreciate that he has tailored his advising and guidance towards my particular goals. Not only has his guidance, discussion, and support allowed me to complete the work in this dissertation, but it has also helped me clarify my future career and take meaningful steps towards it during graduate school.

I would like to thank my dissertation committee: my advisor Dr. Robert J. Webster III, Dr. Nilanjan Sarkar, Dr. Benoit Dawant, Dr. David Merryman, Dr. Duke Herrell, and Dr. Karl Zelik for their support, counsel, and feedback. I would also like to thank Dr. Eric Barth, Dr. Nabil Simaan, Dr. Michael Goldfarb, and Dr. Pietro Valdastri for their teaching expertise in mechanical engineering. I feel very fortunate to have been taught by each of these individuals, and I appreciate their dedication

to teaching their respective subjects at such a high level. I would also like to thank Dr. Marie Thursby, who helped me look at innovation and entrepreneurship through a different lens.

The work presented in this dissertation has been a collaboration throughout. For the prostate system work presented in Chapter 2, I owe Dr. Duke Herrell, Dr. Christopher Mitchell, and my advisor, Dr. Robert Webster a great deal. Without the constant, weekly collaboration between the surgeons and engineers, this work would not have been possible, and the results in this chapter are the result of efforts from all of these people, not mine alone. For the elastic stability work compiled in Chapter 3, I owe my former lab mate, and now professor, Dr. Hunter Gilbert a great deal. We worked on this specific problem together for years, and the results found in this dissertation would not have been possible without his collaboration and the numerous hours of spirited discussion we had on the topic. For the work presented in Chapter 4, I would like to thank my lab mate Patrick Anderson. The simulations were compiled collaboratively, and this work benefited greatly from discussions with him on how to approach this problem. Finally, for the work presented in Chapter 5, I would like to thank my lab mate Margaret Rox, undergraduate student Evan Blum, and neurosurgeon Dr. Rob Naftel. Margaret has been instrumental in finishing the design of the robotic system in Chapter 5, preparing for and administering the experiments, and analyzing the data. Evan has helped me build this robotic system, particularly software aspects of the system for about two years, and is one of the most talented undergraduate engineers I have ever had the pleasure of working with. Dr. Naftel has been a very willing collaborator on this project, inspired the original idea to use this concept in endoscopic neurosurgery, and has provided tremendous feedback along the way for the experimental setup and design presented in Chapter 5.

In addition to these large collaborations, every day at the MED lab is full of micro-collaborations. I can honestly say that going into the lab over the past five

years has been something that I look forward to every single day, and that is because of the people that I work with. This includes Dr. Phil Swaney, Dr. Hunter Gilbert, Dr. Neal Dillon, Dr. Raul Wirz, Dr. Art Mahoney, Dr. Isuru Godage, Dr. Jessica Burgner, Dr. Ray Lathrop, Dr. Jenna Gorlewicz, Dr. Lou Kratchman, Dr. Dave Comber, Dr. Smita De, Dr. Loris Fichera, Dr. Tom Withrow, Trevor Bruns, Andria Remirez, Michael Siebold, Patrick Wellborn, Patrick Anderson, Margaret Rox, Katy Riojas, and James Ferguson. I would like to especially thank Hunter and Phil, who supported me throughout all of graduate school, were constantly thinking outside of themselves, and who made working in the MED Lab particularly fun for me.

I would like to thank all of the surgeons I have been able to work with in some capacity over the past five years including Dr. Lola Chambless, Dr. Fabien Maldonado, Dr. Otis Rickman, Dr. Duke Herrell, Dr. Smita De, Dr. Christopher Mitchell, and Dr. Rob Naftel.

I would also like to thank Myrtle Daniels, Suzanne Weiss, Renee Tomlin, and Jean Miller for their administrative support over the past five years. In particular, Myrtle has always gone above and beyond to help me when I run into any challenging administrative or ordering problem, and I sincerely appreciate her dedication to her job.

Finally, I would like to thank the National Science Foundation and the National Institutes of Health for the research funding that made many of these projects possible.

TABLE OF CONTENTS

LIST OF TABLES

LIST OF FIGURES

CHAPTER 1

INTRODUCTION

1.1 Motivation

sur·ger·y *noun*

The treatment of injuries or disorders of the body by incision or manipulation, especially with instruments.[1]

The motivation for this dissertation is embedded in the definition of surgery. At its core, this work is all about improving instrument manipulation and giving surgeons new, enhanced capabilities for minimally invasive surgical procedures.

Over the past few decades, it has become increasingly clear that entering the body in the most minimally invasive way possible provides tremendous patient benefit. To this point, an article in The New England Journal of Medicine recently stated that "Minimization of the invasiveness of surgical procedures is an advance that is arguably as significant as the discovery of anesthesia [2]." While the uptake of minimally invasive surgery has provided superior patient outcome, it has also created a major engineering challenge: to provide instrument manipulation at smaller and smaller scales, with less and less ability to tilt these instruments outside of the body. The work in this dissertation is motivated by providing a solution to this problem for transendoscopic instruments.

1.2 Dissertation Overview

This dissertation focuses on a specific class of minimally invasive surgery, rigid endoscopic surgery. The tools used through rigid endoscopes, in particular, suffer from a lack of dexterity and capability. In this dissertation, we study the use of miniature,

flexible, needle-sized robotic manipulators as tools through rigid endoscopes. In doing this, we focus on the design of these robotic systems, and explore applications in both urologic surgery and neurological surgery. These system designs are heavily motivated by the idea that these robotic systems should be small, compact, hand-held devices to have minimal impact on the operating room workflow and be more easily integrated into the operating room. A challenge with these flexible robotic tools is that they have the potential to lose elastic stability, and this work explores this phenomenon in detail from a modeling perspective and reveals critical insights into how stability effects the design, control, and performance of these flexible manipulators. Finally, we examine control strategies that use "extra" robotic degrees of freedom to accomplish secondary objectives, in addition to following a desired trajectory with the manipulator, which is a technique known as redundancy resolution. Specifically, we describe control techniques that utilize redundancy to optimize the stiffness of the device and maintain elastic stability while still tracking a desired trajectory.

1.3 Background: Minimally Invasive Surgery

Minimally invasive surgery (MIS) is a general term used to describe any surgical procedure that enters the body without large, open incisions. Laparoscopic surgery is as type of MIS that delivers long, rigid instruments and visualization (i.e. an endoscope) through small ports in the body, as shown in Figure 1.1. In laparoscopic surgery, the endoscope is usually used only for visualization of the surgical field and does not have tools passing through it. The tools are pivoted outside of the body and through the incision port to provide instrument manipulation at the surgical site. Manual laparoscopic surgery is common in both abdominal, pelvic, and thoracic procedures, where it is termed video-assisted thoracoscopic surgery (VATS) (see Figure 1.1 – Right).

Another subset of minimally invasive surgery is endoscopic surgery. While laparoscopic surgery uses endoscopes to provide visualization, endoscopic surgery differs in

Figure 1.1: Laparoscopic surgery utilizes endoscopes to look inside of the body, and instrument(s) through small ports to manipulate objects inside of the body. (Left) A general schematic of laparoscopic surgery [3]. (Center) An example laparoscopic tool [4]. (Right) Video-assisted thoracoscopic surgery, a type of laparoscopic surgery [5].

Figure 1.2: Rigid endoscopes: (Left) The rigid endoscope has a working channel which straight instruments can pass through. It also has attachments for a camera, light source, and irrigation [6]. (Right) The endoscope tip with instruments emerging from the distal tip [7].

that the instruments are passed through a working channel of the endoscope tube itself, as shown in Figure 1.2. These instruments can include scissors, forceps, laser fibers, and monopolar/bipolar cautery, among others. There are both rigid and flexible endoscopes - rigid endoscopes are used for surgeries where a straight, linear path can be taken from the outside of the body to the surgical site (see Figure 1.2), while flexible endoscopes are used when winding through curving anatomy is required. Endoscopes can be inserted into the body percutaneously (i.e. through a skin incision) or through natural orifices.

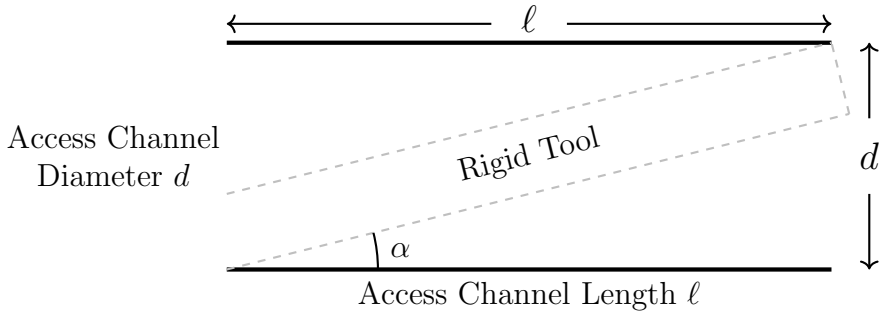

Figure 1.3: When rigid tools operate down long, narrow anatomical channels, they lose their ability to freely articulate.

1.3.1 The Limits of Laparoscopy

The tool manipulation in laparoscopic surgery is created by pivoting long, rigid shafts through ports in the body. For surgery in the insufflated abdomen, chest cavity, pelvis, or any other anatomical working volume with sufficient space, this concept often provides an excellent minimally invasive solution for delivering instrument manipulation. Anytime the surgical site is down a long, narrow anatomical channel, however, the ability to pivot these long, rigid shafts diminishes.

Figure 1.3 is a conceptual sketch that supports this. The figure shows a long, rigid tool operating through a narrow access channel. The angle this tool can achieve, which can be considered a heuristic for manipulation capability, drops off sharply as the access channel becomes longer and/or narrower, as shown in Figure 1.4. This figure also shows an estimate of where some anatomical working spaces would be located on this plot. Much of current robotic surgery has focused on roboticizing laparoscopic tools, targeting surgeries where tool pivoting is possible. The work in this dissertation, however, is focused on surgical spaces where tool pivoting is not a realistic option.

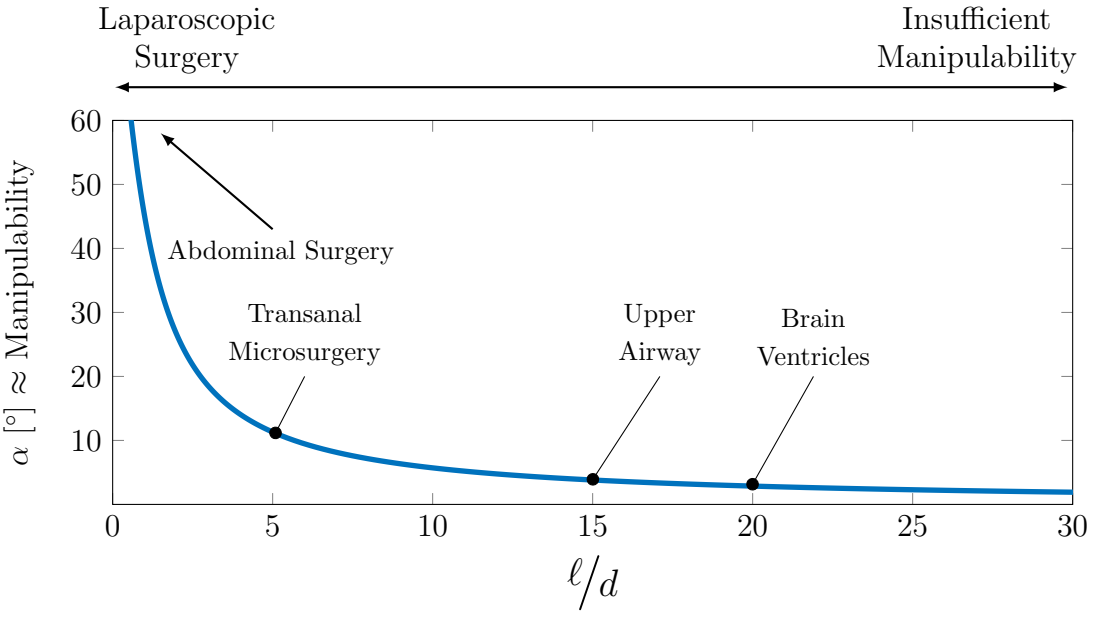

Figure 1.4: When rigid tools operate down long, narrow anatomical channels, their ability to articulate becomes severely limited. ℓ is the length of the access channel, d is the diameter of the access channel, α is the angle the tool can achieve, see Figure 1.3. Note that the locations of these anatomical channels are rough estimates and is intended only to be illustrative of the tool manipulation challenge when working through narrow channels.

1.3.2 The Challenges of Rigid Endoscopic Surgery

Rigid endoscopes are used all over the body and are now a common tool across the surgical specialties. A few example surgeries include transurethral prostate surgery, transoral tumor removal in the central airways, and brain surgery in the ventricles. Tools that operate through the working channel of rigid endoscopes are similar to laparoscopic tools in that they are normally straight, rigid tools. Conventionally, these tools are limited to two degree-of-freedom motion relative to the endoscope. The tool can insert/retract and spin axially about the endoscope axis as shown in Figure 1.5. Additionally, for the vast majority of rigid endoscopic procedures, the surgeon can only get one instrument at a time to the surgical site due to the small size of the working channel. This eliminates the possibility for cooperative, two-handed

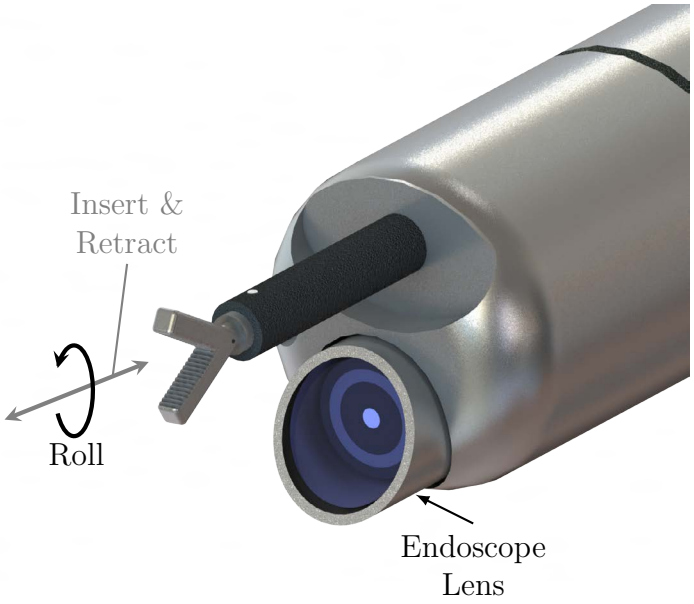

Figure 1.5: Tools through rigid endoscopes typically have two degrees of freedom. The tools can insert/retract and spin axially. Note that the tools can achieve a very small (usually negligible) angle inside of the endoscope channel itself.

(i.e. bimanual) tasks.

For some rigid endoscopic procedures, the surgeon may have the ability to pivot/tilt this endoscope outside of the body, creating a laparoscopic surgery-like movement of the instrument. These tilting motions are particularly challenging for surgeons during endoscopic surgery because any time the endoscope moves, the field of view of the endoscope moves along with it. The limited degrees of freedom, the constantly moving field-of-view, the limitation to a single tool, and the lack of instrument dexterity at the tip of the endoscope has made endoscopic surgery a particularly challenging subset of minimally invasive surgery. Often surgeons will train specifically in endoscopic fellowships to learn the special techniques to operate through these devices. Part of the motivation of this dissertation is to make working through rigid endoscopes easier for surgeons by providing them with more capable tools to deploy through rigid endoscopes.

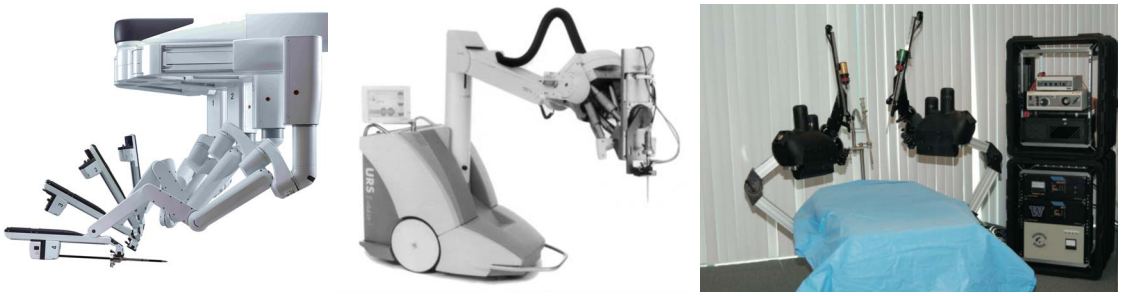

Figure 1.6: Robotic systems which tilt the instruments outside of the body: (Left) the da Vinci Xi model (Intuitive Surgical) [8], (Center) the Evolution 1 (U.R.S. Universal Robot Systems) [9], (Right) and the Raven Surgical Robot [10].

1.4 Robots in Minimally Invasive Surgery

Surgical robots have great potential to aid in instrument manipulation. After all, surgery requires precision, spatial reasoning, and dexterity, which are all things robots are particularly skilled at. The potential for surgical robotics is no longer hypothetical – surgical robots have gained widespread adoption throughout the world and have been utilized in hundreds of thousands of procedures, mostly with Intuitive Surgical's da Vinci system, as shown in Figure 1.6 (Left). The majority of surgical robotic systems designed thus far that aid in instrument manipulation, both in research labs and commercially, can generally be categorized into pivoted and flexible tools.

Examples of some pivoted, laparoscopic-like systems include the da Vinci robot (Intuitive Surgical, Inc.) [8], the Evolution 1 (U.R.S. Universal Robot System [9]), and the Raven Surgical Robot [10], as shown in Figure 1.6. All of these systems gain instrument manipulation in the same way that laparoscopic tools do: by tilting through a port in the body.

For surgical applications where tilting or pivoting of the tools is not possible outside of the body, several groups in the research community have been developing surgical robotic systems based on flexible elements over the past several years. These systems are often referred to as *continuum robots*, defined as "a continuously bending, infinite degree of freedom robot with an elastic structure" [11] or as "an ac-

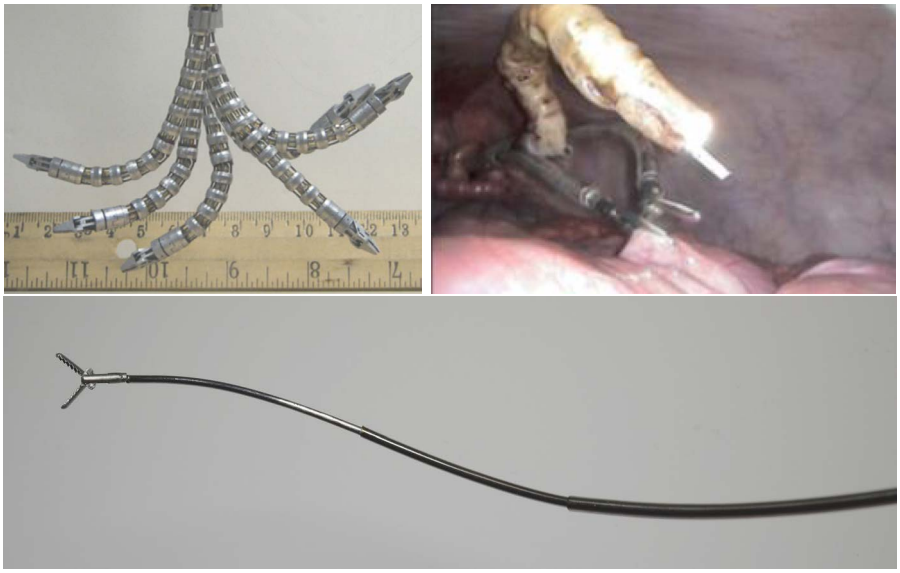

Figure 1.7: Some example continuum robot designs: (Top Left) The continuum manipulator known as the Insertable Robotic Effectors Platform shows several overlaid configurations of the manipulator (IREP) [13]. (Top Right) A system with two flexible, continuum arms and an articulated camera head [14]. (Bottom) A concentric tube robot.

tuatable structure whose constitutive material forms curves with continuous tangent vectors." [12]. A comprehensive review of continuum robots for medical applications is outside of the scope of this dissertation (see e.g. [12]). Here, we will only include a few representative examples of continuum robots for surgery.

The multi-segment backbone of the continuum robot shown in Figure 1.7 (Top Left) is composed of spacer discs and several elastic rods which can be pushed/pulled, creating a series of controllable active and passive bending sections [13]. The device shown in Figure 1.7 (Top Right) is made from an outer elastic tube that has been machined with cuts along its length to reduce its bending stiffness. Tendons are attached inside the tube at various arc lengths, and pulling of these tendons generates controllable bending of the continuum arms [14].

Concentric tube manipulators, as shown in Figure 1.7 (Bottom), are a class of miniature, needle-sized continuum robot composed of concentric, precurved, elastic tubes first proposed for use as robotic manipulators simultaneously in [15] and [16].

They are typically made of superelastic nitinol, which is well-suited for this application because it has large recoverable strain and can be shape set into desired curves while maintaining its superelasticity. When these precurved tubes are translated and rotated at their bases, their elastic interaction creates controllable "tentacle-like" motion (elongation and bending) of the device. These concentric tube manipulators are the miniature, flexible, needle-sized manipulators that are the focus of this dissertation.

1.5 Related Work

1.5.1 Hand-Held Robots For Surgery

A challenge in the clinical adoption of many robotic systems is that they often significantly affect the clinical workflow, for example by moving the surgeon from direct interaction at the patient's bedside to a console away from the patient. Indeed, it has been suggested that future surgical robotic systems should devote increasing attention to clinical workflow by including features such as smaller, more ergonomic actuation units (see e.g. [17]), with compact functionality (see e.g. [18]), and hands-on surgeon interfaces (see e.g. [19]).

The hand-held approach in surgical robotic devices has been previously beneficially applied in the context of articulated laparoscopic forceps [20], hand-held da Vinci tools [21], steerable needles [22], and articulated endoscopic tools [23], among others (see Figure 1.8). For concentric tube robots, a single-tube robot has been employed as a reach extender in eye surgery [24] and in neuroendoscopy to deliver an electrocautery wire [25]. In Chapters 2 and 5, hand-held robots that have incorporated multiple concentric tube manipulators will be presented, for urologic and neurological surgery, respectively.

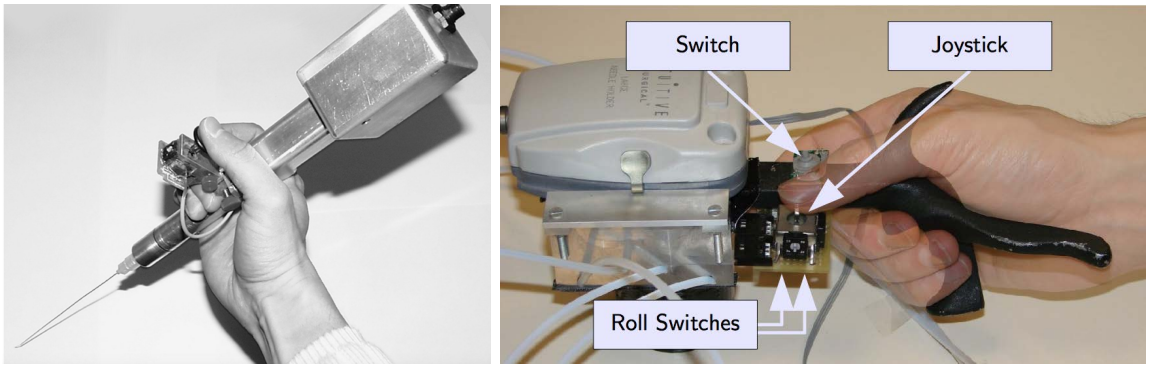

Figure 1.8: Hand-held robotic devices: a steerable needle [22] and a lightweight hand-held da Vinci tool [21].

1.5.2 Elastic Stability

Elastic stability is a subject that has been studied in great detail in the applied mathematics and structural mechanics literature (see e.g. [26]). Researchers in these fields have made recent developments in studying the "post-buckled" behavior of elastic structures, but these results have not yet been translated into robotics.

Elastic instability is a property of concentric tube robots that was first noted in [27]. Today, it has become a well-known challenge associated with concentric tube robots. When the manipulator becomes elastically unstable, the structure suddenly, and potentially violently, releases its strain energy and jumps between configurations. Researchers set out to understand this problem and develop techniques to prevent instability from occurring.

The first paper to model the snapping phenomenon modeled the curved portions of the tubes as torsionally rigid and the straight portions as torsionally compliant [27]. This technique revealed a solution multiplicity, or bifurcation, for this simplified kinematic model. As the literature converged on a more advanced kinematic model [28, 29], the questions about stability remained. The snapping problem has since been approached from design (see e.g [30, 31, 32, 33]), modeling (see e.g [34, 35, 36, 33, 37, 38]), and planning perspectives (see e.g. [39, 38]).

The work in this dissertation approached the problem from a design and modeling perspective, seeking to answer two fundamental questions; first, what are the constraints on the manipulator design that guarantee elastic stability everywhere in the workspace for an arbitrary concentric tube robot? And second, how can one predict where elastic instability will occur in actuation space for an arbitrary concentric tube robot? These questions will be answered in Chapter 3 of this dissertation. In addition to these fundamental theoretical questions, we also explore in detail the effect that maintaining stability has on the design space, controllability, stiffness, and dexterity of concentric tube manipulators in Chapters 4 and 5.

1.5.3 Redundancy Resolution in Continuum Robotics

A manipulator is called redundant when it provides more degrees of freedom than are required for the task it is accomplishing. These redundant degrees of freedom can be used to optimize secondary objectives in a technique called redundancy resolution. This idea has been successfully applied to continuum robotics in several examples, but has yet to be applied to concentric tube robots.

In [40], Simaan added a redundant secondary backbone to a snake-like robot to reduce the amount of force acting on the primary backbone and reduce the risk of buckling, which improved the miniaturization of their continuum manipulator. Chirikjian and Burdick used redundancy resolution to solve the inverse kinematic problem for hyper-redundant robots and showed that they can command the backbone of these manipulators to follow a desired continuous backbone curve [41, 42]. Camarillo et al. used redundant degrees of freedom to control tendon-actuated continuum robots to minimize the two-norm of the tendon forces in the backbone [43]. Edelmann et al. recently utilized redundancy to improve the stability of magnetically controlled catheters by minimizing the least negative eigenvalue of the catheter tip stiffness matrix [44]. The work of Edelmann et al. is conceptually a very similar idea to the

redundancy resolution techniques we had previously applied for instability avoidance and comes from a relationship between stiffness and stability, which will be explored for concentric tube manipulators in Chapter 4.

1.5.4 Continuum Robotic Tools in Endoscopic Neurosurgery

Over the past roughly three decades, the research community has been interested in robotics in neurosurgery – mainly for stereotactic aiming with registration to preoperative images. Recently, however, there has been a surge in interest in miniature flexible robotic tools in endoscopic neurosurgery.

Drake et al. has been investigating passing multiple concentric tube robots through a rigid neuroendoscope for treatment of endoscopic third ventriculostomy [45, 46, 47], and designed an interactive software application for patient-specific concentric tube neurosurgical instruments [48]. This system has been qualitatively demonstrated to complete the motions required for endoscopic third ventriculostomy (see Figure 1.9 – Left). Additionally, a concentric tube robot was added to a conventional flexible neuroendoscope for enhanced manipulation and control [25]. This system added a single curved nitinol tube and a cautery wire to a flexible neuroendoscope and successfully robotically targeted points inside of a 3D printed brain ventricle. A new proposed concept is an MRI compatible nueroendoscope that could deploy continuum robots (or conventional instruments) through either the front port or the side port, with visual feedback through both ports using CMOS cameras [49, 50]. Another fascinating concept for endoscopic neurosurgery is to suspend the endoscopic tools from cables and operate through an 11 mm commercially available cylindrical retraction device. This concept was demonstrated as a manual (non-motorized) system in [51] (see Figure 1.9 – Right).

While substantial progress has been made in robotic neuroendoscopy, there remains a gap in the literature in quantifying the value that these systems can bring

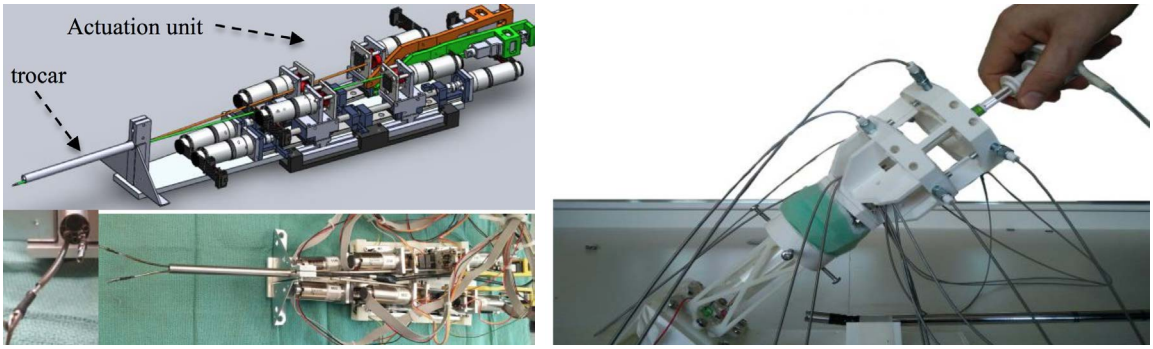

Figure 1.9: Neuroendoscopic systems: a neuroendoscopic, two handed concentric tube robot system for endoscopic third ventriculostomy [47] (Left) and a neuroendoscopic system called the neuroCYCLOPS [51] (Right).

in comparison to traditional endoscopic neurosurgery in simulated surgical scenarios. Chapter 5 will describe a new two-armed system for endoscopic neurosurgery, and its performance will be quantified in comparison to conventional, manual neuroendoscopy.

1.6 Dissertation Contributions

The primary contribution of Chapter 2 is the first ever hand-held robotic surgical device with multiple manipulators, and validates that a surgeon is capable of simultaneously (1) manually manipulating the entire system, and (2) robotically controlling two robotic manipulators. This device is also the first robot proposed for holmium laser enucleation of the prostate.

The primary contributions of Chapter 3 are answering the theoretical questions surrounding concentric tube robot elastic stability of (1) what are the design constraints to prevent elastic instability for any concentric tube robot and (2) is there a way to predict where instability will occur in joint space for any concentric tube robot? This chapter also provides experimental validation of the theoretical results.

The primary contribution of Chapter 4 is to apply redundancy resolution techniques to concentric tube robots for the first time. Stiffness optimization and insta-

bility avoidance are novel secondary objectives that are explored for concentric tube manipulators in this chapter. The instability avoidance technique is the first control technique that handles instability in a real-time controller. This potentially can enable the use of high curvature concentric tube designs that were previously thought to be off-limits because of elastic instability, which may open up new applications for concentric tube robots.

The primary contribution of Chapter 5 is an experimental comparison of robotic versus manual endoscopic neurosurgery using a custom-designed two-armed concentric tube robot system. This chapter also provides a manipulator design optimization framework for designing two-tube concentric tube robots, presented in the context of endoscopic neurosurgery. It provides several key design concepts, particularly related to elastic stability, that facilitate improved design of concentric tube manipulators.

CHAPTER 2

A HAND-HELD ROBOT FOR ENDOSCOPIC PROSTATE SURGERY

This chapter describes the system design and experimental evaluation of a hand-held robot for endoscopic prostate surgery. This system addresses the limitations of rigid endoscopic enlarged prostate surgery by delivering two, independent, dexterous, needle-sized arms through the rigid endoscope. The majority of this chapter is adapted from a paper published in *The International Journal of Robotics Research* in 2015 entitled "Hand-held Transendoscopic Robotic Manipulators: A Transurethral Laser Prostate Surgery Case Study" [52][1]. The content in this chapter also resulted in the following publications [53, 54, 55, 56].

2.1 Contributions

The primary contribution of this chapter is to establish the feasibility of single-operator hand-held control of an endoscope and two articulated transendoscopic manipulators. Within the prostate surgery application, the system we describe is the first hand-held robot for transurethral surgery, and also the first robotic system specifically designed to facilitate the Holmium Laser Enucleation of the Prostate (HoLEP) procedure. A design contribution is the idea of using field of view reachability as an objective function for optimally selecting tube parameters in a concentric tube robot. Experimental contributions include a comparison of task space control versus joint space control and a demonstration of the system's practicality via phantom and cadaver HoLEP resection experiments.

[1]Link: `https://doi.org/10.1177/0278364915585397` – Reprinted by permission of SAGE Publications.

2.2 Motivation and Background

2.2.1 Catalyzing The Utilization of a Superior Procedure for BPH

An estimated 210 million men worldwide, or roughly 6% of the world's male population, suffer from benign prostatic hyperplasia (BPH) [57]. It is "potentially the most prevalent symptomatic disease in men" and diagnosed in 13.5% of men over 50 and 27.8% of men over 65 [58]. As briefly mentioned earlier, our system is clinically motivated by the prospect of increasing the utilization of HoLEP to treat BPH, a procedure that has demonstrated excellent clinical outcomes, yet is rarely used (approximately 1.7% of the time [59]) because of its degree of difficulty for the surgeon [60, 61, 62, 63, 64].

HoLEP is currently conducted using a straight, rigid endoscope, which the surgeon holds and introduces transurethrally into the prostate, as shown in Figure 2.1. A straight holmium laser fiber is passed through the working channel of the endoscope and used to resect (i.e cut, not thermally ablate) the tissue. The holmium laser is a "contact laser" intended to be positioned in close proximity to the target tissue to be

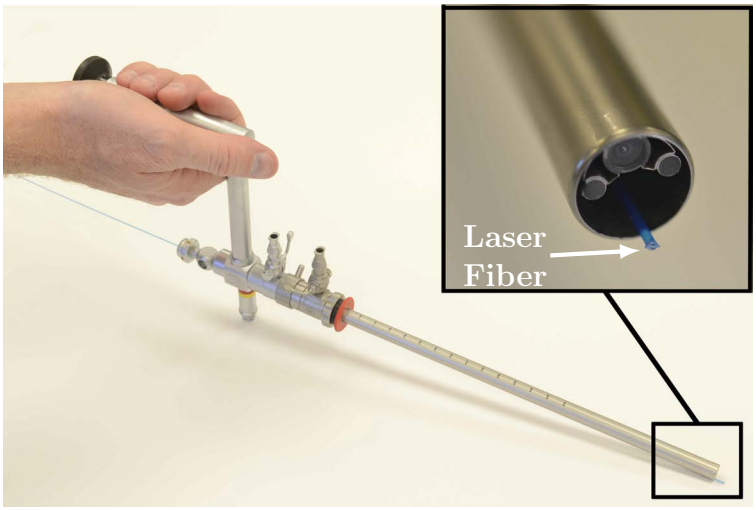

Figure 2.1: A transurethral endoscope (Storz, Inc. 27292 AMA) with a HoLEP laser fiber introduced through the working channel.

cut. Holmium lasers "possess the ideal combination of cutting and coagulation" [65], with only 0.2 mm of tissue penetration [66]. Enucleation refers to the use of the laser to resect the prostate tissue as a solid mass ("peeling" internal prostate tissue away from the prostate capsule without cutting into it), as shown in Figure 2.2 (Right). Once the mass of tissue is free, it is then pushed into the bladder. A device called a morcellator is then introduced through the urethra into the bladder and used to simultaneously cut the prostate tissue into small pieces and remove it from the body using suction.

A procedure called Transurethral Resection of the Prostate, or TURP, is currently the gold standard treatment for BPH, and a comparison of the surgical technique for TURP and HoLEP is shown in Figure 2.2. Multiple randomized controlled trials [67, 68, 69, 70] have demonstrated the long-term benefits of HoLEP in comparison to TURP. HoLEP has been shown to reduce the need for reoperations [67, 69] and blood transfusions [71, 67, 69, 70], which is particularly compelling in light of recent research showing transfusions may be much more dangerous to the patient than previously realized [72]. HoLEP also has been shown to reduce hospitalization time (from 2.1 days to 1.2 days) and catheterization time (from 1.9 days to 0.7 days) versus TURP [67]. A meta-analysis of HoLEP outcomes suggests that its lower re-operation rate is "likely due to the fact that the technique actually removes the entire adenoma rather than just opening a channel that is likely to regrow and require further treatment" [73]. Indeed, randomized controlled trials have shown HoLEP removes 39% more tissue than TURP [67]. All of the above data has led many to suggest that HoLEP should become the new clinical gold standard for BPH treatment (see e.g. [74, 75, 73]).

Despite these compelling clinical advantages, HoLEP is currently conducted at only a few institutions because it is extremely challenging for the surgeon. It is physically demanding because large forces are required to angle the endoscope, due to the

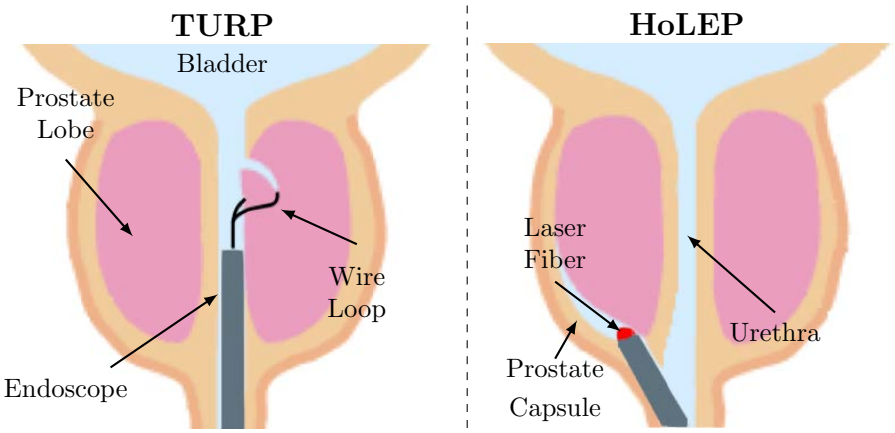

Figure 2.2: (Left) Transurethral Resection of the Prostate, or TURP, uses a wire loop to remove piece-by-piece the enlarged prostate lobe. (Right) Holmium Laser Enucleation of the Prostate, or HoLEP, uses a laser fiber to enucleate entire lobes of the prostate.

soft tissues surrounding it. To make matters worse, the surgeon must simultaneously manipulate soft tissue using the endoscope itself, and bring the laser fiber (which has no articulation, aiming straight out from the endoscope at a fixed position with respect to the image) to bear on the desired surgical target, which requires a high degree of surgical skill. The robotic system described in this chapter, as shown in Figure 2.3 is designed to make HoLEP easier by providing two independent concentric tube manipulators, introduced through the existing working channel of a standard clinical endoscope. These two concentric tube manipulators can be used cooperatively by the surgeon: one arm facilitates tissue manipulation and retraction, while the other aims the laser fiber.

2.2.2 Introduction to Concentric Tube Manipulators

Concentric tube manipulators are a type of miniature, needle-sized continuum robot composed of concentric, precurved, elastic tubes first proposed for use as robotic manipulators simultaneously in [15] and [16], as shown in Figure 2.4. They are typically made of superelastic nitinol, which is well-suited for this application because it has

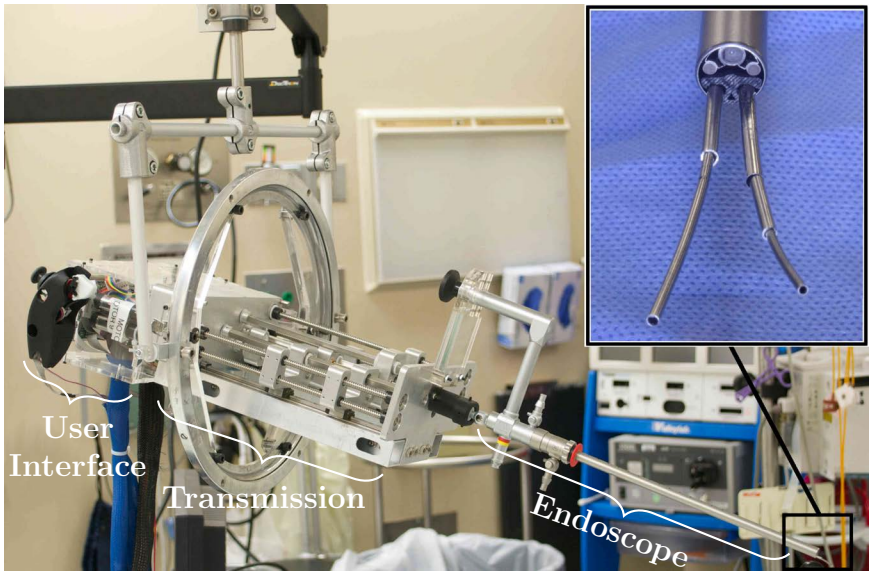

Figure 2.3: Our new robotic system integrates two concentric tube manipulators with a standard clinical endoscope in a hand-held (counterbalanced) system. The system fits seamlessly into the clinical workflow because the surgeon still has direct manual control of endoscope pose, and can simultaneously control the manipulators that extend through the endoscope with thumb and finger motions.

large recoverable strain and can be shape set into desired curves while maintaining its superelasticity. When these precurved tubes are translated and rotated at their bases, their elastic interaction creates "tentacle-like" motion (elongation and bending) of the device. Figure 2.4 shows a schematic of a typical concentric tube manipulator with typical joint definitions (α_i and β_i) labeled. Geometrically exact mechanics-based models now exist for these manipulators [76, 77] and a variety of real-time control methods have been described [77, 78, 79]. Concentric tube robots are particularly well-suited to the hand-held paradigm due to the small size and weight of the manipulators and the fact that actuators can be located remotely from the surgical site, at tube bases.

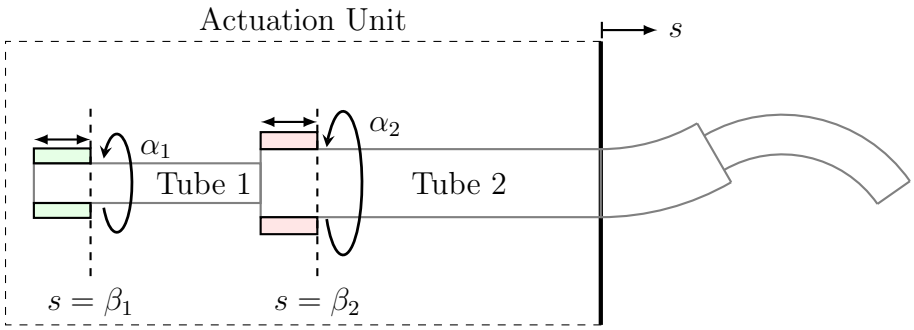

Figure 2.4: A schematic of a two tube concentric tube manipulator. Each tube can be independently translated and rotated, and the tubes are held straight before they exit the actuation unit (which defines $s = 0$). The joint variables α_i and β_i are shown. The elastic interaction of the precurved tubes creates a controllable tentacle-like motion.

2.3 Related Work

2.3.1 Robots in Natural Orifice and Single Port Surgery

Endoscopic surgery enables access to surgical sites through small incisions and has become the standard of care for many types of surgeries. In recent years, there has been increasing interest in further reducing invasiveness by eliminating skin incisions completely, in favor of delivering endoscopes and manipulators through natural orifices. A major challenge in natural orifice surgeries is maintaining the dexterity of both the endoscope and surgical instruments in the presence of the constraints imposed by the natural orifice and anatomical pathway to the surgical site. Because of this, natural orifice procedures are typically difficult to complete when first conceived of by forward-thinking surgeons, because procedure-specific instrumentation has yet to be developed.

The surgical robotics community has been actively engaged in remedying this in recent years by developing small manipulators which can be passed through (or alongside) endoscopes, to provide surgeons with enhanced dexterity and larger workspaces. There has been a great deal of interest in particular in single port surgeries, where the robot enters the body through a small incision, typically in the abdomen. For exam-

ple, the system design of [80] delivered two 6 degree-of-freedom (DOF) manipulators, with motors embedded in the manipulator arms, through a 30 mm umbilical access port. The elbow-based design of [81] delivered two 4 DOF arms, one for cautery and one equipped with a gripper, for dissection tasks through a 26 mm abdominal port. A 24 mm system was demonstrated by [82] that could be delivered via the mouth or anus with an endoscope and two 6 DOF manipulators driven by Bowden cables for scarless gastrointestinal surgery. The 19 mm ViaCath system was introduced in [83], and delivered two 6 DOF flexible, nylon manipulators and a standard flexible endoscope through the mouth to access the GI tract. The compact design of [14] delivered two articulated arms with interchangeable instruments and an articulated camera through a 16 mm port. The single-port design with perhaps the smallest diameter to date that delivers two manipulators was shown by [13]. Their flexible robotic platform provides two 7 DOF continuum manipulators and a 3 DOF stereo vision module via a single 15 mm incision. The above are just a few of the many examples of the surgical robotics community's active and ongoing efforts to increase the dexterity, visualization capability, and workspace of surgeons in single port and natural orifice settings.

These systems demonstrate the remarkable progress that has been made in the design and miniaturization of robotic surgical systems, but some of the most demanding natural orifice applications (e.g. nostril, ear canal, or transurethral procedures) require further miniaturization. The transurethral approach in our system draws inspiration from several prior robotic systems. TURP was one of the earliest surgical robotics applications [84, 85], in which a robotized endoscope was used for autonomous dissection of the prostate, based on medical imaging. Somewhat surprisingly, since this pioneering work, only a few research groups have developed robotic systems designed for transurethral deployment. In 2001, robotic transurethral laser resection of the prostate through a standard endoscope was briefly mentioned [86],

though the authors' main focus was on the Nd:YAG laser used, rather than on the robotic system. In 2002, master-slave teleoperation of a robot holding an endoscope for TURP was described [87]. In 2004, a 4 DOF manipulator for prostate resection delivering a drill and cutter through an 8 mm rigid tube, with ultrasound guidance, was developed [88]. Here, a major focus was on the removal of excised tissue from the body, since a morcellator was not available. In 2013, the feasibility of transurethral robotic bladder access was demonstrated by Simaan and colleagues, which was the first use of a continuum robot in a transurethral application. This robot consisted of a 5 mm continuum manipulator that delivered a laser fiber, a fiberscope, and biopsy forceps into the bladder for visual inspection and tumor resection [89]. Our system follows the same continuum robot paradigm, but focuses on the prostate rather than the bladder. It also differs in the use of the continuum robots as manipulators at the tip of the endoscope rather than as an outer deflectable tube for carrying instruments to the surgical site.

2.3.2 Maintaining the Clinical Workflow with Hand-Held Robots

Another challenge in the clinical adoption of many robotic systems is that they often significantly affect the clinical workflow, for example by moving the surgeon from direct interaction at the patient's bedside to a console away from the patient. Indeed, it has been suggested that future surgical robotic systems should devote increasing attention to clinical workflow by including features such as smaller, more ergonomic actuation units (see e.g. [17]), with compact functionality (see e.g. [18]), and hands-on surgeon interfaces (see e.g. [19]). In keeping with these ideas, in this chapter we present a hand-held system that fits seamlessly into the current clinical workflow for transurethral laser-based treatment of benign prostatic hyperplasia.

The hand-held approach in surgical robotic devices has been previously beneficially applied in the context of articulated laparoscopic forceps [20], hand-held da

Vinci tools [21], steerable needles [22], and articulated endoscopic tools [23], among others. For concentric tube robots, a single-tube robot has been employed as a reach extender in eye surgery [24] and in neuroendoscopy to deliver an electrocautery wire [25]. Our robot follows the hand-held paradigm of these prior systems, but is the first system to incorporate multiple concentric tube manipulators in a hand-held device.

2.4 System Design

There are two elements to the design of our system: the mechanical design of the actuation unit and user interface, and the selection of tube curvatures in the manipulators. The overall system consists of four main modules: the user interface (Figure 2.5 – Left), the transmission (Figure 2.5 – Right), the endoscope (Figure 2.7 – Left), and the counterbalance (Figure 2.7 – Right).

2.4.1 Mechanical Design

At the end of the robot nearest the surgeon is the user interface module (see Figures 2.3 and 2.5 – Left). This module is designed to quick connect to the transmission module through spring-loaded shaft couplings and houses nine, 16 mm, 8 W brushless motors with 29:1 gearheads (Maxon Motor, Inc.). Fixed to the outside of the user interface module are handles, where the surgeon grasps the robot and can manually manipulate the entire system to control endoscope pose. Each handle has an embedded joystick and trigger that are used to control the concentric tube manipulators. A screen is also placed between the surgeon's hands, which can be used to display the endoscopic view.

The transmission section (see Figures 2.3 and 2.5 – Right) converts the rotation of the motors in the user interface module into translation and rotation of the tubes. The transmission was designed such that one concentric tube manipulator could include three precurved tubes (6 DOF), while the other manipulator could include two tubes

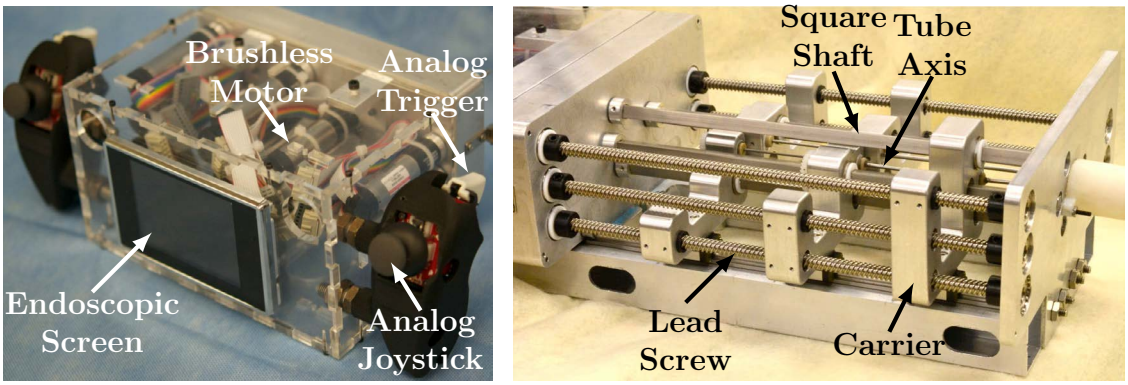

Figure 2.5: (Left) The user interface section houses the motors and has two handles which are equipped with joysticks and triggers that give the surgeon control of each manipulator, while a screen displays the endoscopic view. (Right) The transmission section: square shafts transmit torque to rotate the concentric tubes, and lead screws drive tube carriers to translate the tubes.

with the outer tube straight (3 DOF). In the set of experiments described in this chapter, however, both arms were configured as two tube, 3 DOF manipulators. Linear motion of the tubes is achieved via lead screws (pitch of $0.33\,{}^{\text{in}}/_{\text{rev}}$), which drive tube carriers that ride on ball bearing blocks on a guide rail. Rotation of the tubes is achieved via square shafts, which transmit torque through a gear train to

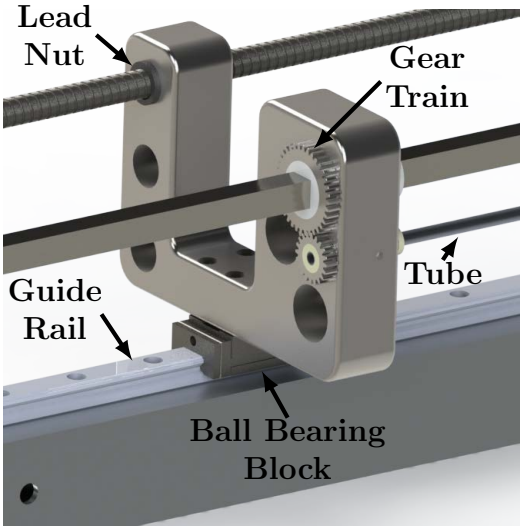

Figure 2.6: A detailed view of a single carrier is shown. Rotation of the square shaft transmits torque through the gear train and rotates the tube. Rotation of the lead screw translates the carrier on the guide rail which translates the tube.

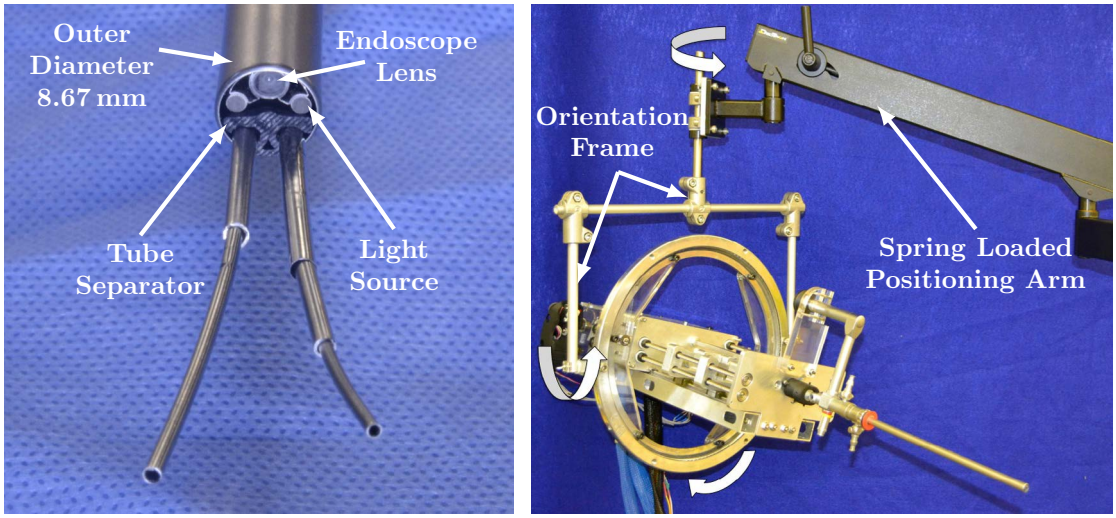

Figure 2.7: (Left) The rigid endoscope is shown with two concentric tube robots passing through it. The endoscope and two fiber optic bundles providing illumination are built into the endoscope. The two manipulators pass through a single 5 mm port inside the endoscope. A custom plastic tube separator constrains the exit axes of each manipulator at the endoscope tip. (Right) A spring loaded positioning arm provides passive gravity compensation and a custom orientation frame provides orientation degrees of freedom for the surgeon.

the tube, see Figure 2.6 for a detailed view of a single carrier. By using square shafts that run the entire length of the transmission section, torque can be transmitted over a variable distance, allowing the motors to be static and compactly packaged. Friction was mitigated throughout the transmission section by choosing plastic (PET) lead nuts, a ball bearing block that rides on the guide rail, and a PTFE sleeve that translates on the square shaft. Friction between the interacting tubes also affects the system. The effect is minimal in translation, since the axial stiffness of the tubes make it easy to break static friction. In rotation, however, the tubes can store torsion such that the tube rotation at its base is not equal to the tube rotation at the tip. To mitigate this effect, adequate clearance between the tubes is critical.

The endoscope (see Figures 2.3 and 2.7 – Right) is mounted to the front of the transmission section and is a clinical 26 Fr (8.67 mm) endoscope (Storz, Inc. 27292 AMA). Because this endoscope is rigidly mounted to the robot, manipulation of the

robot via the user interface handles also manipulates the endoscope. This endoscope contains optics and light sources as well as a 5 mm tool channel, through which we pass our concentric tube robots. A 500 μm laser fiber is passed through the inner channel of one of the robotic arms. Because the manipulators and the endoscope lens have a fixed geometric relationship independent of endoscope pose, the transformations between the user interface, endoscope, and manipulator frames are all constant.

To assist the surgeon by supporting the weight of the hand-held robot, a spring-loaded counterbalanced arm (Dectron, USA) is provided (Figure 2.7 – Right). A custom orientation frame was also constructed, providing three passive orientation degrees of freedom so that the overall counterbalance system enables the surgeon to manipulate the robot freely in 6 DOF without perceiving the system as having any weight. When the robot is used in transurethral prostate surgery, the endoscope approximately operates through an anatomically constrained center of motion near the front of the prostate. This constraint is created by the soft tissue pressure provided by the urogenital diaphragm. Thus, the surgeon must typically manually coordinate 4 DOF endoscope motion (roll, pitch, yaw, and insertion) during surgery.

2.5 Tube Design: Optimizing the Reachable Field of View

Design optimization of concentric tube robots is an active area of research. Tube parameters can be optimized to maximize the reachability of a target anatomical volume [90], or to navigate through constrained anatomy and reach specified target positions [91]. Tube design optimization will be discussed in detail in Chapter 5 in the context of neuroendoscopy. In HoLEP, since the endoscope view and manipulator bases will move together and be repositioned during surgery, it is desirable for the manipulators to be able to reach as much of the endoscope's field of view as possible. Thus, to design optimal manipulators for HoLEP, we maximize the overlap between the endoscopic field of view and the workspace of the manipulator (i.e. the "reachable

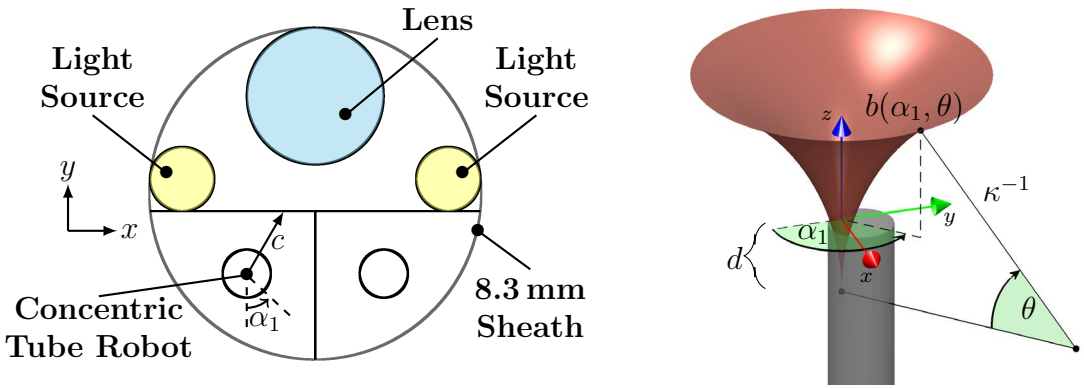

Figure 2.8: (Left) A cross-section of the endoscope tip. The concentric tube manipulator base frame is located a short distance inside the tip of the endoscope, and its workspace is partially defined by the boundary indicated in black straight lines in the figure above. The boundary is defined by the endoscope sheath, a line tangent to the light sources, and the midline of the endoscope between the two manipulators. (Right) The workspace surface, $b(\alpha_1, \theta)$, of a concentric tube robot is shown. The chosen coordinate frame and all parameters required to calculate the surface are illustrated for an example point on the surface.

field of view" – RFOV). To determine the RFOV, we must model both the endoscope's field of view and the concentric tube robot's workspace, and then compute the intersection of the two.

We model the field of view of the endoscope as a cone with its vertex at the lens. Manufacturer specifications describe this endoscope as having a 6° angle of view, 103° field of view, 30 mm depth of view, and we determined that the lens is located approximately 1.2 mm inside the tip of the endoscope. The modeled field of view is shown in Figure 2.9. In considering manipulator workspace, we note that while it is possible to use several tubes and non-constant precurvatures, in this chapter we restrict our attention to manipulators consisting of a straight, rigid outer tube and a constant curvature inner tube. This simplified selection of component tubes eliminates the possibility of elastic instability. These tubes can move in three degrees of freedom, and RFOV optimization is conducted over one parameter, namely the curvature (κ) of the inner tube.

The concentric tube manipulator's position in the endoscope cross section is shown

in Figure 2.8. In the absence of constraints, the manipulator's trumpet-shaped workspace can be analytically determined by revolving a circular arc with a cylinder appended, as shown in Figure 2.9. In practice, RFOV can be increased by placing the base of the concentric tube robot a short distance inside the tip of the endoscope, so that the manipulator can begin to curve before passing out of the tip of the endoscope. This modification requires pushing the tube separator from Figure 2.7 a short distance into the tip of the endoscope. Under these conditions, the concentric tube manipulator's workspace is also limited by the boundary shown in Figure 2.8. Important quantities in mathematically describing this boundary on the workspace include the rotation of the inner tube (α_1), the clearance between the manipulator axis and the boundary ($c(\alpha_1)$), the radius of the inner tube (r), the angle subtended by the curved portion of the inner tube (θ), and the critical angle subtended by the inner tube at which it collides with the boundary (θ_c). This angle and the distance behind the tip of the endoscope where the straight tube should end to achieve it, d,

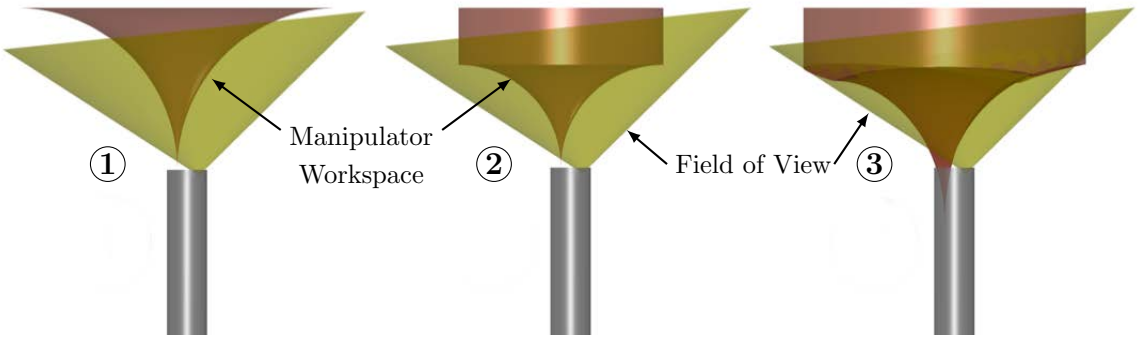

Figure 2.9: Manipulator workspace overlaid on field of view for: ① a tube design of κ=30.1 m^{-1} (RFOV=8.9%), ② optimal design with manipulator base at endoscope tip (κ=47.8 m^{-1}, RFOV=29.5%), ③ optimal design (κ=34.6 m^{-1}, RFOV=64.9%) when the manipulator base is located inside the tip of the endoscope.

are given by

$$\theta_c = \cos^{-1}\left(\frac{c\kappa - 1}{r\kappa - 1}\right), \tag{2.1}$$

$$d = \kappa^{-1}\sin(\theta_c). \tag{2.2}$$

From this, the trumpet-shaped workspace boundary surface, b, can be shown to be

$$b(\alpha_1, \theta) = \begin{bmatrix} -\kappa^{-1}\sin(\alpha_1)(\cos(\theta) - 1) \\ \kappa^{-1}\cos(\alpha_1)(\cos(\theta) - 1) \\ \kappa^{-1}\sin(\theta) - d \end{bmatrix}, \tag{2.3}$$

where $\alpha_1 \in [0\ \ 2\pi)$, $\theta \in [0\ \ \pi/2]$, and an origin on the tube axis at the endoscope tip is assumed as shown in Figure 2.8 – Right. The closed curve defined at $\theta = 90°$ forms the bottom of a cylinder that extends axially to form the remainder of the workspace boundary, which can be accessed by extending out both tubes together.

We began by discretizing the curvature of the inner tube into 100 evenly spaced values within a range of $20\,\mathrm{m}^{-1}$ to $70\,\mathrm{m}^{-1}$. The lower curvature bound was selected because it was clear geometrically that this workspace would have little overlap with the field of view, while the upper curvature bound approaches the limit of a tube that we could shape set. We defined the radius of the inner tube as $r = 0.5\,\mathrm{mm}$ to approximate our initial prototypes. For each curvature, the workspace was computed and the percentage of the visualization volume covered was determined. This was done by discretizing the visualization cone into a total of n isotropic 0.5 mm voxels and counting the n_r total voxels whose centers are inside the manipulator's workspace. This allows us to define the reachable field of view metric as RFOV $= n_r/n$. Three different example cases of overlaid workspace and view volume are shown in Figure 2.9, and RFOV versus κ is shown in Figure 2.10.

The most noteworthy result from this study is that locating the base of the con-

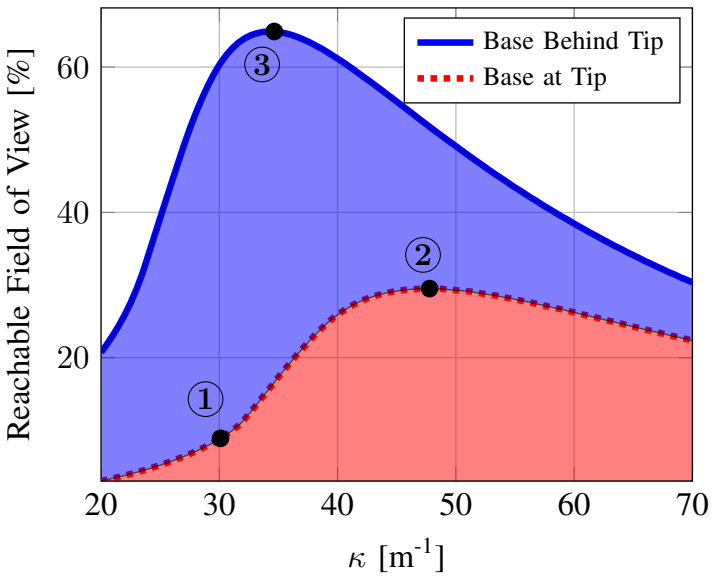

Figure 2.10: Reachable field of view (RFOV) as a function of tube curvature. The three labeled points correspond to the numbered illustrations in Figure 2.9. Base at tip refers to the base of the manipulator being at the tip of the endoscope. Base behind tip refers to the base of the manipulator being located a short distance inside the endoscope.

centric tube manipulator a short distance inside the endoscope behind its tip is useful for reaching the maximum percentage of the visualization volume, with lower required curvature, and that this relationship is very sensitive. Therefore, it is possible to get very large improvements in RFOV by only moving the base of the concentric tube manipulator slightly.

2.6 Manipulator Kinematics and Control

This section begins by discussing the kinematics and Jacobian of the concentric tube manipulators in our hand-held robotic HoLEP system. We then describe the singularity-robust resolved rates algorithm used to map surgeon inputs to manipulator tip motions.

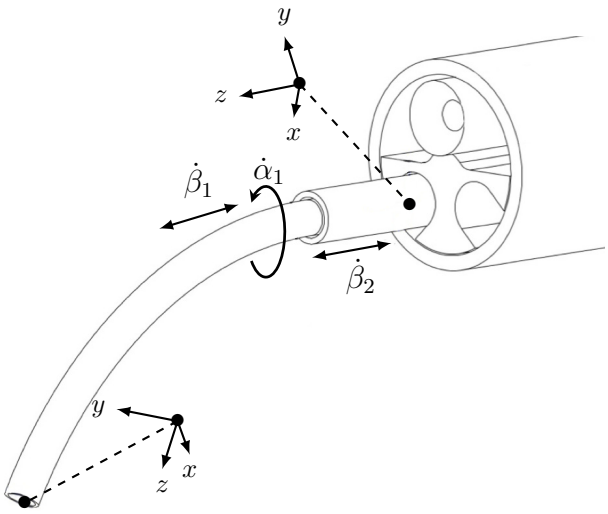

Figure 2.11: The concentric tube manipulators used in our experiments are a special case where the outer tube is straight and stiff and the inner tube is curved and flexible. We define the fixed base frame of the manipulator at the tip of the endoscope, and a body-attached frame at the tip of the inner tube. Rotation of the inner tube, translation of the inner tube, and translation of the outer tube are given by the variables α_1, β_1, and β_2, respectively.

2.6.1 Manipulator Forward Kinematics and Jacobian

The two-tube concentric tube manipulator discussed previously in the design section (Figure 2.11), is a special case of the general concentric tube robot model given in [76, 77]. The general model must be solved numerically, but this special case enables the kinematics and Jacobian of the manipulator to be written in closed form. The actuation variables are $q = \begin{bmatrix} \alpha_1 & \beta_1 & \beta_2 \end{bmatrix}^T$, where α_1 denotes the angular rotation of the inner tube, β_1 denotes the location where the inner tube is held by its carrier, and β_2 denotes the location where the outer straight tube is held by its carrier. We define $s = 0$ at the tip of the endoscope, with positive s out of the endoscope. See Figure 2.4 for an illustration of these variables. Let ℓ_1 and ℓ_2 be the total lengths (i.e. the sum of the straight and curved lengths) of the inner and outer tube, respectively. We define a fixed frame at the endoscope tip, with z-axis tangent to the endoscopic axis, and its x-axis defined as the direction about which the inner tube curves at

$\alpha_1 = 0$, as shown in Figure 2.11. We also define a body attached frame at the tip of the robot with its z-axis tangent to the robot backbone and x-axis in the direction about which the tube curves. Using these definitions, the forward kinematic map, g_{st}, is given by:

$$g_{st} = \begin{bmatrix} R & d \\ 0 & 1 \end{bmatrix}, \quad R = \begin{bmatrix} c_{\alpha_1} & -s_{\alpha_1}c_\gamma & s_{\alpha_1}s_\gamma \\ s_{\alpha_1} & c_{\alpha_1}c_\gamma & -c_{\alpha_1}s_\gamma \\ 0 & s_\gamma & c_\gamma \end{bmatrix}, \quad d = \begin{bmatrix} -\kappa^{-1}s_{\alpha_1}(c_\gamma - 1) \\ \kappa^{-1}c_{\alpha_1}(c_\gamma - 1) \\ l_2 + \beta_2 + \kappa^{-1}s_\gamma \end{bmatrix}, \tag{2.4}$$

where $\gamma = \kappa(\beta_1 - \beta_2 + \ell_1 - \ell_2)$. It is shown in [92], that a spatial Jacobian can be determined from the forward kinematics. We prefer to express the velocity mapping via the hybrid Jacobian, so we convert this spatial Jacobian to a body Jacobian and then express the twists in the fixed frame, which results in the following hybrid Jacobian:

$$J_h = \begin{bmatrix} \kappa^{-1}c_{\alpha_1}(1 - c_\gamma) & \kappa^{-1}s_{\alpha_1}(1 - c_\gamma) & 0 & 0 & 0 & 1 \\ s_{\alpha_1}s_\gamma & -s_\gamma c_{\alpha_1} & c_\gamma & \kappa c_{\alpha_1} & \kappa s_{\alpha_1} & 0 \\ -s_{\alpha_1}s_\gamma & s_\gamma c_{\alpha_1} & 1 - c_\gamma & -\kappa c_{\alpha_1} & -\kappa s_{\alpha_1} & 0 \end{bmatrix}^T \tag{2.5}$$

For a detailed description of this analysis in the context of constant curvature continuum robots, see [93].

2.6.2 Manipulator Control

A singularity exists for this simplified concentric tube manipulator when the two tubes have their tips at the same point, which occurs when the two tubes extend out of the tip of the endoscope the same distance. To account for this singularity, we implemented a singularity-robust resolved rates algorithm based on [94]. The update

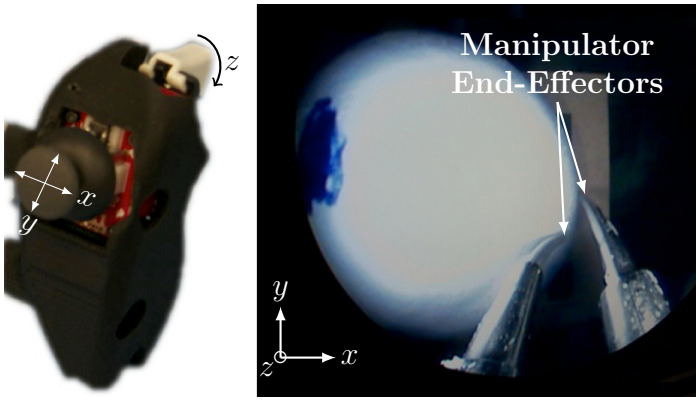

Figure 2.12: (Left) One of the handles of the user interface, illustrating an analog joystick (with pushbutton) and trigger. The joystick provides for two bidirectional inputs, and the trigger gives a third unidirectional input. The pushbutton is used to reverse the direction of the trigger input. (Right) The endoscopic view is shown with the task space mapping from the user interface to the motion of the manipulator end-effectors.

step in this algorithm is given as

$$\dot{q} = (J_h^T J_h + \lambda^2 I)^{-1} J_h^T \dot{x}, \tag{2.6}$$

where

$$\lambda^2 = \begin{cases} 0, & \sigma_m \geq \epsilon \\ (1 - \frac{\sigma_m}{\epsilon}^2)\lambda_{max}^2, & \sigma_m < \epsilon \end{cases}. \tag{2.7}$$

Here ϵ determines how close to singularity one wishes the system to be before implementing the damping factor, λ_{max} is the maximum damping factor, and σ_m is the minimum singular value of J_h, which indicates how well-conditioned the Jacobian is [95].

2.6.3 User Interface Mappings

The surgeon manipulates the concentric tube robots via the embedded joystick (with pushbutton capability) under his/her thumb and an analog trigger under his/her index finger. Initially, likely due to familiarity with manipulating manual clinical

tools through endoscope ports, surgeons expected to prefer direct joint space control of the rotation and axial extension of the tubes. In task space control, surgeons were initially surprised by rapid robot motions near singularities, perceiving these as a lack of control of the concentric tube robot. However, this disagreed with the idea that task space teleoperation is often preferable in robotic systems. To explore this apparent contradiction, we implemented both joint and task space control in order to experimentally compare the two in user studies.

In joint space mode, the index finger trigger was mapped to rotational velocity of the inner tube ($\dot{\alpha}_1$), and upward motion of the joysticks (on each handle) were mapped to translational velocity of the tubes ($\dot{\beta}_1$, $\dot{\beta}_2$). The surgeon was able to reverse the direction of rotation by clicking the joystick and then again depressing the index finger trigger. All commanded velocities were linearly proportional to the deflection of the relevant analog input from thumb joysticks and index finger triggers. In task space mode (shown in Figure 2.12), the tips of the manipulators move relative to the camera frame. Thumb joystick deflections (both vertical and horizontal) were mapped to end-effector velocity commands in the plane of the endoscopic view. The index finger trigger was mapped to end effector velocity perpendicular to the image plane, and clicking the joystick reversed the direction of motion perpendicular to the image plane. In this mode, each manipulator can be independently controlled by the handle on the corresponding side of the robot, which enables bimanual operation.

2.7 Experiments

We evaluate the ability of surgeons to use this system to accomplish surgical objectives through four experiments described in this section. The purposes of these experiments are (1) to explore the surgeons' ability to access a larger area of relevant surgical positions with the robot compared to a standard straight endoscope, (2) to compare the surgeons' ability to follow a desired tip path using task and joint space user

interface mappings, (3) to show that surgeons can use our system to perform a realistic laser resection in an anthropomorphic phantom prostate, and (4) to demonstrate a HoLEP resection procedure on an ex-vivo cadaveric prostate specimen. The expert surgeons in this set of experiments are Dr. Duke Herrell and Dr. Christopher Mitchell.

2.7.1 Desired Resection Surface Access Experiment

One of the primary intended benefits of our robotic system over conventional HoLEP instrumentation is that the manipulators should give the surgeons easier access to resection targets, and/or access to a greater number of useful targets. In this experiment, we set out to evaluate how well the surgeon can access the intended resection surface in the prostate in a geometric sense (i.e. without tissue deformation). This test is conservative, since tissue deformation tends to help expose targets, and therefore make access easier. Disallowing deformation is a starting point in experimental validation of our system only; subsequent experiments will evaluate the ability of surgeons to use our robot for HoLEP under realistic conditions with soft tissue de-

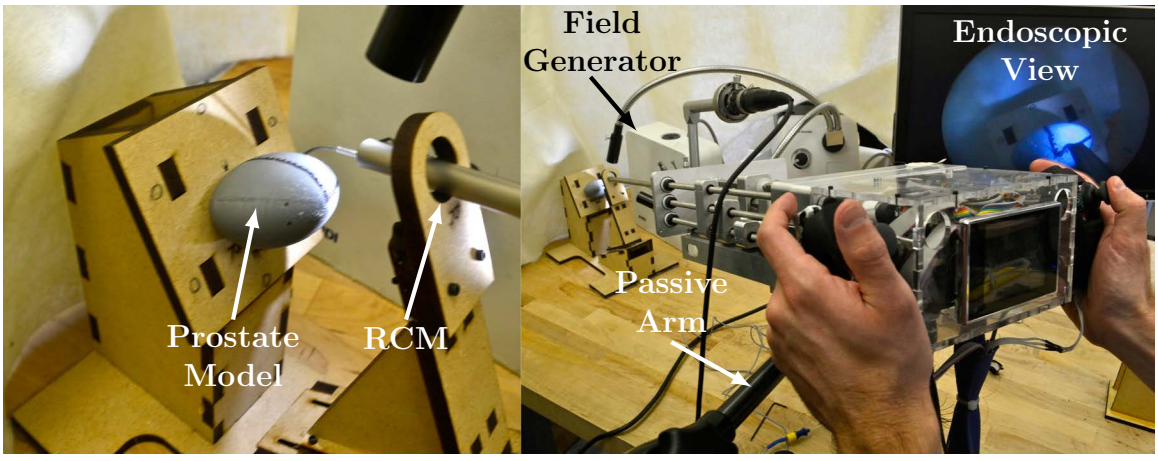

Figure 2.13: The experimental setup constrains the endoscope to operate through an approximate anatomically constrained center of motion. The surgeon scans the desired resection surface (the surface of the plastic model) with the instrument tip using endoscopic video feedback. The instrument tip is magnetically tracked.

formation.

To approximate the remote center of motion (RCM) imposed by the patient's soft tissues in a benchtop setting, we used a wooden support with a hole through it, positioned at an anatomically accurate distance from the prostate resection surface model. To simulate the surgeon's desired surface for laser resection in HoLEP, we affixed a 3D printed ellipsoid of anatomically correct dimensions (30 mm x 42 mm x 47 mm, [96]) made of hard plastic behind this center of motion as shown in Figure 2.13. A magnetic tracking system (Aurora Electromagnetic Measurement System, Northern Digital Inc.) was registered to the test stand, and a 0.5 mm electromagnetic tracking coil was embedded in the tip of the concentric tube robot.

Two experienced urologic surgeons then used the system to scan the surface of the desired resection ellipsoid. One two-tube, 3 DOF manipulator was used under both joint space and task space control and the surgeons scanned one quadrant of the axially symmetric model. This experiment was completed prior to the design of the counterbalance arm, so a passive lockable arm was used to support the robot. It was locked in place during the experiment, but the surgeons were allowed to pause surface scanning, unlock the arm and reposition the robot, and then re-lock the arm and continue scanning, as often as desired during the experiment.

The experimental results are shown in Figure 2.14, and a typical endoscope image during the experiment is shown in Figure 2.15. A cannula tip point was considered to be on the surface of the resection ellipsoid if the point was less than 2 mm from the surface in order to account for test setup registration error and magnetic tracking error. Figure 2.14 illustrates that surgeons were able to access nearly the entire available ellipsoidal surface of the model with both control mappings. The lighter area in Figure 2.14 shows the theoretical reachable area of a conventional, straight endoscope. It was computed using tangent lines to the ellipsoid that pass through the RCM. This experiment shows that our robot is capable of reaching points relevant

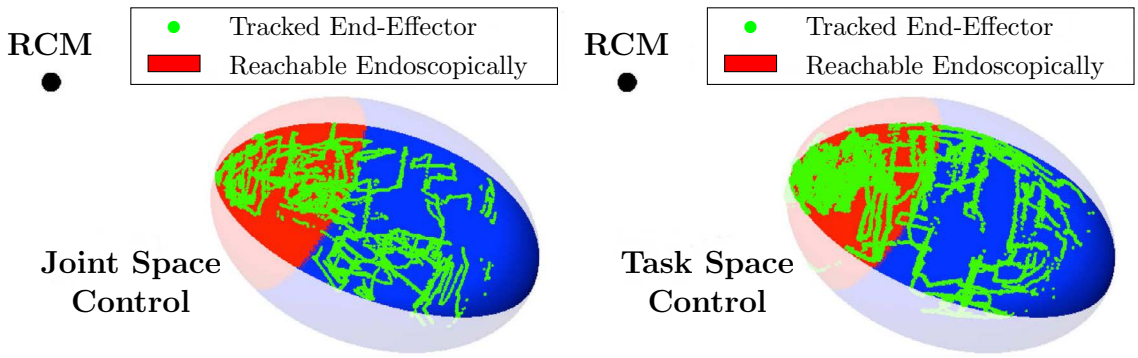

Figure 2.14: Magnetic tracking data showing the positions on the desired resection surface accessed by two surgeons using the system in joint space mode (Left) and task space mode (Right). The lighter colored region indicates the best-case scenario for the surface reachable by a conventional straight endoscope, without tissue deformation (i.e. the reachable area without using the robot and using only a straight, rigid endoscope).

to prostate resection. Tissue deformation is evaluated in subsequent experiments. In addition, this experiment did not reveal a difference between joint and task space operation in terms of reachability, which motivated experiments to compare them in terms of trajectory tracking, as described in the following subsection.

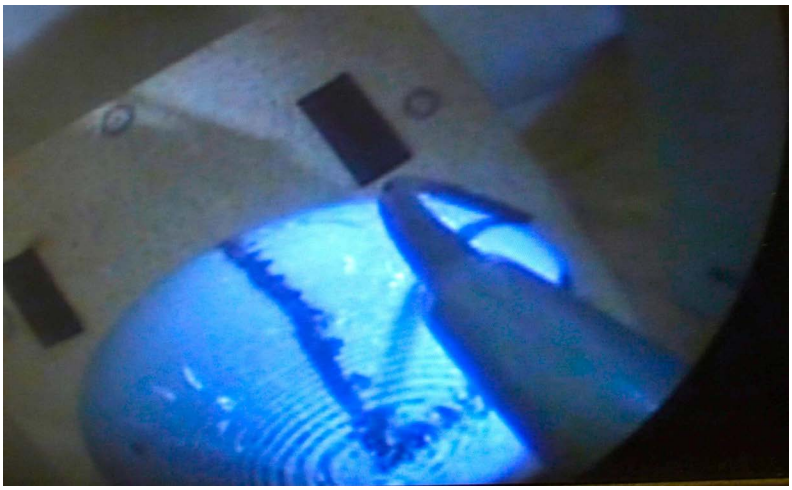

Figure 2.15: Endoscopic view of a surgeon scanning the desired resection surface model.

2.7.2 Trajectory Tracking Experiment

This experiment used the experimental setup described in the previous subsection, but rather than asking surgeons to scan the surface we asked them to follow a specified three-dimensional curve along the surface. Both accuracy and task completion time were recorded, and surgeons were alerted to the fact that both metrics would be used for evaluation before the experiment commenced. This experiment was done once with the arm unlocked (so that the surgeons could position and orient the endoscope as well as the concentric tube manipulators to follow the path) and once with the arm locked (requiring surgeons to use only the concentric tube manipulators, without changing the endoscope pose). The paths for the two scenarios can be seen in Figure 2.16. These paths were drawn on the model with input from the surgeons and are intended to approximate the circumferential cuts required in a HoLEP procedure. Nevertheless, the primary aim of this experiment was to characterize the surgeon's ability to follow a desired tip path using different control modes. The ability to accomplish the entirety of a HoLEP procedure is not evaluated here, but rather in subsequent phantom and cadaver experiments presented in subsections 2.7.3 and 2.7.4.

The first path was traced with counterbalance assistance by two surgeons, each using both control modes on separate trials, each performing two trials per mode,

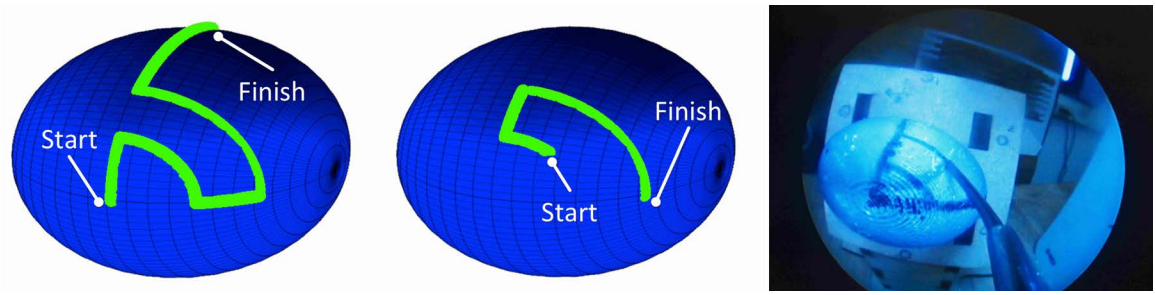

Figure 2.16: (Left) Desired path of concentric tube robot tip for the experiment with free endoscope manipulation. (Center) Desired path of concentric tube robot tip for the experiment with a fixed endoscope pose. (Right) Concentric tube robot following the desired path on the prostate resection surface model.

yielding a total of eight experimental runs. The mean accuracies for both control modes with counterbalance assistance were 1.5 mm for joint space and 1.6 mm for task space. The maximum error during each run averaged 6.4 mm with joint space control and 4.3 mm with task space control. Total time to complete the task averaged 70.2 s for joint space control and 41.9 s for task space control. These results indicate that the surgeons are capable of using either control mode to follow the prescribed path, but that joint space mode required substantially more time, while also occasionally resulting in relatively large errors. Figure 2.17 illustrates time surgeons spent at various levels of error.

Noting qualitatively that surgeons were using substantial endoscope manipulation – particularly with joint space control – we performed another similar experiment in which we fixed the endoscope pose by locking the counterbalanced support arm. Surgeons were then asked to trace the path shown in the center of Figure 2.16 using only the concentric tube manipulators. Again, two surgeons attempted to complete this task in both control modes, twice each per mode, for a total of eight experimental runs.

The results of this experiment showed substantial differences for joint and task space control. First, task space control results did not change substantially from the free endoscope experiment, with a mean error of 1.6 mm and an average maximum error of 4.0 mm. The only significant difference in comparing task space control in this experiment to task space control with free endoscope movement was that surgeons traced the path more slowly. It took them approximately the same amount of time (40.3 s) to trace a shorter path in this experiment as it did to trace the longer path in the experiment with free endoscope manipulation.

The joint space control results, however, revealed a sharp contrast between free endoscope manipulation and fixed endoscope pose. Completion of the task was not achievable within a reasonable amount of time for the surgeon using joint space control

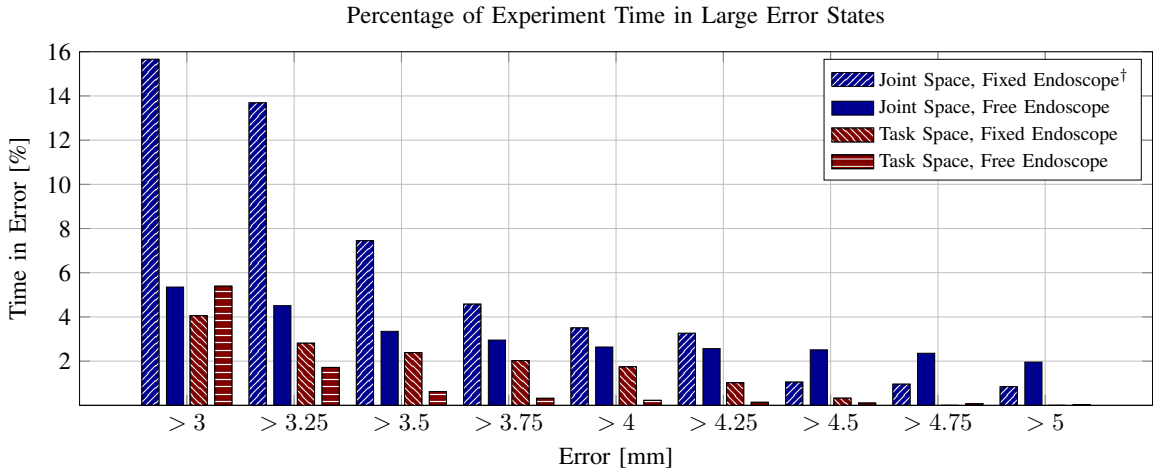

Figure 2.17: An illustration of the time spent at various levels of error in the two path tracing experiments, with and without endoscope pose manipulation. †The surgeons requested termination of this experiment prior to completion.

with a fixed endoscope. On all four runs, the experiment was ended at surgeon request after an average time of 2 minutes, with over 15% of the time spent in excess of 3 mm error. We do not report the mean or maximum error since the task could not be completed, but the percentage of experiment time spent in large error states is shown in Figure 2.17. This indicates that the joint space control mapping was too mentally taxing for the surgeons to achieve rapidly and accurately without the assistance of endoscope pose manipulation. This means that surgeons were likely primarily using endoscope pose manipulation to trace the path in the corresponding experiment with free endoscope manipulation. This agrees with prior results where increased mental fatigue was noted with joint space operation of 3D flexible endoscopes, in which it was noted that operating these devices "quickly overwhelms the mental and motor abilities of most surgeons" [97].

2.7.3 Laser Resection of an Anthropomorphic Prostate Phantom

In this experiment, we set out to experimentally test our system in a realistic HoLEP model. We aimed to evaluate the performance of the system in an anatomically

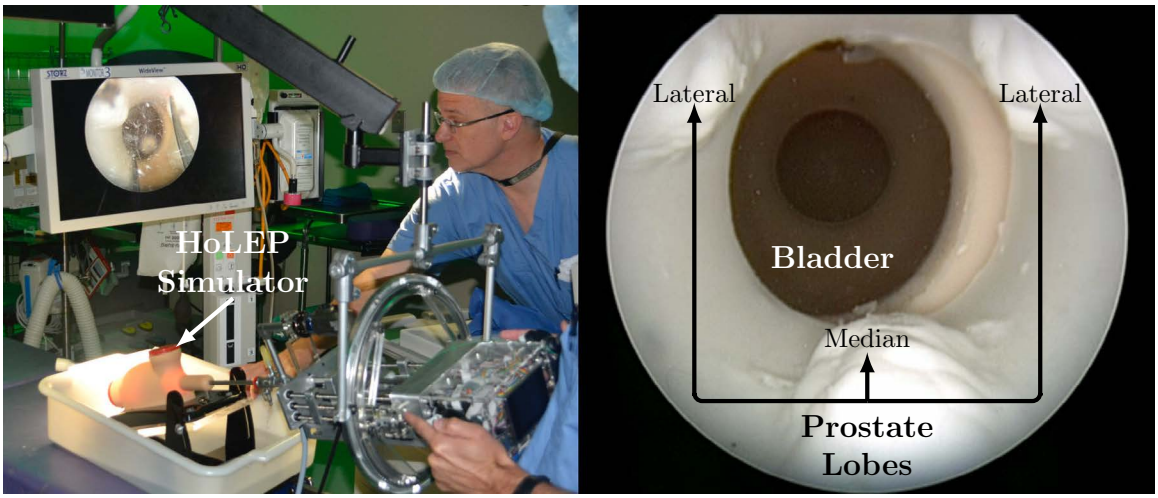

Figure 2.18: (Left) The counterbalanced robot operates transurethrally through the HoLEP simulator. The surgeons visually servo the concentric tube manipulator tips in task space with high definition endoscopic video feedback. (Right) The endoscopic view shows the three lobes of the synthetic prostate. Each surgeon was tasked with laser resecting one lobe of the prostate phantom.

Figure 2.19: (Left) The left manipulator retracts the tissue, exposing the targets for the right manipulator to cut with the holmium laser. (Right) A photograph of what the prostate model looked like before and after the experiment.

accurate model, and to explore the surgeon's ability to coordinate two concentric tube manipulators simultaneously (one to expose tissue and one to laser resect tissue).

We utilized a TruLase Prostate HoLEP simulator (TPR100, TruCorp Ltd.), which is designed for training surgeons in HoLEP (see Figure 2.18). This anatomically accurate simulator enables laser enucleation of a synthetic prostate specimen in a fluid-filled environment that mimics the conditions in clinical HoLEP surgery. The surgeon used both concentric tube manipulators in task space control, with a 500 μm holmium laser fiber passed through one manipulator, and the other used for tissue retraction. Both manipulators were identical two-tube, 3-DOF devices, as shown in Figure 2.11.

The simulator was filled with saline solution and endoscopic saline irrigation was used in the same manner as in a clinical HoLEP procedure. The synthetic prostate used in this experiment was the three lobe prostate insert (TPRO-03, TruCorp Ltd.) as shown in Figure 2.18. A clinical 80 W holmium laser was used, and the surgeon could fire the laser on demand using a foot pedal, just as they would in a clinical HoLEP case. The counterbalance arm was used and the endoscope (and robot) were free to be spatially oriented as desired. Two surgeons were asked to laser resect and remove a single lobe of the prostate and push it into the bladder, just as they would in a clinical HoLEP case (the specimen then gets morcellated within the bladder in the current clinical HoLEP procedure, and our system is designed to follow the same protocol for specimen removal). There were no restrictions or instructions regarding use of robotic manipulators versus endoscope pose control; surgeons were free to use both as they wished. Qualitatively we noticed that surgeons manipulated both endoscope pose and concentric tube manipulators simultaneously during the procedure and were not relying primarily on endoscope pose manipulation. It is also worth noting that this was each surgeon's first experience using both manipulators simultaneously.

Two lobes were successfully laser resected from the prostate model and pushed

into the bladder, one by each surgeon. One surgeon removed the median lobe (the lobe in the center of Figure 2.18), while the other removed one of the lateral lobes. The post-experiment synthetic prostate model can be seen in Figure 2.19. After a short learning curve in which the surgeons focused primarily on the laser arm, surgeons began to use coordinated movement of both arms, increasingly relying on retraction from the retraction arm. The retraction arm was used to expose desired targets within tissue and the laser arm to cut the exposed surface with the laser.

2.7.4 Ex-Vivo Laser Resection of a Cadaveric Prostate Specimen

To evaluate the system in biological tissues we used a dissected urethra, prostate, and bladder specimen for a lobe removal experiment similar to that conducted in phantoms in the previous section. The surgeon's goal in this experiment was to remove one of the lateral lobes of the prostate (the lateral lobes are considered more challenging to remove than the median lobe).

A challenge in this experiment was holding the specimen in a manner that approximates the surrounding tissue constraints present in the human body. To approximate

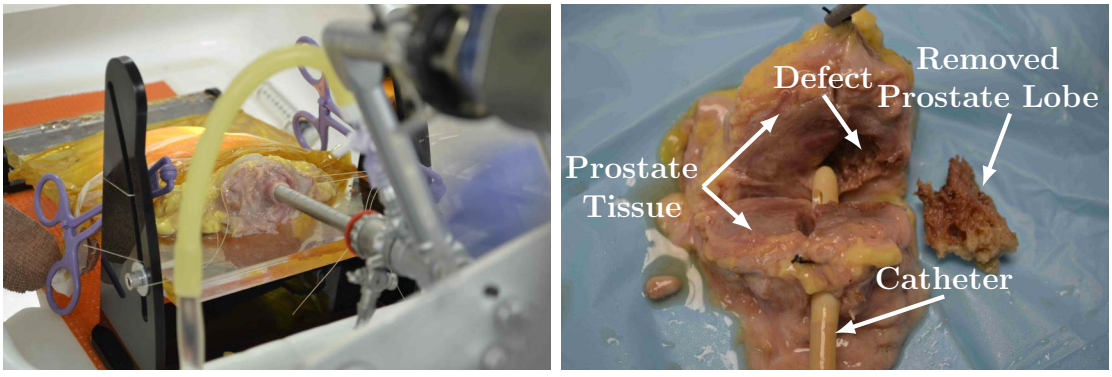

Figure 2.20: (Left) The experimental setup shows the endoscope inserted into the specimen. The specimen is held with an adhesive plastic wrap and sutures through the specimen and the test stand. (Right) The dissected, sectioned post-operative specimen is shown. A catheter is placed through the urethra for reference, and the robotically removed 2.7 g lateral lobe is shown next to the specimen. The defect in the prostate where the lobe was removed is also visible.

these, we used sutures to loosely hold the specimen in place, with a layer of adhesive plastic wrap to provide a compliant support to the bladder, prostate, and urethra. To perform the resection we again used the clinical 80 W holmium laser, which the surgeon could fire on demand using a foot pedal. Saline irrigation was provided through the endoscope, both manipulators were active, and the counterbalance was used. The experimental setup is shown in Figure 2.20 and two endoscopic views are shown in Figure 2.21.

The surgeon successfully removed a 2.7 g lateral lobe from the specimen (see Figure 2.20), using the robotic system for the entire procedure. The surgeon was able to resect the tissue up to the outside edge of the prostate (i.e. the prostate capsule) and enucleate the lobe, following the capsule around the organ during enucleation, mimicking the current surgical technique. The dissected and sectioned lobe of the prostate is shown postoperatively in Figure 2.20. We did note one small capsule perforation, indicating the need for further refinement and testing of the system, as well as perhaps the need for additional surgeon experience and training with the robot system (this was the surgeon's first cadaver case with the system). Future experiments are also needed to compare the robot to standard HoLEP in terms of procedure completion time, correspondence of actual enucleation volume to planned enucleation volume, and complication rates.

2.8 Summary and Future Work

This chapter has introduced a new system that enables hand-held coordination of both an endoscope and two concentric tube manipulators delivered through its 5 mm working channel. One useful feature of this robot is that it fits seamlessly into the clinical workflow of the HoLEP procedure in the sense that the surgeon maintains hand-held control of the endoscope and the patient and surgeon positions in the operating room are the same as in the current clinical workflow. We presented the

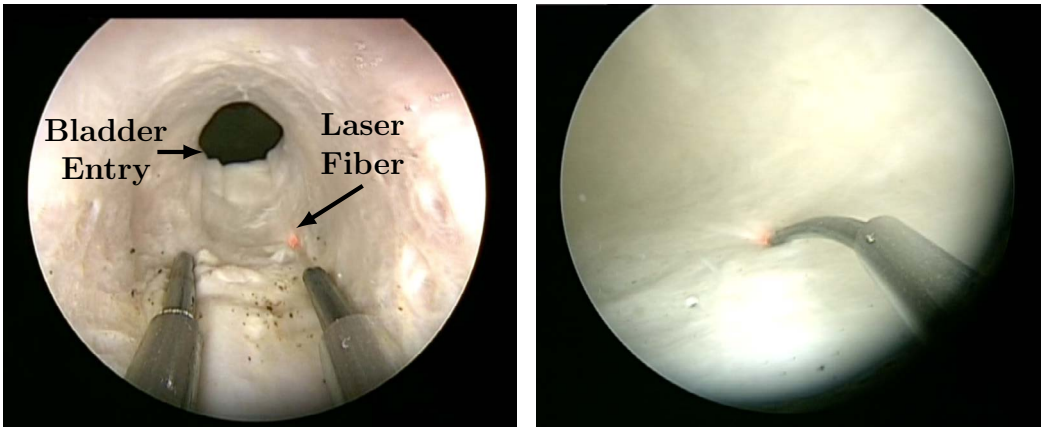

Figure 2.21: (Left) An endoscopic view inside of the prostatic urethra shows both manipulators. (Right) The laser manipulator is shown endoscopically in the bladder.

mechanical design of the system and a method to select tube parameters in the concentric tube manipulator for optimal overlap of the manipulator's workspace and the endoscope's field of view. We also described the kinematics of the system and compared task and joint space control mappings via user studies with surgeons. This user study showed that the experimenting surgeons spent more time in large error states when utilizing joint space mode. Lastly, we described initial phantom and cadaver studies, which showed that the system can be used by surgeons to resect prostate lobes with the holmium laser.

In future studies, the system should be compared directly against the current manual approach in a series of user studies with experienced surgeons to explore the hypothesis that this robot system has the potential to make HoLEP surgery easier to perform accurately and safely. If this hypothesis is proved correct, then the robot described in this chapter may pave the way to wider use of the HoLEP procedure, and thereby enable many more patients to benefit from its demonstrated clinical benefits. We also believe that the basic concept behind our system, namely hand-held control of concentric tube robots extending through endoscopes, is generalizable to many other locations in the human body. Examples include endonasal surgery, throat surgery, brain surgery (which will be described in Chapter 5), and other surgeries that can

benefit from dexterity in manipulators delivered through endoscopes. We believe that the hand-held paradigm is broadly applicable in surgical robotics, and user interfaces like the one we propose in this chapter are a key to making them fit well enough into the existing workflow of the operating room that clinical personnel can easily adopt them.

CHAPTER 3

BIFURCATION AND ELASTIC STABILITY OF CONCENTRIC TUBE ROBOTS

Chapter 2 described a hand-held robotic system for laser prostate surgery which delivered two concentric tube robots through an endoscope. The tube design in Chapter 2 was simplified to prevent elastic instability from being possible by utilizing a straight outer tube. However, this simplified set of tubes introduces other problems including the loss of a degree of freedom, a singularity in the center of the workspace, and decreased dexterity. Therefore, we would prefer to use multiple curved tubes for these transendoscopic applications, but this necessitates an understanding of elastic stability of these flexible concentric tube structures.

The aim of this chapter is to address fundamental theoretical questions surrounding elastic stability of concentric tube robots, so that more advanced tube designs, which provide enhanced dexterity and functionality can be used in future transendoscopic concentric tube robot designs, including the system presented in Chapter 5. In particular, we seek to determine design bounds that guarantee an elastically stable system and a measure to indicate "closeness" to instability.

The content of this chapter is mainly adapted from the journal publication "Elastic Stability of Concentric Tube Robots: A Stability Measure and Design Test," which was published in *IEEE Transactions on Robotics*[1] and co-first authored with Dr. Hunter Gilbert [37], and also includes results published at a conference [33].

[1] © 2015 IEEE. Reprinted, with permission, from Hunter B. Gilbert, Richard J. Hendrick, and Robert J. Webster III, Elastic Stability of Concentric Tube Robots: A Stability Measure and Design Test, IEEE Transactions on Robotics, December 2015.

3.1 Introduction to Elastic Stability in Concentric Tube Robots

Concentric tube robots appear promising in many kinds of minimally invasive surgical interventions that require small diameter robots with articulation inside the body. Examples include surgery in the eye [98], heart [99], sinuses [100], lungs [101], prostate [52], brain [39], and other areas. In most of these applications, higher curvature is generally desirable to enable the robot to turn "tighter corners" inside the human body and work dexterously at the surgical site. In the context of transendoscopic surgery, the precurvatures of the tubes determine how closely the manipulators can work to the tip of the endoscope, which is very important during endoscopic surgery.

However, it was noted early in the development of concentric tube robots that unless gradual tube curvatures are used or minimal overlap of curved tube sections is ensured, tubes can exhibit elastic instabilities [27] (also previously referred to as "snaps" and "bifurcations"). Elastic instabilities occur due to torsional elastic energy storage in the tubes that make up a concentric tube robot. An instability occurs when this energy is rapidly released, and the robot "snaps" to a new configuration. Unforeseen snapping is clearly not desirable and could be dangerous in surgical applications.

The snapping problem has been approached from design, modeling, and planning perspectives. With the exception of the early work in [27], these studies have used the mechanics-based model of concentric tube robots found in [28, 29]. For example, it has recently been shown that tubes can be laser machined to reduce the ratio of bending to torsional stiffness, which improves stability [30, 31]. However, even using this approach, snaps will still occur if high curvatures are employed, so methods for design and snap prediction will still be needed. Another approach is to use non-constant precurvature tubes to enhance the elastic stability, as shown by Ha et al. [34, 36]. In that work, analytical stability conditions for a two-tube robot with planar precurvatures are presented, and an optimal control problem is formulated to

design tube precurvatures which result in a completely stable actuation space. The work in this chapter complements theirs by analyzing the stability of robots which possess unstable configurations in their actuation space. We also consider designs of an arbitrary number of tubes with more general precurvature. It is important to note that, at the same time this dissertation work was being completed, these same problems were also approached independently from an optimal control perspective, which generated similar theoretical results that were published in [38].

It is also possible to plan stable paths for robots that do have the potential to snap, as shown by Bergeles et al. [39, 102, 103], by examining the relative axial angle between the base of a tube and its tip for all possible rotations for a given set of tubes. While this work provides a method to design and use high-curvature robots, the stability condition chosen by the authors was stated as a definition. Another model-based approach is that of Xu et al. [35], who sought design parameter bounds for constant curvature robots to ensure a snap-free unloaded robot workspace. Xu et al. provided exact design bounds for a two-tube robot and non-exact, conservative bounds for robots with more than two tubes. In addition, the solutions in [35] for more than two tubes only apply to robot configurations where the precurved portions of tubes are precisely aligned in arc length.

3.2 Contributions

In this chapter, we characterize the solution multiplicity and elastic stability of unloaded concentric tube robots with any number of tubes, each of which may be preshaped as a general space curve. We do this by analyzing the stability properties predicted by the accepted model which has been experimentally validated in the literature [28, 29]. We connect concentric tube robot stability analysis to the analysis of post-buckled Euler beams from the mechanics literature [104, 105, 106]. Based on this analysis, we also propose a measure for relative stability, which can be used to

inform real-time controllers, planners, and automated designers to safely design and operate a robot that would otherwise snap. We also show that from the perspective of bifurcation theory [26], one can derive an exact, analytic method which predicts stability properties throughout the entire actuation space of a concentric tube robot with constant precurvature tubes.

3.3 The Beam Buckling Analogy

A two-tube concentric tube robot and a loaded beam are analogous systems, and both systems exhibit buckling and snapping. To build intuition, we begin by describing these analogous behaviors. Concentric tube robots are controlled by prescribing relative translations and rotations at the proximal ends of the tubes. The tubes twist and bend one another along their arc length s. When there are two circularly precurved tubes the twist angle between them, $\theta(s)$, is governed by the same differential equation as a beam under a dead load as shown in Figure 3.1. The configuration of both systems is determined by the nonlinear boundary value problem

$$f[\lambda, \theta(s)] = \theta'' - \lambda \sin(\theta) = 0, \;\; \theta(0) = \theta_0, \;\; \theta'(1) = 0 \; , \tag{3.1}$$

where the equations have been normalized to unit length, so that $0 \leq s \leq 1$. For both the beam and the concentric tube robot, it is known that increasing values of the parameter λ can lead to buckling and instability. For the beam, this parameter is controlled by the material properties, the geometry, and the magnitude of the dead load. Likewise, for the robot, λ involves the material properties and geometry of the tubes, but the dead load is replaced by the influence of the tube precurvatures.

In the set of solutions to (3.1), two straight, trivial beam configurations exist: $\theta(s) = 0$ and $\theta(s) = \pi$, which represent the beam in pure tension and compression, respectively. Similarly, for concentric tubes, two torsionless, trivial solutions exist in

which the tube precurvatures are aligned and anti-aligned, respectively. Just as a beam in tension cannot buckle, a robot configuration with aligned precurvatures is stable. In contrast, when the beam is compressed (Figure 3.1a) or when the concentric tube robot has anti-aligned precurvatures (Figure 3.1b), the configurations which are straight for the beam and torsionless for the robot can buckle if λ exceeds a critical value. Buckling occurs because the solution to (3.1) becomes non-unique when λ is large enough, and two new, energetically favorable solutions arise in a process known

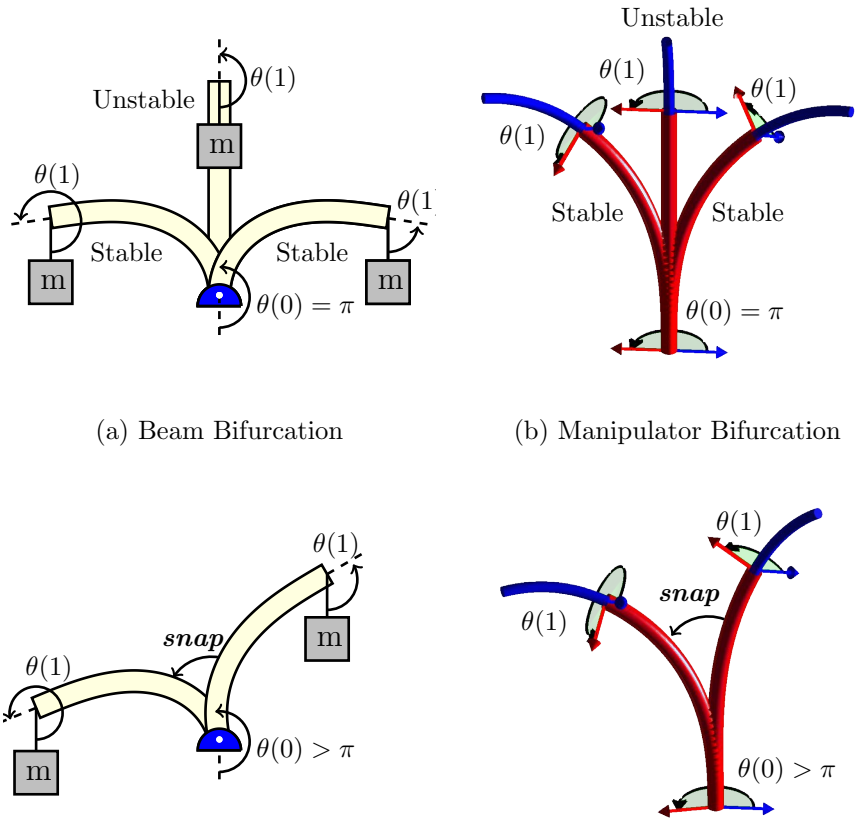

(a) Beam Bifurcation

(b) Manipulator Bifurcation

(c) Beam Snapping

(d) Manipulator Snapping

Figure 3.1: The analogy between an Euler beam and a two-tube concentric tube manipulator for λ greater than its critical value. For the beam, $\theta(s)$ denotes the angle of the beam, while for the manipulator it denotes the angle between precurvature vectors. (a, b) There are three solutions when $\theta(0) = \pi$. The straight/torsionless solution is unstable and the two buckled solutions are stable. (c, d) At some $\theta(0) > \pi$, the beam/manipulator snaps into a new, stable configuration. Note that the value of $\theta(0)$ when the snap occurs depends on λ.

as bifurcation (see Figure 3.1a and 3.1b). The two new solutions are stable, and the original solution becomes unstable at the point of bifurcation.

For many applications of beam theory, like column buckling, the instability of the trivial, straight configuration is all that is important, but concentric tube robots typically operate far from these areas and may exhibit instability at other configurations and snap across their workspace as shown in Figure 3.1d. The equivalent phenomenon for a beam is shown in Figure 3.1c. Consider an active counter-clockwise beam rotation of $\theta(0)$ starting from $\theta(0) = 0$. If λ is small enough, we expect that the beam will pass stably through a straight configuration when $\theta(0) = \pi$, and the concentric tube robot will pass stably through the configuration with anti-aligned precurvatures. On the other hand, when λ exceeds the critical value, even when $\theta(0) = \pi$, the beam will never straighten out and will instead settle into a buckled configuration, and the concentric tube robot will settle into a high-torsion configuration. Eventually, as $\theta(0)$ increases to some value beyond π, the buckled configuration becomes unstable and some of the stored energy is released as each system snaps to a new configuration.

In our stability analysis, since we control $\theta(0)$ for concentric tube robots, we seek the value of $\theta(0)$ at which a concentric tube robot will snap. In the beam buckling literature, this problem is referred to as the stability of postbuckled equilibrium states, and important results have emerged in this area in recent years [104, 105, 106]. There has also been recent interest in robotics in the stable quasistatic manipulation of rods [107]. Before applying these results to concentric tube robots, we first present the mechanics-based kinematic model.

3.4 Concentric Tube Robot Kinematics

In Chapter 2, we found the kinematics for a simplified concentric tube robot which could not become elastically unstable. Now, we provide a self-contained description of the more general kinematic model which is derived from energy, which we will

use heavily later in this chapter to derive stability results. The kinematic model presented here was first derived in [29] and [108]. We present the model in a concise form suitable for implementation, and discuss the simplification of the multi-point boundary value problem to a two-point boundary value problem, which was also mentioned in [29]. We choose the angle of twist and the torsional moment as the model states, which results in continuous solutions even across discontinuities caused by precurvature functions or tube endpoints.

Table 3.1 provides a list of variable definitions, and Figure 3.2 shows the frame definitions for each tube. Each tube has a predefined shape which is described with a material-attached coordinate frame assignment $\boldsymbol{g}_i^*(s_i) = (\mathbf{R}_i^*, \boldsymbol{p}_i^*) : \mathbb{R} \to SE(3)$, where $\boldsymbol{p}_i^*(s_i)$ is the origin of the frame and $\mathbf{R}_i^*(s_i)$ is the orientation of the frame. The frame propagates along the tube with its $\boldsymbol{z}$-axis tangent to the tube centerline and with unit velocity so that the variable s_i is arc length along the i^{th} tube, and $0 \leq s_i \leq L_i$, where L_i is the length of the tube. Without loss of generality, the frames $\boldsymbol{g}_i^*$ are chosen as Bishop frames and obey the differential relationship

$$\frac{\partial}{\partial s_i}\boldsymbol{g}_i^*(s_i) = \boldsymbol{g}_i^*(s_i)\widehat{\boldsymbol{\xi}}_i^*(s_i)$$

for $\widehat{\boldsymbol{\xi}}_i^*(s_i) \in \mathfrak{se}(3)$. In this case, the "hat" denotes the conversion $\widehat{(\cdot)} : \mathbb{R}^6 \to \mathfrak{se}(3)$ as defined in [109]. By the preceding definitions, $\boldsymbol{\xi}_i^*(s_i) = \begin{bmatrix} (\boldsymbol{v}^*)^T & (\boldsymbol{u}_i^*(s_i))^T \end{bmatrix}^T$, with $\boldsymbol{v}^* = \boldsymbol{e}_3$ and $\boldsymbol{u}_i^*(s_i) = \begin{bmatrix} u_{ix}^*(s_i) & u_{iy}^*(s_i) & 0 \end{bmatrix}^T$.

The model assumes that the combined tubes follow a common centerline, which we define as another Bishop frame $(\mathbf{R}_B, \boldsymbol{p}_B)$. After the conformation of the tubes, we define the resulting material-attached frame of each tube as $\boldsymbol{g}_i = (\mathbf{R}_i, \boldsymbol{p}_i)$. While the $\boldsymbol{z}$-axes of each $\boldsymbol{g}_i$ frame must lie tangent to the $\boldsymbol{z}$-axis of $\mathbf{R}_B$, the other axes are free to rotate axially with respect to one another. Thus we have, by definition, that $\mathbf{R}_i = \mathbf{R}_B\mathbf{R}_{\psi_i}$ where $\mathbf{R}_{\psi_i}$ is shorthand for the standard $\boldsymbol{z}$-axis rotation about

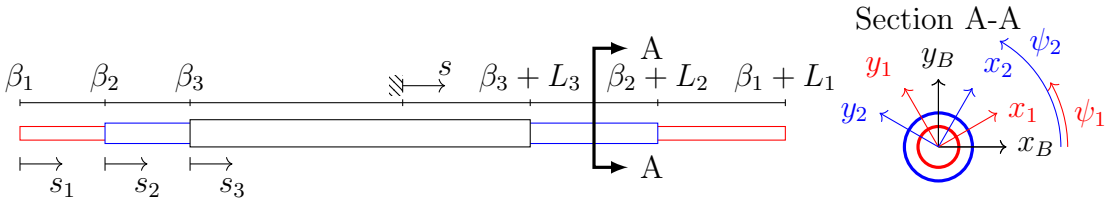

Figure 3.2: A depiction of a three tube concentric tube robot which has been straightened for clarity. The arc length variables and body-attached frame assignments needed for the kinematic model are illustrated. © 2015 IEEE.

Table 3.1: Nomenclature

$\boldsymbol{a}$	Bold typeface for vectors
$\mathbf{A}$	Bold, upright typeface for matrices
n	Number of tubes in concentric tube robot
$\boldsymbol{p}_B$	Position of backbone Bishop frame
$\mathbf{R}_B$	Rotation matrix of backbone Bishop frame
ψ_i	Angle between the material frame of tube i and $\mathbf{R}_B$
$\mathbf{R}_\psi$	Canonical rotation about z-axis of angle ψ
$\boldsymbol{u}_B$	Bishop frame curvature
$\widehat{\cdot}$	The conversion from $\mathbb{R}^3$ to the cross product matrix
$(\cdot)^\vee$	Inverse function of $\widehat{\cdot}$, i.e. $(\widehat{\boldsymbol{x}})^\vee = \boldsymbol{x}$
$(\cdot)^*$	Denotes variable in undeformed state
$\boldsymbol{u}_i^*$	Precurvature of the i^{th} tube in the local material frame
k_{ib}	Bending stiffness of tube i
k_{it}	Torsional stiffness of tube i
$\mathbf{K}_i$	Linear elastic constitutive map
β_i	Arc length where tube i is held
α_i	Absolute rotational actuation of tube i
L_i	Total length of tube i
β	$\min_i\{\beta_i\}$
L	$\max_i\{\beta_i + L_i\}$
$(\cdot)'$	Derivative with respect to arc length/dimensionless length
$\boldsymbol{e}_i$	i^{th} standard basis vector
$\boldsymbol{u}_i$	Curvature of the i^{th} tube in the local material frame
θ_i	Relative angle $\psi_i - \psi_1$
$h, \boldsymbol{h}, h_i$	Allowable variation function(s)
$\boldsymbol{\mathcal{S}}$	Linear second variation operator
σ	Dimensionless arc length
F_α	Partial derivative of a function F with respect to α
λ	Bifurcation parameter

the angle ψ_i. The curvature of the i^{th} tube is $\boldsymbol{u}_i = \left(\mathbf{R}_i^T \mathbf{R}_i'\right)^\vee$. Since the predefined frame assignment $\boldsymbol{g}_i^*$ is chosen in the Bishop convention, ψ_i' is proportional to the axial moment carried by the i^{th} tube.

The energy of each tube is given according to the Kirchhoff kinetic analogy, in which the stored elastic energy is that of a slender rod that undergoes bending and torsion, but not elongation or shear, according to an arc-length parameterized linear elastic constitutive map $\mathbf{K}_i(s_i) : \mathbb{R}^3 \to \mathbb{R}^3$ from curvature to moment. When expressed in the frame $\mathbf{R}_i$, the constitutive map is diagonal for annular tubes,

$$\mathbf{K}_i(s_i) = \begin{bmatrix} k_{ib}(s_i) & 0 & 0 \\ 0 & k_{ib}(s_i) & 0 \\ 0 & 0 & k_{it}(s_i) \end{bmatrix}, \tag{3.2}$$

where k_{ib} represents the bending stiffness, and k_{it} represents the torsional stiffness. Then, the total energy for n tubes is given by

$$E[\boldsymbol{u}_1, ..., \boldsymbol{u}_n] = \sum_{i=1}^{n} \int_0^{L_i} \Delta \boldsymbol{u}_i^T \mathbf{K}_i \Delta \boldsymbol{u}_i \, ds_i \,, \tag{3.3}$$

where $\Delta \boldsymbol{u}_i = \boldsymbol{u}_i - \boldsymbol{u}_i^*$. The robot arc length s is defined so that $s = 0$ occurs at the constrained point where the tubes exit the actuation unit. The tubes are actuated at robot arc lengths $\beta_i \leq 0$ so that we have n functions $s_i(s) = s - \beta_i$, which relate the robot arc length to the tube arc length. The robot arc length s is then defined on the interval $\beta \leq s \leq L$ where

$$\beta = \min_i \{\beta_i\}, \;\; L = \max_i \{\beta_i + L_i\} \tag{3.4}$$

The actuators also impose rotational actuation of the tubes, modeled as the algebraic conditions $\psi_i(\beta_i) = \alpha_i$. The various functions of interest, $\boldsymbol{u}_i$, ψ_i, $\mathbf{K}_i$, etc. may thus be considered functions of either s_i or of s. From here forward, when an expression

explicitly includes any function with the robot arc length s as an argument, all other functions in the expression are assumed, unless otherwise noted, to be evaluated at s as well.

Define the operator $[\cdot]_{xy}$ as the orthogonal projection onto the first two coordinate axes, i.e. $[\boldsymbol{x}]_{xy} = \left(\mathbf{I} - \boldsymbol{e}_3\boldsymbol{e}_3^T\right)\boldsymbol{x}$. It has been previously shown in the literature by Rucker et al. [108] and Dupont et al. [29] that under these assumptions, extremals of the energy functional require that the backbone curvature $\boldsymbol{u}_B = \left(\mathbf{R}_B^T\mathbf{R}_B'\right)^\vee$ satisfy

$$[\boldsymbol{u}_B(s)]_{xy} = \left[\mathbf{K}^{-1}\sum_{i\in P(s)}\mathbf{K}_i\mathbf{R}_{\psi_i}\boldsymbol{u}_i^*\right]_{xy}, \tag{3.5}$$

with

$$\mathbf{K}(s) = \sum_{i\in P(s)}\mathbf{K}_i(s)\ ,$$

and the set $P(s) = \{i \in \mathbb{N} : 1 \leq i \leq n \wedge 0 \leq s_i(s) \leq L_i\}$ is the set of indices of tubes which are present at the arc length s. Note that by definition, $\boldsymbol{u}_B \cdot \boldsymbol{e}_3 = 0$.

Since the unknowns $\boldsymbol{u}_i$ in (3.3) are related algebraically to $\boldsymbol{u}_B$ through ψ_i, the energy functional may be written in the form

$$E[\boldsymbol{\psi}] = \int_\beta^L F(\boldsymbol{\psi}, \boldsymbol{\psi}', s)\, ds$$

where $\boldsymbol{\psi} = \begin{bmatrix}\psi_1 & \dots & \psi_n\end{bmatrix}^T$. After substituting the relation $\boldsymbol{u}_i = \mathbf{R}_{\psi_i}^T\boldsymbol{u}_B + \psi_i'\boldsymbol{e}_3$ into $\Delta\boldsymbol{u}_i$ and the resulting expression into the energy functional, the Euler-Lagrange equations can be applied directly to this functional for each pair of variables ψ_i, ψ_i'. After some simplifications arising from the equal principal bending stiffnesses and the choice of precurvature frames, the kinematic equations are found.

Concentric Tube Robot Kinematics. The spatial configuration of a concentric

tube robot is determined by the solution to a boundary value problem with first order states ψ_i, $(k_{it}\psi_i')$, $\boldsymbol{p}_B$, and $\mathbf{R}_B$. The solution is governed by the differential equations

$$\psi_i' = \begin{cases} k_{it}^{-1}(k_{it}\psi_i') & 0 \leq s_i(s) \leq L_i \\ 0 & \text{otherwise} \end{cases} \tag{3.6a}$$

$$(k_{it}\psi_i')' = \begin{cases} -\boldsymbol{u}_B^T \mathbf{K}_i \dfrac{\partial \mathbf{R}_{\psi_i}}{\partial \psi_i} \boldsymbol{u}_i^* & 0 \leq s_i(s) \leq L_i \\ 0 & \text{otherwise} \end{cases} \tag{3.6b}$$

$$\boldsymbol{p}_B' = \mathbf{R}_B \boldsymbol{e}_3 \tag{3.6c}$$

$$\mathbf{R}_B' = \mathbf{R}_B \widehat{\boldsymbol{u}_B} \tag{3.6d}$$

with boundary conditions

$$\boldsymbol{p}_B(0) = \mathbf{0}, \quad \mathbf{R}_B(0) = \mathbf{I} \tag{3.7a}$$

$$\psi_i(\beta) = \alpha_i, \quad (k_{it}\psi_i')(L) = 0 \tag{3.7b}$$

Equations (3.6a) and (3.6b) are the equations which determine the angle of twist and torsional moment carried by each tube along its arc length. For the elastic stability analysis, we will focus on the second-order form of (3.6a) and (3.6b) taken together, along with the boundary conditions of (3.7b). The elastic stability is independent of (3.6c), (3.6d), and (3.7a).

The boundary conditions (3.7a) assume that the tubes are constrained at the location chosen as $s = 0$. If, additionally, some physical constraint is present which straightens the tubes when $s < 0$, then $\boldsymbol{u}_B = 0$ trivially over that region. We assume that there is an arc length $s^* > \beta_{max}$ such that

$$\boldsymbol{u}_B(s) = \mathbf{0}, \ \ \forall\, s < s^*, \tag{3.8}$$

which implies that tubes have no curvature between where the tubes are physically held. Where the i^{th} tube does not physically exist, it is extended by a non-physical entity that has infinite torsional stiffness (i.e. $k_{it}^{-1} \to 0$) and zero bending stiffness (i.e. $k_{ib} = 0$). Intuitively, this must contribute no energy, since neither an infinite nor zero-stiffness element stores energy, and therefore this modification will not change the solution to the energy minimization problem. This extension converts the multi-point boundary value problem uniquely into a two-point boundary value problem at β and L for the states ψ_i and $(k_{it}\psi_i')$.

Although the most general results will apply to equations (3.6a) and (3.6b), we utilize the following simplification in the bifurcation analysis for the sake of finding closed form expressions. In the case that all tubes have planar precurvature, which is a common design, the precurvature functions can be expressed as $\boldsymbol{u}_i^* = \kappa_i(s)\boldsymbol{e}_1$, and the torsional evolution equation (3.6b) simplifies to

$$(k_{it}\psi_i')' = \begin{cases} \dfrac{k_{ib}}{k_b}\displaystyle\sum_{j=1}^{n} k_{jb}\kappa_i\kappa_j \sin(\psi_i - \psi_j) & 0 \le s_i(s) \le L_i \\ 0 & \text{otherwise} , \end{cases} \tag{3.9}$$

where $k_b = \sum_{i=1}^{n} k_{ib}$. Due to the difference of angles in the expression $\sin(\psi_i - \psi_j)$ on the right hand side, the evolution of torsion is invariant under a constant rotational offset of all angles, which is equivalent to saying the torsional problem is independent of a rigid body rotation of the collection of tubes. Equation (3.9) may thus be expressed in terms of relative angles $\theta_i = \psi_i - \psi_1$, which we will use for the analysis of two tubes and for plotting results for three tubes.

3.5 Bifurcation and Elastic Stability of Two-Tube Robots

In Sections 3.5 and 3.6, we will show that a bifurcation analysis can be used to provide results on how to design concentric tube robots that are guaranteed to be elastically

stable, while the elastic stability analysis will allow us to determine a measure for "closeness" to elastic instability which can be used effectively for a path planner or controller. These results are not independent from one another, despite the fact that the analyses seem disparate, we will show that the more general elastic stability analysis actually subsumes the bifurcation results. The bifurcation results, however, provide a simple, closed-form test, while the elastic stability results require numeric integration of an initial value problem. Before proceeding to the analysis of many-tube robots, for clarity we first present the analysis of both bifurcation and stability for two-tubes.

3.5.1 Local Bifurcation Analysis

Consider a problem defined by an operator f which takes two arguments, $\boldsymbol{\lambda} \in \mathbb{R}^n$ and $\boldsymbol{x} \in V$. The space V is the configuration space. For the concentric tube robots this is a space of real-valued functions of a single argument, together with the boundary conditions that must be satisfied. The operator f defines a problem $f[\boldsymbol{\lambda}, \boldsymbol{x}] = 0$. An equilibrium $\boldsymbol{x}(s) = \boldsymbol{x}_e$ is a fixed point (i.e. it does not change in arc length s) that solves $f[\boldsymbol{\lambda}, \boldsymbol{x}_e] = 0$. Note that an equilibrium in this sense is not the same concept as static equilibrium of a mechanical system. A point $(\boldsymbol{\lambda}_0, \boldsymbol{x}_e)$ on the trivial branch of an equilibrium is called a bifurcation point on this branch if and only if in every neighborhood of this point there is a solution pair $(\boldsymbol{\lambda}, \boldsymbol{x})$ with $\boldsymbol{x} \neq \boldsymbol{x}_e$ [26, p. 149].

The strategy of the local bifurcation analysis is to linearize f about $\boldsymbol{x}_e$ and search for nontrivial solutions $\boldsymbol{x} \neq \boldsymbol{x}_e$ to the linearized problem. The presence of a nontrivial solution is equivalent to the linearized operator failing to have a bounded inverse, which is a necessary condition for a bifurcation point [26, Theorem 5.4.1].

For two-tube robots with constant precurvature, equation (3.9) simplifies to

$$f[\lambda, \theta(\sigma)] = \theta'' - \lambda \sin(\theta) = 0 \tag{3.10a}$$

$$\theta(0) = \theta(\beta_\sigma) - \beta_\sigma \theta'(0) \tag{3.10b}$$

$$\theta'(1) = 0 \ , \tag{3.10c}$$

where we have nondimensionalized the problem, moved the proximal boundary condition to $s = 0$, and assumed the tubes have equal transmission length β. Arc length has been nondimensionalized as $\sigma = s/L_c$ and the dimensionless transmission length $\beta_\sigma = \beta/L_c$, where L_c is the length over which both tubes are present and precurved. The parameter

$$\lambda = L_c^2 \kappa_1 \kappa_2 \frac{k_{1b}}{k_{1t}} \frac{k_{2b}}{k_{2t}} \frac{k_{1t} + k_{2t}}{k_{1b} + k_{2b}} \ .$$

Result 1 (Bifurcation of Two-Tube Robots) *A bifurcation point exists at the point* (λ, π) *where* λ *obeys*

$$\beta_\sigma = \frac{-\cot(\sqrt{\lambda})}{\sqrt{\lambda}} \ . \tag{3.11}$$

We can prove this result by linearizing (3.10a) at the trivial anti-aligned solution $\theta(\sigma) = \pi$ and finding a non-trivial solution. The linearization is given by

$$\theta'' + \lambda(\theta - \pi) = 0 \ , \tag{3.12}$$

which has the general solution

$$\theta(\sigma) = C_1 \cos(\sqrt{\lambda}\sigma) + C_2 \sin(\sqrt{\lambda}\sigma) + \pi \ .$$

Enforcing the proximal boundary (3.10b) requires $C_1 = -\beta_\sigma \sqrt{\lambda} C_2$, and substituting

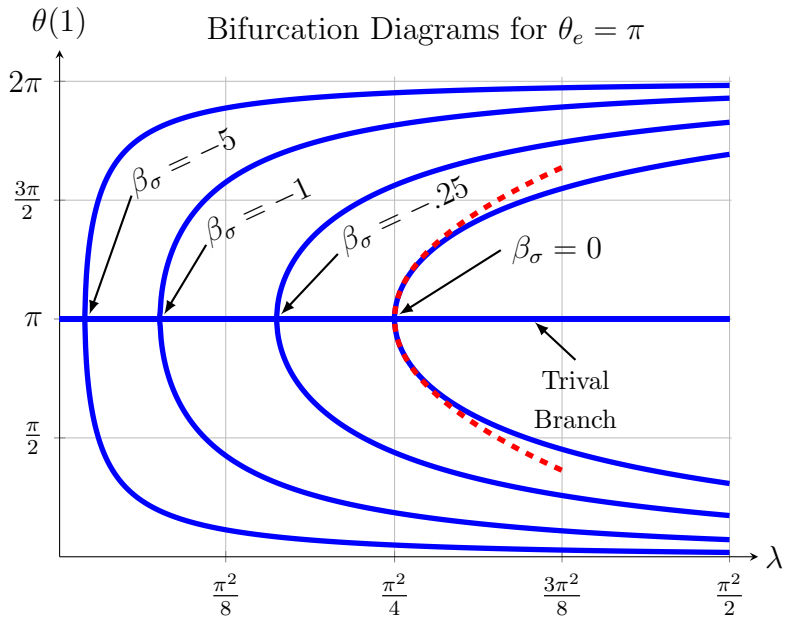

Figure 3.3: Bifurcation diagrams are shown for various transmission lengths. As the transmission length grows, the bifurcation points, indicated by the arrowheads, are pushed closer to $\lambda = 0$. The red dashed line shows equation (3.13), which describes the behavior near the bifurcation point $\lambda_0 = \pi^2/4$.

this relation into the distal boundary (3.10c) condition gives

$$\sqrt{\lambda}C_2\left[\beta_\sigma\sqrt{\lambda}\sin(\sqrt{\lambda}) + \cos(\sqrt{\lambda})\right] = 0\ .$$

$C_2 = 0$ results in the trivial solution $\theta(\sigma) = \pi$, but C_2 can take any value if the bracketed quantity goes to zero, which recovers (3.11) from Result 1.

When $\beta_\sigma = 0$, this simplifies to $\lambda = \pi^2/4$, the well-known result for two tubes with no straight lengths [28, 29]. This result is found in a different form in [35] as an inequality that, if satisfied, guarantees a unique solution to the state-linearized model. A bifurcation diagram which plots the solutions of the nonlinear boundary value problem at $\theta(1)$ against the parameter λ for several values of β_σ is shown in Figure 3.3. The transmission length β_σ can be visualized as "pushing" the bifurcation point towards $\lambda = 0$, reducing the bifurcation-free design space.

This type of bifurcation is known as a supercritical pitchfork bifurcation because

the bifurcation only occurs for values equal to or exceeding the critical bifurcation parameter. Using perturbation methods, an algebraic relationship between $\theta(1)$ and λ near $\lambda_0 = \pi^2/4$ can be found as

$$\theta(1) = \pi \pm 2\sqrt{2}\sqrt{\frac{\lambda - \lambda_0}{\lambda_0}} \ , \ \ \lambda \geq \frac{\pi^2}{4} \ , \tag{3.13}$$

which is derived in [26] for the beam buckling problem. From equation (3.13) and Figure 3.3, we see that the non-trivial branches intersect the trivial branch with infinite slope, which explains why snaps may occur when the bifurcation parameter is only slightly greater than the critical value.

In a physical manifestation of a concentric tube robot, the straight transmission lengths will not be equal since each tube must be exposed to be held in the actuation unit. However, it is possible to remedy this such that (3.11) still applies by finding an equivalent transmission length.

Result 2 (Two-Tube Equivalent Transmission Length) *Any two-tube robot can be equivalently represented as two tubes with equal transmission lengths given by*

$$\beta_{eq,\sigma} = \frac{\beta_{1,\sigma} k_{2t} + \beta_{2,\sigma} k_{1t}}{k_{1t} + k_{2t}} \ . \tag{3.14}$$

We can prove this result by first giving the proximal boundary condition with differing transmission lengths

$$\theta(0) = \alpha_2 - \alpha_1 - \beta_{2,\sigma}\psi_2'(0) + \beta_{1,\sigma}\psi_1'(0) \ . \tag{3.15}$$

Next, we give the torsional equilibrium equations, which must be satisfied at every arc length

$$k_{1t}\psi_1'(0) + k_{2t}\psi_2'(0) = 0 \ . \tag{3.16}$$

The last equation necessary to prove (3.14) is the definition of $\theta'(0)$

$$\theta'(0) = \psi_2'(0) - \psi_1'(0) \; . \tag{3.17}$$

Combining (3.16) and (3.17) defines a relationship for both $\psi_1'(0)$ and $\psi_2'(0)$ in terms of $\theta'(0)$. This can be substituted into (3.15) to allow re-expression of the proximal boundary in the same form as (3.10b) (note that $\theta(\beta_\sigma) = \alpha_2 - \alpha_1$) where β_σ is given by (3.14) from Result 2.

Results 1 and 2 can be combined to answer the question of whether or not a general, constant precurvature two-tube concentric tube robot, in any translational configuration has bifurcated via a closed-form test. If $\beta_\sigma > -\lambda^{-1/2}\cot(\sqrt{\lambda})$, then the system has not bifurcated, and elastic instability is not possible, since the system cannot snap between kinematic solutions.

3.5.2 Local Stability Analysis

The bifurcation analysis gives information on what parameters give rise to multiple kinematic solutions and insight into the local behavior of the system near equilibria, but it does not reveal information about stability away from the equilibria. To obtain this information, we look to the energy landscape of the system. Specifically, we seek to answer this question: when are solutions to Euler's equations local minima of the energy functional? The answer to this question will also provide a relative measure of stability, which gives an indication of which solutions are closer to instability.

We begin by constructing the energy functional which corresponds to the simplified, non-dimensional boundary value problem of (3.10). The functional

$$E[\theta] = \int_{\beta_\sigma}^{0} \frac{1}{2}(\theta')^2 \, d\sigma + \int_0^1 \left(\frac{1}{2}(\theta')^2 - \lambda\cos(\theta) \right) d\sigma = \int_{\beta_\sigma}^{1} F(\sigma, \theta, \theta') \, d\sigma \tag{3.18}$$

will give the desired result after application of the Euler-Lagrange equation on each

interval $[\beta_\sigma, 0]$ and $[0, 1]$,

$$(F_{\theta'})' - F_\theta = 0. \tag{3.19}$$

The energy functional (3.18) in terms of θ is related to the functional (3.3) by a scaling and constant offset, and therefore defines an equivalent minimization problem.

Much like the finite dimensional case where the eigenvalues of the Hessian matrix classify stationary points of functions into minima, maxima, and saddle points, we use the second order information about solutions to determine elastic stability. The second variation operator $\mathcal{S}$ takes the place of the Hessian matrix, and, in the case where the mixed partial derivatives $F_{\theta\theta'} = 0$, it is given by

$$\mathcal{S}h = -\left(F_{\theta'\theta'}h'\right)' + F_{\theta\theta}h \ , \tag{3.20}$$

where h is a variation of θ which satisfies the necessary boundary conditions, i.e. $(\theta + h)(\beta_\sigma) = \theta(\beta_\sigma)$ and $(\theta + h)'(1) = 0$. The elastic stability is determined by the eigenvalues of the operator $\mathcal{S}$, which is in this case a Sturm-Liouville operator. Some further details connecting the eigenvalues of $\mathcal{S}$ with the energy functional are provided in Appendix A.

From the energy functional (3.18), the second variation operator $\mathcal{S}$ is defined from (3.20) as

$$\mathcal{S}h = -h'' + \lambda u(\sigma)\cos(\theta)h \ , \tag{3.21}$$

together with its domain, where $u(\sigma)$ is the unit step function introduced for conciseness. The domain of $\mathcal{S}$ includes the boundary conditions $h(\beta_\sigma) = 0$ and $h'(1) = 0$, which are necessary for $\theta + h$ to satisfy the boundary values of the original problem. The second variation of the energy $\delta^2 E[h] > 0$ if and only if all eigenvalues of $\mathcal{S}$ are positive. This condition can be ensured by solving the following initial value problem.

Result 3 (Stability of Two-Tube Robots) *A solution θ to the boundary value problem*

$$\theta'' - \lambda \sin(\theta) = 0,\ \theta(0) = \theta(\beta_\sigma) - \beta_\sigma \theta'(0),\ \theta'(1) = 0$$

is stable if the solution to the initial value problem defined by

$$\mathcal{S}h = 0,\ h(\beta_\sigma) = 0,\ h'(\beta_\sigma) = 1 \tag{3.22}$$

satisfies $h'(\sigma) > 0$ for $\beta_\sigma \leq \sigma \leq 1$.

See Appendix B for a proof of this result.

This result indicates that a sufficient condition for determining the stability of a solution entails only an integration of an initial value problem, which can be performed numerically. Importantly, the exact same reasoning which produced Result 3 can be repeated in reverse in arc length, which produces the following corollary.

Corollary 1 *The stability of a solution θ can also be determined by solution of the initial value problem defined by*

$$\mathcal{S}h = 0,\ h'(1) = 0,\ h(1) = 1 \tag{3.23}$$

The solution is stable if $h(\sigma) > 0$ for $\beta_\sigma \leq \sigma \leq 1$.

Due to the choice of the boundary conditions of the Corollary, and noting that $\mathcal{S}h = 0$ is equivalent to what we obtain if (3.10) is differentiated by $\theta(1)$, the solution h of Corollary 1 can be interpreted as the slope $h(s) = \partial\theta(s)/\partial\theta(1)$. The equations and boundary conditions of Corollary 1 were previously derived in [34], but the result in terms of local stability was not stated and the result was not derived in the context of examining the system energy. We also have the following corollary due to the continuity of $h'(1)$ and $h(\beta_\sigma)$ with respect to changes in λ and rotational actuation and the symmetry of the two stability problems.

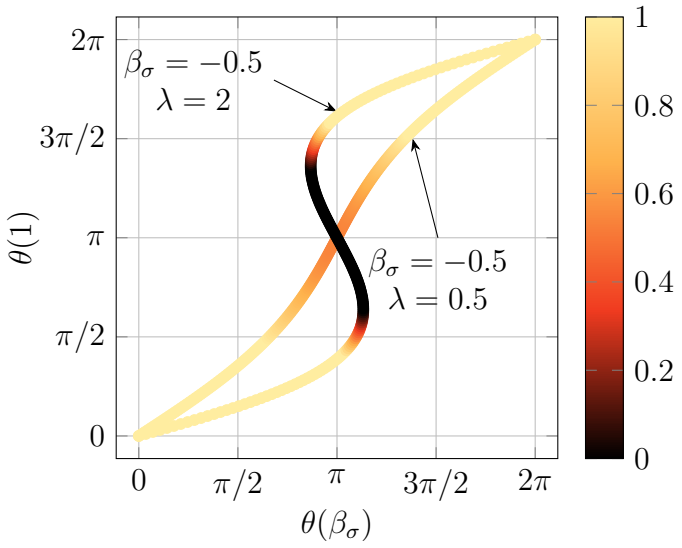

Figure 3.4: An S-Curve is shown for two different choices of parameters β_σ and λ. The curve is colored based on the relative stability measure $\mathbb{S} = h'(1)$, with the color axis truncated at 0 and 1.

Corollary 2 *The value $h'(1)$ in Result 3, or the value of $h(\beta_\sigma)$ in Corollary 1, may be used as a measure of relative stability $\mathbb{S}$ when the conditions of Result 3 and Corollary 1 are met, where larger positive values indicate greater stability. Moreover, the values $h'(1)$ and $h(\beta_\sigma)$ in the two tests are the same.*

The results of the stability test for a two-tube robot with different values of λ and nonzero transmission length are shown in Figure 3.4 on an S-curve, which plots solutions to (3.10) at the proximal and distal endpoints. The S-curve was previously used to visualize the stability of two tubes by Dupont et al. [29]. The test clearly reproduces the known result that the negative slope region of the S-Curve is unstable and thus these configurations are not physically possible in concentric tube robots. Note especially that the relative stability measure varies continuously with respect to $\theta(1)$.

The elastic stability test of Result 3 also implicitly contains the bifurcation results of Section 3.5.1, despite being derived from different approaches. This is illustrated in Figure 3.5 where the bifurcation result from (3.11) plots β_σ against λ at the

equilibrium $\theta_e = \pi$, while the entire space is colored according to relative stability. Equation (3.11) occurs exactly at the points where the relative stability is zero. This means that when the solution under test is the equilibrium $\theta(\sigma) = \pi$, the appearance of a conjugate point exactly at the end of the domain is the same as the appearance of a non-trivial solution to the linearized problem, since the second variation operator and the linearization of (3.10) are equivalent at equilibria.

From Figure 3.5 it is also clear that transmission lengths are very important to consider for guaranteed elastic stability. The designer should consider ways to reduce these lengths, if possible. Alternatively, if the transmission sections do not need to be superelastic, replacing these sections with stiffer sections can dramatically improve the stability of the design. This idea is explored in great detail in Chapter 5 by introducing the concept of torque tubes (i.e. stiff transmission sections), and exploring its effect on the stability of the design.

The stability analysis also reveals why the instability always appears first at equilibrium solutions. Compare a solution $h_\pi(\sigma)$ to the initial value problem of Result 3, where $\theta(\sigma) = \pi$, to a second solution $h_2(\sigma)$, with $\theta(\sigma) \neq \pi$. Note that $\theta = \pi$ maximizes the coefficient of h in (3.21). If the function $h'_\pi(\sigma)$ does not cross zero on its domain, then neither does $h'_2(\sigma)$, because everywhere $h''_\pi \leq h''_2$. This proves that if the equilibrium $\theta(s) = \pi$ has not bifurcated for a given λ, all tube rotations are elastically stable. This fact was formerly given by Ha et al. in [34].

3.6 Bifurcation and Elastic Stability of Many-Tube Robots

The purpose of this section is to extend the analysis from the preceding section to n arbitrary component tubes. The notation will get more cumbersome, but the underlying framework is identical to the previous section. The bifurcation analysis will produce a closed-form bifurcation check algorithm that will work for general constant precurvature concentric tube robots, while the stability analysis will provide

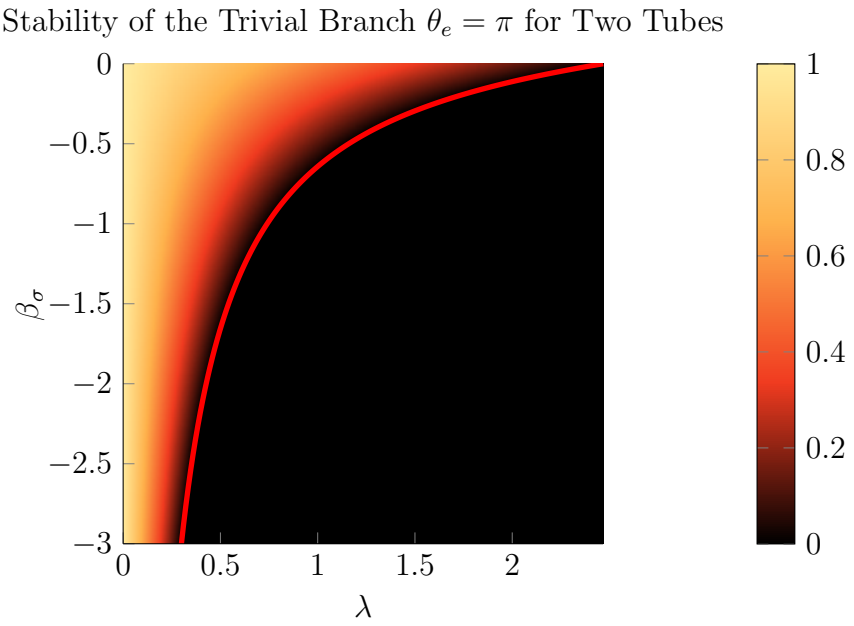

Figure 3.5: This plot shows the relative stability of the $\theta_e = \pi$ trivial branch. The red curve gives the bifurcation result from (3.11). A point above this curve guarantees stability for two tubes across all rotational actuation, while a point below indicates a bifurcation, and a snap will be seen for some rotational actuation. Relative stability values less than 0 have been truncated to 0.

a general stability measure, that is valid for n tubes, of arbitrary precurvatures and stiffnesses. The stability results given in this section actually subsume all of the results given in this chapter but require an integration of an initial value problem.

3.6.1 Local Bifurcation Analysis

Consider the simplified model of a many-tube concentric tube robot given by equation (3.9) where the boundaries are

$$\begin{aligned} \psi_i(0) &= \alpha_i - \beta_i \psi_i'(0) \\ (k_{it}\psi_i')(L) &= 0 \ . \end{aligned} \tag{3.24}$$

For our initial analysis, we assume the transmission lengths of the tubes are equal such that $\beta_i = \beta$ (we will relax this constraint later). We define $\boldsymbol{\psi}_e \in \mathbb{R}^n$ as an

equilibrium point of (3.9), and linearizing (3.9) at the equilibrium gives

$$(\mathbf{K}_t\boldsymbol{\psi}')' = \mathbf{A}_e(\boldsymbol{\psi} - \boldsymbol{\psi_e}),\ \ \mathbf{A}_e = \left.\frac{\partial(\mathbf{K}_t\boldsymbol{\psi}')'}{\partial\boldsymbol{\psi}}\right|_{\boldsymbol{\psi}=\boldsymbol{\psi}_e}, \tag{3.25}$$

where $\mathbf{K}_t = \text{diag}(k_{1t}, ..., k_{nt})$. The entries of the symmetric matrix $\mathbf{A}_e$ are given by

$$\mathbf{A}_e(i,j) = \begin{cases} \sum_{\substack{k=1 \\ k\neq j}}^{n} \Phi_{ik}c_{ik} & i = j \\ -\Phi_{ij}c_{ij} & i \neq j \end{cases} \tag{3.26}$$

where $c_{ij} = \cos(\psi_i - \psi_j)$ and

$$\Phi_{ij} = \frac{k_{ib}k_{jb}\kappa_i\kappa_j}{k_b}\ . \tag{3.27}$$

Result 4 (Bifurcation of n Tube Robots) *The equilibrium $\boldsymbol{\psi}_e$ bifurcates when*

$$\frac{\beta}{L} = \beta_\sigma = \frac{-\cot(\sqrt{\gamma_i})}{\sqrt{\gamma_i}}\ , \tag{3.28}$$

where $\gamma_i = -L^2\lambda_i$ and λ_i is any of the eigenvalues of $\mathbf{K}_t^{-1}\mathbf{A}_e$.

We begin the proof of this result by re-expressing (3.25) as a first order system. We define the state vector

$$\boldsymbol{x} = \begin{bmatrix} \boldsymbol{\psi} - \boldsymbol{\psi}_e \\ \mathbf{K}_t\boldsymbol{\psi}' \end{bmatrix}\ , \tag{3.29}$$

such that (3.25) becomes

$$\boldsymbol{x}' = \underbrace{\begin{bmatrix} \mathbf{0} & \mathbf{K}_t^{-1} \\ \mathbf{A}_e & \mathbf{0} \end{bmatrix}}_{\boldsymbol{\Gamma}_e}\boldsymbol{x}\ . \tag{3.30}$$

Consider a section of the robot (s_1, s_2) of length ℓ_s where both the precurvature of each tube and the number of tubes is constant, (3.30) can be solved in closed form as

$$\boldsymbol{x}(s_2) = e^{\ell_s \boldsymbol{\Gamma}_e} \boldsymbol{x}(s_1). \tag{3.31}$$

For intuition, consider the most simple several tube case where $\boldsymbol{\Gamma}_e$ is constant for $s \geq 0$. This corresponds to a fully overlapped configuration where the precurved portion of each tube begins at $s = 0$ and terminates at $s = L$. The linearized twist and moment at $s = L$ is

$$\boldsymbol{x}(L) = e^{L \boldsymbol{\Gamma}_e} \boldsymbol{x}(0), \tag{3.32}$$

which can be simplified further by decomposing $\mathbf{K}_t^{-1}\mathbf{A}_e$ into its eigendecomposition[2] as $\mathbf{K}_t^{-1}\mathbf{A}_e = \mathbf{V}\boldsymbol{\Lambda}\mathbf{V}^{-1}$. With this simplification, (3.32) becomes

$$\boldsymbol{x}(L) = \mathbf{T}\mathbf{G}\mathbf{T}^{-1}\boldsymbol{x}(0),$$

where

$$\mathbf{G} = \begin{bmatrix} \cosh(L\sqrt{\boldsymbol{\Lambda}}) & \sqrt{\boldsymbol{\Lambda}}^{-1}\sinh(L\sqrt{\boldsymbol{\Lambda}}) \\ \sqrt{\boldsymbol{\Lambda}}\sinh(L\sqrt{\boldsymbol{\Lambda}}) & \cosh(L\sqrt{\boldsymbol{\Lambda}}) \end{bmatrix},$$

and

$$\mathbf{T} = \begin{bmatrix} \mathbf{V} & \mathbf{0} \\ \mathbf{0} & \mathbf{K}_t\mathbf{V} \end{bmatrix}.$$

More details of this computation can be found in Appendix D. Note that the hyperbolic trigonometric functions only operate on the diagonal elements of the matrix argument, such that the four resulting blocks of $\mathbf{G}$ are diagonal. Also note that one of the eigenvalues of $\mathbf{K}_t^{-1}\mathbf{A}_e$ will always be zero since (3.9) is invariant under a rotational shift of all angles $\psi_i \to \psi_i + \delta$. Note that the function $\sinh(L\sqrt{\lambda})/\sqrt{\lambda}$ takes

[2]The matrix $\mathbf{K}_t^{-1}\mathbf{A}_e$ is guaranteed to be non-defective and have real eigenvalues since it is similar to the symmetric matrix $\mathbf{K}_t^{-1/2}\mathbf{A}_e\mathbf{K}_t^{-1/2}$.

the value L at $\lambda = 0$.

We can express the proximal and distal bounds from (3.24) in state form as

$$\begin{bmatrix} \mathbf{I} & \beta\mathbf{K}_t^{-1} \end{bmatrix} \boldsymbol{x}(0) = \mathbf{0}$$
$$\begin{bmatrix} \mathbf{0} & \mathbf{I} \end{bmatrix} \boldsymbol{x}(L) = \mathbf{0}, \tag{3.33}$$

and substituting (3.32) into the distal bound of (3.33) gives

$$\begin{bmatrix} \mathbf{0} & \mathbf{I} \end{bmatrix} e^{\mathbf{\Gamma}_e L} \boldsymbol{x}(0) = \mathbf{0}.$$

Combining the boundary conditions into a single matrix equation, we have

$$\mathbf{M}\boldsymbol{x}(0) = \mathbf{0},$$

where

$$\mathbf{M} = \begin{bmatrix} \mathbf{I} & \beta\mathbf{K}_t^{-1} \\ \mathbf{M}_{21} & \mathbf{M}_{22} \end{bmatrix},$$

and

$$\mathbf{M}_{21} = \mathbf{K}_t \mathbf{V} \sqrt{\mathbf{\Lambda}} \sinh(L\sqrt{\mathbf{\Lambda}}) \mathbf{V}^{-1}$$
$$\mathbf{M}_{22} = \mathbf{K}_t \mathbf{V} \cosh(L\sqrt{\mathbf{\Lambda}}) \mathbf{V}^{-1} \mathbf{K}_t^{-1}.$$

For a given equilibrium point, when $\mathbf{M}$ drops rank, a non-trivial solution exists that solves (3.9) with the boundaries from (3.24), which indicates the equilibrium point has bifurcated. The matrix $\mathbf{M}$ will drop rank when its determinant is zero, which, because $\mathbf{V}$ is full rank, simplifies to

$$|\cosh(L\sqrt{\mathbf{\Lambda}}) - \sqrt{\mathbf{\Lambda}} \sinh(L\sqrt{\mathbf{\Lambda}})\beta| = 0.$$

Since $\mathbf{\Lambda}$ is diagonal, this determinant evaluates to zero when

$$\beta = \frac{\coth(L\sqrt{\lambda_i})}{\sqrt{\lambda_i}} \tag{3.34}$$

for any λ_i, where λ_i is the i^{th} eigenvalue of $\mathbf{K}_t^{-1}\mathbf{A}_e$. This equation is only solvable for $-\pi^2/4 \leq \lambda_i < 0$ since $\beta \leq 0$. If we let $\gamma_i = -L^2\lambda_i$, then equation (3.34) may be rewritten as (3.28) from Result 4, which is exactly analogous to equation (3.11) for two tubes. For $\beta = 0$, the value of λ_j which solves this equation is $L^2\lambda_j = -\pi^2/4$, which is a generalization of the design condition shown in the literature for snap-free two-tube robots.

3.6.2 Local Stability Analysis

The local stability analysis of solutions for n tubes is analogous to the procedure for two tubes. Just as for two tubes, the condition $\delta^2 E > 0$ is simplified to requiring all eigenvalues of the second variation operator $\boldsymbol{\mathcal{S}}$ to be positive. Fortunately, the eigenvectors of $\boldsymbol{\mathcal{S}}$ still form an orthonormal basis for the underlying space of allowable variations, but each eigenvector now consists of n functions rather than a single function. The extension of the scalar Sturm-Liouville problem to a matrix Sturm-Liouville problem is considered in depth in [110].

It is a standard result in the calculus of variations that the generalization of the conjugate point test to n unknown functions involves a condition on the determinant of the fundamental solution matrix of the Jacobi equations, which are the equations $\boldsymbol{\mathcal{S}}\boldsymbol{h} = 0$ [111]. As before, the result is usually only derived for Dirichlet boundary conditions, but again we apply the modified test proposed by Manning [105]. Reference [104, Section II] provides an excellent high level overview of the arguments necessary to conclude that the following result is a sufficient condition. A straightforward generalization of the argument in the proof of Result 3 for why the eigenvalues

are positive on a small interval for the two-tube problem results in the conclusion that this also holds in the case of n tubes. The following result provides the stability test for n tubes at an arbitrary solution $\boldsymbol{\psi}(s)$ of Euler's equations.

Result 5 (Stability of Solutions for n Tubes) *A solution $\boldsymbol{\psi}(s)$ to* (3.6)*, with boundary conditions* (3.7)*, is stable if the $2n \times 2n$ fundamental solution matrix $\mathbf{H}$ for the differential equations*

$$\mathbf{H}' = \boldsymbol{\Gamma}\mathbf{H} \,,$$

$$\mathbf{H}(\beta) = \mathbf{I} \,,$$

where the matrix

$$\boldsymbol{\Gamma}(s) = \begin{bmatrix} \mathbf{0} & \mathbf{F}^{-1}_{\boldsymbol{\psi}'\boldsymbol{\psi}'} \\ \mathbf{F}_{\boldsymbol{\psi}\boldsymbol{\psi}} & \mathbf{0} \end{bmatrix} \,,$$

satisfies the condition $\det \mathbf{H}_{22}(s) > 0$*, where $\mathbf{H}_{22}$ is the $n \times n$ lower-right sub-matrix of $\mathbf{H}$, for all $s \in [\beta, L]$. The matrices $\mathbf{F}^{-1}_{\boldsymbol{\psi}'\boldsymbol{\psi}'}$ and $\mathbf{F}_{\boldsymbol{\psi}\boldsymbol{\psi}}$ are defined element-wise, and as functions of arc length, as*

$$\mathbf{F}^{-1}_{\boldsymbol{\psi}'\boldsymbol{\psi}'}(i,j) = \begin{cases} k_{it}^{-1} & i = j \text{ and } s \in [\beta_i, \beta_i + L_i] \\ 0 & \text{otherwise} \end{cases}$$

$$\mathbf{F}_{\boldsymbol{\psi}\boldsymbol{\psi}}(i,j) = \begin{cases} 0 & s \notin [\beta_i, \beta_i + L_i] \cap [\beta_j, \beta_j + L_j] \\ F_{ii} & i = j \wedge s \in [\beta_i, \beta_i + L_i] \cap [\beta_j, \beta_j + L_j] \\ F_{ij} & i \neq j \wedge s \in [\beta_i, \beta_i + L_i] \cap [\beta_j, \beta_j + L_j] \end{cases}$$

where

$$F_{ii} = -\frac{\partial \boldsymbol{u}_B}{\partial \psi_i}^T \frac{\partial \mathbf{R}_{\psi_i}}{\partial \psi_i} \mathbf{K}_i \boldsymbol{u}_i^* - \boldsymbol{u}_B^T \frac{\partial^2 \mathbf{R}_{\psi_i}}{\partial \psi_i^2} \mathbf{K}_i \boldsymbol{u}_i^*$$

$$F_{ij} = -\frac{\partial \boldsymbol{u}_B}{\partial \psi_j}^T \frac{\partial \mathbf{R}_{\psi_i}}{\partial \psi_i} \mathbf{K}_i \boldsymbol{u}_i^*$$

See Appendix C for a proof of this result.

Corollary 3 *The stability of a solution* $\boldsymbol{\psi}(s)$ *may also be determined by solution of the differential system of equations in Result 5 with initial condition* $\mathbf{H}(L) = \mathbf{I}$*, with the stability condition now replaced by* $\det \mathbf{H}_{11}(s) > 0$.

Corollary 4 *The value of* $\det \mathbf{H}_{22}(L)$ *in Result 5, or the value of* $\det \mathbf{H}_{11}(\beta)$ *in Corollary 3, may be used as a measure of relative stability* $\mathbb{S}$ *when the solution is stable, where larger positive values indicate greater stability. Furthermore, the values* $\det \mathbf{H}_{22}(L)$ *and* $\det \mathbf{H}_{11}(\beta)$ *for the two tests are the same.*

Once again, the stability results capture the bifurcation results when applied to equilibrium solutions. In fact, the matrix $\boldsymbol{\Gamma}$ is equal to the matrix $\boldsymbol{\Gamma}_e$ of equation (3.30) when $\boldsymbol{\psi}(s) = \boldsymbol{\psi}_e$ is chosen as the solution under test. Thus, the equations of Result 5 can be used to provide all of the results in this chapter.

3.7 Preventing Snap for All Actuation: Implementation

To this point, our bifurcation results for robots composed of n tubes has been limited to the case when the tubes start and end at the same arc length and have equal straight transmission lengths. This case is very useful for gaining intuition and seeing the relationship between two-tube robots and many-tube robots but is a rarely-seen configuration for physical prototypes. A general many-tube robot configuration will have several distinct sections with differing numbers of tubes and tube precurvatures as well as differing transmission lengths. The purpose of this section is to provide an algorithm which is capable of testing for bifurcation of equilibria for this case.

3.7.1 Finding Equilibria

For this section, we will assume that the ends of each tube are not precisely aligned in arc length, which is a standard requirement for concentric tube robot prototypes. This requirement means we will have distinct sections where $1, 2, 3, \ldots, n$ tubes are

present. Enforcing this requirement ensures that the only equilibria present in the system are when the tubes are aligned or anti-aligned. This can be easily understood as follows: in the two-tube section of the robot, there are only two equilibria (i.e. tubes aligned and anti-aligned), and as you move back towards the base of the robot, the three tube section must have the third tube in the same plane as the two tubes within it (i.e. it must be aligned/anti-aligned relative to the tubes within it) so that the two-tube section remains at an equilibrium. This argument propagates backwards from the tip of the robot to the section with n tubes, and guarantees that the only equilibria are those where the tubes are aligned/anti-aligned.

When the ends of tubes exactly overlap, additional equilibria arise. In fact, when there are more than three tubes which are exactly overlapped, there are infinite equilibria. In simulations, we have found that these special-case equilibria bifurcate after the anti-aligned equilibria, but because we have not proven this, we limit our algorithm to tube configurations where the tubes ends are not precisely at the same arc length. Because the designer only needs to consider aligned/anti-aligned equilibria, the only $\boldsymbol{\theta}_e$ that needs to be considered is composed of only zero and π elements. Therefore, for an n tube robot, the designer needs to only consider 2^{n-1} equilibria.

3.7.2 Checking Equilibria for Bifurcation

For each section (which we identify with the index q) of the robot, where the number of tubes present and the precurvature of each tube is constant, there will be a different $\boldsymbol{\Gamma}_{q,e}$ from (3.30). We assume that the most proximal section corresponds to $q = 1$ and that there are m total sections. The state $\boldsymbol{x}$ in each section is given by (3.30). For the first section of the robot, $s \in [0, s_1]$; the twist and moment at s_1 are $\boldsymbol{x}(s_1) = e^{s_1\Gamma_{1,e}}\boldsymbol{x}(0)$. Similarly, for the second section of the robot, $s \in [s_1, s_2]$, the twist and moment at s_2 are $\boldsymbol{x}(s_2) = e^{(s_2-s_1)\Gamma_{2,e}}\boldsymbol{x}(s_1)$. By propagating the proximal boundary

through the sections to the most distal arc length of the robot, $s = L$,we have that

$$\boldsymbol{x}(L) = \mathbf{P}\boldsymbol{x}(0) \ , \tag{3.35}$$

where

$$\mathbf{P} = e^{\ell_m \Gamma_{m,e}} e^{\ell_{m-1}\Gamma_{m-1,e}} \dots e^{\ell_1 \Gamma_{1,e}} \ , \tag{3.36}$$

and ℓ_i is the length of section i. In matrix form, the proximal boundary condition from (3.24) can be written as

$$\boldsymbol{x}(0) = \begin{bmatrix} -\mathbf{B}\mathbf{K}_t^{-1} \\ \mathbf{I} \end{bmatrix} (\mathbf{K}_t \boldsymbol{\psi}')(0)$$

where $\mathbf{B}$ is $\text{diag}(\beta_i, \dots, \beta_n)$. This can be substituted into (3.35) to produce

$$\boldsymbol{x}(L) = \underbrace{\mathbf{P} \begin{bmatrix} -\mathbf{B}\mathbf{K}_t^{-1} \\ \mathbf{I} \end{bmatrix}}_{\mathbf{W}} (\mathbf{K}_t \boldsymbol{\psi}')(0) \ . \tag{3.37}$$

In the bottom half of this system, the distal, moment-free boundary condition at $s = L$, from equation (3.7b), is embedded and must be equal to zero.

If the bottom half of $\mathbf{W}$, denoted $\mathbf{W}_2$, is singular, then a non-trivial solution can be found (i.e. a non-equilibrium solution can be found that solves the linearized boundary value problem) and this indicates that the equilibrium is at a bifurcation point. Since a bifurcation indicates that our system has lost its uniqueness, we know that the robot could snap between configurations.

As tube parameters and translational actuation values are smoothly varied, the determinant will vary in a smooth way, even across a bifurcation point. We know that $|\mathbf{W}_2| > 0$ for non-bifurcated configurations (this can easily be shown with straight tubes, for example), so any configuration with $|\mathbf{W}_2| \leq 0$ indicates the equilibrium

Algorithm 1 Determining a Bifurcation-Free Actuation Space

Input: Tube parameters (geometry, material, lengths): p
Translational actuation: $\mathbf{B}$
All equilibria: $\{e_1, \ldots, e_n\} \in e$
Output: Bifurcation: **true/false**

define m sections $\leftarrow$ using $\mathbf{B}, p$
for $k = 1$ to m **do**
  $\mathbf{\Phi}_k \leftarrow$ Eq. (3.27) using p
end for
for all e **do**
  for $k = 1$ to m **do**
    $\mathbf{\Gamma}_{k,e} \leftarrow$ Eq. (3.30), (3.26) using $\mathbf{\Phi}_k, e$
  end for
  $\mathbf{P} \leftarrow$ Eq. (3.36) using $\mathbf{\Gamma}_{1,e}, \ldots, \mathbf{\Gamma}_{m,e}$.
  $\mathbf{W}_2 \leftarrow$ Eq. (3.37) using $\mathbf{P}, \mathbf{B}$.
  if $\det(\mathbf{W}_2) \leq 0$ **then**
    return true
  end if
end for
return false

configuration assessed has previously bifurcated. We note that $|\mathbf{W}_2| = 0$ at every mode of bifurcation, similar to how a beam has additional buckling modes, and therefore it is good practice to initialize a simulation in a known stable configuration and vary parameters from this configuration, checking each step for a zero crossing of the determinant.

Algorithm 1 gives a test to determine if a circularly precurved robot in any configuration (where the ends of tubes are not exactly overlapped), composed of any number of tubes with varying transmission lengths has any bifurcated equilibria. We believe, and have tested in simulation, that if no equilibria has bifurcated, then the entire actuation space is elastically stable (this is proven only for two tubes). Therefore, we believe that Algorithm 1 can be used to determine if the entire actuation space is elastically stable. However, because we have not proven for more than two tubes that instability is guaranteed to arise at an equilibrium, we title the algorithm "Determining a bifurcation-free actuation space." We also note that to be certain a

design which results from Algorithm 1 contains no elastic instabilities, Result 5 can be used. To see an example application of this algorithm for a three tube robot, see [33].

3.8 Experimental Validation

To validate the bifurcation and stability analysis, we performed experiments with two circularly precurved Nitinol tubes. The tubes were designed so that they would snap or pass stably through the anti-aligned configuration depending on the choice of base location where the inner tube is grasped.

3.8.1 Materials & Methods

The tube parameter data for the two tubes used in the experiments are shown in Table 3.2. The experimental setup is shown in Figure 3.6. The outer tube is grasped and held fixed at the front plate of the actuation unit, while the inner tube is grasped at varied distances proximal to this point. For each transmission length tested, one of four straight, rigid sheaths may be added to the front of the robot which physically straightens the tubes over that length. It can be shown that the model predicts that this situation is equivalent to the tubes simply not having any precurvature over the length where the sheath is present, thus allowing us to test model predictions which vary over both dimensionless parameters λ and β_σ with a single set of tubes.

Table 3.2: The tube parameters used for the bifurcation/stability experimental validation.

Parameter	**Tube 1**	**Tube 2**
Outer Diameter	1.02 mm	1.78 mm
Inner Diameter	0.86 mm	1.27 mm
Precurvature	$10.78\,\mathrm{m}^{-1}$	$9.96\,\mathrm{m}^{-1}$
Curved Length	100 mm	100 mm

The lengths of the sheaths, denoted by L_{sheath}, were 0, 10, 20, 30, and 40 mm,

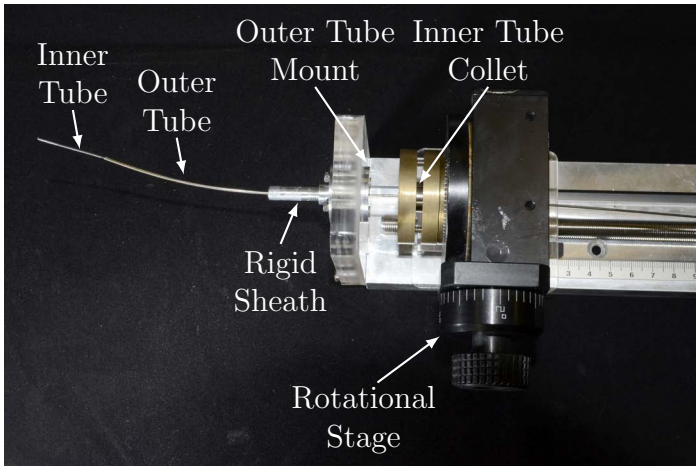

Figure 3.6: The experimental setup for the bifurcation/elastic stability experiments. © 2015 IEEE.

and the grasp locations for tube 1, denoted by β_*, were -23, -30, -40, -50, -60, -70, -80, -90, and -100 mm. Since the point $s = 0$ is defined at the most distal point on the sheath, the values of β_1 and β_2 are given by

$$\beta_1 = \beta_* - L_{sheath} \qquad \beta_2 = -L_{sheath}. \tag{3.38}$$

Let L_c be the overlapped length given by $L_c = 100\,\text{mm} - L_{sheath}$. Then, λ is calculated as $\lambda = L_c^2 u_{1x}^* u_{2x}^* (1 + \nu)$, where u_{1x}^* and u_{2x}^* are the precurvatures of the inner and outer tube. For Poisson's ratio ν we assume a value of 0.33 as quoted by Nitinol manufacturers. The equivalent transmission length $\beta_{eq,\sigma}$ is calculated using equation (3.14).

For each pair L_{sheath} and β_* which were tested, the tubes were first checked for a bifurcation. Bifurcation was determined by attaching a paper flag to the end of the inner tube and observing whether all tip rotations were achievable and stable through rotations of the base. If some tip rotations were not achievable, then the snap angle was determined by rotating the tubes through four snaps. First, the snap was approached by rotating the inner tube base counter-clockwise as viewed

from behind. When a snap was visibly or audibly observed, the angle was recorded. Second, the inner tube was rotated clockwise through a snap at the same speed, and the angle recorded. The third and fourth observations were made by repeating the two previous steps. All rotations through the snaps were performed at a speed of approximately 1 degree/s.

Denote the four recorded angles $\theta_{ccw,1}$, $\theta_{cw,1}$, $\theta_{ccw,2}$, and $\theta_{cw,2}$. Because of the symmetry in the graph of Figure 3.4, the snap angle (in radians) is given by π plus half of the average distance between the snaps,

$$\theta_{snap} = \pi + \left| \frac{\theta_{cw,1} - \theta_{ccw,1} + \theta_{cw,2} - \theta_{ccw,2}}{4} \right| . \tag{3.39}$$

For each experimental trial, we also found the model predicted snap angle using the conditions of Corollary 3. A bisection routine was used to find the relative tip angle at which the condition $\det \mathbf{H}_{11}(\beta) = \mathbb{S} = 0$ is met, and the corresponding modeled relative base angle is then used as the modeled snap angle prediction for comparison against θ_{snap}.

3.8.2 Experimental Results & Discussion

The results of the experiment are shown in Figures 3.7 and 3.8, which assess the accuracy of the model predictions for bifurcation and stability, respectively. Figure 3.7 plots the observation of whether the anti-aligned equilibrium is stable versus the λ and β_σ pairs for each experimental trial. Configurations above the bifurcation boundary do not exhibit snapping, while those below do exhibit snapping. The model correctly predicted 42 of the 45 data points. The model predicted that three of the configurations would not snap when in fact they did, and all of these erroneous predictions were near the bifurcation boundary.

Figure 3.8 shows the error in the modeled snap angle as a function of the observed

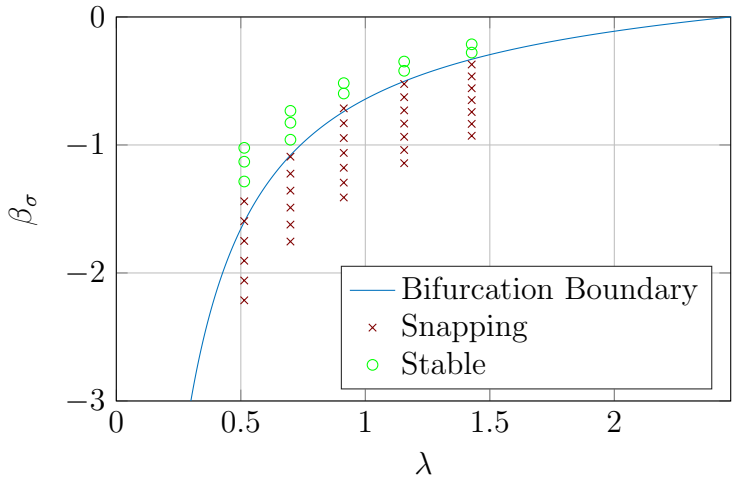

Figure 3.7: Graph of bifurcated and non-bifurcated configurations. Bifurcation was predicted correctly in all but three configurations, with all three of the incorrect predictions near the bifurcation boundary. These results are an experimental validation of Figure 3.5. © 2015 IEEE.

snap angle. All errors were less than 20 °, and the general trend is for the error to increase as the snap angle does. All model data predicts the snap at a lesser angle than was observed experimentally.

Sources of error in these predictions include both unmodeled effects such as friction and nonlinear material behavior, and measurement errors in the tube design parameters such as the curved length and precurvature. In addition, there is a small amount of uncertainty (± 1 mm) in the value of β_* since these lengths were measured by ruler.

The predictions of snap angle can be made significantly more accurate by altering the assumed ratio of bending stiffness to torsional stiffness. It was previously noted by Lock and Dupont that a value of $\nu = 0.6$ yielded a good fit for the experimentally measured torsional relationship between tip and base angles [112]. Although this value of Poisson's ratio is not physically realistic, the material behavior of Nitinol under bending and torsion is known to differ from traditional strength of materials formulas due to tension/compression asymmetry, and thus the simplification $k_{ib}/k_{it} = 1+\nu$ may

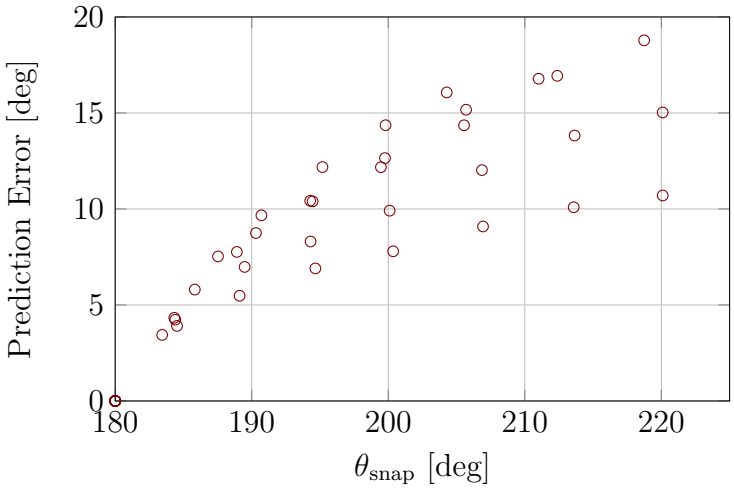

Figure 3.8: Graph of snap angle prediction error vs. the measured snap angle. Generally, as the snap angle increases the prediction becomes increasingly conservative. All model data predicts the snap at a lesser angle than was observed experimentally. © 2015 IEEE.

not be valid even for small strains [113]. We used a nonlinear least-squares regression to fit the snap angle data and found a best fit of $k_{ib}/k_{it} = 1.605$, which resulted in a mean absolute prediction error of 2.06°. This also corroborates the previous finding that $\nu \approx 0.6$. Although a more in-depth analysis of nonlinear material effects is outside the scope of this article, it is possible that future work will be able to make better model predictions by taking into account the nonlinear elastic behavior of Nitinol.

3.9 Design, Control, and Path Planning Implications

The preceding analysis reveals insights about the stability of concentric tube robots and enables prevention of snaps in high curvature robots. For example, the addition of a third tube may allow actuators to steer around instabilities. In addition, path planners and controllers can take advantage of the smooth relative stability measure to plan stable paths and to avoid instability during teleoperation. A resolved-rates style controller leveraging redundancy will be used to do exactly this in Chapter 4.

The following example shows how the stability theory outlined above has ramifications for motion planners and controllers. Existing approaches for dealing with solution stability in motion planning methods have relied on the fact that the kinematic solutions are almost everywhere locally continuous with respect to the set of variables $\boldsymbol{q}_0 = \begin{bmatrix} \beta_1 & ... & \beta_n & \alpha_1(\beta_1) & ... & \alpha_n(\beta_n) \end{bmatrix}$. However, from the standpoint of the topology of the solutions, a much better choice for planning purposes is the distal angles $\alpha_1(L), ..., \alpha_n(L)$, since this makes all components of the kinematic solution continuous with respect to the set of configuration variables $\boldsymbol{q}_L = \begin{bmatrix} \beta_1 & ... & \beta_n & \alpha_1(L) & ... & \alpha_n(L) \end{bmatrix}$. Then, the motion planning problem can be considered as finding continuous, admissible paths in both the physical space occupied by the robot and the configuration variable space.

Previously, without a test which could accurately determine the stability of an arbitrarily chosen configuration $\boldsymbol{q}_L$, sampling based planning methods could not guarantee that the resulting planned trajectory is everywhere elastically stable. Figure 3.9 shows for a three-tube robot how a continuous path in the distal angle space remains continuous in the proximal angles, but the shape of the trajectory becomes distorted when the relative stability measure $\mathbb{S}$ approaches zero. If these distortions are allowed to become too large, then very small changes in the proximal relative angles of the tubes can result in large but stable angular displacements at the distal end, which can create a control sensitivity issue. The relationship between the stability measure $\mathbb{S}$ and dexterity will be discussed in Chapter 5. Furthermore, near these points of ill-conditioning, modeling errors or unpredictable external loads may make it possible for the manipulator to snap.

At present, the relative stability measure $\mathbb{S}$ is a heuristic that indicates which solutions are closer to instability, hence the use of the word "relative." It is important to note that we have not associated this measure with energetic units, and also have not proven bounds on how rapidly the measure can change across the actuation space.

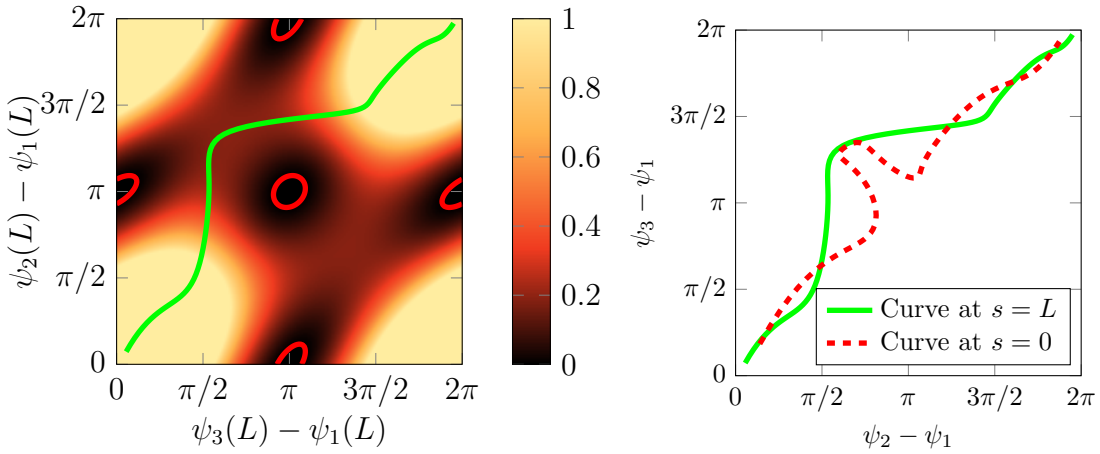

Figure 3.9: The stability measure $\mathbb{S} = \det \mathbf{H}_{11}$ of Corollary 3 is shown on the left for a system of three tubes of equal stiffness and circular precurvature which subtend a total arc of 78.2 degrees in the undeformed state. Each tube is assumed to be actuated rotationally at $s = 0$, and is precurved over the entire length of the tube. If there were only two tubes, no continuous path would exist for the tubes to be rotated fully 360 degrees with respect to one another. With three tubes, however, a continuous path can be found which allows tubes 2 and 3 to be rotated 360 degrees with respect to tube 1. The green line drawn on the left chart shows a chosen stable path in the distal angle space, and the right chart shows how that path transforms to the proximal angles which are actuated. The amount of distortion in the curve is related to the stability measure, with lower stability measures indicating greater distortion.

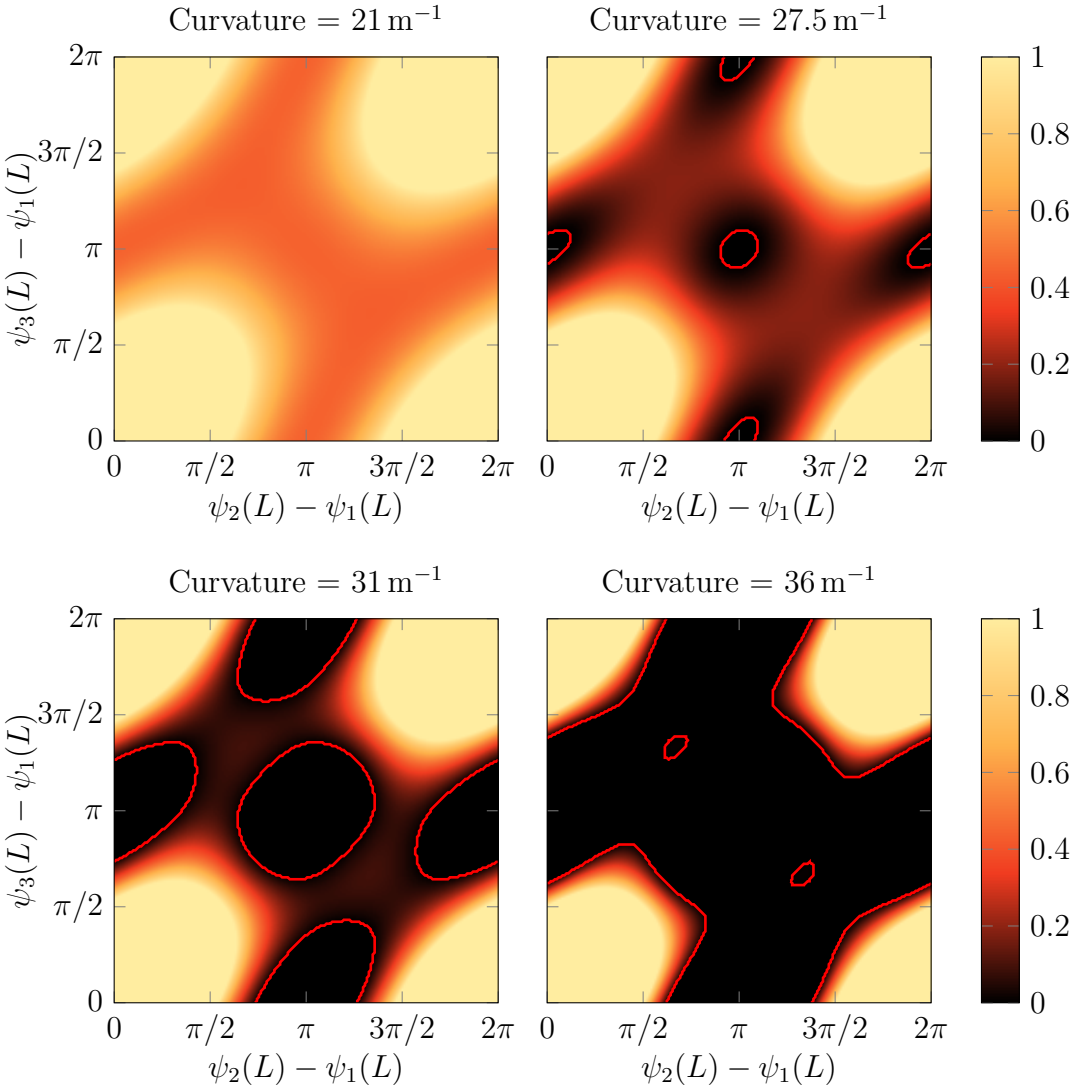

Figure 3.10: In these plots we show the effect of increasing component tube curvature on the relative stability measure $\mathbb{S}$. We simulated three fully overlapping tubes with zero transmission length and an overlapped length of 50 mm and equal curvature and stiffness. As the curvature increases, the regions of instability grow from the bifurcated equilibria until they disconnect the stable equilibria. In the last figure it can be seen that very small contours surround the special case equilibria at $(2\pi/3, 4\pi/3)$ and $(4\pi/3, 2\pi/3)$, where the precurvatures are offset by 120°, which are remarkably still stable despite the entire area surrounding them being unstable.

In principle, the smallest eigenvalue of $\boldsymbol{\mathcal{S}}$ could give a more direct measurement of stability, but in practice this quantity is much more difficult to compute.

One important consequence of the step from two tubes to three tubes is that the third tube can actually provide paths in actuation space for the tubes to make complete rotations with respect to one another without snapping, which would not be possible with only two tubes. This effect exists for designs that are beyond the bifurcation of the anti-aligned equilibria, but for which the regions of instability in the rotational actuation space have not yet connected. For circularly precurved tubes, we suspect the growth of instability from the bifurcating equilibria is a fundamental property regardless of the number of tubes, but we leave proof of this to future work. For complex, non-planar tube designs, there may not exist any equilibria, so it is less clear where instability will first arise; however, Result 5 still predicts the instability.

Note that the true rotational actuator space is of each angle modulo 2π, so that the opposite edges of the graphs in Figure 3.10 are equivalent to one another. In the last plot of Figure 3.10, the connection between the unstable regions has prevented all paths which traverse complete relative rotations of any tube with respect to any other tube. In some cases such a full rotation is possible between one pair of tubes but not another pair.

Resolved-rate style control methods can also take advantage of the relative stability measure for redundancy resolution or for a secondary weighted objective optimization. By computing or precomputing the gradient of the relative stability measure resolved-rate methods can locally enforce a minimum stability measure to ensure that a relative margin of stability is maintained from snapping configurations.

In terms of stability over the entire rotational actuation space, increasing transmission lengths and tube precurvatures tend to continuously destabilize the system. We show this effect by plotting the relative stability measure for every relative angle $\psi_i - \psi_1$ at the distal tip L. This space contains all possible configurations up to a rigid

body rotation. Figure 3.10 shows how increases of the tube precurvature in a three tube robot cause instability to arise at the equilibria with curvatures anti-aligned, and the regions of instability eventually grow until the space of stable tip rotations becomes disconnected and traversing the full relative rotation of any tube can only occur through a snap.

3.10 Elastic Stability Conclusions and Future Work

In this chapter, we have provided an analysis of bifurcation and elastic stability of unloaded concentric tube robots. This chapter has proposed an energy-based stability computation which assigns a relative measure of stability $\mathbb{S}$ to each configuration of the robot, which we believe will be useful for future work in design, control and motion planning. We have also connected existing frameworks from the mechanics literature on Euler beams to concentric tube robots. The bifurcation analysis enables a systematic, computationally inexpensive, and closed form algorithm for designers to create snap-free robots, and will be used in Chapter 5 for a two tube robot.

One important future advancement to the stability theory will be a physical understanding of the stability measure $\mathbb{S}$. This measure clearly has implications for control, dexterity, and instability prevention, but if a more physical meaning could be assigned to the measure, it would help to define allowable safety thresholds for the operation of concentric tube manipulators. Our results have provided an approach to understanding concentric tube robot stability, and it is our hope that this work will facilitate the use of high curvature concentric tube robot designs that were previously avoided.

The theory outlined in this chapter will be used heavily in Chapter 4, where we will use the stability measure $\mathbb{S}$ to design a controller to avoid instabilities, and Chapter 5, where we will rely on the understanding of stability to design optimal manipulators for neuroendoscopic surgery.

CHAPTER 4

REDUNDANCY RESOLUTION: INSTABILITY AVOIDANCE AND STIFFNESS TUNING

4.1 Motivation for Redundancy Resolution

For most surgical robotic systems, manufacturing becomes significantly more challenging as the device is shrunk down in size, or additional degrees of freedom are added. Concentric tube robots, however, are particularly well-suited to scaling down in size since the addition of a tube to an arm adds about 0.3 mm to the overall diameter at the scale of conventional prototypes, including tube clearances. Additionally, the degrees of freedom (DOF) scale as DOF $= 2n$, where n is the number of tubes, since each tube can be independently translated and rotated. Furthermore, it requires no additional manufacturing; nitinol tubes are available off-the-shelf down to outer diameters of 0.2 mm. Just as a concrete example, it is possible to design and build a six tube, 12 degree of freedom concentric tube robot, with the smallest tube having an outer diameter of 1.0 mm within a total outer diameter of 2.5 mm.

Since concentric tube manipulators are capable of delivering several degrees of freedom in a compact overall diameter, it is possible to provide more degrees of freedom than are actually required for tracking the surgeon's movements, and these "extra" degrees of freedom can be used to do useful things. In general, when a robot provides more degrees of freedom than are required for the task it is accomplishing, the robot is said to be redundant. This chapter will explore redundancy resolution algorithms for concentric tube manipulators that maintain high fidelity tracking of a desired trajectory while also simultaneously prioritizing secondary objectives like instability avoidance and stiffness optimization.

4.2 Contributions

The most general contribution of this chapter is that redundancy resolution has yet to be investigated in detail for concentric tube robots. In fact, in [114], redundancy resolution methods were identified as an "open topic in control" for concentric tube robots.

The work in this chapter represents the first real-time instability avoidance algorithm for concentric tube manipulators. There has been work trying to understand when the system becomes unstable, and there has also been work on planning stable trajectories, but this is the first real-time controller which is stability-aware. We also show that, even though the joint space of a concentric tube robot contains elastic instabilities, a useful stable workspace may still remain. We demonstrate trajectory stabilization using our algorithm and the relative stability measure $\mathbb{S}$ derived in Chapter 3. The framework outlined here is applicable beyond concentric tube manipulators. The stabilization control framework applies directly to other manipulators that exhibit elastic instabilities like the parallel continuum robot from [115] and the magnetically guided continuum catheter from [44], for example. The instability avoidance algorithm provides a method that opens up the design space of concentric tube robots by intelligently moving in actuation space to avoid instability. This enables the use of higher curvature manipulators which could potentially even enable new applications.

Another contribution is a redundancy resolution method, which requires no additional sensing, that locally optimizes stiffness while tracking a desired trajectory and a simulation quantifying its performance versus a standard tracking algorithm. This stiffness tuning algorithm provides a method for a surgeon to be in a "high stiffness" or "low stiffness" mode so that the surgeon can intraoperatively respond to the surgical context, and we show that the variability in stiffness is likely to be meaningful for surgical tasks. This chapter ends by the important relationship between stability

and stiffness.

4.3 Mathematical and Theoretical Framework

The focus of this chapter is a teleoperation scenario of concentric tube robots. During resolved rates (see e. g. [94, 116]) style teleoperation, typically the surgeon commands a desired trajectory through the user interface, which is converted to a desired task space velocity command $\dot{\boldsymbol{x}}_d \in \mathbb{R}^{m\times 1}$. The instantaneous joint velocities $\dot{\boldsymbol{q}} \in \mathbb{R}^{n\times 1}$ required to produce this task space velocity are mapped by the manipulator's Jacobian $\mathbf{J} \in \mathbb{R}^{m\times n}$. For tracking of the surgeon's command, the Jacobian maps $\dot{\boldsymbol{q}}$ to $\dot{\boldsymbol{x}}_d$ as

$$\mathbf{J}\dot{\boldsymbol{q}} = \dot{\boldsymbol{x}}_d \, . \tag{4.1}$$

For practical control of concentric tube robots, there are several other control requirements during operation. The tubes should respect joint limits, and high linear/angular velocities of the tubes should be damped for both numerical stability and mechanical bandwidth considerations within the actuation unit. A well-known control technique for integrating these competing goals is a generalized damped least squares implementation, as was initially proposed by Wampler in [94], and used successfully to control concentic tube robots in [100]. The basic idea of damped least squares is to define a cost function that weighs these competing goals. The cost function H, utilizing the notation from [100], can be defined as

$$H = \frac{1}{2}\Big((\mathbf{J}\dot{\boldsymbol{q}} - \dot{\boldsymbol{x}}_d)^T \mathbf{W}_0 (\mathbf{J}\dot{\boldsymbol{q}} - \dot{\boldsymbol{x}}_d) + \sum_{i=1}^{p} (\dot{\boldsymbol{q}} - \boldsymbol{v}_i)^T \mathbf{W}_i (\dot{\boldsymbol{q}} - \boldsymbol{v}_i) \Big) \, , \tag{4.2}$$

where $\mathbf{W}_i$ are non-negative symmetric weighting matrices. The first term penalizes a joint velocity $\dot{\boldsymbol{q}}$ that does not follow the surgeon's command. The second summed term can be used to damp high velocities (if $\boldsymbol{v}_i$ is set to zero), to penalize joint configurations that are near joint limits, or to encourage joint velocities in the direction

Table 4.1: The tube parameters used throughout all simulations in this chapter. Each undeformed tube is a straight section appended with a circular arc at the tip. The precurvatures of each tube will change throughout the chapter and will be given in the body of the text when necessary.

Parameter	**Tube 1**	**Tube 2**	**Tube 3**	**Units**
Outer Diameter	1.1	1.4	1.7	mm
Inner Diameter	1.0	1.3	1.6	mm
Total Tube Length	150.0	100.0	50.0	mm
Straight Tube Length	100.0	60.0	25.0	mm
Young's Modulus	50.0	50.0	50.0	GPa
Poisson's Ratio	0.4	0.4	0.4	unitless

of the gradient of some objective function (if $\boldsymbol{v}_i$ is chosen to be a scaled joint gradient of the objective function). The necessary condition for $\dot{\boldsymbol{q}}$ to minimize H is found by setting $\frac{\partial H}{\partial \dot{\boldsymbol{q}}} = 0$, and can be shown to be

$$\dot{\boldsymbol{q}} = \left(\mathbf{J}^T\mathbf{W}_0\mathbf{J} + \sum_{i=1}^{p}\mathbf{W}_i\right)^{-1}\left(\mathbf{J}^T\mathbf{W}_0\dot{\boldsymbol{x}}_d + \sum_{i=1}^{p}\mathbf{W}_i\boldsymbol{v}_i\right). \tag{4.3}$$

4.4 Assumptions and Preliminaries

In this chapter, we will simulate a three-tube, six degree of freedom concentric tube manipulator. The constant tube parameters are shown in Table 4.1. The precurvatures of the tubes will vary based on the particular simulation. For each simulation, the system will be tasked with following a desired position trajectory in $\mathbb{R}^3$, leaving three redundant degrees of freedom for secondary tasks. We will consider the joint variable $\boldsymbol{q}$ in this section to be defined as

$$\boldsymbol{q} = \begin{bmatrix}\psi_{1L} & \psi_{2L} & \psi_{3L} & x_1 & x_2 & x_3\end{bmatrix}^T = \begin{bmatrix}\boldsymbol{\psi}_L^T & \boldsymbol{x}^T\end{bmatrix}^T, \tag{4.4}$$

where ψ_{iL} is the angle between the material frame of tube i and the bishop frame $\mathbf{R}_B$ at the tip of the manipulator, and x_i is the exposed length of each tube, or

$$\begin{aligned} x_1 &= \beta_1 + L_1 - \beta_2 + L_2 \\ x_2 &= \beta_2 + L_2 - \beta_3 + L_3 \ , \\ x_3 &= \beta_3 + L_3 \end{aligned} \tag{4.5}$$

where L_i is the total length of tube i, and β_i is the negative arc length s where tube i is grasped, with $s = 0$ defined to be at the constrained exit point of the tubes. The subscripts 1, 2, and 3 correspond to the inner, middle, and outer tube, respectively. Refer to Chapter 3, Figure 3.2 for a review of these variable definitions and nomenclature.

4.5 Damped Least Squares with Joint Limit Avoidance

Before using the manipulator's redundancy to explore instability avoidance and stiffness optimization, we will first define a control law which provides stable tracking, joint limit avoidance, and damping. This control law will often be used as a reference control law to compare the performance of the instability avoidance algorithms and stiffness optimization algorithms explored later in this chapter.

For concentric tube robots, it is critical that each component tube always surround the next smaller tube within it at all arc lengths to maintain sufficiently small clearances. For example, we want to make sure the outer tube always has the middle tube within it at every arc length. If there were a section of the robot where the middle tube was retracted inside of the outer tube, there would be large clearances between the inner tube and the outer tube, creating large kinematic model error. In addition, the tip of the inner tube is usually considered the end-effector of the manipulator, so it must remain exposed. Both of the aforementioned joint constraints can

be maintained by setting $\boldsymbol{x}_{min}$. In addition to this joint limit, we also set $\boldsymbol{x}_{max}$, which constrains the total allowable arc length of the manipulator. For all of the simulations in this chapter, we set each component of $\boldsymbol{x}_{min}$ to 1 mm and each component of $\boldsymbol{x}_{max}$ to 40 mm.

To avoid these joint limits, we adopt the strategy outlined by Dubey and Chan in [117]. We first define a joint limit penalty function $J(\boldsymbol{x})$ as

$$J(\boldsymbol{x}) = \sum_{i=1}^{3} \frac{1}{4} \frac{(x_{i,max} - x_{i,min})^2}{(x_{i,max} - x_i)(x_i - x_{i,min})} \ . \tag{4.6}$$

This joint limit penalty function approaches infinity as any x_i approaches $x_{i,min}$ or $x_{i,max}$, and is normalized so that each term of the sum is unity when centered between the joint limits. Taking the gradient of J with respect to $\boldsymbol{x}$, we have that each component of the gradient J_{x_i} is

$$J_{x_i} = \frac{\partial J}{\partial x_i} = \frac{(x_{i,max} - x_{i,min})^2 (2x_i - x_{i,max} - x_{i,min})}{4(x_{i,max} - x_i)^2 (x_i - x_{i,min})^2} \ . \tag{4.7}$$

We can use this gradient to apply joint configuration-dependent damping to the cost function from (4.2). Let us define the joint limit damping matrix $\mathbf{W}_J(\boldsymbol{q}) \in \mathbb{R}^{6\times 6}$, where we damp joint velocities that are near their joint limits using the gradient of $J(\boldsymbol{q})$, such that

$$\mathbf{W}_J(\boldsymbol{q}) = \alpha_J \ \mathrm{diag}(1 + |\nabla J_{\boldsymbol{q}}|) \ , \tag{4.8}$$

where

$$\nabla J_{\boldsymbol{q}} = \begin{bmatrix} 0 & 0 & 0 & J_{x_1} & J_{x_2} & J_{x_3} \end{bmatrix} \ , \tag{4.9}$$

and α_J is a proportional gain term. Notice that the first three elements of $\nabla J_{\boldsymbol{q}}$ are zero because the joint limit penalty function J is independent of $\boldsymbol{\psi}_L$ (i.e. there are no rotational joint limits).

In addition to the joint configuration-dependent damping, which will really only

affect the control algorithm when the translational joint variables approach their joint limits, we also apply damping independent of the particular joint configuration. Let us define the damping matrix $\mathbf{W}_D \in \mathbb{R}^{6\times 6}$ as

$$\mathbf{W}_D = \alpha_D \begin{bmatrix} b_R\mathbf{I} & \mathbf{0} \\ \mathbf{0} & b_T\mathbf{I} \end{bmatrix} , \tag{4.10}$$

where α_D is a proportional gain term that increases the overall damping, b_R is the nominal rotational damping, and b_T is the nominal translational damping. If just implementing tracking, joint limit avoidance, and damping, the cost function from (4.2) becomes

$$H = \frac{1}{2}\Big(\underbrace{(\mathbf{J}\dot{\boldsymbol{q}} - \dot{\boldsymbol{x}}_d)^T\mathbf{W}_0(\mathbf{J}\dot{\boldsymbol{q}} - \dot{\boldsymbol{x}}_d)}_{\text{Tracking}} + \underbrace{\dot{\boldsymbol{q}}^T\mathbf{W}_D\dot{\boldsymbol{q}}}_{\text{Damping}} + \underbrace{\dot{\boldsymbol{q}}^T\mathbf{W}_J(\boldsymbol{q})\dot{\boldsymbol{q}}}_{\substack{\text{Joint Limit} \\ \text{Avoidance}}} \Big) , \tag{4.11}$$

and the control update law from (4.3) reduces to

$$\dot{\boldsymbol{q}} = \Big(\mathbf{J}^T\mathbf{W}_0\mathbf{J} + \mathbf{W}_D + \mathbf{W}_J(\boldsymbol{q})\Big)^{-1}\Big(\mathbf{J}^T\mathbf{W}_0\dot{\boldsymbol{x}}_d\Big) . \tag{4.12}$$

Since only position tracking will be considered in this chapter, $\mathbf{W}_0 \in \mathbb{R}^{3\times 3}$, and tracking is weighted equally importantly in the x, y, and z direction so that

$$\mathbf{W}_0 = \alpha_0\mathbf{I} . \tag{4.13}$$

Table 4.2 shows the parameters used to form each of these weighting matrices, which were determined heuristically to provide excellent tracking, realistic joint velocities, and joint limit avoidance. These parameters will be used in each of the simulations remaining in this chapter.

Table 4.2: The control values used for tracking, damping, and joint limit avoidance. Note that the units of the joints are in radians and meters, so what appear as large gains are reasonable when you consider task space and translational joint velocities are in the $^{mm}/_{s}$ range.

Parameter	**Symbol**	**Value**
Joint Limit Damping Proportional Gain	α_J	20.0
Tracking Proportional Gain	α_0	1.0×10^8
General Damping Proportional Gain	α_D	0.1
Nominal Translation Damping	b_T	5.0×10^8
Nominal Rotation Damping	b_R	$(180/2\pi)^2$

4.6 Performance of a Damped/Joint Limited Controller

4.6.1 Calculating the Desired Velocity

We calculate the desired velocity $\dot{\boldsymbol{x}}_d$ based on the current position of the tip of the manipulator $\boldsymbol{p}_{tip}$ and the desired position of the tip of the manipulator $\boldsymbol{p}_{des}$. The current position can be found at any time from the kinematic model. The desired velocity is in the direction of the error vector, and scaled by some velocity magnitude v_{mag}.

$$\dot{\boldsymbol{x}}_{des} = v_{mag} \frac{\boldsymbol{e}}{\|\boldsymbol{e}\|} \tag{4.14}$$

where $\boldsymbol{e} = \boldsymbol{p}_{des} - \boldsymbol{p}_{tip}$, and v_{mag} is a piecewise continuous function of the error magnitude given by

$$v_{mag} = \begin{cases} 0 & \|\boldsymbol{e}\| < \rho \\ v_{min} & \rho \leq \|\boldsymbol{e}\| \leq e_{min} \\ \frac{v_{max} - v_{min}}{e_{max} - e_{min}}(\|\boldsymbol{e}\| - e_{max}) + v_{max} & e_{min} < \|\boldsymbol{e}\| < e_{max} \\ v_{max} & \|\boldsymbol{e}\| \geq e_{max} \end{cases}, \tag{4.15}$$

where ρ is the converged radius, within which no velocity is commanded. The values of each of the constants are shown in Table 4.3.

Table 4.3: The control values used for selecting the desired task space velocity $\dot{\boldsymbol{x}}_{des}$.

Parameter	**Symbol**	**Value**	**Units**
Maximum Task Space Velocity	v_{max}	100.0	$^{\text{mm}}/_{\text{s}}$
Minimum Task Space Velocity	v_{min}	13.0	$^{\text{mm}}/_{\text{s}}$
Maximum Velocity Error	e_{max}	5.0	mm
Minimum Velocity Error	e_{min}	1 .0	mm
Converged Radius	ρ	1.0×10^{-5}	mm

Table 4.4: The parameters which define the desired trajectory of a helix wrapping around a torus.

Parameter	**Symbol**	**Value**	**Units**
Torus Major Radius	R	15.0	mm
Torus Minor Radius	r	3.0	mm
Number of Helix Turns	N_T	5	Turns
Offset From x-y plane	z_{off}	55.0	mm

4.6.2 The Desired Trajectory

While a trajectory must be chosen for simulation purposes, ultimately the desire is for the control algorithm to be robust to arbitrary velocities commanded by the surgeon. To simulate an interesting trajectory, however, we chose to parameterize a helix wrapping around a torus. This same trajectory will be used for all simulations in this chapter, unless otherwise noted. The equations for the desired position of the tip $\boldsymbol{p}_{des}$ are

$$\boldsymbol{p}_{des} = \begin{bmatrix} \big(R + r\cos(N_T\theta)\big)\cos(\theta) \\ \big(R + r\cos(N_T\theta)\big)\sin(\theta) \\ r\sin(N_T\theta) + z_{off} \end{bmatrix}, \tag{4.16}$$

where R is the major radius of the torus, r is the minor radius of the torus, N_T is the number of turns of the helix, z_{off} is the offset from the x-y plane, and $\theta \in [0, 2\pi]$. The parameters used for this desired trajectory are shown in Table 4.4.

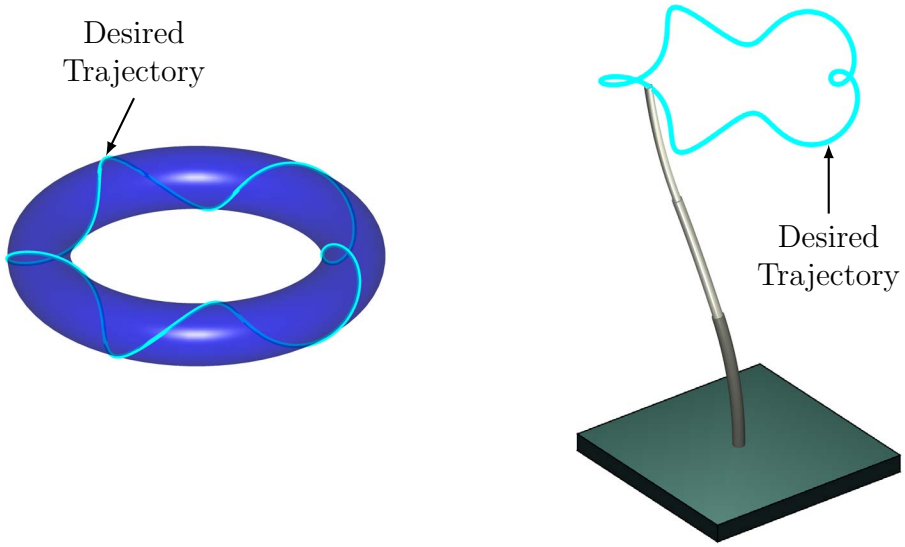

Figure 4.1: (Left) The desired trajectory of a helix wrapping around a torus. (Right) The concentric tube manipulator following the desired trajectory.

4.6.3 Nominal Algorithm Performance

The purpose of the first simulation is to establish a baseline "normal" tracking performance of the algorithm, without considerations for secondary tasks beyond damping and joint limit avoidance. For this simulation, we tracked the aforementioned desired trajectory, using an inner tube curvature of $10\,\mathrm{m}^{-1}$, a middle tube precurvature of $12\,\mathrm{m}^{-1}$, and an outer tube precurvature of $22\,\mathrm{m}^{-1}$. This selection of precurvatures and joint limits ensures stability of the manipulator. The trajectory was commanded over 10 s with a 5 ms step time. The home position was defined as $\boldsymbol{\psi}_L = \mathbf{0}$ and $x_1 = x_2 = x_3 = 20\,\mathrm{mm}$. The tracking performance of the manipulator, the joint trajectories, and the evolution of the relative stability measure $\mathbb{S}$ are shown in Figure 4.2. The algorithm quickly reduces tracking error, although it lags a bit behind ($\approx 1\,\mathrm{mm}$) $\boldsymbol{p}_{des}$ because the tube motions are heavily damped. Note that when regulating a desired position, tracking quickly reduces to within the converged radius ρ.

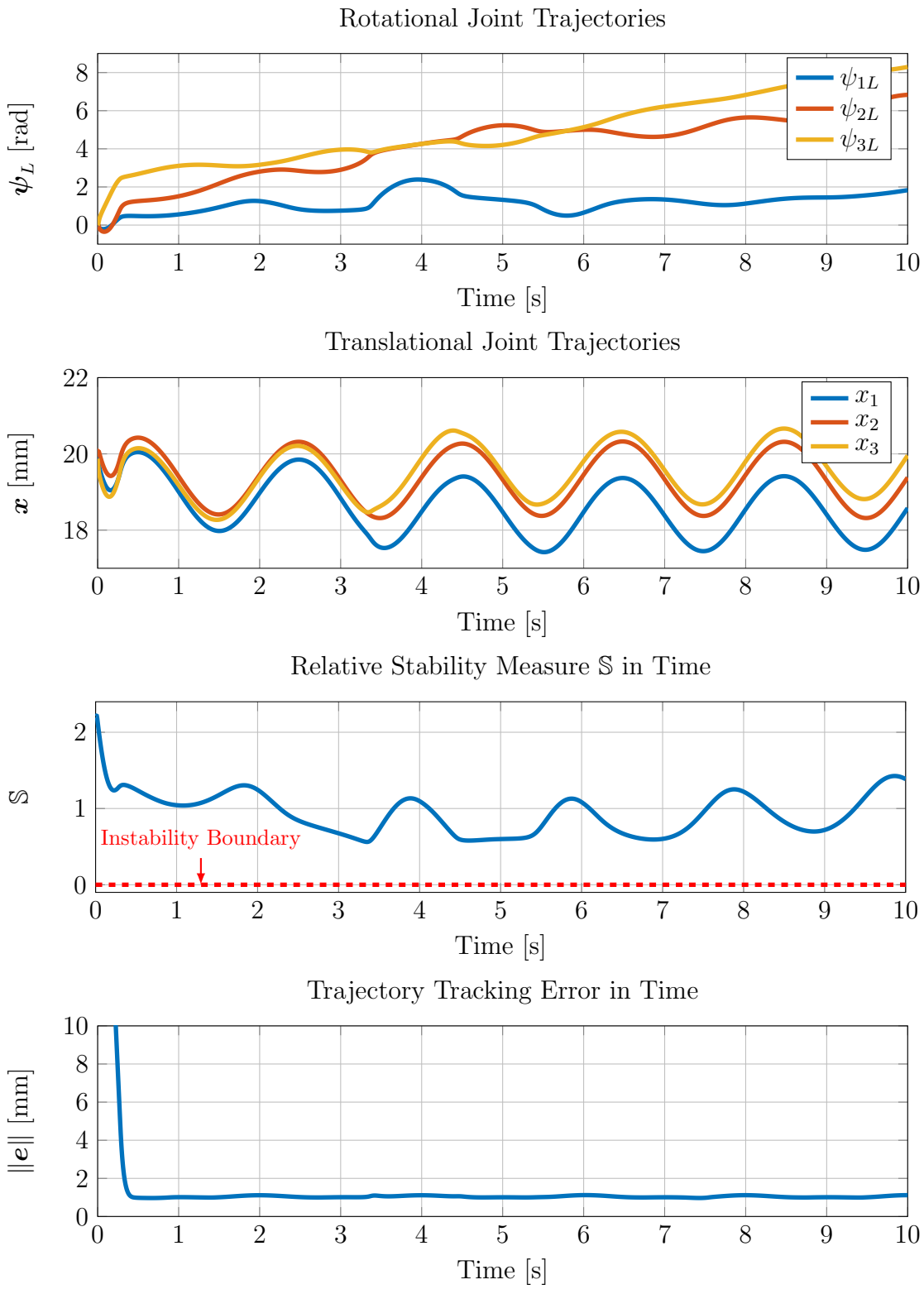

Figure 4.2: The joint trajectories, relative stability measure, and tracking error are shown in time for a stable trajectory from (4.16), using the cost function from (4.11), and the update law from (4.12).

4.7 Redundancy Resolution for Instability Avoidance

One of the major contributions of Chapter 3 was the derivation of a measure for the relative stability of a concentric tube manipulator operating in free space. Without this measure, the design of concentric tube manipulators is restricted to slightly curved tubes that do not exhibit elastic instabilities anywhere in their joint space. With this new measure, however, it may be possible to open up the design space to include higher curvature tubes which *could* snap, and control the manipulator to make sure it never moves to these unstable configurations. This idea implies that a designer of concentric tube manipulators can sacrifice actuation freedom for enhanced design freedom. This concept, however, begs the question: does the restricted actuation space still generate a useful workspace?

4.7.1 An Example Unstable Workspace

To answer this question, we looked at an example based on the tubes from Table 4.1, each with a precurvature of $30\,\mathrm{m}^{-1}$. We simulated through the joint space with a translational step of 1 mm and a rotational step of 10° (see Section 4.5 for joint limits), and generated a point cloud of tip locations for both (1) stable configurations and (2) unstable configurations. We projected the (x, y, z) tip position into the (R, z) plane where $R = \sqrt{x^2 + y^2}$. Both of the stable and unstable point clouds generated a closed area. Because of the aggressive curvatures, 45% of the joint configurations were unstable with this joint space discretization. However, the simulated tip positions that were generated from unstable configurations, were almost completely enveloped by the simulated tip positions that were generated from stable configurations, as shown in Figure 4.3. Therefore, the unstable joint space – which is 45% of the joint space – generates almost exclusively tip configurations that are also achievable in a stable configuration. This strongly motivates the need for a controller than can intelligently

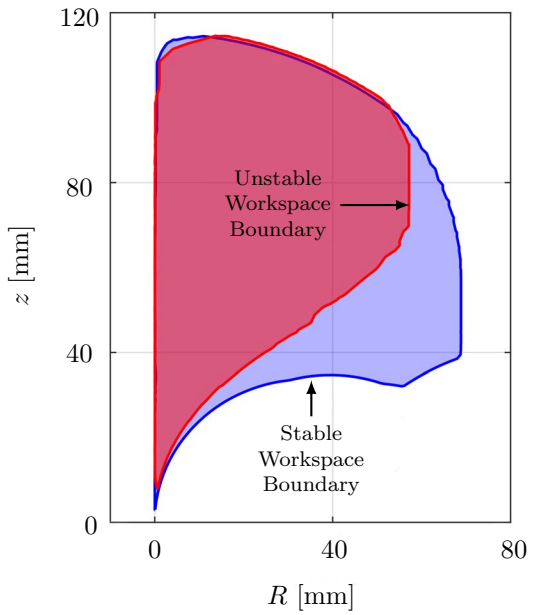

Figure 4.3: An example of how an unstable joint space does not necessarily imply a significant loss in workspace. The stable workspace boundary almost completely envelopes the unstable workspace boundary. In this example, 45% of the discretized joint space (1 mm, 10° joint steps) is unstable, but nearly every tip position that is achievable in an unstable configuration is also achievable in a stable configuration.

maneuver through joint space to find the stable configurations and avoid the unstable ones.

4.7.2 Example of an Unstable Trajectory

Prior to developing the stabilizing controller, we will first investigate how the current controller responds to tubes that may go unstable. If we repeat the exact same simulation as section 4.6.3, but increase the precurvatures of each of the tubes to $30\,\mathrm{m}^{-1}$, we introduce the potential for instability into the joint space of the manipulator (as was shown in Figure 4.3). Nevertheless, as shown in Figure 4.4, the algorithm generates reasonable joint trajectories and excellent *model* tracking. However, because the control law from (4.12) is unaware of instability, it moves the manipulator's trajectory through unstable configurations. At the moment that the relative stability measure

$\mathbb{S} = 0$, the physical robot loses elastic stability and snaps to a new configuration (usually far away). The remainder of the simulation after that point is non-physical, because there is a mismatch between the physical space and the model space. In the next section we will address how to modify the control law to avoid elastic instability for this same simulation.

4.7.3 An Instability Avoidance Control Law

As was discussed in Chapter 3, the relative stability measure $\mathbb{S}$ changes continuously with the joint values $\boldsymbol{q}$, and it was hinted at that this property could likely be used to stabilize joint trajectories that would otherwise go unstable. In this section, we will formalize a strategy to do exactly that. We start by modifying the cost function H from (4.11) to include an instability avoidance term.

$$H = \frac{1}{2}\Big(\underbrace{(\mathbf{J}\dot{\boldsymbol{q}} - \dot{\boldsymbol{x}}_d)^T \mathbf{W}_0 (\mathbf{J}\dot{\boldsymbol{q}} - \dot{\boldsymbol{x}}_d)}_{\text{Tracking}} + \underbrace{\dot{\boldsymbol{q}}^T \mathbf{W}_D \dot{\boldsymbol{q}}}_{\text{Damping}} + \underbrace{\dot{\boldsymbol{q}}^T \mathbf{W}_J \dot{\boldsymbol{q}}}_{\substack{\text{Joint Limit} \\ \text{Avoidance}}} + \underbrace{(\dot{\boldsymbol{q}} - \boldsymbol{v}_{\mathbb{S}})^T \mathbf{W}_{\mathbb{S}} (\dot{\boldsymbol{q}} - \boldsymbol{v}_{\mathbb{S}})}_{\substack{\text{Instability} \\ \text{Avoidance}}} \Big) \quad (4.17)$$

With this small change, the control law, based on (4.3), becomes

$$\dot{\boldsymbol{q}} = \Big(\mathbf{J}^T \mathbf{W}_0 \mathbf{J} + \mathbf{W}_D + \mathbf{W}_J(\boldsymbol{q}) + \mathbf{W}_{\mathbb{S}}(\boldsymbol{q}) \Big)^{-1} \Big(\mathbf{J}^T \mathbf{W}_0 \dot{\boldsymbol{x}}_d + \mathbf{W}_{\mathbb{S}}(\boldsymbol{q}) \boldsymbol{v}_{\mathbb{S}} \Big) \,. \quad (4.18)$$

The basic idea of this control law is that as $\mathbb{S}$ approaches some relative stability threshold $\mathbb{S}^*$, we want the instability avoidance term to dominate the cost function so that the controller will generate joint velocities that stabilize the manipulator. To achieve this effect, we define

$$\mathbf{W}_{\mathbb{S}} = (e^{\frac{1}{\mathbb{S}-\mathbb{S}^*}} - 1)\mathbf{I} \quad (4.19)$$

so that each diagonal element of $\mathbf{W}_{\mathbb{S}}$ approaches infinity as $\mathbb{S}$ approaches $\mathbb{S}^*$. Other choices are possible for $\mathbf{W}_{\mathbb{S}}$, but we heuristically found that this choice provided a very good compromise between tracking and instability avoidance.

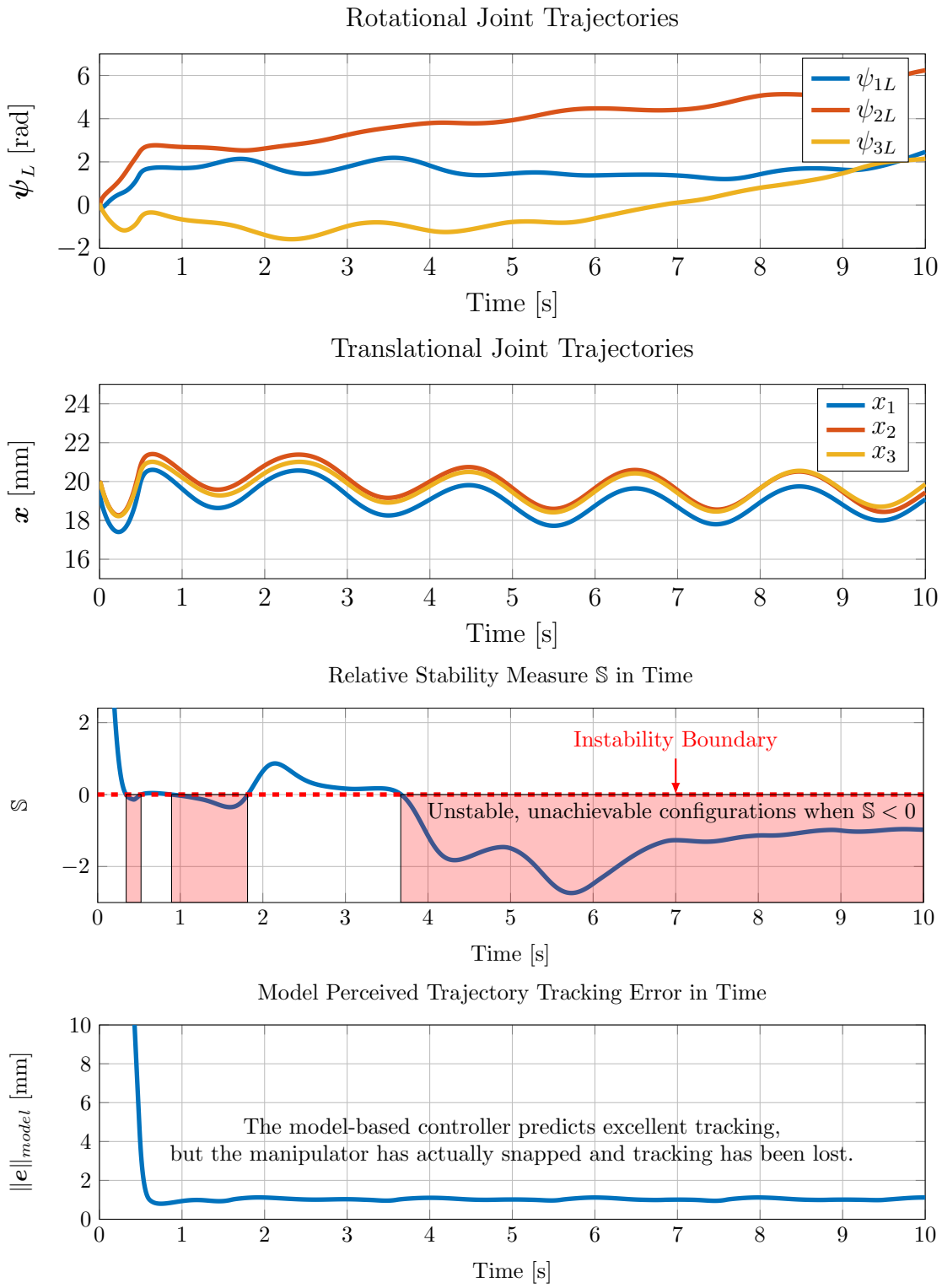

Figure 4.4: The same simulation as Figure 4.2 but with higher tube precurvatures. When the relative stability measure crosses to $\mathbb{S} < 0$, the manipulator snaps to a configuration far away. The model-based controller predicts excellent tracking, but there is a disconnect between physical tracking and model tracking because the model does not consider instability.

In addition to making sure the instability avoidance term dominates when near instability, we must also capture the direction the system should move to avoid instability. To do this, we define $\boldsymbol{v}_{\mathbb{S}}$ as

$$\boldsymbol{v}_{\mathbb{S}} = \alpha_{\mathbb{S}} \frac{\partial \mathbb{S}}{\partial \boldsymbol{q}} = \alpha_{\mathbb{S}} \nabla \mathbb{S}_{\boldsymbol{q}} \; . \tag{4.20}$$

If we choose $\alpha_{\mathbb{S}} > 0$, this points $\boldsymbol{v}_{\mathbb{S}}$ towards the positive gradient of relative stability measure. If the instability avoidance term is dominating the cost function, the system should approximate gradient ascent, moving in joint space to locally maximize $\mathbb{S}$. We use $\alpha_{\mathbb{S}}$ as a gain term to convert the gradient of the relative stability measure into a desired velocity in joint space. We numerically compute the relative stability measure gradient $\nabla \mathbb{S}_{\boldsymbol{q}}$ using centered finite differences, with a translational step of 0.01 mm and a rotational step of 0.05 °.

4.7.4 Trajectory Stabilization Simulations

Using the new instability avoidance control law from (4.18) with $\alpha_{\mathbb{S}} = 10$, and $\mathbb{S}^* = 0$ (so that the relative stability measure threshold is $\mathbb{S} = 0$), we re-ran the simulation from Section 4.7.2 and Figure 4.4. There were no other changes to the simulation. The results of this simulation are shown in Figure 4.5, which shows that the controller was able to avoid instability while also maintaining good tracking. Just as in Figure 4.4, $\mathbb{S}$ quickly moves towards instability, but this time the controller moves away from the boundary so that no snap occurs.

One challenge about this algorithm is that there are a lot of interacting variables: damping, joint limit avoidance, tracking, and instability avoidance are all interacting in a complex way. Selecting gains can be challenging and the performance of the algorithm can be sensitive to these gain selections. There was one analysis tool that proved particularly useful towards selecting these gains. If we define the 6×6 inverted

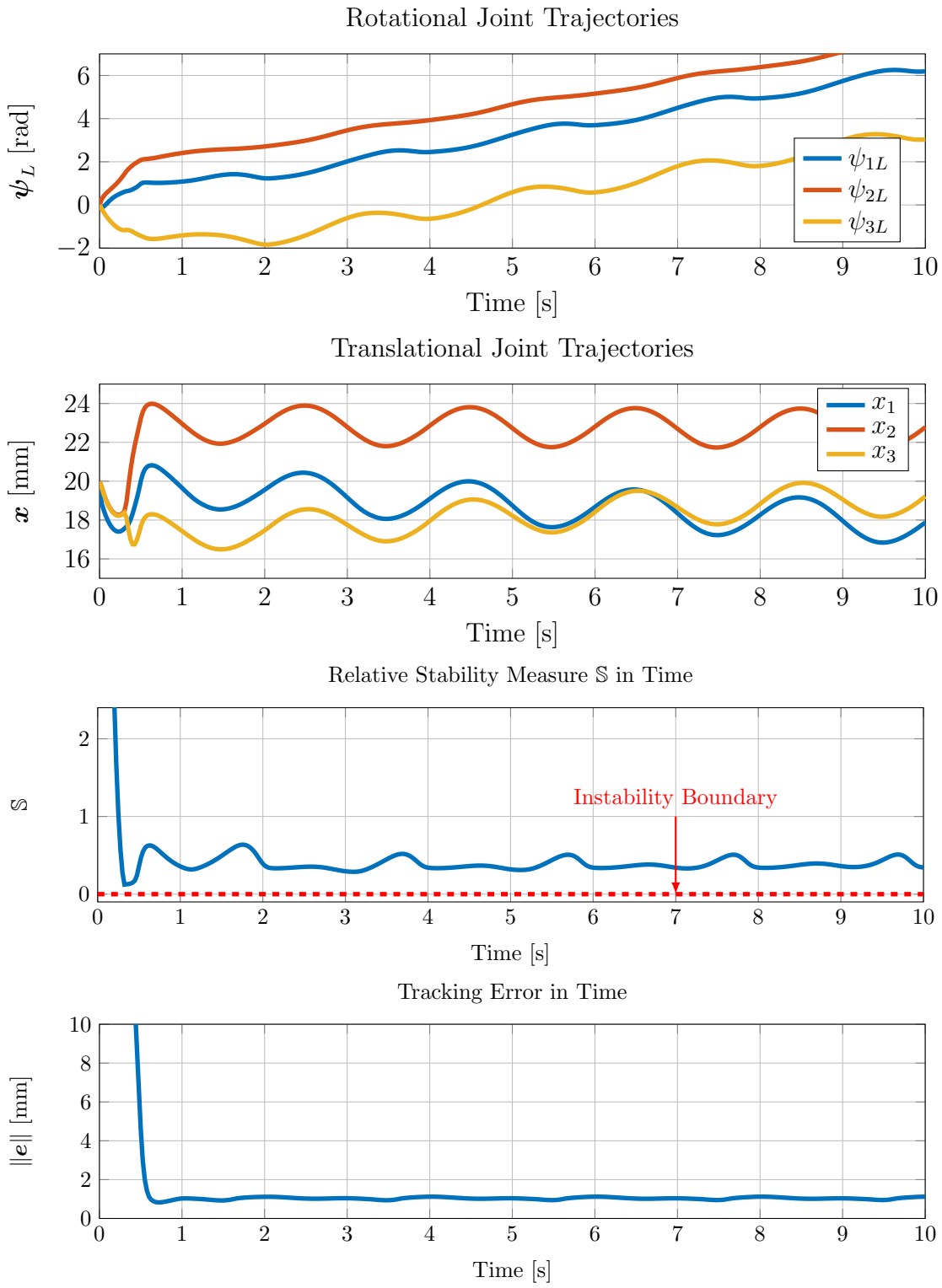

Figure 4.5: A stabilized trajectory: this simulation utilizes the control law from (4.18) and is otherwise identical to the simulation from Figure 4.4. When $\mathbb{S}$ is low, the controller moves away from instability while maintaining tracking.

matrix from (4.18) as $\mathbf{A}$, then we can re-express this update law as

$$\dot{\boldsymbol{q}} = \underbrace{\mathbf{A}\mathbf{J}^T\mathbf{W}_0\dot{\boldsymbol{x}}_d}_{\dot{\boldsymbol{q}}_T} + \underbrace{\mathbf{A}\mathbf{W}_{\mathbb{S}}(\boldsymbol{q})\boldsymbol{v}_{\mathbb{S}}}_{\dot{\boldsymbol{q}}_{\mathbb{S}}} , \tag{4.21}$$

and it becomes clear that the joint velocity $\dot{\boldsymbol{q}}_T$ is related to tracking, and the joint velocity $\dot{\boldsymbol{q}}_{\mathbb{S}}$ is related to instability avoidance. We can compare the norm of these two competing joint velocities to help understand which term is dominating the simulation. Figure 4.6 shows the relative norm of these joint velocities, or

$$\phi = \frac{\|\dot{\boldsymbol{q}}_{\mathbb{S}}\|}{\|\dot{\boldsymbol{q}}_{\mathbb{S}}\| + \|\dot{\boldsymbol{q}}_T\|} , \tag{4.22}$$

for both rotational (ϕ_R) and translational (ϕ_T) joint velocities for the simulation. As is clear from this figure, when $\mathbb{S}$ is low, the effect of $\dot{\boldsymbol{q}}_{\mathbb{S}}$ becomes more prominent, and there appears to be an oscillating exchange of control priority from tracking to instability avoidance.

4.7.5 The Effect of the Stability Threshold

We re-ran the simulation from the preceding section three more times with $\mathbb{S}^*$ chosen as 0.1, 0.2, and 0.3. In all cases, the controller was able to track well and respect the relative stability measure thresholds. For higher values of $\mathbb{S}^*$, up to around 0.8 for this particular trajectory, tracking was still possible, but the joint trajectories began to noticeably chatter. Eventually, with high enough $\mathbb{S}^*$, the control algorithm can no longer maintain tracking because the commanded trajectory is no longer in the stable workspace (the workspace where each configuration satisfies $\mathbb{S} > \mathbb{S}^*$).

There are a few interesting trends to note as $\mathbb{S}^*$ increases, as shown in Figure 4.7. First, the relative stability measure trajectories look nearly identical except for an offset in $\mathbb{S}$. Secondly, the initial stability response becomes increasingly noisy as $\mathbb{S}^*$

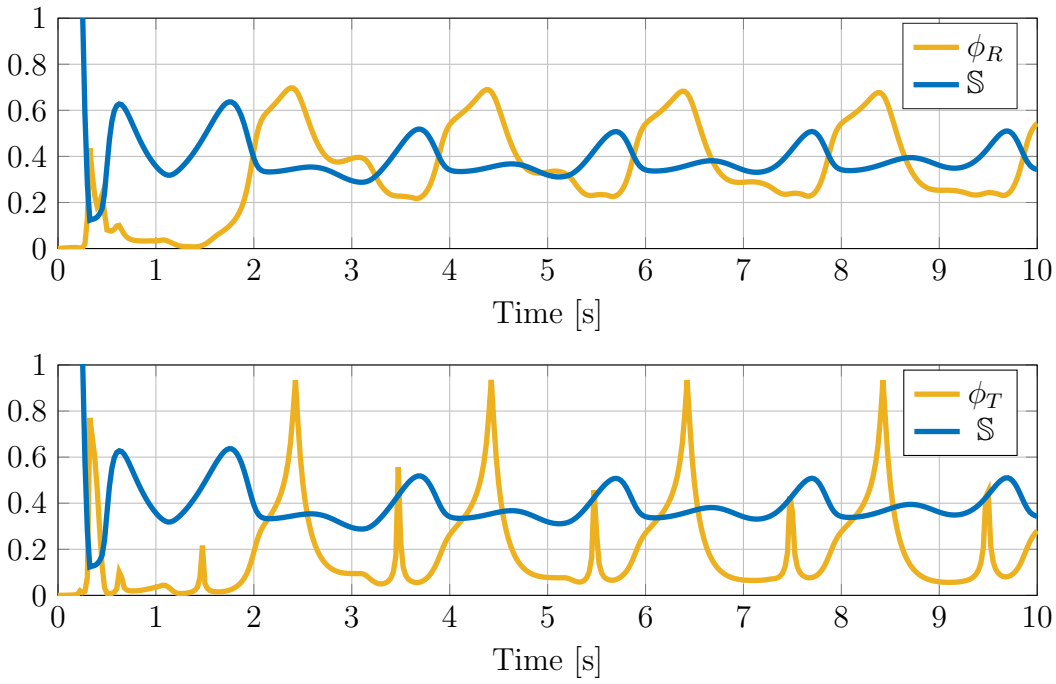

Figure 4.6: Results from the simulation in subsection 4.7.4. (Top) ϕ_R and $\mathbb{S}$ in time. When the relative stability measure is low, stabilizing rotational joint velocities become more prominent. (Bottom) ϕ_T and $\mathbb{S}$ in time. When stabilility is low, there are bursts of stabilizing translational joint velocities.

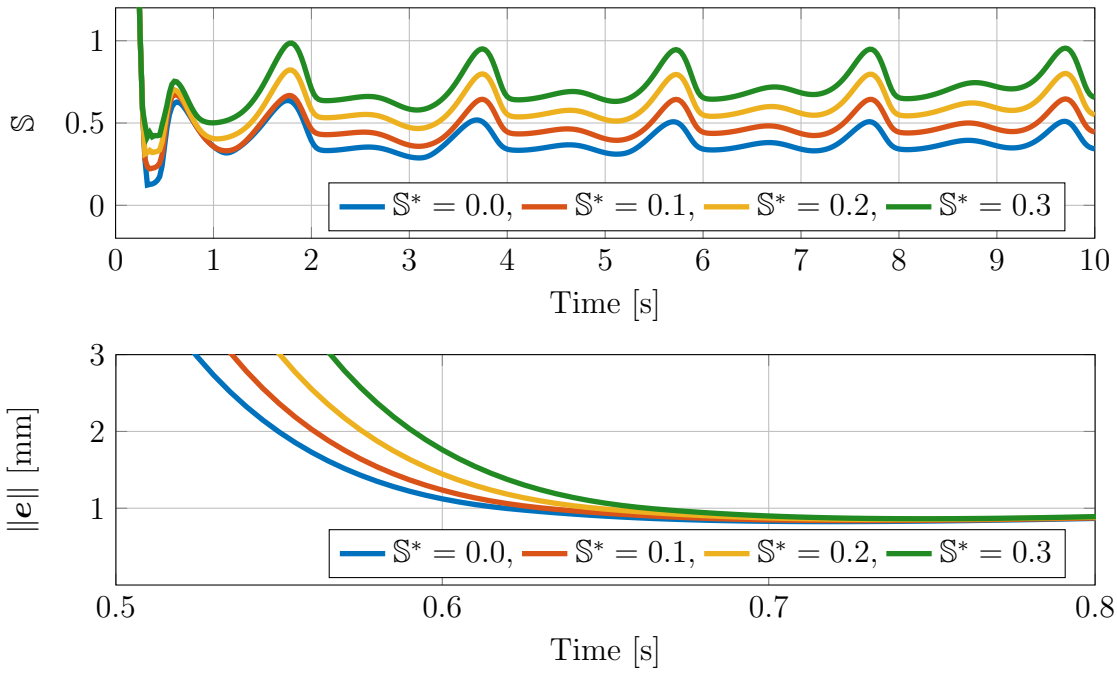

Figure 4.7: (Top) The relative stability measure $\mathbb{S}$ in time for varying choices of $\mathbb{S}^*$. (Bottom) The tracking error in time for varying choices of $\mathbb{S}^*$. The tracking response time is correlated with the choice of $\mathbb{S}^*$.

increases. This is likely due to the fact that the manipulator starts far from the trajectory, and the stability term and the tracking term of the cost function both become very large simultaneously. Finally, the tracking response time seems to be tightly correlated to the choice of $\mathbb{S}^*$. The higher the relative stability measure threshold $\mathbb{S}^*$, the longer it takes to track the trajectory. Eventually, all of the trajectories seem to track equally well, but trajectories with lower $\mathbb{S}^*$ begin tracking well more quickly.

4.8 Redundancy Resolution for Instability Avoidance: Discussion

4.8.1 What Are the Limits of This Algorithm?

The preceding analysis has clearly shown that this control algorithm is capable of stabilizing a trajectory that would otherwise be unstable and that the algorithm can maintain a margin from instability while still tracking the trajectory. What remains

to be seen is the limits of this algorithm; for example, as the tubes get even more curved, at what point is the algorithm no longer useful. One limiting factor is, of course, the stable workspace, but as was shown earlier, the elimination of a large part of the joint space does not necessarily correspond to a large reduction in the manipulator's workspace. The mapping from joint space to task space is very complex, and in these simulations we found that often the size of the manipulator's workspace is very robust to a shrinking joint space. This observation, though anecdotal and imprecise at this point, is very encouraging towards future applications of concentric tube manipulators. Instability can be a challenging design limitation for concentric tube manipulators and has greatly reduced the space of viable designs. In general, higher tube precurvatures mean a larger workspace and that the system can turn tighter corners. These properties are particularly important in a surgical context, and this control strategy may allow designers to re-consider designs that were previously considered infeasible.

As an example of the robustness of this algorithm, we chose a design that is well beyond the limit of what we would previously consider feasible. In the following simulation, the precurvatures of the inner, middle, and outer tube are selected to be $80\,\mathrm{m}^{-1}$, $40\,\mathrm{m}^{-1}$, and $20\,\mathrm{m}^{-1}$. As we expected, when the stabilizing controller was not used (i.e. using the control update law from (4.12)), the system immediately became extremely unstable, and the controller commanded configurations that were elastically unstable (i.e. not physically achievable) for the remainder of the simulation, as shown in Figure 4.8. After switching to the stabilizing control law from (4.18), the stability and tracking are shown in Figure 4.9. While this is, again, just an illustration of the potential of the algorithm, it shows that this algorithm will likely be useful for designs beyond the limits of what has been considered reasonable in the past.

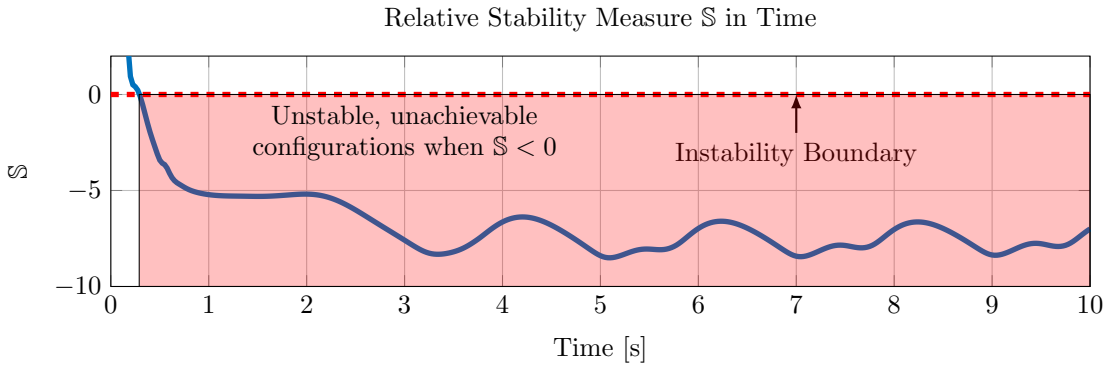

Figure 4.8: The same simulated trajectory, but with a design that is extremely susceptible to elastic instability. This design would not be considered to be a viable design candidate in the past. This trajectory is simulated without the stabilizing controller, using the update law from (4.12).

4.9 Redundancy Resolution for Tunable Arm Stiffness

4.9.1 Motivation for Tunable Arm Stiffness

During surgery, sometimes high tool stiffness is a good thing, but sometimes it is not. When suturing, significant forces are needed to drive a needle, but when manipulating around sensitive brain tissue, the surgeon may prefer for the instruments to be very compliant. Unlike many other design objectives, whether the manipulator should be stiff, compliant, or somewhere in between, depends on the surgical context.

A fascinating aspect of continuum manipulators is that they can respond to this context and adjust their stiffness properties during the operation. Since continuum robots are constantly reconfiguring their backbone, they are also unavoidably constantly re-defining their response to loads. If a manipulator has redundant degrees of freedom, these redundant degrees of freedom can be commanded to maximize or minimize stiffness while still tracking the surgeon's motions.

Potentially, a controller like the one we discuss here could be used in surgery to allow the surgeon to switch between a "stiff manipulation mode" and a "compliant manipulation mode". This concept could potentially be useful across a broad spec-

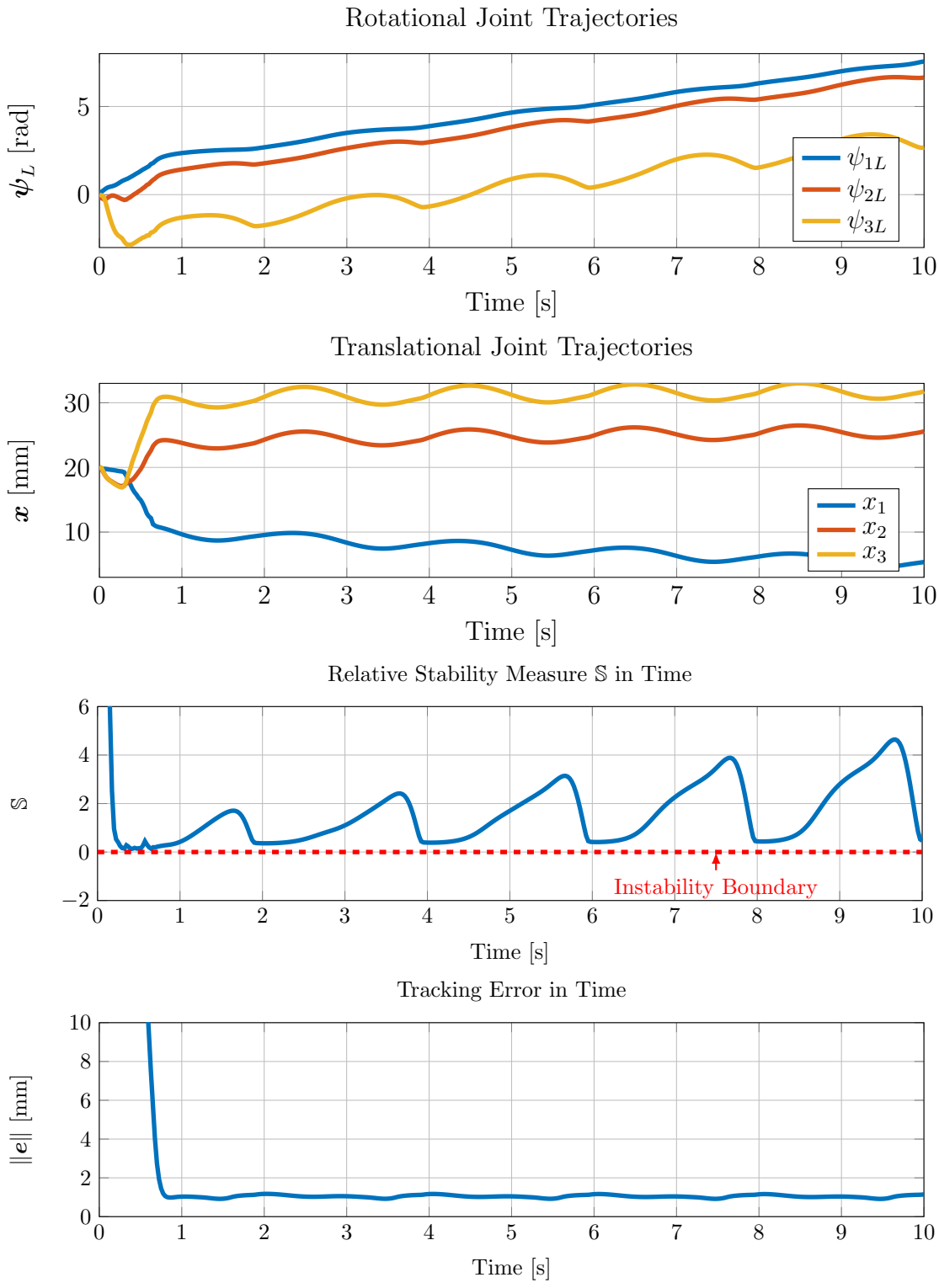

Figure 4.9: A simulation of the stabilized trajectory with a manipulator that is extremely susceptible to instability. This is the same manipulator that generated Figure 4.8 without the stabilizing controller. Note that the relative stability measure $\mathbb{S}$ is also greater when the tubes are aligned for high precurvature tubes.

trum of surgical procedures, and would also potentially give surgeons a new way to think about their tools. This could ultimately be implemented with a simple push button that would smoothly re-configure the manipulator, while holding the tip position constant.

4.9.2 The Stiffness Optimizing Control Law

The compliance matrix $\mathbf{C} \in \mathbb{R}^{6\times6}$ maps a tip wrench $\boldsymbol{w} \in \mathbb{R}^6$ to a deflection $\boldsymbol{\delta} \in \mathbb{R}^6$ at the tip of the robot as $\mathbf{C}\boldsymbol{w} = \boldsymbol{\delta}$. In this chapter, we choose to look specifically at the mapping between force $\boldsymbol{f}$ and positional deflection $\boldsymbol{\delta_x}$, which is the top left 3×3 block of $\mathbf{C}$, or $\mathbf{C_f}$ (see Figure 4.10). We choose to utilize the maximum singular value of $\mathbf{C_f}$, which we define with the symbol $\sigma_{\mathbf{C}}$, as the metric which we will use to redefine our objective function from (4.2). More precisely, we have that

$$\mathbf{C_f} = \mathbf{U}\boldsymbol{\Sigma}\mathbf{V^T} \tag{4.23}$$

and define $\sigma_{\mathbf{C}}$ as

$$\sigma_{\mathbf{C}} \triangleq \max\Big(\mathrm{diag}(\boldsymbol{\Sigma})\Big)\,. \tag{4.24}$$

This means that when the controller generates joint velocities that increase $\sigma_{\mathbf{C}}$, the manipulator will become more compliant in its most compliant direction. On the other hand, when $\sigma_{\mathbf{C}}$ decreases, the manipulator will become less compliant in its most compliant direction. Using this new definition, we redefine the objective function for our damped least squares control law from (4.2) as

$$H = \frac{1}{2}\Big(\underbrace{(\mathbf{J}\dot{\boldsymbol{q}} - \dot{\boldsymbol{x}}_d)^T\mathbf{W}_0(\mathbf{J}\dot{\boldsymbol{q}} - \dot{\boldsymbol{x}}_d)}_{\text{Tracking}} + \underbrace{\dot{\boldsymbol{q}}^T\mathbf{W}_D\dot{\boldsymbol{q}}}_{\text{Damping}} + \underbrace{\dot{\boldsymbol{q}}^T\mathbf{W}_J\dot{\boldsymbol{q}}}_{\substack{\text{Joint Limit}\\ \text{Avoidance}}} + \underbrace{(\dot{\boldsymbol{q}} - \boldsymbol{v}_{\mathbf{C}})^T\mathbf{W}_{\mathbf{C}}(\dot{\boldsymbol{q}} - \boldsymbol{v}_{\mathbf{C}})}_{\substack{\text{Compliance/Stiffness}\\ \text{Optimization}}}\Big)\,. \tag{4.25}$$

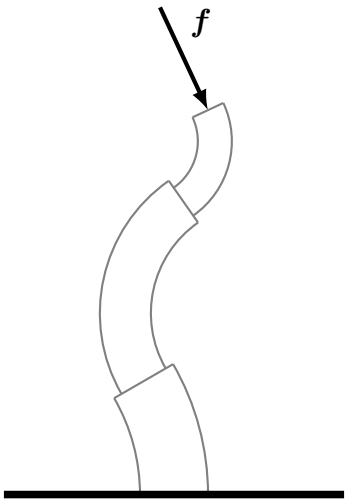

Figure 4.10: A three tube concentric tube manipulator subject to a tip load $\boldsymbol{f}$. The force compliance matrix $\mathbf{C}_{\boldsymbol{f}} \in \mathbb{R}^{3\times3}$ maps the tip load $\boldsymbol{f} \in \mathbb{R}^3$ to a positional tip deflection $\boldsymbol{\delta}_{\boldsymbol{x}} \in \mathbb{R}^3$.

The control law from (4.3) then becomes

$$\dot{\boldsymbol{q}} = \Big(\mathbf{J}^T\mathbf{W}_0\mathbf{J} + \mathbf{W}_D + \mathbf{W}_J(\boldsymbol{q}) + \mathbf{W}_{\mathbf{C}}(\boldsymbol{q})\Big)^{-1}\Big(\mathbf{J}^T\mathbf{W}_0\dot{\boldsymbol{x}}_d + \mathbf{W}_{\mathbf{C}}(\boldsymbol{q})\boldsymbol{v}_{\mathbf{C}}\Big)\,. \tag{4.26}$$

We define the desired joint space velocity $\boldsymbol{v}_{\mathbf{C}}$ in the (positive or negative) direction of the gradient of $\sigma_{\mathbf{C}}$ as

$$\boldsymbol{v}_{\mathbf{C}} = \alpha_{\mathbf{C}}\frac{\partial\sigma_{\mathbf{C}}}{\partial\boldsymbol{q}} = \alpha_{\mathbf{C}}\nabla\sigma_{\mathbf{C}}\,. \tag{4.27}$$

If $\alpha_{\mathbf{C}} > 0$, this points $\boldsymbol{v}_{\mathbf{C}}$ towards the positive gradient of $\sigma_{\mathbf{C}}$, so the system should try and achieve velocities in the direction which makes the system more compliant (in its most compliant direction). If the opposite is true and $\alpha_{\mathbf{C}} < 0$, the system will try and achieve joint velocities to make the system less compliant, or stiffer (in its most compliant direction). We numerically compute the gradient $\nabla\sigma_{\mathbf{C}}$ using centered finite differences, with a translational step of 0.01 mm and a rotational step of 0.05 °. Finally, we also add a proportional gain term to increase or decrease the effect of the compliance term in the objective function. This is simply a diagonal matrix defined

as

$$\mathbf{W_C} = k_{\mathbf{C}}\mathbf{I}\,, \tag{4.28}$$

where $k_{\mathbf{C}}$ is a proportional gain scalar. For the following simulations, we have heuristically chosen $k_{\mathbf{C}} = 1000$ and $\alpha_{\mathbf{C}} = \pm 300$.

4.9.3 Control Algorithm Performance

To investigate this control algorithm, we simulated the trajectory described in subsection 4.6.2 three times using the tubes from Table 4.1. The precurvatures for this simulation will return to the stable precurvatures from subsection 4.6.3 of $10\,\mathrm{m}^{-1}$, $12\,\mathrm{m}^{-1}$, and $22\,\mathrm{m}^{-1}$ for the inner, middle, and outer tube, respectively.

The first simulation update law did not utilize compliance redundancy resolution and utilized the update law from (4.12), the second attempts to maximize the compliance metric $\sigma_{\mathbf{C}}$ using the update law from (4.26) with $\alpha_{\mathbf{C}} = 300$, while the third attempts to minimize the compliance metric $\sigma_{\mathbf{C}}$ using the update law from (4.26) with $\alpha_{\mathbf{C}} = -300$. The results of this simulation are shown in Figure 4.11.

All three simulations effectively tracked the trajectory, with very reasonable joint trajectories. The nominal compliance response had an oscillating compliance around 20 $^{\mathrm{mm}}/_{\mathrm{N}}$, the maximum compliance response slowly increased its compliance over the 10 s simulation from roughly 20 $^{\mathrm{mm}}/_{\mathrm{N}}$ to 40 $^{\mathrm{mm}}/_{\mathrm{N}}$, and the minimum compliance response slowly decreased its compliance from roughly 20 $^{\mathrm{mm}}/_{\mathrm{N}}$ to 10 $^{\mathrm{mm}}/_{\mathrm{N}}$.

It is interesting to compare $\sigma_{\mathbf{C}}$ between the maximum compliance trajectory and the minimum compliance trajectory. The two trajectories start with the same compliance (by definition), but by the end of the 10 s simulation the maximum compliance simulation is about four times more compliant than the minimum compliance simulation. It is likely this difference would be very apparent to a surgeon. It has been shown that the peak forces during minimally invasive surgery are around 2 N for su-

turing skin, around 1 N for suturing muscle, and typically less than 0.5 N for suturing liver tissue [118]. The forces during other tissue interactions (i.e. not driving needles) are typically much less than these.

As a specific example of the potential utility of this control law, consider a 0.5 N force on the tip of the concentric tube manipulator investigated here. In max compliance mode, this could generate a deflection of up to 20 mm, and in minimum compliance mode, this would generate a deflection as small as 5 mm. This could very well be the difference between being able to drive the needle and not drive the needle. This is just one example, the absolute compliance of these manipulators is very sensitive to the wall thickness (stiffness is proportional to the fourth power of outer and inner diameter), and how far out of its constrained exit point the manipulator is operating (bending stiffness decreases with the third power of length for cantilevered beams, which our system approximates). For this reason, it is perhaps more informative to investigate the ratio between the max/min compliance trajectories as is shown in Figure 4.11 (Middle).

4.9.4 Compliance Optimization with Tip Position Regulation

As an alternative way to analyze this control law, we commanded a static tip trajectory at a position near the center of the manipulator's workspace at (x, y, z) =(1,1,55) mm. Every 10 seconds, the simulation switches between maximizing and minimizing compliance, as shown in Figure 4.12.

Interestingly, the system appears to respond quickly to become more compliant, but it takes much longer for the system to stiffen from a compliant configuration. Notice that the translational joint trajectories extend the inner tube out very far and almost completely retract the outer tube when maximizing compliance. This is intuitive since the outer tube is considerably stiffer than the inner tube. The system tracked the desired point within 0.1 mm of error in 0.5 s after starting over 10 mm from

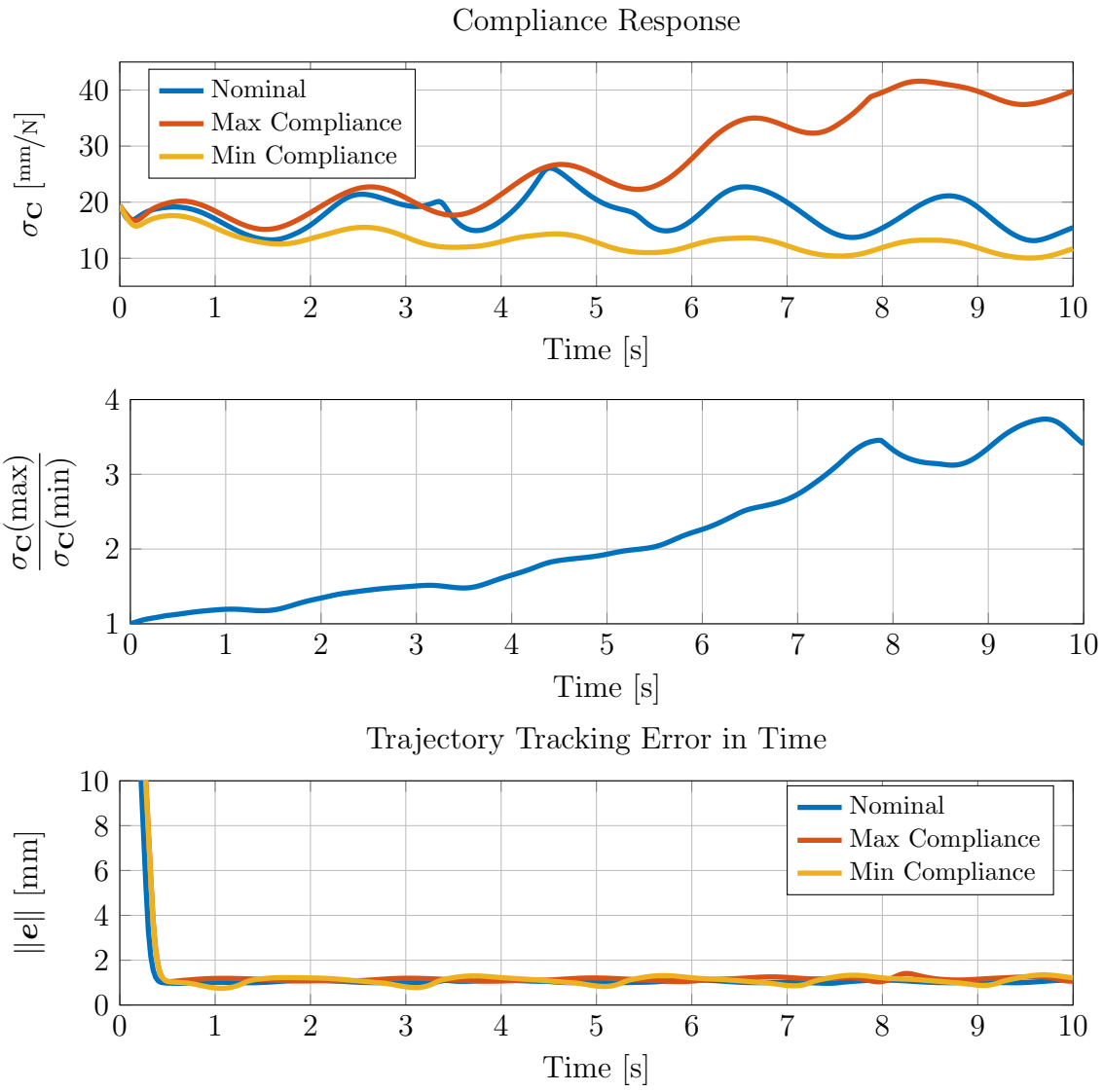

Figure 4.11: (Top) Trajectories of the compliance metric $\sigma_{\mathbf{C}}$ following the path described in Table 4.4 with the tubes from Table 4.1. For the nominal trajectory, we utilize the control law from (4.12). For the minimum and maximum compliance trajectories we utilize the update law from (4.26) with $\alpha_{\mathbf{C}} = -300$ and $\alpha_{\mathbf{C}} = 300$, respectively. (Middle) The ratio of $\sigma_{\mathbf{C}}$ in the maximum compliance trajectory to $\sigma_{\mathbf{C}}$ in the minimum compliance trajectory. The manipulator becomes about four times more compliant by the end of the trajectory, which is likely to be significant in a surgical scenario. (Bottom) All three trajectories have similar tracking performance.

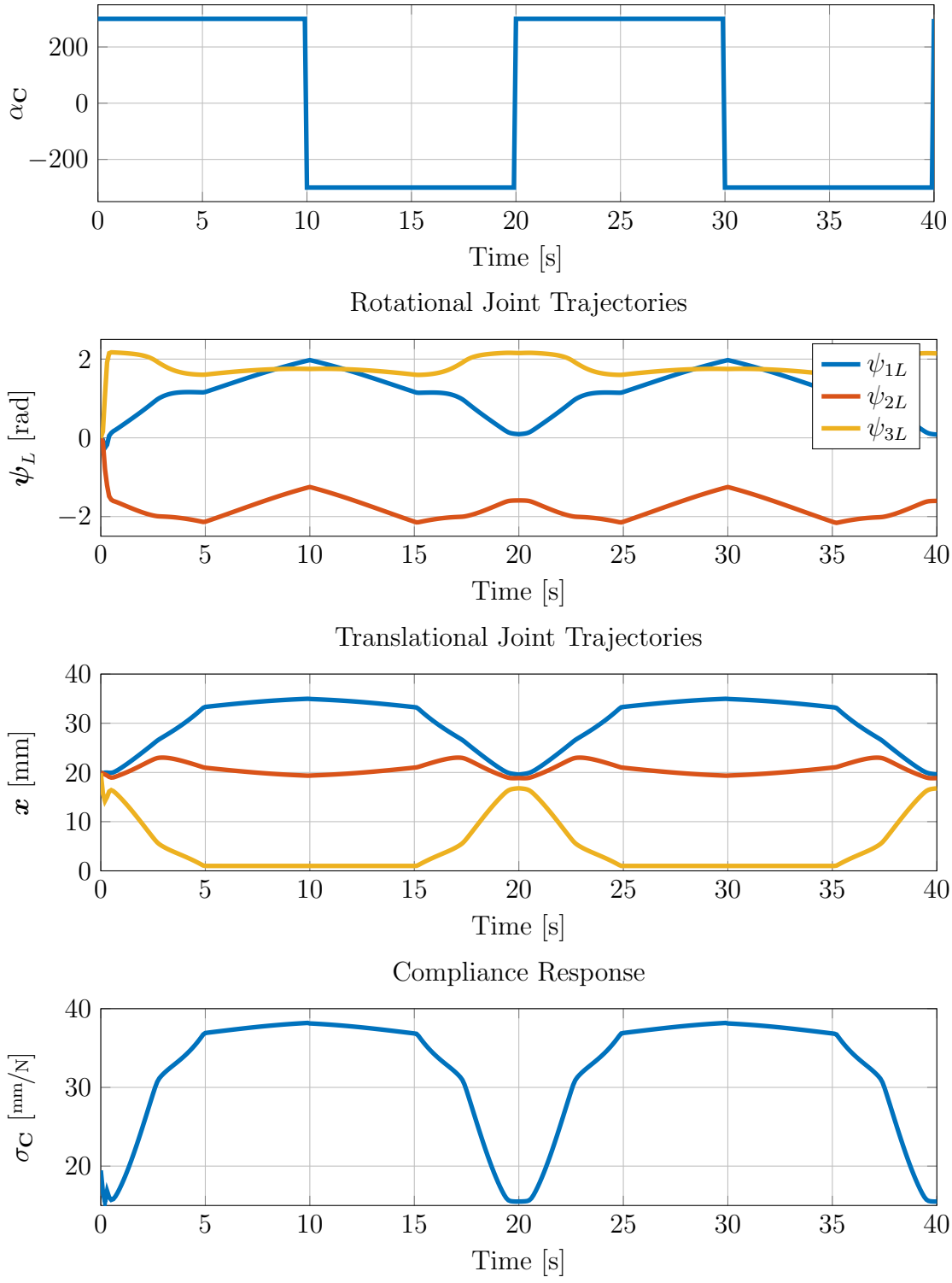

Figure 4.12: In this simulation, the manipulator regulates its tip position at fixed target. Every 10 seconds, the system switches between maximizing and minimizing the compliance metric. Notice that the inner tube extends and the outer tube retracts to maximize compliance, and the opposite happens to minimize compliance. The tracking error (not shown) decreases below 0.1 mm in 0.5 s and remains there.

the trajectory, and regulated tracking $<0.1\,\text{mm}$ for the remainder of the simulation.

4.9.5 The Link Between Stability and Compliance

It is intuitive that there must be a link between stability and stiffness/compliance. If the system is stable, one would expect a temporary external load to momentarily deflect the manipulator and for it to quickly return to its minimum energy configuration. This is analogous to a mass, spring, damper system at its equilibrium resting configuration, subject to a temporary step force. If the spring stiffness and the damping constant are positive, a temporary load will perturb the system from its rest configuration, but it will move back towards its equilibrium. On the other hand, if the spring constant is negative, an infinitesimal perturbation will force the system away from the equilibrium - making it an unstable equilibrium. Without a positive, restoring stiffness, the system can behave in an unstable way.

The concentric tube manipulator, although considerably more complex, should behave similarly. The metric we have defined for compliance optimization $\sigma_{\mathbf{C}}$ is the maximum compliance, or alternatively, the minimum stiffness in any direction of the manipulator. We hypothesize that $\sigma_{\mathbf{C}}^{-1}$ should go to zero when the relative stability measure $\mathbb{S}$ goes to zero. To confirm this, we re-ran the simulation from Section 4.7.2 and Figure 4.4, where each tube precurvature was set to $30\,\text{m}^{-1}$; this trajectory is known to be unstable.

A comparison of the relative stability measure $\mathbb{S}$ and the inverse of the compliance metric $\sigma_{\mathbf{C}}^{-1}$ are shown in Figure 4.13. This figure demonstrates the correlation between minimum stiffness and the relative stability measure. Namely, they share the property that they both go to zero at the same time; we have confirmed this property through several simulations but have not rigorously proven this fact in a general way. However, the general shape of the trajectories in time are not identical, so resolving redundancy for stiffness maximization and stability maximization will

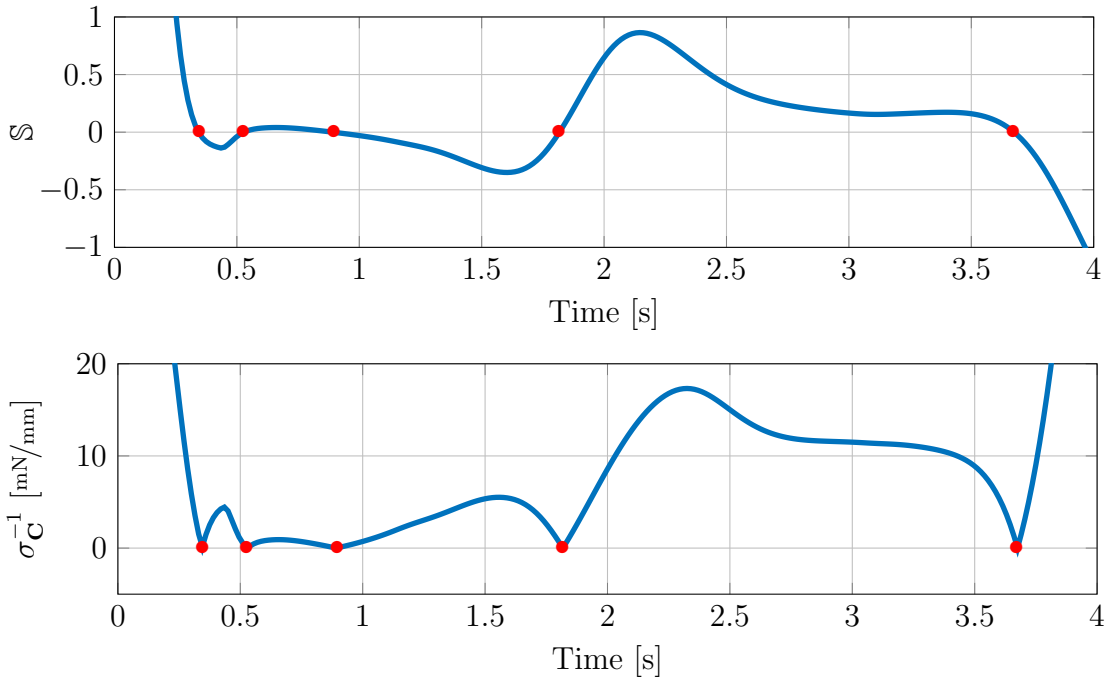

Figure 4.13: The relative stability measure $\mathbb{S}$ trajectory and the minimum stiffness trajectory for the simulation from Figure 4.4. The relative stability measure and the minimum stiffness approach zero simultaneously.

provide different paths through joint space. Nevertheless, we hypothesize that $\sigma_{\mathbf{C}}^{-1}$ could be used as a replacement for $\mathbb{S}$ in the elastic instability avoidance control law and produce very similar instability avoidance, although we have not yet tested this hypothesis rigorously in simulation.

4.10 Redundancy Resolution Conclusions

This chapter investigated redundancy resolution for elastic instability avoidance and compliance optimization for concentric tube manipulators. The elastic stability control results in this chapter are particularly promising since they show that the high curvature designs that were previously considered out of the question due to instability concerns may now be back in play even for real-time teleoperation applications. This chapter contributes a control law that allows one to define a relative stability measure threshold and treat it very similarly to a joint limit. This allows the user to

have confidence that the system will never go unstable, without pre-planning the trajectory the system must take. It is important to note that this work does not consider external loads, but it is likely that a similar strategy can be used to avoid instability in the presence of external loads, if a bound on the magnitude of the potential load is known. This chapter has also contributed a strategy for maximizing compliance and stiffness while still tracking a desired trajectory and demonstrated the connection between the relative stability measure and the compliance of this system.

Future work remains to confirm that physical teleoperation will perform as anticipated using the control laws defined in this chapter. It is worth noting here that the joint trajectories generated in these simulations are realizable in a physical prototype system. It will also be interesting to push the limits of these control laws and try to understand when a manipulator is so susceptible to instability that it is no longer useful. The answer to this question undoubtedly depends on the specific application requirements, but these results enable interesting new possibilities for the design and operation of concentric tube manipulators.

Similarly, for the stiffness and compliance redundancy resolution, it would be informative to do physical experiments under teleoperation scenarios where the surgeon has the opportunity to utilize the different control modes. It would be particularly impressive if a future experiment could prove that a task was enabled by switching between compliance modes. Should this idea prove valuable in continuum surgical robotics, it could potentially enable surgeons to think about their tools in a different way.

CHAPTER 5

TWO-ARMED ROBOTIC NEUROENDOSCOPY: SYSTEM DESIGN, MANIPULATOR OPTIMIZATION, AND EXPERIMENTAL VALIDATION

5.1 Outline

The purpose of the work in this chapter is to design, optimize, and experimentally test a robotic system featuring two miniature concentric tube arms for use in endoscopic brain surgery. There is an opportunity to utilize the properties of concentric tube manipulators to greatly enhance the neurosurgeon's capabilities during these sensitive procedures. This chapter will begin by laying out the clinical motivation for a rigid neuroendoscopic system and will review the related work in robotic endoscopic neurosurgery. There are three main research aspects to this chapter. First, we will present the design of a new miniaturized, embedded, teleoperated, robotic system for neurosurgery. Second, we will perform a detailed tube design optimization, with particular emphasis on how stability enters the design problem. The chapter will finish with a phantom validation experiment comparing the performance of the robotic system to manual endoscopic neurosurgery for the removal of colloid cysts.

5.2 Motivation and Background

The challenges of rigid endoscopy are exacerbated during neuroendoscopy because tilting of the endoscope is very limited and potentially dangerous [119] since the endoscope is passing through sensitive brain tissue. Thus, neuroendoscopy is another application that could benefit from a system like the one described in Chapter 2. The neurosurgical procedures we will focus on here are surgeries in the brain ventricles.

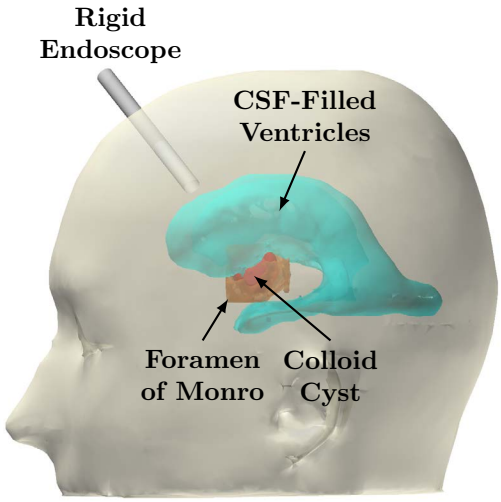

Figure 5.1: A diagram of rigid endoscopic neurosurgery. This figure shows a colloid cyst in the center of the brain, which is one application of rigid neuroendoscopy.

The ventricles are cavities located near the center of the brain that are full of cerebrospinal fluid, see Figure 5.1. Patients may have a variety of tumors or cysts in or very near the ventricles. These tumors/cysts are particularly challenging to approach surgically because so much brain tissue has to be traversed to access the tumor. Colloid cysts, benign tumors between the two brain hemispheres, account for 2% of primary brain tumors and 15-20% of intraventricular masses [120, 121, 122], and are one of the types of brain tumors that have been approached endoscopically. The conventional approach is open surgery, which includes a craniotomy (i.e. the removal of part of the bone from the skull to expose the brain tissue) and brain tissue retraction. In this approach, two tools are held by the surgeon outside of the patient and the tumor or cyst is manually resected under a microscope. Endoscopic approaches, which require only a burr hole in the skull and trocar to access the ventricles, are also an option for many of these tumors and offer significant morbidity advantages. In 1994, a study by Lewis et al. compared open treatment of colloid cysts under a microscope to the endoscopic approach [123]. The authors found that the operative time was 206 minutes versus 127 minutes, the ICU stay was 9.5 days versus 4

days, and patients returned to work after 59 days versus 26 days for the open versus endoscopic approach, respectively. Another more recent, similar study by Horn et al. found that the endoscopic approach offered similar advantages: the operative time was 267 minutes versus 173 minutes, the ICU stay was 3.3 days versus 2.3 days, and the hospital stays was 6.3 days versus 5.4 days, and additionally the infection rate was significantly lower, with similar efficacy [124].

While the morbidity advantages are clear, they do not necessarily come without a cost. It is common throughout the endoscopic neurosurgical literature for authors to express a need for improved endoscopic instrumentation. For example, Greenlee et al. reported in a broad study on endoscopic resection of colloid cysts that "...there is a clear need for improved endoscopic instrumentation to allow precise, bimanual dissection" [125]. Gaining this bimanual manipulation, however, is challenging. Surgeons typically hold the endoscope in one hand and the transendoscopic instrument in the other, so it is not possible to simultaneously manipulate two instruments. One possible technique is to adopt a two-surgeon approach, where one surgeon holds the endoscope and the other controls multiple instruments [125], but this brings additional coordination challenges. Other surgeones reference that they widen the edges of the burr hole incision to allow for greater maneuvering of the endoscope, to provide some instrument manipulation by tilting the endoscope outside of the patient [126]. However, as the trocar is widened or the burr hole is opened more than the minimum amount, the invasiveness benefits of the minimally invasive endoscopic approach are reduced.

5.3 Related Work: Robots in Endoscopic Neurosurgery

Robots have been active in neurosurgery dating all the way back to the late 1980s and early 1990s with the work of Benabid et al. and Davies et al. Much of the early robotic neurosurgery research focused on a stereotactic approach to brain surgery

and integration of preoperative imaging. For an overview of robots in neurosurgery, see [127], we will focus on surgical robots that have been specifically designed for neuroendoscopy.

Recently, there has been a sharp increase in the number of endoscopic robotic neurosurgical devices. A hexapod parallel robot for endoscopic positioning (pivoting/insertion) has been used in patients for endoscopic third ventriculostomy [9]. This system requires a 14 mm burr hole in the skull, but claims a precision of less than $200\,\mu m$. The motion of the rigid endoscope and tools are derived from pivoting in the oversized burr hole. Benabid et al. developed a stereotactic frame robot that integrates preoperative imaging, which has evolved over the years, and has now been commercialized by Renishaw and is brand-named the Neuromate [128, 129, 130]. This system can be used in "stereotactic applications in neuroendoscopy" according to the company's website. Around the same time that Benabid began this work, Davies et al. began working on a control of a rigid neuroscope [131]. This system provided four degrees of freedom and was based on the same robot design developed earlier for robotic prostatectomy [84]. NeuRobot is a recent innovation that delivers a roboticized endoscope that is only 10 mm in diameter and can deliver three, 3 degree of freedom instruments. The system requires a 20 mm burr hole in the skull. These instruments can insert, rotate, and "neck-swing" (i.e. a wrist tilt maneuver) [132], and this system has been used in human studies in Japan.

Concentric tube robots have also been looked at in the context of neuroendoscopy. A group has investigated passing multiple concentric tube robots through a rigid neuroendoscope for treatment of endoscopic third ventriculostomy [45, 46] and designed an interactive software application for patient-specific concentric tube neurosurgical instruments [48]. Another group has adapted concentric tube robots to a conventional flexible neuroendoscope for enhanced manipulation and control [25]. Similarly, it has very recently been proposed that a neuroendoscope could be developed featur-

ing side ports and multiple cameras to deploy robotic, continuum arms out of these side ports [50].

5.4 Contributions

The primary contribution of this chapter is a quantitative, experimental comparison of a bimanual robotic neuroendoscopic system versus manual, conventional endoscopic neurosurgery. A constrained design optimization for two-tube concentric tube manipulator design is presented in the neurosurgical context, using an objective function based on the manipulator's global dexterity throughout its workspace. As part of the design optimization, we also provide a discussion of the connection between stability and dexterity, and several design concepts inspired by the understanding of the stability of these flexible manipulators. We also present a new, custom robotic system which is designed to be hand-held, teleoperated, with embedded low-level control, and deliver two concentric tube manipulators through the working channel of a neuroendoscope.

5.5 Neuroendoscopic Robotic System Design

5.5.1 High-Level System Design

The main priority of the design of this new neuroendoscopic system, in comparison to the system presented in Chapter 2, is miniaturization and embedded integration to a system that is similar in size to other tools currently present in the operating room (like an orthopedic drill, for example). The goal of the design is not for the surgeon to be able to hold the robot for the entire procedure, but rather for the surgeon and operating room staff to be able to comfortably move the system around the operating room, and easily be able to hold the system in one hand without assistance during setup. The design presented in Chapter 2 did not meet this requirement; it could

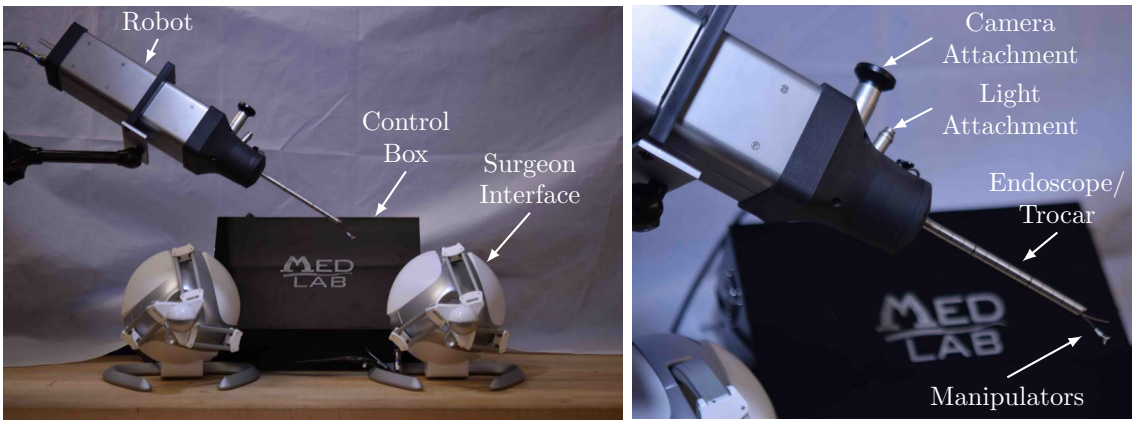

Figure 5.2: (Left) The neuroendoscopic robotic system: the robot provides two flexible, continuum manipulators. Each manipulator is made from two concentric tubes, and each tube has two degrees of freedom. The robot has 8 motors and 20 sensors. The control box has a computer and a power supply within it and communicates with the surgeon interfaces. (Right) A close-up view of the endoscope/trocar with the manipulators coming out from the tip.

easily be manipulated with counterbalance assistance, but weighed roughly 10 lb. Towards this goal, a major priority was embedding the electronics so that a large tether would not be necessary (the previous system had roughly 200 conductors in its tether, which added significant weight to the system). In contrast to the previous system, this neuroendoscopic system will be teleoperated, so there is no requirement for the user interface to be physically attached to the robot. The high-level system architecture is shown in Figure 5.2 and outlined as a schematic/block diagram in Figure 5.3.

The control box has two main elements: a power supply and a computer. The box contains two AC-DC converters outputting DC 12 V and 30 V. The 12 V signal is routed to the robot while the 30 V signal provides power to the surgeon interfaces. The surgeon interfaces plug into the control box to obtain 30 V power, and the robot and the surgeon interfaces communicate with the computer over USB. On board the robot, the 12 V power is converted into 3.3 V, 5 V, and 6 V DC power lines by a custom designed printed circuit board with switching regulators. The 5 V signal is needed for

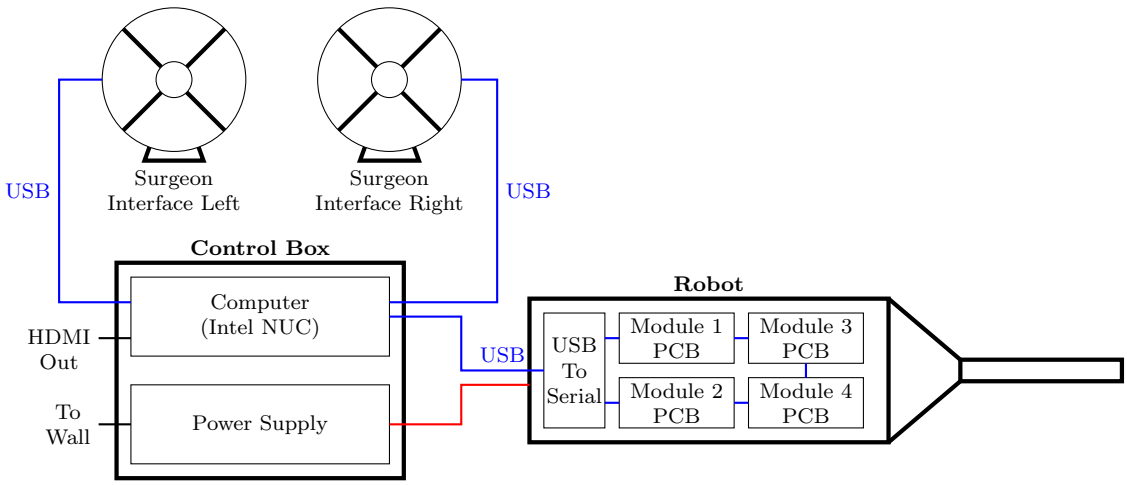

Figure 5.3: The high-level robotic system architecture: the control box contains a computer and power. The computer interfaces with two haptic devices and with the robot. The USB signal to the robot is converted to a serial signal, which communicates between the tube modules. The kinematics and high-level control are computed on the computer, while low-level control of the motors/sensors are handled on the tube module control boards.

the encoders and sensors, the 3.3 V signal is the logic level for the microcontroller, and the 6 V signal is the power rail for the motors. The robot is equipped with a USB to serial converter (FTDI, FT232H) that converts the USB signal to a serial peripheral interface (SPI) protocol.

5.5.2 Low-Level System Design

The functional unit of the robot is referred to as a tube module, and is shown in Figure 5.4. The robot has four tube modules, since each arm is composed of two tubes. Since each tube is independently translated and rotated, each module provides two degrees of freedom, and the entire robot provides eight degrees of freedom. Each tube module is electromechanically equivalent and is capable of (1) controlling two DC motors to rotate and translate the tube within it, (2) reading five sensors, and (3) communicating with the control computer. Because of the latency/buffering in the USB protocol, the tube modules are daisy-chained, meaning that they are con-

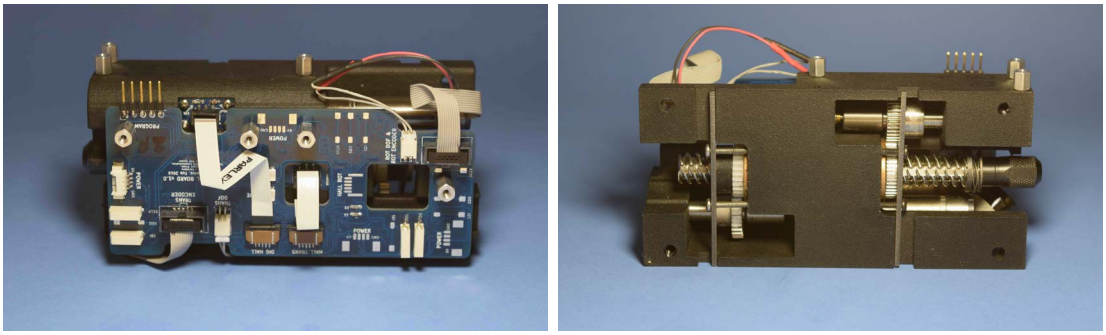

Figure 5.4: (Left) A single tube module as viewed from the tube module control board side. (Right) A tube module as viewed from the bolt side.

nected serially to one another, and chip select is not used to address an individual module. This means that any data coming from the control box proceeds through all four modules and eventually is clocked back into the USB to serial converter. Using a daisy-chained setup allowed the communication protocol to achieve a fixed communication rate of 250 Hz from the control box to the robot.

The mechanism design of the tube module features a differential drive, as shown in Figure 5.5. The tube is held within a bolt; the bolt is threaded along its length and also features a keyway. A spur gear which is internally threaded translates the bolt, and a spur gear with the mating key creates a helical, coupled translation/rotation of the bolt. A pure rotation can be generated by commanding a differential rotation of both the threaded gear and keyed gear simultaneously. The internal structure of the robot is formed by assembling the four modules together. Two modules are assembled along the axis of the endoscope to form the actuation for one arm, and this is mirrored about the midline of the system to create the actuation for the other arm. The robot is shown without its outer housing in Figure 5.6. The inner tube from each manipulator arm passes all the way through the system, so that the surgeon has access to the back ends of the tubes via the back of the robot and can insert tools through their working channels such as suction, cautery, grippers, laser fibers, etc.

The five sensors within the tube module are: two encoders, a digital hall sensor,

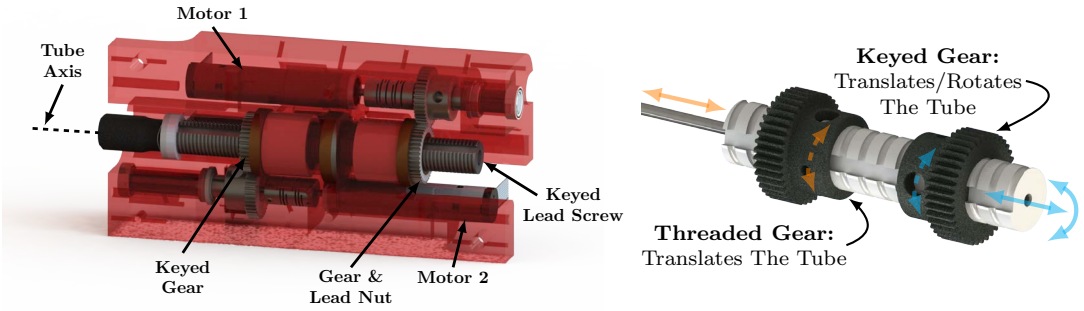

Figure 5.5: (Left) The mechanism design of a single tube module. (Right) A close up of the keyed bolt mechanism showing the details of its differential drive actuation.

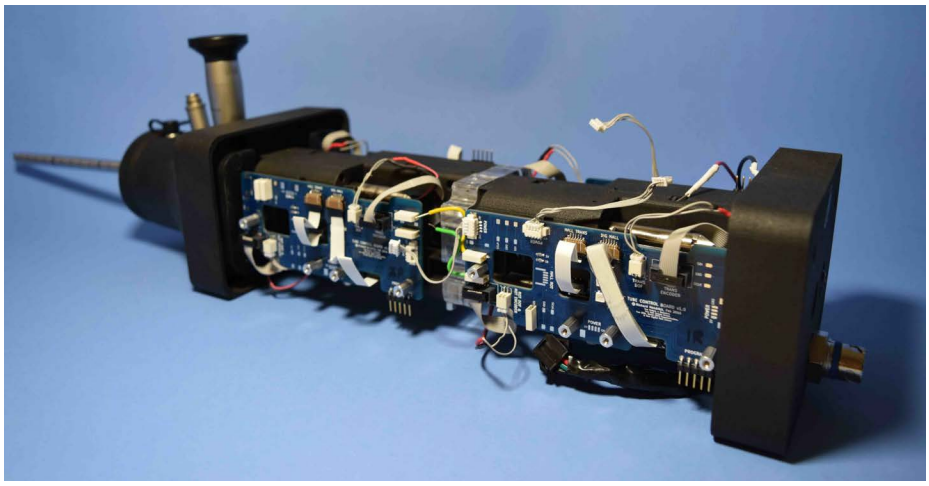

Figure 5.6: The robot without its outer housing. Four tube modules are combined to provide the actuation for the robot. Two of the modules can be seen clearly here, and the other two modules are mirrored about the midline of the robot.

a linear magnetic position sensor, and a rotary magnetic position sensor. These sensors (except for the encoders) can be seen in Figure 5.7. The linear magnetic position sensor reads from a multipole strip magnet that translates along with the bolt. This provides redundant position sensing for the bolt position (in addition to the encoder), and the sensor can also sense the end of the magnet, allowing it to be used for translational homing of the bolt. This design also allows sensing of the backlash present between the motor and the translation of the bolt. The magnetic rotary position sensor senses the angular position of the bolt. This cannot find an absolute angular position, but can be used for redundant sensing of tube rotation and for backlash detection in the rotation of the tube. Finally, the digital hall sensor senses the magnetic field generated by a magnet embedded in the hub of the gear which rotates the bolt. This sensor will flip from low to high when the field strength exceeds a threshold and is used to find a repeatable rotational home for the tube. The combination of these sensors result in a system with redundant position sensing on the tubes and automatic homing. The motor position controllers are designed to operate on encoder feedback, but the redundant sensing can be used for safety measures.

A block diagram of the tube module control board is shown in Figure 5.8. The main component of the control board is the microcontroller (dsPIC33F, Microchip). This microcontroller is designed specifically for motor control applications and includes a peripheral quadrature encoder interface (QEI). The control board implements a lead-lag controller which updates on a 1 kHz timer interrupt to control the angular position of the motor shaft. The control signal is the duty cycle of a 40 kHz pulse width modulated (PWM) signal, and the loop is closed with incremental optical encoders which are mounted directly to the motors. The PWM signals are input to a dual full bridge output motor driver (Avago A4990), which sources the current necessary to drive both motors. The magnetic position sensors communicate with the

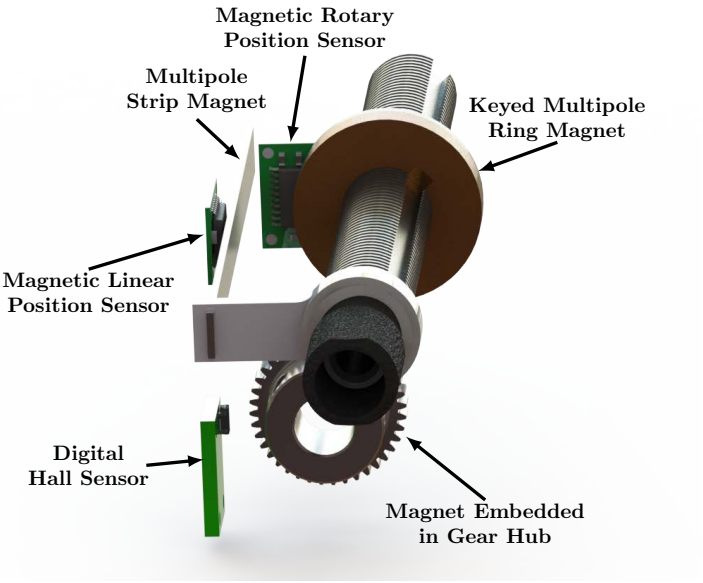

Figure 5.7: The magnetic sensors featured within the tube module. The translation of the tube is sensed with the linear position sensor, the rotation of the tube is sensed with the rotary position sensor, and the rotation of the tube is homed with the digital hall sensor.

microcontroller via a serial I^2C protocol, and the digital signal from the hall sensor is routed to a digital input pin on the microcontroller.

5.5.3 The Manipulator Arms

The purpose of the entire high-level and low-level design is to precisely control needle-sized manipulators at the tip of the rigid endoscope. These manipulators can be seen in Figure 5.9. The surgeon teleoperates the position of the tip of each of these arms with visual, endoscopic feedback. The surgeon's motions via the surgeon interface command a desired tip position in 3D, and a control algorithm on the computer computes the necessary motor/tube motions to accomplish the surgeon's desired motions. This is accomplished with a resolved-rates style routine with damping and joint limit avoidance as was described in Chapter 4. In the following section, we will describe a design optimization technique for selecting the parameters which make up the component tubes of the manipulators.

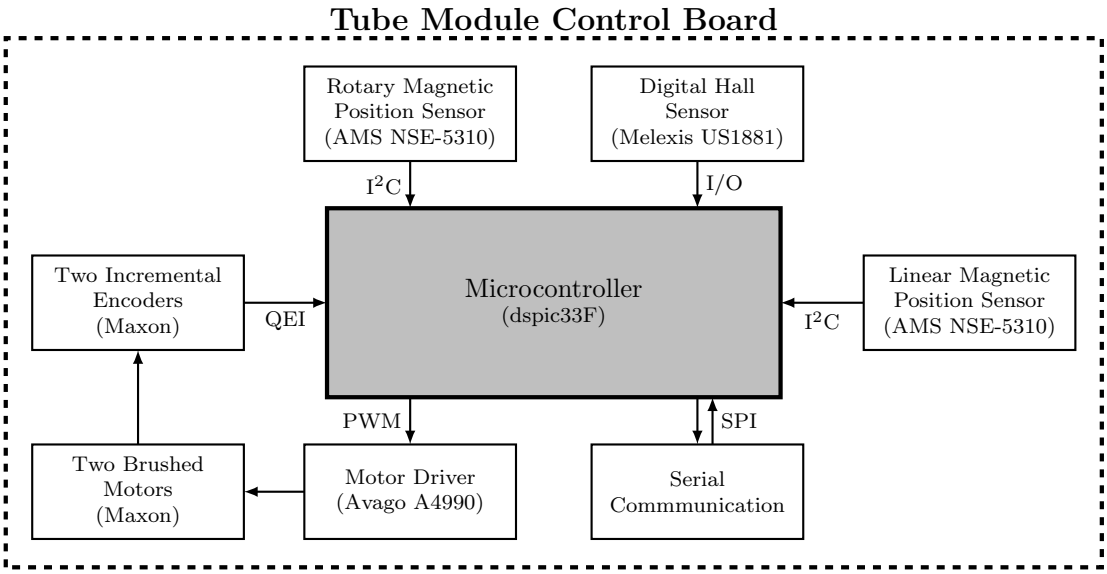

Figure 5.8: The tube module control board controls two motors and five sensors (two encoders, two magnetic position sensors, and one digital hall sensor). The desired motor position comes in via serial communication from the control computer, and low-level motor control is implemented on board the microcontroller at 1 kHz. The system is capable of automatic homing and redundant position sensing for both tube translation and rotation.

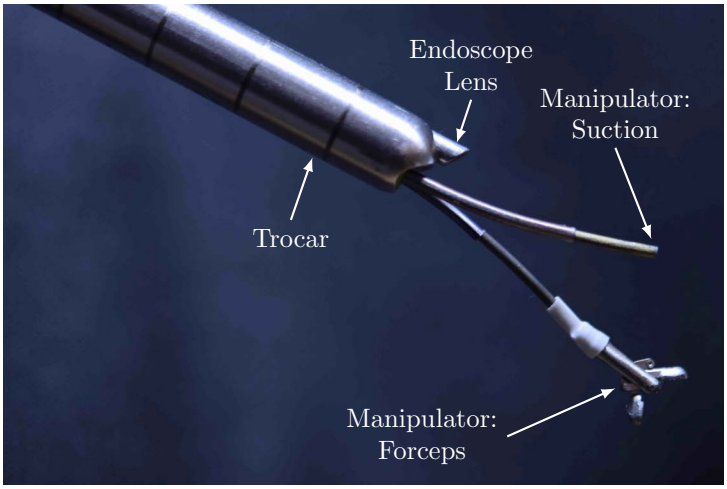

Figure 5.9: The concentric tube manipulator arms at the tip of the rigid neuroendoscope. Both arms emerge from the working channel within the endoscope and are visualized by the surgeon from the endoscope lens. The trocar diameter is 8.3 mm.

5.6 Tube Design Optimization

5.6.1 Introduction

The design space of concentric tube robots is rich with numerous choices for the designer: the diameters, wall thicknesses, lengths, precurved shape, and cross-sectional geometry may all be free variables (or even free functions of arc length). While this gives the designer great power over the ultimate functioning of the manipulator, the functional effect of each design variable is unclear, highly nonlinear, and tightly coupled. Historically, this has pushed designers towards safe tube designs, or those with slight (or even zero) curvatures to simplify the problem. While these simplifications have speed-of-implementation advantages, it is possible that concentric tube robots have yet to reach their design potential.

In this section, we approach this design challenge without significant simplifications, guided by the overarching goal of designing a two-tube concentric tube manipulator that meets the following five criteria: the manipulator (1) must reach all of the desired workspace, (2) must maintain a margin to instability, (3) must not move too fast or too slow (i.e. no kinematic singularities or uncontrollable motion), (4) must be manufacturable, and (5) has optimal global dexterity. We present this work in the context of neuroendoscopy, but believe this framework is generalizable.

In what follows, we will discuss previous work in this area, the constraints of this problem, the formulation of the design and joint space, the dexterity objective function, the numerical techniques used in the simulation, and discuss the key insights discovered through this work. Throughout this section, we provide detailed discussion on certain design aspects of concentric tube manipulators that are important to understand, particularly with respect to the stability of the manipulator.

5.6.2 Related Work

Tube design optimization has been an active area of research for concentric tube robots. The first approaches to the design problem recommended heuristics to guide the design process. This included using dominant tube stiffness sections for follow-the-leader navigational deployment of the manipulators, and then balanced stiffness tip sections for manipulation tasks [77]. These heuristics were applied to neurosurgical applications in the brain ventricles in [91, 39]. In [39], heuristics were also used to avoid elastic instabilities. In [133], the tubes were optimized to navigate through the constrained brain ventricular anatomy with minimal constant curvature sections. This paper also pointed out that designs with elastic instabilities in the joint space can still be useful towards surgical applications as long as the system avoids the unstable joint space locations. In [90] the design of concentric tubes for endonasal pituitary surgery were optimized to reach the maximum desired workspace while also constraining the backbone of the manipulator to avoid off-limits anatomy. In [101] and [134], design optimization is considered simultaneously with path planning for concentric tubes navigating through constrained anatomy.

5.6.3 Two-Tube, Constant Curvature Kinematic Equations

The forward kinematics of a two tube concentric tube robot with planar, constant precurvatures can be computed by integrating the following initial value problem.

$$\begin{aligned} \theta''(s) &= \kappa_1 \kappa_2 (1+\nu)\sin(\theta) \\ \boldsymbol{p}'(s) &= \mathbf{R}\boldsymbol{e}_3 \\ \mathbf{R}'(s) &= \mathbf{R}\hat{\boldsymbol{u}} \end{aligned} \tag{5.1}$$

with boundary conditions given by

$$\theta(L + L_2) = \theta_L \tag{5.1a}$$

$$\theta'(L + L_2) = 0 \tag{5.1b}$$

$$\boldsymbol{p}(0) = \mathbf{0} \tag{5.1c}$$

$$\mathbf{R}(0) = \mathbf{R}_{\psi_{1,0}} \tag{5.1d}$$

and local curvature vector $\boldsymbol{u} \in \mathbb{R}^3$, given by

$$u_x(s) = (1 + \gamma_b)^{-1}[\kappa_1 + \gamma_b \kappa_2 \cos(\theta)] \tag{5.1e}$$

$$u_y(s) = (1 + \gamma_b)^{-1}\gamma_b \kappa_2 \sin(\theta) \tag{5.1f}$$

$$u_z(s) = -(1 + \gamma_t)^{-1}\gamma_t \theta' \tag{5.1g}$$

The states of this initial value problem are the angle between the outer tube and the inner tube precurvature planes $\theta(s)$, its arc length derivative $\theta'(s)$, the backbone position vector $\boldsymbol{p}(s)$, and the backbone rotation matrix $\mathbf{R}(s)$. The curvature vector $\boldsymbol{u}$ enters the state equations, but is not a state itself, and the vector $\boldsymbol{e}_3$ is the standard z-axis unit vector. The parameter $\kappa_i(s)$ gives the precurvature of the tube i, where $i = 1$ indicates the inner tube and $i = 2$ indicates the outer tube. The parameter ν is Poisson's ratio of the tube material (usually Nitinol). The variables $\gamma_b(s)$ and $\gamma_t(s)$ give the bending/torsional stiffness ratio of the outer tube to the inner tube. When a tube is not present at a certain arc length s, it can be equivalently replaced by a "tube" with zero bending stiffness, infinite torsional stiffness, and zero curvature. This assumption does not change the system energy and ensures that that the state can be integrated along the entire arc length of the robot, even when tubes appear/disappear. The integrator should stop and restart at each discontinuity (tube start/ends and curvature discontinuities). The matrix $\mathbf{R}_{\psi_{1,0}}$ is the standard z-axis rotation matrix

by the angle $\psi_{1,0}$. These equations assume that the tubes exit a constrained point at $s = 0$ and that at all arc lengths $s < 0$ the tubes are constrained to be straight. We consider the configuration space of the robot to be defined by the joint variable $\boldsymbol{q}_c \in \mathbb{R}^4$ where

$$\boldsymbol{q}_c = \begin{bmatrix} \theta_L & \psi_{1,0} & L & L_2 \end{bmatrix}^T \tag{5.2}$$

The variable θ_L is the angle between the outer tube and the inner tube precurvature planes at the tip of the robot, $\psi_{1,0}$ is the absolute angular rotation of the inner tube at $s = 0$, measured with respect to an inertial frame, and L and L_2 are the translational variables shown in Figure 5.10. The variable $\psi_{1,0}$ can be considered a rigid body rotation with this parameterization, since only the variable θ_L is needed to compute the deformation of the tubes. For a full review of the kinematics in much greater detail, see Chapter 3. For this simulation, it is also required to compute the manipulator Jacobian. This can be done numerically using a finite difference method and the results from integrating the kinematic equations from (5.1). Several other techniques for computing the Jacobian have been explained in detail in the literature (e.g. [135, 29]).

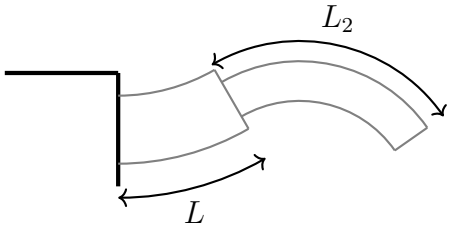

Figure 5.10: The definitions of the translational joint variables for a single arm.

5.6.4 Design Space

We have chosen to optimize a 7-dimensional design space for a two tube concentric tube manipulator. The design space is given by $\boldsymbol{d} \in \mathbb{R}^7$ and is defined by the elements

$$\boldsymbol{d} = \begin{bmatrix} \kappa_1 & \kappa_2 & \gamma & \mu_1 & \mu_2 & \ell_1 & \ell_2 \end{bmatrix}^T . \tag{5.3}$$

The variable κ_i is precurvature of tube i, the variable ℓ_i is the length of nitinol tubing of tube i, the variable μ_i represents the percentage of ℓ_i which is precurved. We make the assumption that the tip of the tubes are precurved. Finally, the variable γ gives the stiffness ratio of the outer nitinol tube to the inner nitinol tube ($\gamma_b = \gamma_t = \gamma$ when both tubes are present). This 7-dimensional space does not fully define our system from a design perspective, several other design assumptions have been made. We have assumed that each component tube is actually composed of two tubular parts: a "torque" tube and a nitinol tube. The two are simply glued together, with the torque tube surrounding the nitinol tube to form a component tube of the manipulator, as shown in Figure 5.11.

The torque tubes are made from a stiffer material and often also have a slightly larger cross sectional area, which has important stability/dexterity consequences. For each of the two tubes, we need to select an inner diameter, outer diameter, inner torque tube diameter, and outer torque tube diameter. The diameter of the inner tube's tip is typically set by application payload requirements. Thus, we take it as an optimization input rather than a design parameter. The inner torque tube diameters are chosen to mate with the inner nitinol tube. The inner diameter of the outer nitinol tube is chosen to have proper clearance with the inner tube, and the outer diameter of the outer torque tube is chosen based on diameter requirements. We assume that the outer diameter of the outer nitinol tube and the inner diameter of the torque tube are the same, since they will fit tightly together. We compute the outer tube outer

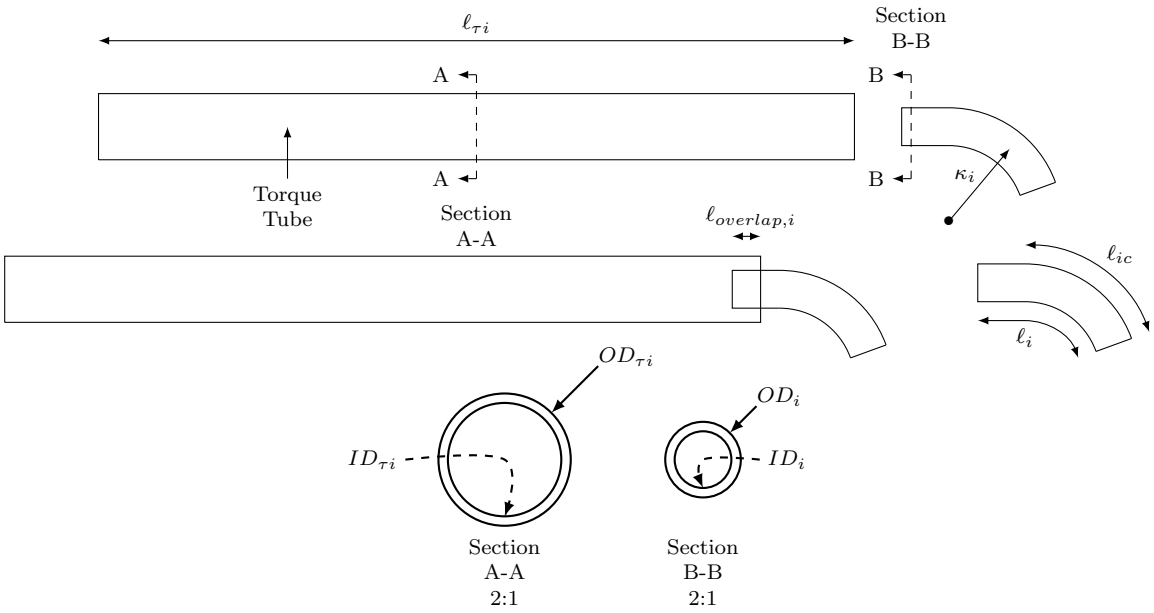

Figure 5.11: A torque tube assembled to a nitinol tube. We utilize torque tubes made from stainless steel.

diameter based on the definition of γ as

$$OD_2 = \sqrt[4]{\gamma OD_1^4 - \gamma ID_1^4 + ID_2^4}\,, \tag{5.4}$$

and we assume that the inner diameter of its torque tube has the same diameter. The length of the inner torque tube and outer torque tube are based on the actuation unit/endoscope length. All other required variables are design variables or material parameters. See Table 5.1 for a summary of these design choices.

5.6.5 Optimization Constraints

Workspace Constraint

For surgical applications, the workspace may enter the problem as either a constraint or as part of an objective function. For endoscopic neurosurgery, we consider the desired workspace to be a constraint. Here, the size and shape of this desired workspace

Table 5.1: The tube parameters necessary for the model implementation. We assume that each component tube is made from a torque tube and a nitinol tube. A • in the $\boldsymbol{d}$ column indicates a design variable, and some parameters are computed as functions of design variables.

Variable	**Symbol**	**Value**	**DV**
Young's Modulus Torque Tube	E_{torque}	195.0 GPa	x
Poisson's Ratio Torque Tube	ν_{torque}	0.305	x
Young's Modulus Flex Tube	E_{flex}	60.0 GPa	x
Poisson's Ratio Flex Tube	ν_{flex}	0.333	x
Torque Tube/NiTi Tube Overlap	$\ell_{overlap}$	20 mm	x
Outer Tube/Inner Tube Stiffness Ratio	γ	γ	•
Inner Tube Inner Diameter	ID_1	1.0414 mm	x
Inner Tube Outer Diameter	OD_1	1.1176 mm	x
Inner Torque Tube Inner Diameter	$ID_{\tau 1}$	0.9652 mm	x
Inner Torque Tube Outer Diameter	$OD_{\tau 1}$	1.27 mm	x
Inner Tube Curvature	κ_1	κ_1	•
Inner Tube Percentage of Tube Curved	μ_1	μ_1	•
Inner Tube Curved Length	ℓ_{1c}	$\mu_1 \ell_1$	x
Inner Tube Total Length	ℓ_1	ℓ_1	•
Inner Torque Tube Length	$\ell_{\tau 1}$	482.6 mm	x
Outer Tube Inner Diameter	ID_2	1.3462 mm	x
Outer Tube Outer Diameter	OD_2	see (5.4)	x
Outer Torque Tube Inner Diameter	$ID_{\tau 2}$	OD_2	x
Outer Torque Tube Outer Diameter	$OD_{\tau 2}$	2.2 mm	x
Outer Tube Curvature	κ_2	κ_2	•
Outer Tube Percentage of Tube Curved	μ_2	μ_2	•
Outer Tube Curved Length	ℓ_{2c}	$\mu_2 \ell_2$	x
Outer Tube Total Length	ℓ_2	ℓ_2	•
Outer Torque Tube Length	$\ell_{\tau 2}$	355.6 mm	x

is defined by the size and shape of the endoscopic field of view and the precurvature limitations of the tubes.

The neuroendoscope utilized in this system is Aesculap's MINOP Invent Neuroendoscope as shown in Figure 5.12. The relevant specifications are the field of view angle (FOV), the depth of view (DOV), and the lens offset h. Each of these variables are shown in the Figure 5.13 (Left) and outlined in Table 5.2. The endoscope features an elliptical working channel (major axis: 6.5 mm, minor axis: 3.7 mm) that is used for passing instruments. This is the most constraining size limitation: two manipulator arms and a small tube separation device for aligning/constraining the axis of each arm within this elliptical cross section must be fit through this channel. The tubes/instruments actually exit the working channel of the endoscope proximal to where the lens starts (by an offset h). This subtlety allows the tubes to begin

Figure 5.12: (Left) The lens offset is shown on the Aesculap Minop Invent. (Center) The distal tip of the endoscope's working channel is shown. (Right) The proximal end of the Minop Invent is shown – the concentric tubes enter through the large elliptical working channel. [136].

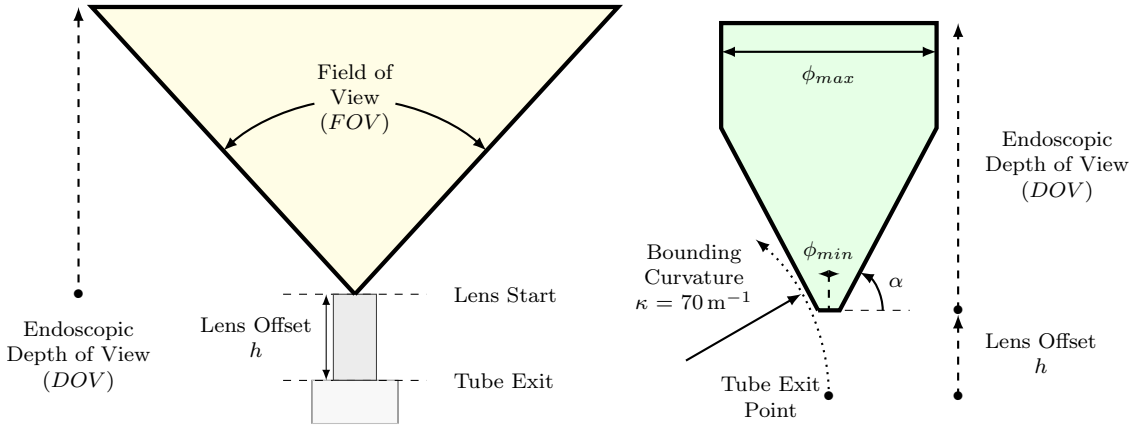

Figure 5.13: (Left) The conical shape of the endoscopic field of view is parameterized with two variables: the field view opening angle (FOV) and the depth of view (DOV). The field of view originates at the tip of the lens, which is offset by h from where the manipulators exit the endoscopic channel. (Right) The desired workspace shape and parameterization.

curving outside of the field of view, so that they have the ability to move laterally even when they first enter the field of view.

Nitinol has been reported to be able to sustain strains up to $\epsilon_{max} = 11\%$ and remain superelastic [137], but the more widely reported value is $\epsilon_{max} = 8\%$. The precurvature limit of a circularly precurved tube is

$$\kappa_{max} = \frac{2\epsilon_{max}}{OD} \ ,$$

Table 5.2: The Workspace Parameterization

Variable	Symbol	Value	See Figure
Tube Offset	Δ	1.5 mm	5.14
Depth of View	DOV	20 mm	5.13
Field of View	FOV	85 °	5.13
Max Diameter	ϕ_{max}	15 mm	5.13
Min Diameter	ϕ_{min}	1.5 mm	5.13
Lens Offset	h	6 mm	5.13
Workspace Angle	α	62°	5.13

where OD is the outer diameter of the tube [27]. For a 1 mm tube, this limits the allowable precurvature to 160 m^{-1} (or a radius of curvature of 6.25 mm), and for a 2 mm tube, this limit is 80 m^{-1} (or a radius of curvature of 12.5 mm). Since the workspace of the manipulators cannot be outside of the limits of a single precurved tube, a bounding curvature of $\kappa = 70\,\mathrm{m}^{-1}$ has been heuristically chosen to limit the size of the pre-defined workspace, as shown in Figure 5.13 (Right).

The desired workspace was chosen to be shaped as a cone (with the point of the cone removed) appended to a cylinder, as shown in Figure 5.13 (Right). The base of this workspace is at the same location that the endoscopic field of view begins. The workspace is parameterized by four variables: the workspace angle α, the depth of view DOV, the cylinder diameter ϕ_{max}, and the diameter of the cone at the base of workspace ϕ_{min}. The central axis of this workspace is offset from the axis of the field of view by a distance Δ, for both the left and the right arm. The chosen shape/parameterization of this workspace enables the manipulators to reach a large percentage of the field of view (see Figure 5.14) and is reasonable, but aggressive, to achieve within our known manufacturing limitations. The final values of the chosen parameters are shown in Table 5.2.

Stability Constraint

The second constraint is stability; the manipulators must remain elastically stable during operation. In Chapter 3, we presented a bifurcation algorithm that takes as

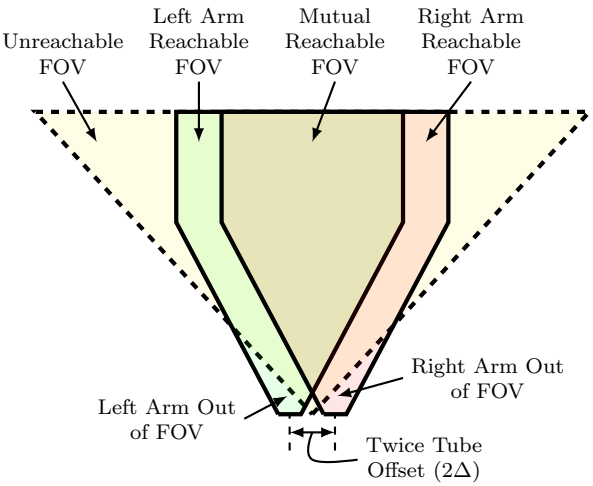

Figure 5.14: The workspaces of the left (green) and right (red) manipulators overlaid on the endoscopic field of view (yellow).

its inputs the manipulator's translational joint position and design parameters and outputs a binary true/false for bifurcation of the solution space. In simple terms, if this algorithm outputs true it means that if the manipulator tubes were constrained to be static translationally, and the tubes traversed all possible relative rotations with respect to one another, at least one snap would occur.

During the optimization presented here, this algorithm is utilized to pare down the potential translational joint space of a design (which is known a priori) by eliminating the translational joint configurations that yield a model-predicted bifurcation. We require that the translational configuration does not bifurcate, and also maintains a margin Δ_β from bifurcation, which will be explained in detail shortly. This is in contrast to eliminating completely designs that lack an entirely stable joint space; this approach allows evaluation of the non-bifurcating workspace of each design, and does not overaggressively eliminate potentially useful designs. In what follows, we will describe the precise implementation of the algorithm in the context of this design optimization problem.

Let us define the variable $\tilde{\ell}$ as the arc length distance along the backbone of a

concentric tube manipulator where both the outer tube and the inner tube are precurved. This variable is a function of the translational actuation of the manipulators and precurved lengths of the tubes, and has a very important role in the bifurcation algorithm. The unitless variable λ, or the bifurcation parameter, was previously defined as $\lambda = \tilde{\ell}^2\kappa_1\kappa_2(1+\nu) = \tilde{\ell}^2 a$, where ν is Poisson's ratio of the material which makes up the component tubes (e.g. Nitinol), and κ_1 and κ_2 are the precurvatures of the inner and outer tubes, respectively. It will prove convenient to express the bifurcation parameter as a product of the length parameter $\tilde{\ell}$, which is dependent on translational actuation, and the precurvature/material parameter, a, which is independent of translational actuation.

Calculating the mutually overlapped length $\tilde{\ell}$ is a matter of finding the most proximal exposed (i.e. extended out of the endoscope) mutually curved arc length, and the most distal exposed mutually curved arc length. When the curved portions of the tubes are retracted inside of the endoscope, they are straightened out so they do not contribute to $\tilde{\ell}$. We assume here that the inner tube is constrained to be extended out of the outer tube by some amount and that the distal end of each tube is precurved, which means the most distal mutually overlapped arc length (if it exists) must occur where the outer tube terminates.

Recall the translational joint variables: L is defined as the arc length distance that the outer tube is extended from the endoscope tip, while L_2 is the arc length that the inner tube is extended from the outer tube. To calculate $\tilde{\ell}$, one must first find the arc length of the most proximal curvature endpoint, s_E. We have that $s_E = \max(0, L)$, because this point must be at the end of the outer tube. Second, one must find the arc length of the most distal curvature starting point, $s_S = \max(0, L - \ell_{2c}, L + L_2 - \ell_{1c})$. $\tilde{\ell}$ is the simply the difference between these two arc lengths, which must be greater than or equal to zero: $\tilde{\ell} = \max(0, s_E - s_S)$. We can summarize this in one equation

as

$$\tilde{\ell}(L, L_2, \ell_{1c}, \ell_{2c}) = \max\Big(0, \max(0, L) - \max(0, L - \ell_{2c}, L + L_2 - \ell_{1c})\Big) \,, \tag{5.5}$$

which handles all of the overlapping cases possible shown in Figure 5.15. The last pieces of information necessary to implement the stability constraint are understanding the "transmission lengths" of the component tubes. Let us define the transmission length of the inner tube and outer tube as β_1 and β_2, respectively. β_1 and β_2 are the absolute lengths from s_S to the most proximal arc length of the tube, as shown in Figure 5.15. We can now express the final bifurcation equation. If

$$\beta < \beta_{allowable} \implies \beta < \frac{\cot(\tilde{\ell}\sqrt{a})}{\sqrt{a}} \implies \frac{\cot(\tilde{\ell}\sqrt{a})}{\sqrt{a}} - \beta > 0 \,, \tag{5.6}$$

then the translational configuration of the concentric tube manipulator is stable for all possible tube rotations. In (5.6), the variable β is a weighted sum of the component tube transmission lengths defined as

$$\beta = \frac{\beta_1 k_{2t} + \beta_2 k_{1t}}{k_{1t} + k_{2t}} \,, \tag{5.7}$$

where k_{it} is the torsional stiffness of tube i. Notice that β is bounded between β_1 and β_2, so it is simple to approximate β even if the torsional stiffnesses (or tube diameters) have not yet been determined/selected. Let us define the margin to bifurcation Δ_β as

$$\Delta_\beta = \beta_{allowable} - \beta = \frac{\cot(\tilde{\ell}\sqrt{a})}{\sqrt{a}} - \beta \,. \tag{5.8}$$

This margin defines how much longer the robot would have to be, in its current translational configuration, for a bifurcation to occur. The metric is meaningful in a "distance to instability" sense, because it provides a physical distance metric that is well understood and precisely controlled, in contrast to the relative stability measure

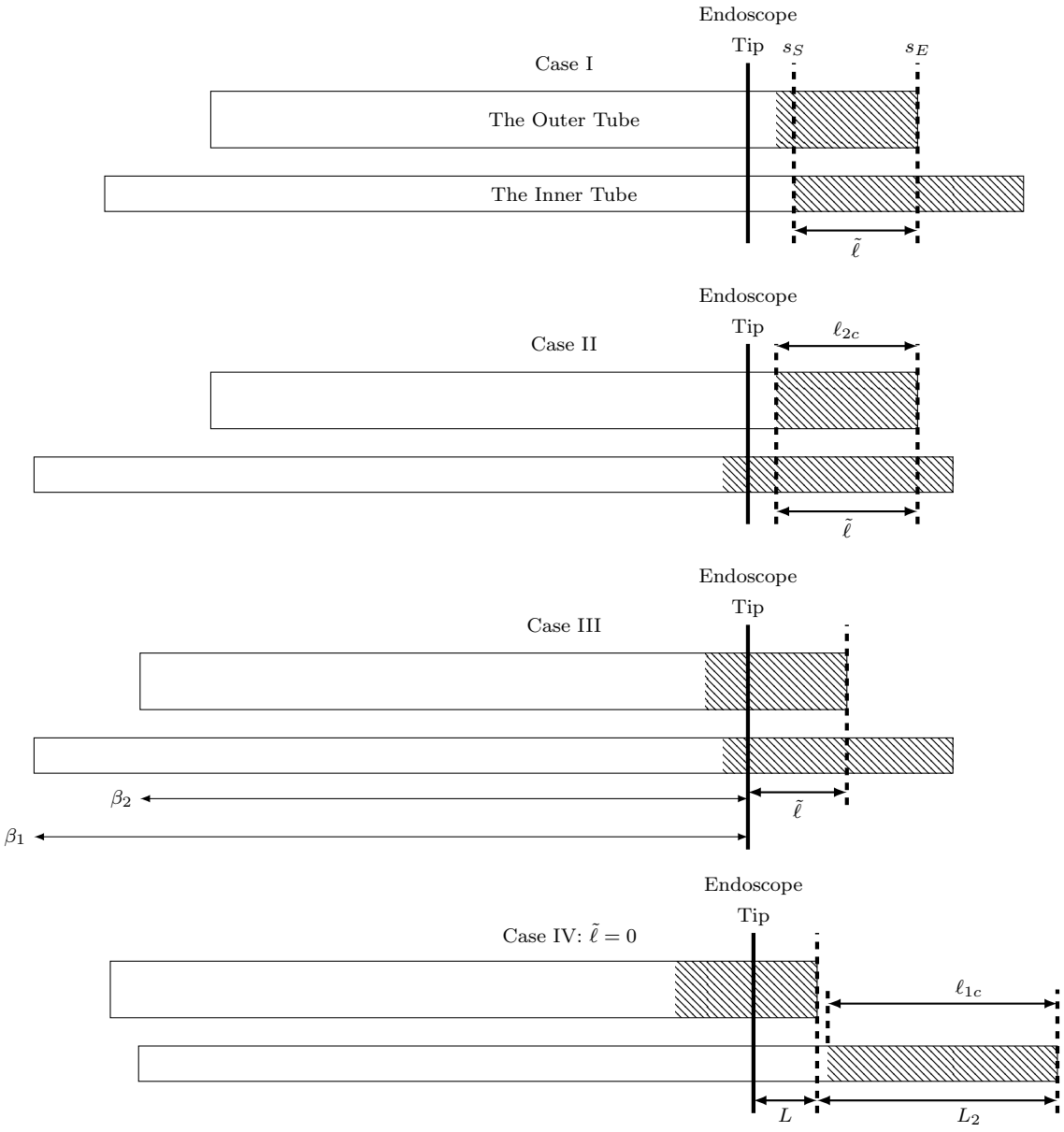

Figure 5.15: The hatched area represents precurvature. Case I represents when the precurvature of the inner tube begins distal to the most proximal precurvature of the outer tube. Case II represents when the precurvature of the outer tube begins distal to the most proximal precurvature of the inner tube. Case III shows that the precurvature is ignored if it occurs inside of the endoscope. Case IV shows the case where there is no mutually curving overlapped sections.

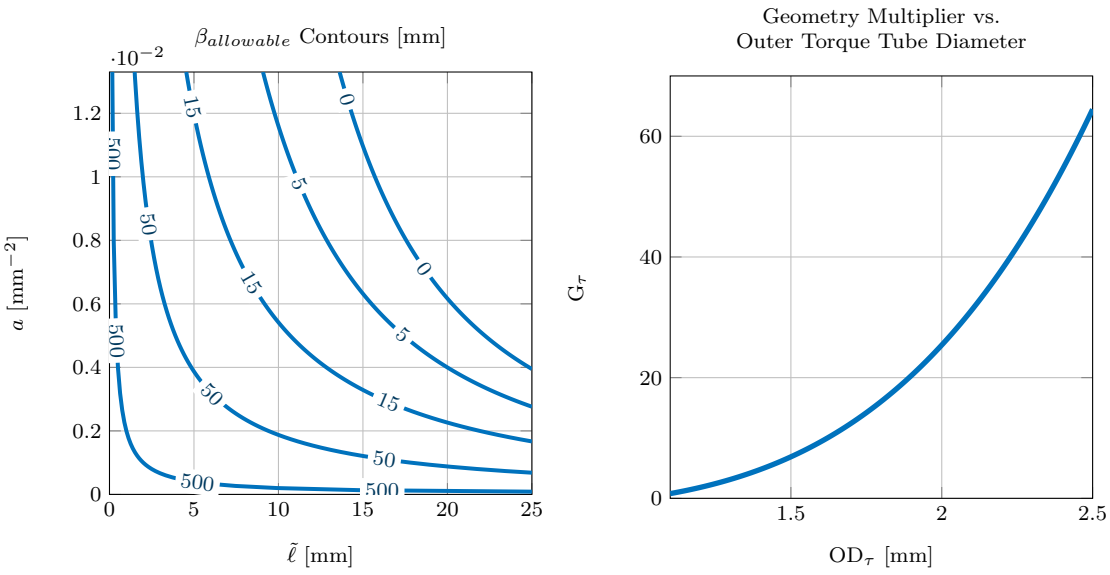

Figure 5.16: (Left) A graphical representation of Equation (5.6). Several contours of the allowable transmission length $\beta_{allowable}$ are plotted in the $(\tilde{\ell}, a)$ plane. Interpretation: if a manipulator design had a trasmission length of $\beta = 50\,\text{mm}$, for example, then the tube design/actuation must restrict $(\tilde{\ell}, a)$ to be left/below the $50\,\text{mm}$ $\beta_{allowable}$ contour. (Right) The torque tube geometry multiplier can realistically reduce the effective length of the transmission by a factor of over 60. This example plot assumes the nitinol tube has a $1.0\,\text{mm}$ OD, a $0.8\,\text{mm}$ ID, and that the ID of the torque tube is $1.0\,\text{mm}$.

$\mathbb{S}$. In the optimization presented here, we require Δ_β to be $10\,\text{mm}$. Figure 5.16 (Left) graphically displays the effect of (5.6). At first glance, it appears that transmission lengths have a devastating impact on the design space of concentric tube manipulators. The rigid endoscope utilized in this optimization is over $300\,\text{mm}$ long, so the tubes would have transmission lengths at least this long, assuming we had no torque tubes. This would seem to limit our potential designs to extremely moderate precurvatures, precurved lengths, and place tight limits on translational actuation. In the next subsection, we discuss torque tubes, which help to overcome this apparent limitation.

Maintaining Stability: Torque Tubes

The transmission lengths for nitinol tubes act as torsional springs. In these regions, the twisting moment is constant and the twisting of the tubes propagates linearly in arc length with a torsional stiffness of $k_{torsional} = \frac{GJ}{\beta}$, where G is the shear modulus of the tube material and J is the polar moment of area of the cross section. Recall from Chapter 3, elastic instability occurs when a small input rotation at the base of a tube creates an infinitely fast manipulator tip rotation as a result of torsional energy storage. Intuitively, if the transmission lengths (which are effectively torsional springs) are stiffer, less actuation rotation is lost to torsional strain energy storage, and hence, the system is more stable. Torque tubes, as shown in Figure 5.11, utilize this concept to stiffen the arc lengths of the component tube which do not need to bend. For example, the portion of the tubes that run through the straight working channel of the endoscope do not need to bend, and, hence, can be replaced with torque tubes. We utilize torque tubes made from stainless steel, and simply glue them over the nitinol tubes. This concept was previously utilized in [138], where the torque tubes were referred to as stainless steel extensions. In this work, these stainless steel tubes were used to reduce torsion in the nitinol sections and eliminate the possibility of buckling (due to bending) along the long straight transmission sections.

When using torque tubes, the transmission length of the manipulator is effectively shortened (versus if the transmissions were made from the same material/geometry along the entire length). These torque tubes will create a stiffness increase from both the material and the geometry of the torque tubes. Let us define the torque tube stiffness multiplier of tube i as $S_{\tau i}$, the torque tube stiffness multiplier due to geometry as $G_{\tau i}$, and the torque tube material multiplier as M. They are each defined as

$$G_{\tau i} = \frac{(OD_{\tau i}^4 - ID_{\tau i}^4)}{(OD_i^4 - ID_i^4)}, \;\; M = \frac{E_{torque}(1+\nu_{NiTi})}{E_{NiTi}(1+\nu_{torque})}, \;\; S_{\tau i} = G_{\tau i} M_{SS} \tag{5.9}$$

As shown for an example torque/nitinol tube combination in Figure 5.16 (Right), $G_{\tau i}$ could realistically be as high as 60. Notice that as the wall thickness of the nitinol tube approaches zero, $G_{\tau i}$ approaches infinity. The bifurcation/stability properties of the manipulator are extremely sensitive to the selection of these relative wall thickness. The material multiplier M is 3.32 for 304 stainless steel (assuming $E_{ss} = 195\,\text{GPa}$, $E_{NiTi} = 60\,\text{GPa}$, $\nu_{SS} = 0.305$, $\nu_{NiTi} = 0.333$). If even more stiffness is needed, tungsten tubing is available that would provide a material multiplier of 7.13 (assuming $E_{ss} = 195\,\text{GPa}$, $E_W = 411\,\text{GPa}$, $\nu_W = 0.280$). Combining these two factors, the effective transmission length can reasonably be reduced by a factor between $S_\tau = 15$ - 500. Thus, torque tubes are the key design element that "open up" the design space. As an illustration of this point, see Figure 5.17, which shows the same 500 mm $\beta_{allowable}$ contour that was shown in Figure 5.16 for varying stiffness multipliers S_τ.

Utilizing the stiffness multiplier, an effective transmission length of the torque tube can be calculated (i.e. the equivalent length of the transmission length if it were made of nitinol of the same geometry as the tip tube) as $\beta_i = \frac{\ell_{\tau i}}{S_{\tau i}}$.

Minimum and Maximum Workspace Velocity Constraint

For serial robots, the primary dexterity concern is avoiding singularities, or locations in the joint space where the manipulator's Jacobian becomes rank-deficient so that there is a direction that the tip of the manipulator cannot instantaneously move. This problem remains a concern for concentric tube robots, but another dexterity concern arises. As the stability of these manipulators decrease, their motion can become ill-conditioned so that a very small actuation input can create an extremely large motion of the tip of the manipulator. In fact, the model predicts an instantaneous infinite manipulator tip velocity exactly when the system goes unstable. This is a situation that it is important that the system avoid, since that could create a control sensitivity

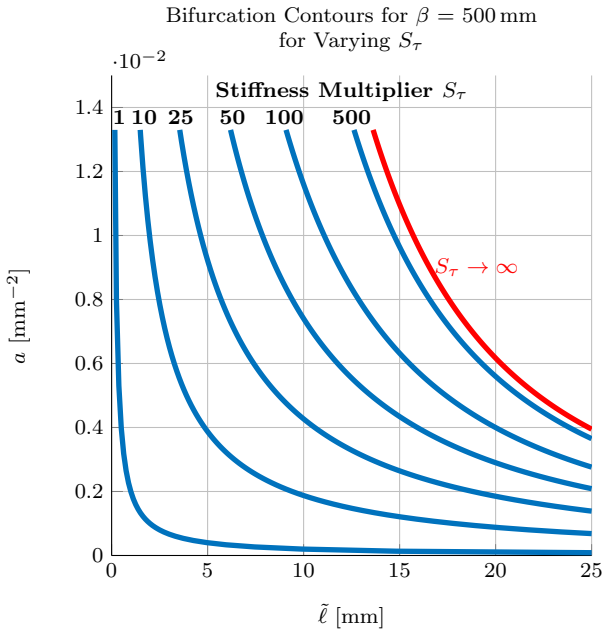

Figure 5.17: This plot shows the bifurcation contours for a concentric tube robot with a transmission length of 500 mm. As the stiffness multiplier of the torque tube increases, the design and actuation space increase quickly. Intuitively, as $S_\tau \to \infty$, it is as if the transmission length does not exist (i.e. the contour approaches the $\beta_{allowable} = 0$ contour from Figure 5.16 - Left).

problem for the system. For this simulation, the minimum and maximum allowable task space velocity generated by a nominal motor rotation was chosen to be $1\,{}^{\text{mm}}/_{\text{s}}$ and $150\,{}^{\text{mm}}/_{\text{s}}$, respectively. These values were chosen heuristically by knowing the approximate velocities the surgeon will require. In the next subsection, we show how stability affects dexterity for a two-tube concentric tube robot.

The Inseparable Nature of Stability and Dexterity

As reviewed in Chapter 3, the configuration space of the robot is defined by the twisting at the tip of each of the component tubes – not at the base where the motors apply the rotation. This is because a rotation at the base could correspond to multiple different robot configurations when the robot has instability in its joint space. The reverse is not true; if the translational configuration of the robot and the twisting at the tip of the robot are both known, a solution to the model equations exists and is unique. This is because defining the twist at the tip of the robot converts the kinematic equations into an initial value problem, rather than a boundary value problem, and guarantees that a solution exists and is unique.[1] Let us then define the configuration space of a two tube concentric tube robot as

$$\boldsymbol{q}_c = \begin{bmatrix} \theta_L & \phi & \beta_1 & \beta_2 \end{bmatrix}^T , \tag{5.10}$$

where θ_L is the twist difference between tube 2 and tube 1 at the tip of the manipulator (i.e. $\theta_L = \psi_2(L) - \psi_1(L)$), ϕ is a rigid body rotation of the collection of tubes, and β_i gives the translational location of tube i. Within the configuration space vector, θ_L is not under direct control of the actuators. Instead, the actuators control the relative rotation of the tubes where they are held, a variable we call θ_β. Let us define, then,

[1] This fact is guaranteed by the Cauchy-Lipschitz theorem, as long as the state derivative equations are Lipschitz continuous functions of state and continuous in time - a constraint that the concentric tube robot equations meet.

the joint vector

$$\boldsymbol{q}_j = \begin{bmatrix} \theta_\beta & \phi & \beta_1 & \beta_2 \end{bmatrix}^T . \tag{5.11}$$

The differential kinematics for configuration space and joint space are then defined as

$$\begin{aligned} \frac{\partial \boldsymbol{x}}{\partial \boldsymbol{q}_c}\dot{\boldsymbol{q}}_c &= \mathbf{J}_c\dot{\boldsymbol{q}}_c = \dot{\boldsymbol{x}} \\ \frac{\partial \boldsymbol{x}}{\partial \boldsymbol{q}_j}\dot{\boldsymbol{q}}_j &= \mathbf{J}_j\dot{\boldsymbol{q}}_j = \dot{\boldsymbol{x}} \end{aligned} \tag{5.12}$$

Let's now decompose $\mathbf{J}_j$ based on the configuration space differential kinematics. We have that

$$\frac{\partial \boldsymbol{x}}{\partial \boldsymbol{q}_j}\dot{\boldsymbol{q}}_j = \frac{\partial \boldsymbol{x}}{\partial \boldsymbol{q}_c}\frac{\partial \boldsymbol{q}_c}{\partial \boldsymbol{q}_j}\dot{\boldsymbol{q}}_j = \mathbf{J}_c\mathbf{J}_\tau\dot{\boldsymbol{q}}_j = \dot{\boldsymbol{x}} . \tag{5.13}$$

The Jacobian $\mathbf{J}_\tau$ is the linear map from joint space velocity to configuration space velocity. However, since a single $\boldsymbol{q}_j$ may correspond to multiple $\boldsymbol{q}_c$, the Jacobian $\mathbf{J}_\tau$ could also be multi-valued. Instead, we calculate $\mathbf{J}_\tau^{-1}$, which will be unique and is the linear map from configuration space velocity to joint space velocity.

$$\frac{\partial \boldsymbol{q}_j}{\partial \boldsymbol{q}_c} = \mathbf{J}_\tau^{-1} = \begin{bmatrix} \dfrac{\partial \theta_\beta}{\partial \theta_L} & 0 & \dfrac{\partial \theta_\beta}{\partial \beta_1} & \dfrac{\partial \theta_\beta}{\partial \beta_2} \\ 0 & 1 & 0 & 0 \\ 0 & 0 & 1 & 0 \\ 0 & 0 & 0 & 1 \end{bmatrix} = \begin{bmatrix} \mathbb{S} & 0 & \dfrac{\partial \theta_\beta}{\partial \beta_1} & \dfrac{\partial \theta_\beta}{\partial \beta_2} \\ 0 & 1 & 0 & 0 \\ 0 & 0 & 1 & 0 \\ 0 & 0 & 0 & 1 \end{bmatrix} \tag{5.14}$$

Recall from Chapter 3, for a two-tube robot the measure in the top left of this matrix is the relative stability measure $\mathbb{S}$. The eigenvalues of $\mathbf{J}_\tau^{-1}$ are

$$\text{eig}\left(\mathbf{J}_\tau^{-1}\right) = \begin{bmatrix} 1 & 1 & 1 & \mathbb{S} \end{bmatrix} , \tag{5.15}$$

so $\mathbf{J}_\tau$ exists if and only if $\mathbb{S} \neq 0$. This means that $\mathbf{J}_j$ only exists when the relative stability measure does not equal zero, which is a very intuitive result since we know the robot snaps from one location to another at exactly the moment when $\mathbb{S} = 0$.

While $\mathbf{J}_j$ does exist when $\mathbb{S} < 0$, its meaning is not particularly useful, because it predicts the differential kinematics related to a configuration which is not physically realizable. The eigenvalues of $\mathbf{J}_\tau$ are clearly

$$\text{eig}\Big(\mathbf{J}_\tau\Big) = \begin{bmatrix} 1 & 1 & 1 & \dfrac{1}{\mathbb{S}} \end{bmatrix} . \tag{5.16}$$

This decomposition displays the controllability issue with concentric tube robots, and its relationship to stability. As the relative stability measure approaches zero, the robot's component tubes twist faster and faster at the tip of the robot, eventually leading to a snap. However, even if the robot remains stable, it is clear that the system's overall controllability benefits from maintaining a higher relative stability measure $\mathbb{S}$. We can make this observation more precise by looking at the manipulability dexterity metric. In [139], Yoshikawa defined manipulability M as

$$M = \sqrt{\det(\mathbf{J}_j \mathbf{J}_j^T)} \tag{5.17}$$

If we assume that the system is not redundant (i.e. that $\mathbf{J}_j$ is square), then M reduces to

$$M = \det(\mathbf{J}_j) = \det(\mathbf{J}_c)\det(\mathbf{J}_\tau) = \frac{\det(\mathbf{J}_c)}{\mathbb{S}} \tag{5.18}$$

This means that the manipulability metric defined in [139] is exactly inversely proportional to the relative stability measure for concentric tube robots. It is also interesting to note that $\mathbb{S}$ is bounded, so the only way for M to go to zero is for $\mathbf{J}_c$ to have an eigenvalue at zero, and the only way for $M \to \infty$ is for $\mathbb{S} = 0$.

Manufacturability Constraints

A couple of manufacturability constraints were implemented in this tube design optimization for concentric tube robots. Since the torque tubes create a step in the

outer diameter of the component tubes, they are not allowed to exit the endoscope. Therefore, the nitinol tubes must be sufficiently long. In the simulation, each of the nitinol tubes are constrained to be at least $\ell_{i,min} = 20\,\text{mm}$. In addition each tube was subject to a minimum curved length requirement, since it is challenging to accurately shape-set very short, highly curved sections. Each of the nitinol tubes are constrained to have a precurved length of at least $\ell_{ic,min} = 4\,\text{mm}$.

5.6.6 The Optimization Function

Any design that meets the constraints presented in the previous subsection is a viable design candidate. To differentiate within these designs, however, a global dexterity metric is optimized. This metric has been previously defined in [140] as isotropy Δ and is given as

$$\Delta = \frac{M}{\Psi}, \quad M = \sqrt[m]{\det(\mathbf{J}\mathbf{J}^T)}, \quad \Psi = \frac{\text{tr}(\mathbf{J}\mathbf{J}^T)}{m} \,. \tag{5.19}$$

This metric gives the ratio of the geometric mean of the eigenvalues of $\mathbf{J}\mathbf{J}^T$ to the arithmetic mean of the eigenvalues of $\mathbf{J}\mathbf{J}^T$. Since $\Psi \geq M$, isotropy is bounded above by 1 and below by zero, or $0 \leq \Delta \leq 1$. This metric is particularly useful for two reasons: first, it is scale independent, and, second, it penalizes both extremely large eigenvalues and extremely small eigenvalues, so designs that are near singularities and designs that are near instability (and, hence, have poor controllability) will be penalized. The isotropy metric, however, is a local measure and not a global measure. Isotropy is important throughout the entire workspace of the manipulator, not just at individual locations in the workspace. In [141], the global conditioning index (GCI) was defined as the workspace-volume weighted inverse condition number

$$\text{GCI} = \frac{\int \kappa^{-1} dW}{\int dW} \,, \tag{5.20}$$

where the condition number κ is given by the ratio of the maximum to minimum singular value of the manipulator's Jacobian.

$$\kappa = \frac{\sigma_{max}}{\sigma_{min}} \, . \tag{5.21}$$

The isotropy metric is very closely related to the inverse condition number, but it considers all of the axes of the manipulability ellipsoid, rather than just the largest and smallest axes. In this work, we choose to define global minimum isotropy index, Δ_G, as

$$\Delta_G = \frac{\int \Delta_{min} dW}{\int dW} \tag{5.22}$$

Δ_{min} indicates that, since our system is redundant, we choose to take the minimum (i.e. worst case) isotropy at every position in the workspace in order to calculate the global metric. This returns a conservative, worst-case metric between 0 and 1. These integrals are calculated numerically in the optimization via a workspace voxelization.

Consistent Units for Dexterity Analysis

The Jacobian matrix for a two-tube concentric tube does not have uniform units; there are two rotational degrees of freedom and two translational degrees of freedom. If we consider only the top three rows of the Jacobian (the positional portion), two columns of the Jacobian map linear joint velocity to linear workspace velocity and two columns of the Jacobian map angular joint velocity to linear workspace velocity. With this mapping, the relative weighting of the singular values lose physical meaning and, hence, it is unclear what the dexterity metrics represent.

To account for this problem, for dexterity, we consider motor inputs. For our robotic system, the same motors are used for translational motion and for rotational motion. If we consider motor rotation as the input to our system and investigate the singular values of this input/output relationship, then each singular value has

consistent units, and their relative weighting then has physical meaning.

For the neuroendoscopy robot, the transmission from the motor rotation to tube motion is via a differential drive. If $\dot{\beta}$ is tube translational velocity, $\dot{\alpha}$ is tube angular velocity, $\dot{m}_r$ is the angular velocity of the rotational motor, and $\dot{m}_t$ is the angular velocity of the translational motor, then we have that

$$\begin{aligned} \dot{\beta} &= \eta_t(\dot{m}_t - \dot{m}_r) \\ \dot{\alpha} &= \eta_r \dot{m}_r \end{aligned} \tag{5.23}$$

where η_t is the translational transmission ratio from motor rotation to tube translation, and η_r is the rotational transmission ratio from motor rotation to tube rotation. If the motor joint vector is defined as

$$\boldsymbol{q}_m = \begin{bmatrix} m_{r1} & m_{r2} & m_{t1} & m_{t2} \, , \end{bmatrix}^T \tag{5.24}$$

then the mapping from motor variables to joint variables $\boldsymbol{q}_j$ is

$$\mathbf{J}_\eta = \frac{\partial \boldsymbol{q}_j}{\partial \boldsymbol{q}_m} = \begin{bmatrix} \eta_r & 0 & 0 & 0 \\ 0 & \eta_r & 0 & 0 \\ -\eta_t & 0 & \eta_t & 0 \\ 0 & -\eta_t & 0 & \eta_t \end{bmatrix} \, , \tag{5.25}$$

where the lower left 2×2 submatrix exists because of the differential drive. The final differential kinematic relationship between motor angular velocity to task space velocity is then

$$\frac{\partial \boldsymbol{x}}{\partial \boldsymbol{q}_m} \dot{\boldsymbol{q}}_m = \dot{\boldsymbol{x}} \implies \frac{\partial \boldsymbol{x}}{\partial \boldsymbol{q}_c} \frac{\partial \boldsymbol{q}_c}{\partial \boldsymbol{q}_j} \frac{\partial \boldsymbol{q}_j}{\partial \boldsymbol{q}_m} \dot{\boldsymbol{q}}_m = \mathbf{J}_c \mathbf{J}_\tau \mathbf{J}_\eta \dot{\boldsymbol{q}}_m = \dot{\boldsymbol{x}} \, . \tag{5.26}$$

Equation (5.26) shows that the dexterity of concentric tube robots can be decom-

posed into three mappings: the mapping between configuration space and task space (i.e. $\mathbf{J}_c$), the mapping between configuration space and joint space (i.e. $\mathbf{J}_\tau$), which is dominated by the relative stability measure, and the mapping between joint space and motor space (i.e. $\mathbf{J}_\eta$), which is defined by ratios in the actuation unit design. In other words, the dexterity of the manipulator is a product of the deformation model, the stability of the manipulator, and the design of the actuation. The singular values of the product of $\mathbf{J}_c\mathbf{J}_\tau\mathbf{J}_\eta$ are considered in the dexterity optimization.

5.6.7 The Joint Space

The joint space is constrained with a minimum/maximum exposed outer tube length (L_{min}, L_{max}), a minimum/maximum exposed inner tube length (L_{2min}, L_{2max}), and a maximum total arc length $s_{max} = L + L_2$. In Figure 5.18, this two dimensional joint space is shown.

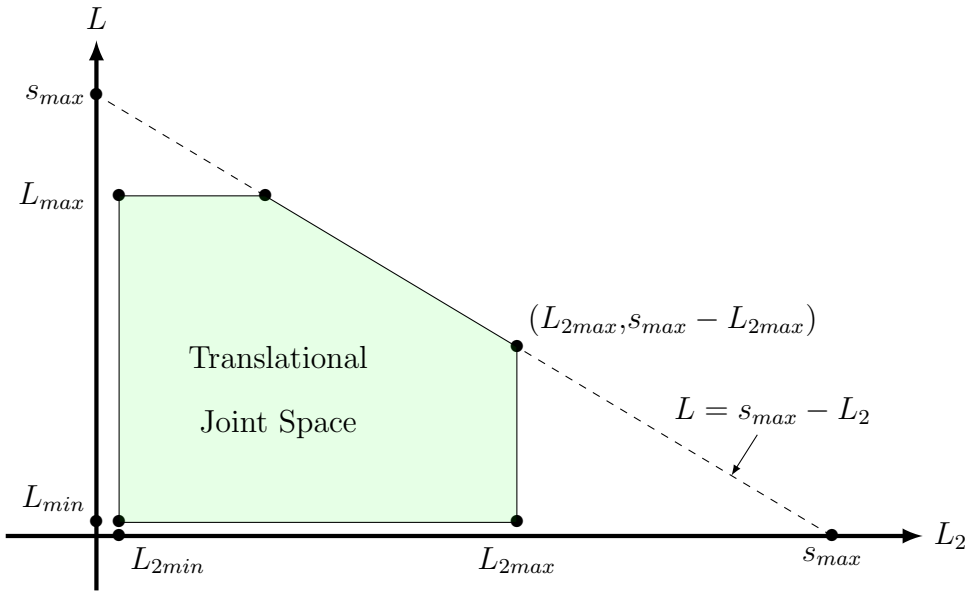

Figure 5.18: The translational joint space of the two tube concentric tube robot.

The rotational joint space is unlimited for the purposes of operating the robot; both tubes can spin infinitely. However, for simulation purposes, it will be important to discretize the rotational joint space as well. Recall, the rotational configuration

space is parameterized by two joint variables: θ_L and $\psi_{1,0}$, where θ_L is the relative twist between the tubes at the tip and $\psi_{1,0}$ is a rigid body rotation of the collection of tubes. The system's configuration space equations are symmetric about $\theta_L = \pi$, so only the values $\theta_L \in [0, \pi]$ are considered in simulation. We do not include $\psi_{1,0}$ (a rigid body rotation of the collection of tubes) in our joint space parameterization at all, because stability is independent of this variable, its effect on the workspace of the robot is clear, and its effect on the dexterity of the robot can be found algebraically. Recognizing this fact substantially reduces the total time for the simulation since we reduce our joint space parameterization to three variables from four. For this simulation, Table 5.3 shows the parameters used to parameterize the translational joint space.

5.6.8 Simulation Implementation

Joint Space Discretization

The translational joint space, shown in Figure 5.18, is discretized by creating a grid of equally spaced points (L_2, L), each separated by Δ_T from one another. The variables span $L_2 \in [L_{2min}, L_{2max}]$ and $L \in [L_{min}, L_{max}]$. Any of the grid points where $L + L_2 > s_{max}$ are eliminated. The rotational space is discretized by equally spaced tip rotation values $\theta_L \in [0, \pi]$, where each point is separated by Δ_R. The parameters we used for this discretization are shown in Table 5.3. Notice that the maximum outer tube extension is limited by the length of the outer nitinol tube, and the maximum total arc length is limited by the length of the inner nitinol tube. This is a consequence of preventing the torque from exiting the endoscope tip.

Table 5.3: The Joint Space Parameterization/Discretization

Variable	**Symbol**	**Value**
Min. Outer Tube Extension	L_{min}	1.0 mm
Max. Outer Tube Extension	L_{max}	ℓ_2
Min. Inner Tube Extension	L_{2min}	1.0 mm
Max. Inner Tube Extension	L_{2max}	18.54 mm
Translational Step	Δ_T	1 mm
Rotational Step	Δ_R	10 °
Max. Total Arc Length	s_{max}	ℓ_1

Workspace Discretization

The workspace is discretized in 2D space, rather than voxelized in 3D space. This is possible due to the symmetry of the workspace about its center axis, which is true for any concentric tube manipulator since the collection of tubes can always be rotated together. Therefore, every 3D point in the workspace is parameterized by a radius R and an axial distance z, where $R = \sqrt{x^2 + y^2}$. This space is pixelized with square pixels of side length w. The pixelization is aligned with the central axis of the workspace, and begins on the most proximal edge of the workspace. The entire pixel is required to fit within the workspace, as shown in Figure 5.19. To compute the required dexterity metric Δ_G from (5.22), the volume of the workspace generated by revolving an individual pixel about the z axis is required. This volume is given by

$$V_{pix} = 2\pi w^2 R_{cen} \ , \tag{5.27}$$

where R_{cen} is the radius R from the z axis to the centroid of the pixel. To find the total volume of the workspace, each of these revolved volumes can be summed.

Design Space Discretization

The inner tube and the outer tube precurvatures, κ_1 and κ_2, respectively, were linearly spaced spaced between $10\,\mathrm{m}^{-1}$ and $85\,\mathrm{m}^{-1}$. From Figure 5.13, it is apparent

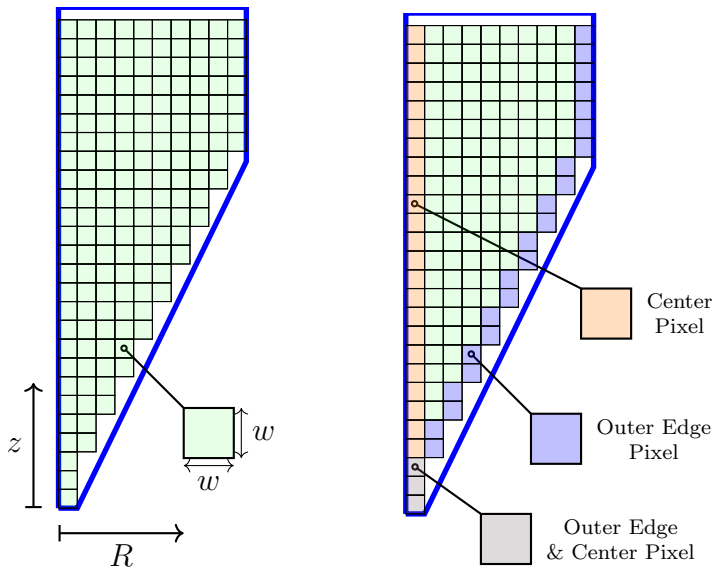

Figure 5.19: An example pixelization of the workspace of the concentric tube manipulator in (R, z) space. In this Figure, w is 0.75 mm. The right image shows the workspace center pixels and outer edge pixels as needed for the workspace edge filter (explained in the subsection 5.6.8).

that fairly high curvatures will be required to reach the workspace, but it is unclear whether the designer should prioritize high outer tube precurvature or high inner tube precurvature, or some combination of both. It is for this reason such a wide span is sought. A total of 10 equally spaced values were chosen for each.

The relative stiffness variable γ was chosen based on a reasonable span on the outer diameter of the outer tube OD_2. OD_2 was spanned from 0.1 mm larger than ID_2 (which is a very small wall thickness), to 0.1 mm smaller than $OD_{\tau 2}$ (a very large wall thickness). Each value of OD_2 uniquely maps to a γ value (see Table 5.1). Four equally spaced values of γ discretized this variable. It became clear in running the simulation several times that the simulation was relatively insensitive to γ, so it was more coarsely discretized.

The variable μ_1 and μ_2 represent the percentage of the nitinol tube that is precurved. On preliminary simulation runs, these variables were each spanned between 0.10 and 1.0. After some initial runs, it became clear that the simulation prioritized

a slightly lower value of μ_1 and a slightly higher of μ_2. For the final run, μ_1 spans $[0.30, 0.60]$ and μ_2 spans $[0.10, 0.40]$, each with eight equally spaced values.

The variable ℓ_1 and ℓ_2 represent the length of nitinol tubing. On preliminary simulation runs, it became clear that the inner tube needed to be very long to reach the entire workspace, and the outer tube could potentially be shorter. In the end, we allowed ℓ_1 to span from 29 mm to 32 mm, with 1 mm equally spaced intervals, and ℓ_2 to span from 5 mm to 32 mm with 5 mm intervals.

In total, this results in 716,800 designs. This is a relatively large design space when you consider that each design must iterate through its entire joint space, which is usually around 8,000 joint steps (depending on tube lengths for the particular design). To run this entire simulation, it would require nearly 6 billion kinematic steps. Luckily, the total amount of steps can be reduced via something we refer to as the workspace edge filter.

The Workspace Edge Filter

The basic idea of the workspace edge filter is to take the entire design space and make sure that an individual design can (1) reach the outer edge of the workspace when the tube precurvatures are aligned, and (2) that it can reach the center of the workspace when the tube precurvatures are anti-aligned, see Figure 5.19. Both of these configurations are torsionless; notice that in equation 5.1, $\theta(s) = 0$ and $\theta(s) = \pi$ are constant solutions. This means that there is no need to integrate, and determining the position of the robot is as simple as determining the position of a serial robot. The input/output relationship of this filter is shown in Figure 5.20.

To implement this, we span the translational joint space with the tubes aligned, and make sure the robot tip hits the outer edge pixels of the discretized workspace, as shown in Figure 5.19. Next we span the translational joint space with the tubes anti-aligned, and make sure the robot tip hits the center pixels of the discretized

Figure 5.20: The basic input/output function of the workspace edge filter is shown. The input is a potential design space, and the output is a subset of designs that stably reach the center and outer edge of the workspace. This filter is numerically efficient because, since the structure is torsionless, the kinematics can be computed without the numerically expensive integration steps.

workspace, as shown in Figure 5.19. This filter guarantees that the remaining designs will be able to reach the outer edge and center of the workspace. Designs that cannot meet this condition should be eliminated prior to doing the computationally expensive kinematic iterations.

For our workspace edge filter, we took very fine translational steps of 0.2 mm and discretized the workspace into 0.5 mm square pixels. After running the entire design space through the filter, 94.7 % of the designs were eliminated, leaving 37,865 remaining design candidates, and reducing the total computation time of the simulation substantially.

This idea was based on the knowledge that certain designs in our design space will certainly not be able to reach the workspace edges. For example, a design of $\kappa_1 = \kappa_2 = 10\,\mathrm{m}^{-1}$ will not be able to reach the workspace edges, and the simulation should not spend significant time on these designs. The workspace edge filter does this elimination in an intelligent way without significant computation.

The Simulation Steps

The flow of the simulation is shown in Figure 5.21. The workspace edge filter begins by efficiently removing potential designs from the total design space that do not reach the center or outer edge of the workspace when the tubes are aligned and anti-aligned. The other key component of the simulation is that translational joint configurations which bifurcate are not considered, so the only workspace considered is guaranteed

to be stable. During the kinematic step, important metrics like tip position, isotropy, and stability are stored and assigned to the corresponding workspace voxel. This simulation was implemented in C++, and at the end of the simulation, each candidate design generates a design report that is further analyzed in MATLAB.

5.6.9 Manipulator Optimization Results and Discussion

The final optimized design is shown in Table 5.4. Of the original 716,800 designs, 62 met all of the constraints. Roughly 95% of the designs were eliminated by the workspace edge filter. Of the remaining designs, 20% did not meet the workspace constraint, 69% did not meet the minimum velocity constraint, and 52% did not meet the minimum Δ_β constraint. All remaining designs met the maximum velocity constraint; we hypothesize this is because designs with stability problems (and hence high workspace velocities) were eliminated by the workspace edge filter.

The optimization clearly favored designs with a highly curved outer tube, contrary to our initial intuition that the inner tube should be the most highly curved. The inner tube precurvature was not as aggressive as the outer tube, but was still required to be relatively high, in comparison with previous designs, to reach the entire workspace. It was clear that this design optimization was dominated by the stability constraint. The optimization clearly preferred designs with very short precurved lengths on the outer tube. Essentially, the simulation favored designs that could reach the entire workspace while introducing minimal torsion into the system (recall, if the precurved sections are not overlapping, the manipulator is torsionless).

The length of the torque tubes ($\ell_{\tau 1} = 482.6\,\text{mm}$, $\ell_{\tau 2} = 355.6\,\text{mm}$) for this design are non-negligible. Even though these lengths are much stiffer, their equivalent length if made from nitinol is still 32.2 mm and 6.1 mm, respectively. When this is combined with the lengths of the nitinol tubing, the total equivalent transmission length can be roughly estimated to be around 50 mm, but depends on the exact translational

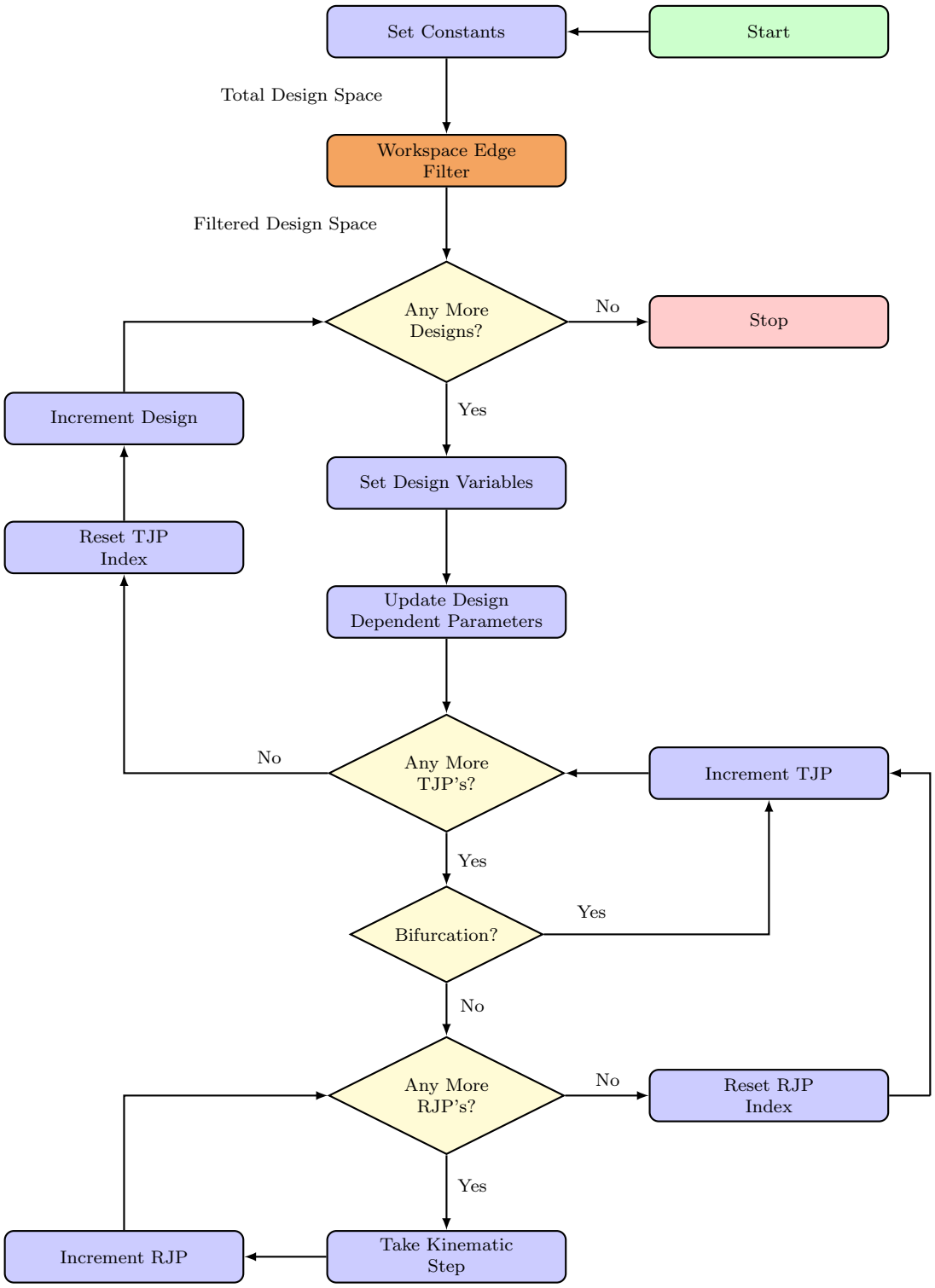

Figure 5.21: This figure shows a flow chart of the simulation implementation. The bifurcation check acts as a filter, removing portions of the translational design space which would result in unstable rotations. TJP = Translational Joint Positions, RJP = Rotational Joint Position.

Table 5.4: The Optimized Design Parameters

Design Variable	Symbol	Value
Inner Tube Precurvature	κ_1	$35.0\,\mathrm{m}^{-1}$
Outer Tube Precurvature	κ_2	$76.7\,\mathrm{m}^{-1}$
Ratio of Outer/Inner Tube Stiffness	γ	2.84
Percentage of Inner Tube That is Precurved	μ_1	0.51
Percentage of Outer Tube That is Precurved	μ_2	0.14
Length of Inner Nitinol Tube	ℓ_1	29.0 mm
Length of Outer Nitinol Tube	ℓ_2	30.0 mm

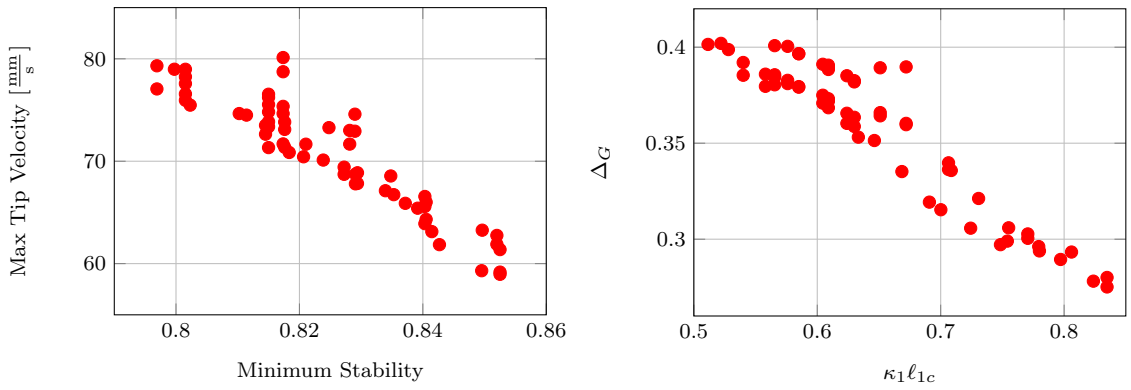

Figure 5.22: Shown above are the final designs that meet the constraints. (Left) The maximum task space velocity generally decreased as the robot stability increases, as predicted. (Right) Contrary to initial intuition, Δ_G tended to decrease as the inner tube precurvature angle (i.e. $\kappa_1\ell_{1c}$) increased.

actuation of the robot. Based on Figure 5.16, one can see that the design space remains somewhat limited - although vastly improved from the 500 mm contour, which is roughly what the design would be limited to if it did not implement torque tubes.

The simulation did show, as expected, designs that had less stable configurations generated higher workspace velocities, as shown in Figure 5.22 (Left). Surprisingly, the simulation also revealed that the global isotropy metric, Δ_G decreased roughly linearly with the inner tube precurvature angle, which is the product of the inner tube precurvature and precurved length, as shown in Figure 5.22 (Right). This may be due to the fact that as the inner tube precurvature angle increases, the design becomes progressively less stable, in general.

In this simulation, we used a volume-weighted global dexterity metric to analyze

the stability of particular concentric tube robot designs. This volume-weighting has particular appeal, since it gives equal value to every workspace location, but for concentric tube manipulators in particular, it may be somewhat deceiving. In general, the shape of a concentric tube manipulator's workspace is trumpet-shaped, so the vast majority of the workspace is far away from the central axis. In contrast, the stability and dexterity issues for these manipulators occur when the tubes are anti-aligned, or more towards the center of the workspace. Therefore, these global, volume-weighted dexterity metrics effectively weigh the stable, outer edges of the workspace as "more important" than the less stable, less dexterous central region of the workspace. Global dexterity metrics for concentric tube manipulators deserve further thought, and these volume-weighted metrics may not be a relevant metric towards creating a device that functions well from the perspective of the surgeon.

5.6.10 Manipulator Optimization Conclusions

The biggest takeaway from this design optimization is that stability is a dominating factor in the design challenge. The constraint of maintaining stability throughout the workspace has a tremendous effect on the size and shape of the design space. Furthermore, even within the remaining stable design space, the relative stability measure is a dominant parameter in the dexterity of the device.

Based on these observations, we propose that an effective design heuristic is to design the most stable manipulator that meets the constraints of the application. Utilizing this overarching design guideline, the designer will also be implicitly creating a design with superior dexterity properties.

As a first step towards any concentric tube manipulator design, the designer should consider all possible stability improvement design techniques. One of the most highly beneficial approaches is torque tubes, which was discussed in great detail here and also utilized in [138]. There are other approaches that improve stability by chang-

ing the precurved shape of the nitinol tubes to non-constant precurvatures [34, 36], prohibiting overlapping curved sections during actuation [32], and pattern machining the tubes to create favorable bending to torsional stiffness ratios [31, 30]. Each of these approaches should be considered part of the design arsenal and used towards creating optimally stable, highly effective concentric tube manipulators. The results of the design optimization problem presented in this section directed the tube design for the neurosurgical system, described in detail in the next section.

5.7 Experimental Evaluation

The purpose of the following set of experiments is to compare manual endoscopic removal of a colloid cyst (i.e. as it is currently done) to bimanual (i.e. two-handed) robotic colloid cyst removal using the system described in Section 5.5. This experimental comparison will be made on a custom-designed phantom based on a patient CT scan.

5.7.1 Design of the Phantom

The experiment is based on a CT scan that contains a colloid cyst that sits within the foramen of Monro. The cyst is roughly 2 cm in diameter and is approximately spherical, as shown in Figure 5.23. The foramen of Monro, the skull, the cyst, and the ventricles were identified as important structures to include in the design of the phantom. Each of these structures were manually segmented from the raw imaging data, as shown in Figure 5.23.

The ventricles are hollow, open structures full of cerebrospinal fluid, the foramen of Monro is formed by a circular ring of tissue and is the connecting channel between the lateral and third ventricle. In this CT scan, the cyst is sitting directly within the foramen of Monro. Colloid cysts have a very thin outer membrane and some contain

fibrous contents within the membrane that must be resected, while others have more fluid-like contents and can be aspirated. In this phantom design, the colloid cyst is designed such that its contents can be aspirated. Colloid cysts are also known to have a fibrous "stalk" attachment. This is a thin, string-like structure that attaches the colloid to the superior (i.e. towards the top of the head) surrounding brain anatomy. The cyst is sometimes described as hanging from its stalk within the foramen of Monro.

A stereolithography (.stl) file was generated for the skull, the foramen of Monro, the ventricles, and the cyst, enabling visualization of each structure in three dimensions. The relevant portion of the segmented skull and ventricles were 3D printed (Skull: Shapeways/Black PLA, Ventricles: Protolab/ PA 850/Black Nylon-11/Selective Laser Sintering). Before printing, two orthogonal, square holes were created that passed through both the skull and the ventricles so that square rods could be assembled to fully define the position/orientation of the ventricles relative to the skull anatomy. A rendering of this concept is shown in Figure 5.24, and the 3D printed assembly is shown in Figure 5.25. Note that the ventricle structure was 3D printed to include a foramen/cyst cavity structure, which forms the foramen of Monro and the cavity for for cyst (this is shown in Figure 5.24 - Right).

A phantom model has previously been established for training surgeons in endoscopic third ventriculostomy [142], and many of the same design concepts were utilized during the construction of the synthetic brain phantom presented in this chapter. As described in [142], a silicone molding technique was used to construct the brain phantom. Because the foramen of Monro structure should be stiffer than the surrounding brain tissue, the foramen/cyst cavity were directly molded onto the 3D printed ventricle structure out of a stiffer silicone material. This was accomplished by taking a metal tube of the appropriate diameter, machining it to fit closely around the foramen/cyst cavity, and then pouring in the silicone mold compound. The pre-molded

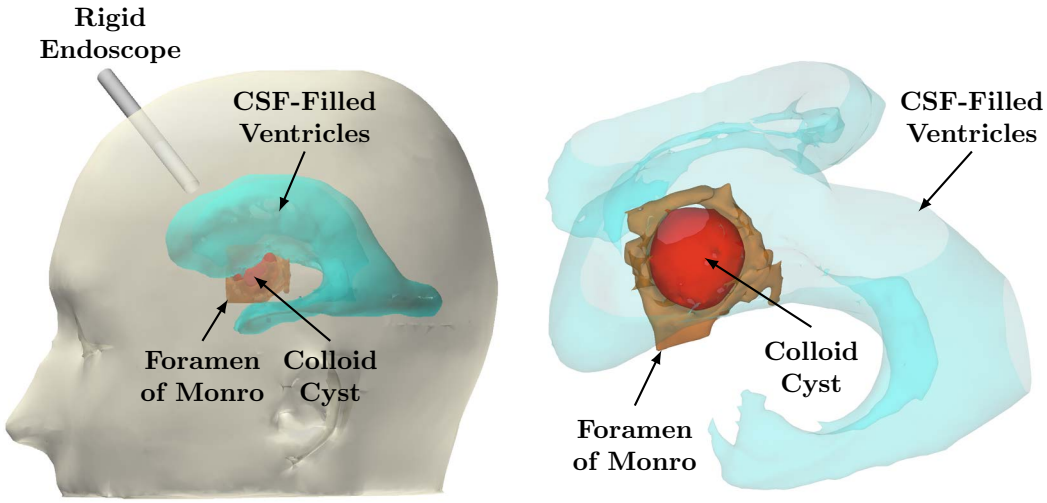

Figure 5.23: The ventricles, colloid cyst, foramen of monro, and skull were all segmented from a CT scan. For endoscopic removal of a colloid cyst, the rigid endoscope is inserted through a burr hole into the ventricles. The colloid cyst sits within the foramen of Monro and can be accessed through the ventricles.

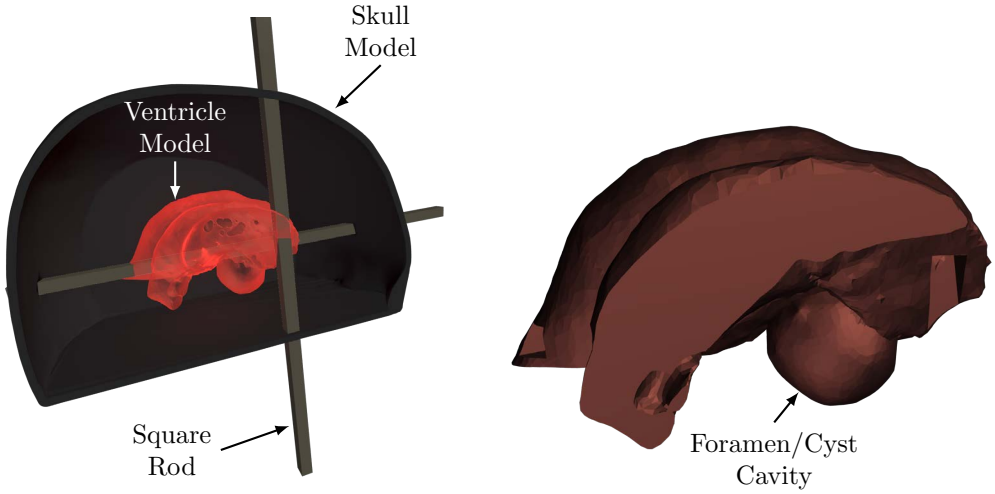

Figure 5.24: (Left) The ventricles are assembled within the skull using two square rods. The skull and ventricles were each 3D printed. (Right) A close-up of the ventricles. The foramen/cyst cavity were included as part of the 3D printed model.

Figure 5.25: (Left) The assembled 3D printed skull and ventricle mold. (Right) The mold with the poured silicone while curing.

foramen/cyst structure can be seen in Figure 5.26. For this stiffer portion of the mold, a two part silicone molding compound (Reynolds Advanced, Dragon Skin 10 FAST) was used with no softening compound added. A very small amount of flesh-tone silicone pigment (Reynolds Advanced, Silc Pig Silicone Pigments, Fleshtone) was added so that the appearance of the phantom was closer to that of tissue. Mold release (Reynolds Advanced, Universal Mold Release) was sprayed on the metal tube prior to casting the silicone. The mold release was intentionally not sprayed on the 3D printed ventricle structure, so that the mold would stick to the 3D printed ventricles after removal of the metal cylinder. After allowing the casting to cure, the metal tube was removed, which left the foramen/cyst molded assembled to the 3D printed brain ventricle. Next, the square rods were assembled and the 3D printed brain ventricle was sprayed with mold release. To prepare the brain tissue silicone compound, a ratio of 2:1 silicone to softening compound (Reynolds Advanced, Slacker) was mixed by volume. Finally, the brain tissue silicone mixture was poured, as shown in Figure 5.26 (Left), until it completely filled the mold, and left to cure for two hours. After complete curing, the square rods were disassembled from the mold and the 3D printed ventricle structure was removed from the center of the mold. This was done by stretching the silicone until it could be removed; while this part was challenging to

Figure 5.26: (Left) The brain tissue silicone is poured with the ventricles assembled using the square rods, and the foramen/cyst cavity already pre-cast out of stiffer silicone. (Right) Cyst preparation: the stretched parafilm is placed over a tube and a syringe is filled with a dilute agarose gel mixture. A string ties off the stretched parafilm to form the spherical cyst and act as the fibrous stalk attachment.

extract, no visual damage was done to the simulated brain tissue during the removal process. After removing the 3D printed ventricle structure, the pre-molded, stiffer foramen/cyst cavity structure remained in the mold.

The design of the colloid cyst was inspired by the model outlined in [49]. Stretched Parafilm (Heathrow Scientific) was used to form the outer membrane of the cyst, and the cyst was filled with a viscous agarose mixture. The desire was to simulate a colloid cyst where the contents of the cyst could be aspirated, without the contents spilling out of the membrane as soon as it was perforated. After some experimentation, we determined that the following protocol produced the desired result. First, 0.4 g of agarose powder was mixed with 100 mL of phosphate buffered saline and heated in the microwave for 90 seconds on high. The mixture was then stirred and placed it back into the microwave for another 90 seconds on high. The resulting agarose was thin enough for a standard syringe (without a needle) to take in when the piston was pulled. Prior to preparing the agarose mixture, the parafilm was stretched and placed over a tube. Using the syringe, 4 cc of the mixture was dispensed into the

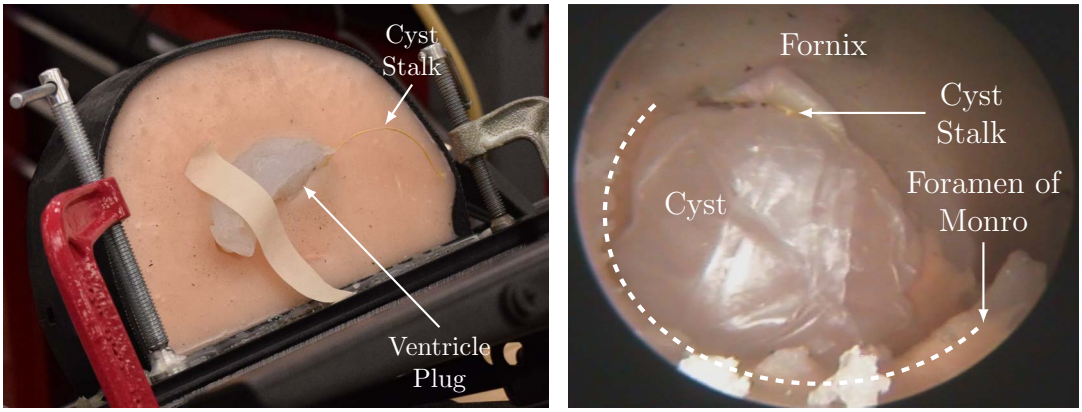

Figure 5.27: (Left) The phantom setup. The mating ventricle plug is shown, and the "stalk" of the cyst (the string) can also be seen. (Right) An endoscopic view of the anatomical layout for the phantom experiment. The foramen of Monro and fornix are cast from silicone, as is the rest of the brain phantom, while the cyst is made from a combination of stretched parafilm and a viscous agarose fluid/gel.

stretched parafilm, as shown in Figure 5.26 (Right). As the contents are inserted into the cyst, the top of the cyst is tied off with a piece of string to retain the cyst contents. This piece of string simulates the fibrous "stalk" that attaches the colloid cyst to its surrounding brain anatomy. The cyst can be placed into the brain phantom by hand, since the 3D printed ventricle structure creates an accessible void in the brain phantom. Prior to the beginning of the experiments, the cyst is placed in the cyst cavity according to surgeon visual feedback. The void that the cyst is inserted through is plugged with a mating ventricle plug. This plug also holds the string (i.e. the stalk of the colloid cyst) so that it is constrained inside of the phantom as shown in Figure 5.27 (Left). An endoscopic view of the anatomy is shown in Figure 5.27 (Right).

5.7.2 Experimental Methods

The entry burr hole was drilled by the experimenting neurosurgeon into the skull phantom. The trajectory was planned by eye, and the surgeon drilled the burr hole to a diameter just larger than the endoscope, as shown in Figure 5.28. The endo-

scope/trocar used in this experiment is the Minop Invent 30° neuroendoscope (Aesculap, Inc.). The manual procedure was completed with two surgeons: an experienced pediatric neurosurgeon and a neurosurgical fellow (neuroendoscopic procedures often take two surgeons to complete). The neurosurgical fellow was in control of the hand tools that pass through the working channel of the trocar, and the pediatric neurosurgeon was in control of the endoscope/trocar, as is shown in Figure 5.30 (Right). For the robotic procedure, the neurosurgeon was in sole control and teleoperated both arms.

There were three basic stages to the experiment; first, the surgeon perforated the thin cyst membrane so that the contents began to flow out. Second, the surgeon aspirated the fluid-like cyst contents until the cyst was sufficiently debulked. Lastly, the surgeon found the stalk attachment point (i.e. the string), and placed the tool on the string to simulate the cut required to free the cyst and remove it. In the experiment, as soon as the tool was placed on the string, the experiment was considered complete, and the surgeon was not required to actually cut the string. During the manual experiment, the forceps were utilized to perforate the cyst. The surgeon then exchanged the forceps for a flexible aspiration tube that was connected to vacuum, and then switched back to the forceps to simulate cutting the stalk. For the robotic

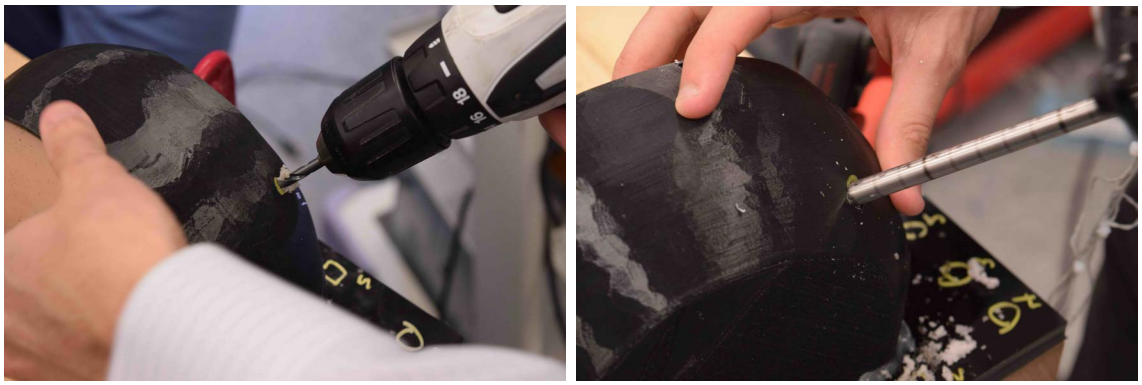

Figure 5.28: (Left) Drilling of the burr hole/trajectory. (Right) The endoscope inserted through the burr hole into the brain phantom.

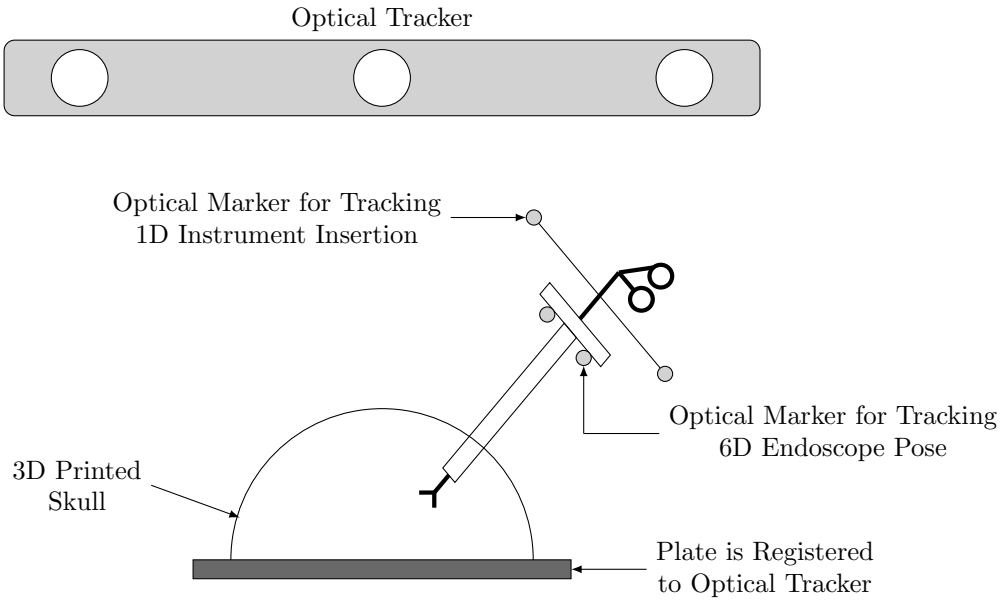

Figure 5.29: The registration set up for the experiment. The phantom is registered to the optical tracker and remains still. The 6D pose of the endoscope is optically tracked, and the 1D insertion of the tool is optically tracked.

experiment, the surgeon had the ability to aspirate with the left arm throughout the entire procedure, and had forceps in the right manipulator for the entire procedure. The forceps were actuated by hand (push/pull - actuated by a graduate student) when the surgeon requested them to open or close.

We tracked the movement of the endoscope during both the manual and the robotic experiment. We utilized the NDI Optotrak (Northern Digital, Inc.), with a custom assembled rigid body to achieve 6D tracking as shown in Figure 5.29 and Figure 5.30 (Left). During the manual experiment, we also tracked the 1D motion of the forceps. We achieved this by tracking at least one of the markers on the forceps tracking rigid body, as shown in Figure 5.29 and Figure 5.30 (Right), and projecting it to the axis of the endoscope, which was simultaneously tracked. Note that the motion of the manual aspiration tube was not tracked because of its flexibility. The experiment began with the endoscope in a neutral (i.e. not tilted) configuration and the forceps at the tip of the endoscope. This enabled tracking of the tip of the forceps

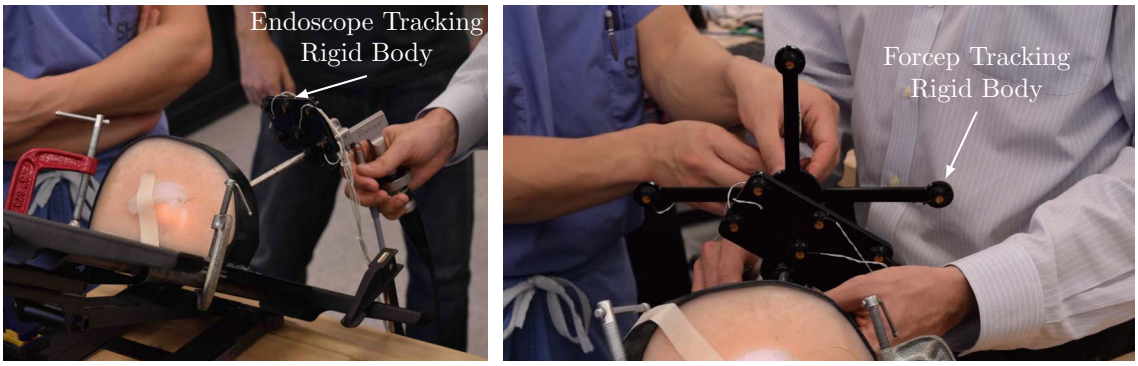

Figure 5.30: (Left) The endoscope/trocar inserted into the phantom. (Right) The endoscope/trocar inserted into the phantom with the forceps passing through the working channel. The forceps were under the control of the neurosurgical fellow and the endoscope was guided by the neurosurgeon.

relative to the endoscope tip (assuming 1D insertion/retraction) and the tilt of the endoscope relative to its neutral configuration at the beginning of the procedure.

The phantom setup was held in place and registered to the NDI Optotrak (we refer to this registration as $\mathbf{T}_S^O$), which allowed expression of endoscope pose and tool position relative to anatomic structures (assuming the anatomy is rigid). The phantom registration was accomplished by touching known points on the phantom setup with a tracked point probe and utilizing well-established point based registration techniques as outlined in [143]. The RMS fuducial registration error was 0.14 mm and 0.21 mm for the manual and robotic experiments, respectively. The custom endoscope tracking rigid body was also registered to the endoscope. In other words, the assumption was not made that the transformation from the endoscope tracking rigid body to the endoscope was known; we refer to this registration as $\mathbf{T}_E^P$. Again, this was accomplished by touching known points on the endoscope with a tracked point probe. The FRE for this registration was 0.43 mm and 0.39 mm for the manual and robotic experiments, respectively. If the Optotrak frame is identified with $\{O\}$, the endoscope frame with $\{E\}$, the phantom (skull) frame with $\{S\}$, the tracked frame on the endoscope with $\{P\}$, and the positions of the forceps tip in the endoscope frame

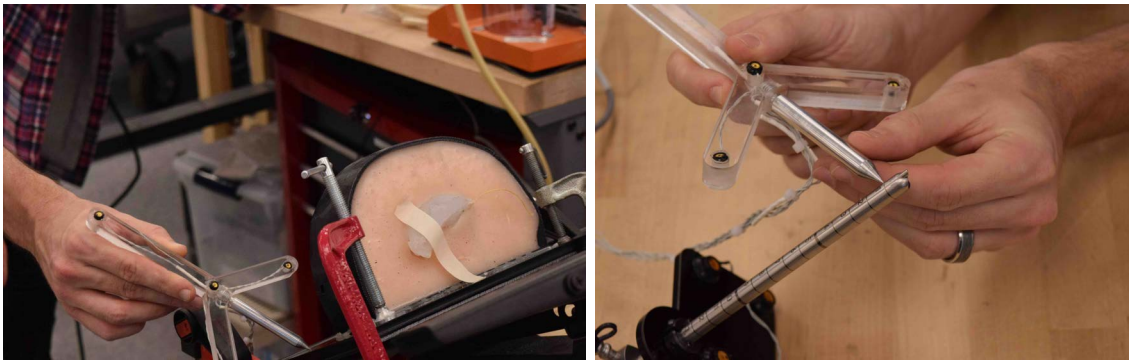

Figure 5.31: (Left) Point based registration of the phantom test stand. (Right) Point based registration of the endoscope.

Figure 5.32: (Left) The robot was aligned properly by the surgeon. Once aligned, the passive arm was locked. (Right) The surgeon teleoperated the left and right manipulator using two haptic devices and visual endoscopic feedback.

as $\boldsymbol{p}_{tip}^{E}$, then the homogeneous transformation representing the endoscope frame $\{E\}$ expressed in the coordinates of $\{S\}$ can be calculated as

$$\mathbf{T}_{E}^{S} = (\mathbf{T}_{S}^{O})^{-1}\mathbf{T}_{P}^{O}\mathbf{T}_{E}^{P} \,,$$

and the position of the forceps tip in the coordinates of $\{S\}$ can be calculated as

$$\boldsymbol{p}_{tip}^{S} = \mathbf{T}_{E}^{S}\boldsymbol{p}_{tip}^{E} \,.$$

Note that all tracking data was recorded at a rate of 100 Hz. For the robotic experiment, the positions of the left and right arm relative to the endoscope are known based on the kinematic model, and these positions were logged at 250 Hz during the

experiment. For the robotic experiment, the robot/endoscope are held by a passive, lockable arm as shown in Figure 5.32 (Left) and the surgeon teleoperated the arms with the haptic user input devices (Novint Falcon, Novint Technologies, Inc.) as shown in Figure 5.32 (Right). The user interface forced the surgeon's hands to stay within the workspace of the manipulators, and a push button was used as a clutch. The scaling between as the surgeon's hand motion and the manipulator motion could be changed on demand during teleoperation by the surgeon. The passive arm could be re-configured if needed by the surgeon during the procedure, and any reconfiguration of the system would be optically tracked. The experiment was started in both the manual and robotic cases when the surgeon was satisfied with the position of the endoscope/tools. In both cases, the surgeon verified the tools could reach the cyst prior to initiating the recording of the experimental data.

5.7.3 Results

The endoscopic angulation ε for both the manual and robotic experiments are shown in Figure 5.33 and summarized in Table 5.5. This was calculated by tracking the $\boldsymbol{z}$ axis of the endoscope fame $\{E\}$, expressed in the coordinates of the phantom setup $\{S\}$, or $\boldsymbol{z}_E^S(t)$, which is aligned with the central axis of the endoscope at all times. We are interested in the angle between the vector $\boldsymbol{z}_E^S(t)$ and the vector $\boldsymbol{z}_E^S(0)$ (i.e. the neutral endoscope axis when the experiment begins). Both of these vectors are unit vectors, so the angle between them can be calculated as

$$\varepsilon(t) = \cos^{-1}\left(\boldsymbol{z}_E^S(t) \cdot \boldsymbol{z}_E^S(0)\right).$$

The mean endoscope angulations were $3.97\,^\circ$ and $0.46\,^\circ$ for the manual and robotic experiments, respectively. The max endoscope angulations were $17.09\,^\circ$ and $1.16\,^\circ$ for

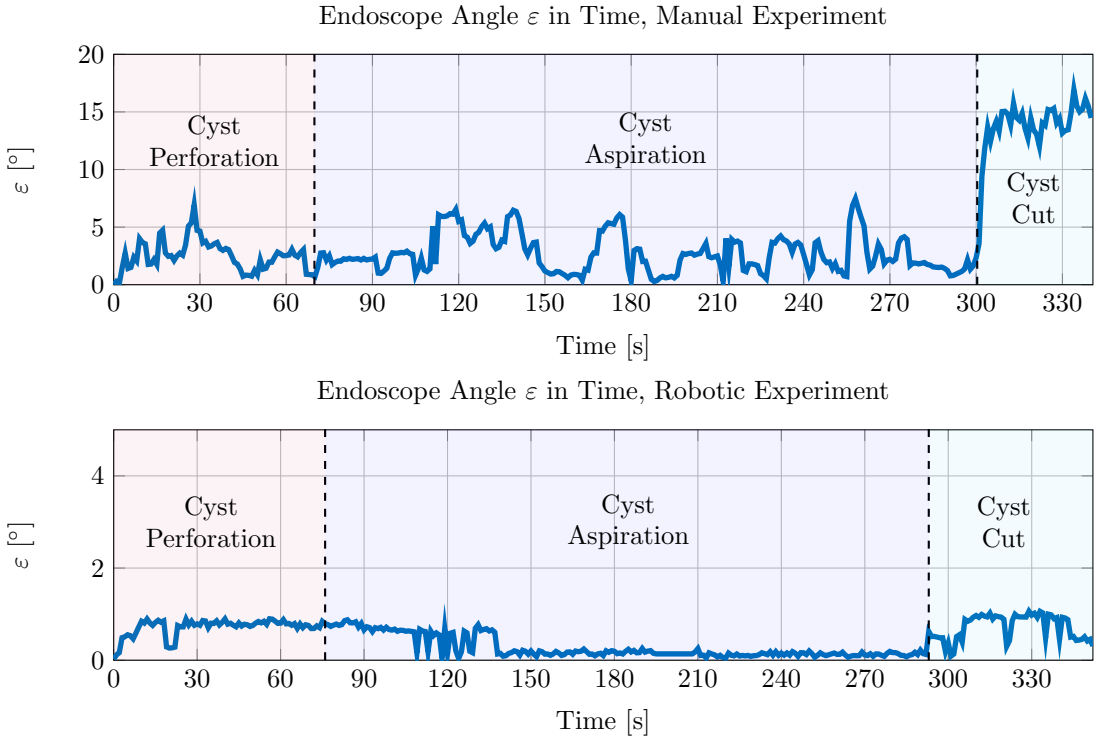

Figure 5.33: The endoscope angle in time for the manual (Top) and robotic (Bottom) phantom colloid cyst removal experiment. Endoscope tracking was lost for 0.42 s of the roughly 350 s manual experiment and for 14.35 s during the robotic experiment. Notice the difference in axis limits.

Table 5.5: The endoscopic angulation ε in time for each of the two phantom experiments.

	Manual	**Robotic**	**Units**
Mean $\varepsilon(t)$	3.97	0.46	deg
Max $\varepsilon(t)$	17.09	1.16	deg
Standard Deviation $\varepsilon(t)$	3.95	0.33	deg
Experiment Time	340.6	353.0	s

the manual and robotic experiments, respectively. The surgeon was able to accomplish the entire robotic procedure without re-configuring the endoscope. The movement of the endoscope in this case is the result of bumps, vibrations, tracking noise, and flexibility of the robot/endoscope structure. Note that tracking was temporarily lost due to line-of-sight obstructions for 0.42 s during the manual procedure and 14.35 s during the robotic experiment. The calculations for ε in Table 5.5 do not include times when tracking was lost, but the total experiment time does.

In Figure 5.33 (Top), the stages were defined to begin/end when the tool was exchanged, and in Figure 5.33 (Bottom), the stages were approximated to begin/end based on the visual motions in the endoscopic video feed. The most noteworthy results from Figure 5.33 are that (1) it was possible to complete the robotic procedure without reconfiguring the endoscope, (2) endoscopic angulation as high as 17.09 ° was observed during the manual procedure during the cyst cut stage of the procedure, and (3) 5-10 ° oscillations in endoscopic angulation were common during the manual procedure.

Figure 5.34 shows the axial tool extensions/retraction $d(t)$ of the forceps during the manual experiment for both the cyst perforation (Figure 5.34 –Top) stage and the cyst cut (Figure 5.34 – Bottom) stage. In these figures, when the tool is retracted inside of the endoscope (i.e. $d < 0$), d is truncated to $d = 0$. As is apparent from Figure 5.34, the forceps are usually extended between 5–20 mm from the tip of the endoscope. The maximum extension of the tool from the endoscope tip was found to be 23.1 mm. This plot gives an indication of both the magnitude and frequency of the axial tool motions during manual endoscopic colloid cyst removal. Importantly, this plot also has future implications towards the design of the manipulators in the robotic system, because it indicates how far out axially away from the endoscope the surgeons are comfortable with their tools working, which has been a specification that has been approximated in the past.

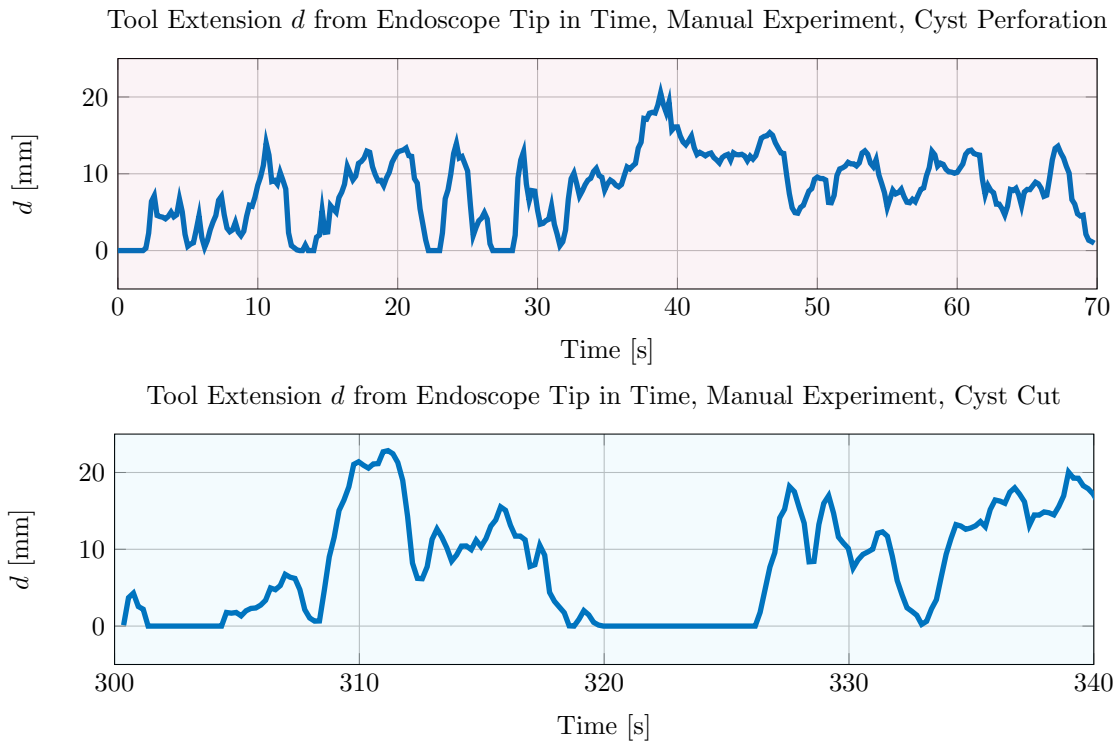

Figure 5.34: The tool extension d is shown during the manual experiment during both the cyst perforation (Top) and cyst cut (Bottom) stage of the procedure. $d = 0$ corresponds to when the tool is exactly at the endoscope tip, and values of $d < 0$ (i.e. when the tool tip is inside of the endoscope) have been truncated to $d = 0$.

The locations, relative to the registered anatomy, that the tips of the tools reached for both the manual and robotic procedure are shown in Figure 5.35. Recall that the aspiration tube movements during the manual procedure were not tracked due to the flexibility of the tube. For the manual procedure, the locations of the tool tip during the cyst perforation stage and the cyst cut stage of the procedure are clearly grouped (shown within ellipses in Figure 5.35 - Left). The point clouds are highly axial, as one would expect, since these points are generated by axial extension/retraction of the tool through the endoscope. As is shown in Figure 5.33 (Top), the endoscope moves considerably, approximately 10-15 $^\circ$ between these two stages of the procedure. The corresponding robotic manipulator positions for the cyst perforate/cut stages of the procedure are shown in Figure 5.35 (Center). As is clear from this Figure, the manipulator tips each move considerably less than the forceps did during the manual procedure. It is also clear that both manipulator arms are used together during the perforation/cut portions of the procedure. Figure 5.35 (Right) shows the manipulator tip positions during the entire experiment; the point clouds approximate the conical workspace that the manipulator tips were constrained to operate within. It appears that during the robotic procedure, the manipulators did not reach the same locations that were accessed during the manual cut portion of the experiment. This is because the endoscope did not move; instead, the surgeon used the bimanual capability of the manipulators to orient the cyst with the right arm so that the string was exposed and then touched the string with the left arm. The positions that the endoscope tip reached during both the manual and robotic experiment are shown in Figure 5.36.

It is possible to quantify the total motion of the tool tips that were required during the manual and robotic experiments. This data is summarized in Table 5.6. The tracking data for the manual procedure and the logged tip position data for the robotic procedure were both downsampled to 10 Hz for this analysis. This was done to reduce the impact of the high frequency tracking noise when calculating the

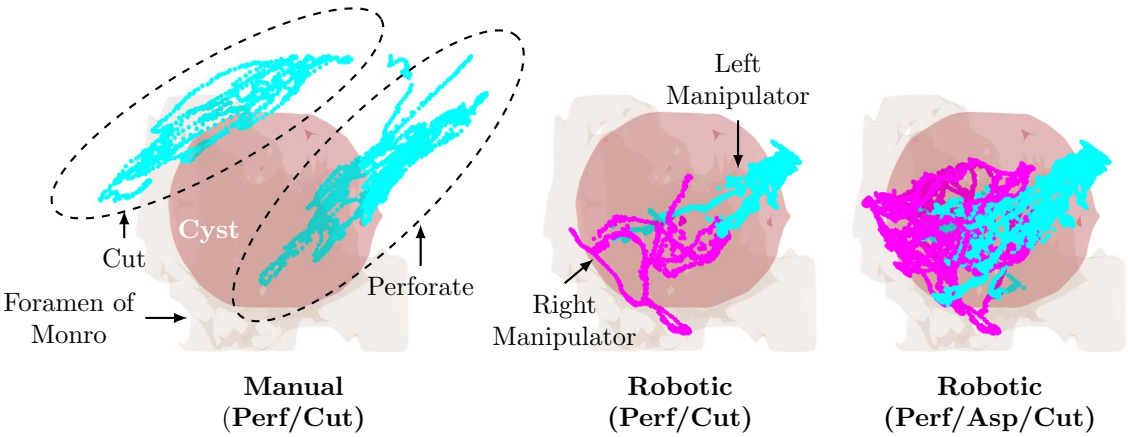

Figure 5.35: The tool tip positions for the manual and robotic experiments. In the manual experiment, aspiration was not tracked. In the robotic experiment, the joint positions of both arms were recorded during the entire experiment. (Left) The manual forceps position during perforation and cutting of the cyst. (Center) The robotic tool positions during perforation and cutting of the cyst. (Right) The robotic tool positions throughout the entire procedure, including aspiration of the cyst.

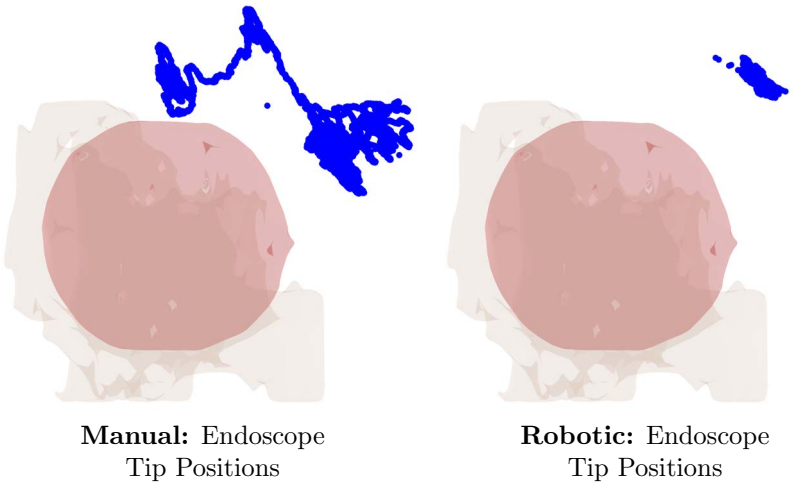

Figure 5.36: The endoscope tip positions during the manual (Left) and robotic (Right) experiments.

Table 5.6: Tool motion data for both the manual and robotic experiments. The endoscope is tracked during both the manual and robotic experiments. The 1D motion of the forceps are tracked during the manual procedure, and the positions of the manipulators are logged in software during the robotic procedure. For the manual procedure, these values include the forceps motion when the tool is inside of the endoscope.

	Manual Forceps	**Robotic** Left Arm	**Robotic** Right Arm	Units
Tip Distance Traveled: Perforation	479	201	218	mm
Total Time: Perforation	70	76	76	s
Average Velocity: Perforation	6.8	2.6	2.9	$^{mm}/_{s}$
Tip Distance Traveled: Cutting	354	230	267	mm
Total Time: Cutting	40	60	60	s
Average Velocity: Cutting	8.9	3.8	4.5	$^{mm}/_{s}$

distance between subsequent tip positions. The tip distance traveled by the forceps during the perforation stage of the manual procedure was 479 mm. In comparison, the tip distance traveled by the left and right manipulator was 201 mm and 218 mm, respectively. The total distance moved was similar between the manual and robotic procedures, but these motions were split over two arms in the robotic portion of the procedure. On average, the manual forceps moved about twice as fast as the robotic manipulators during the experiment. Similar results were found during the cutting stage of the procedure; a discussion of what this data may imply will take place in the next subsection.

5.7.4 Discussion

It is difficult for the quantitative experimental data presented in the preceding subsection to capture how the surgical approach changed between the manual and robotic procedures. It was qualitatively clear that the motions being made manually versus robotically were quite different, mainly due to the presence of a second arm. Figure 5.38 shows an example of these qualitative differences for each of the three stages of the procedure.

For example, first consider the cyst perforation stage of the procedure. When

done manually, the neurosurgeon aligned the endoscope so that the forceps could extend straight to the membrane of the cyst and grab it. Because the surgeon had no ability to apply retraction, when the forceps grabbed the cyst and pulled on it, rather than perforating the membrane, the entire cyst was displaced towards the tip of the endoscope. To actually perforate the membrane, the surgeon twisted/poked the forceps into the membrane until it eventually perforated. In contrast, during the robotic experiment, the surgeon was able to grasp the cyst with the right manipulator (forceps), apply tension, and use the left manipulator to open up the cyst, as is shown in Figure 5.38 (Top Row - Right).

Similarly, during the manual aspiration stage of the procedure, the aspiration tube was poked into the cyst until it was satisfactorily debulked. Some aiming of the aspiration tube was possible by tilting the endoscope. In contrast, during the robotic experiment, the surgeon was able to hold the cyst with the right manipulator and aspirate around it with the left. The surgeon also opened the cyst with the forceps and inserted the aspiration manipulator inside of the cyst. Another maneuver the surgeon utilized during this stage of the procedure was to press against the cyst with the right manipulator and force out the cyst contents and aspirate simultaneously.

Lastly, during the manual cut stage of the procedure, a very large endoscopic movement was required to reach the string (i.e. the stalk of the cyst), see Figure 5.33 (Top) and Figure 5.38 (Bottom Row - Left) - it is clear that the endoscopic view has completely shifted. The ability to complete this task was contingent on the ability to tilt the endoscope. In contrast, during the robotic experiment, the surgeon used the manipulator forceps to manipulate the cyst (i.e. moving the anatomy to the tools) towards the left manipulator. Once the string was in range of the left arm, it reached out and touched the string to simulate cutting it; this type of maneuver was not possible with a single, manual tool and endoscopic angulation.

We hypothesize that the tool motions required for the robotic system can be

reduced even further (in comparison to those presented in Table 5.6) as the user interface is refined, the manipulators are calibrated more precisely, and the surgeon has more experience teleoperating this system; this was the experimenting surgeon's first interaction with the system. Additionally, it is worth noting that the 30° angle of view on the endoscope is not adjusted for in the robotic system, leaving the surgeon to understand that registration mentally. Further, the motion of the tubes can be distracting to the surgeon in the endoscopic view; as the tubes move relative to one another, it can be difficult for the surgeon to focus on the tip of the manipulator. A sheath that hides the relative tube motions would likely help to address this concern, and it is also possible that with increasing experience with the system, surgeons will learn to focus on tool tips and understand that all tubes must move simultaneously to achieve desired tip motions.

There is another element of this procedure that completely changed when switching from a manual procedure to a robotic procedure: the number of surgeons required was reduced from two to one, and the number of hands that are located near the base of the endoscope is reduced from four to zero, as is shown in Figure 5.37. During the manual procedure, coordinated motions and efficient communication are required to accomplish the surgical task – since one surgeon is in control of the endoscope and the other is in control of the tool. This effectively means one surgeon controls the axis of the endoscopic tool and the visualization, while the other controls the extension, retraction, and open/close of the transendoscopic tool. The robotic setup reduces this complexity, returns this to a single surgeon procedure, and eliminates the coordination/communication requirement.

5.7.5 Experimental Conclusions and Future Work

These phantom experiments showed that this two-armed concentric tube robotic system could be used to complete the tasks required for endoscopic surgical treatment

Figure 5.37: (Left) The two surgeons and four hands behind the endoscope during the manual experiment. Coordinated movements and communication are required. (Right) One surgeon is in control during the robotic experiment, the endoscope/robot is mounted, and the surgeon is teleoperating the arms nearby.

of colloid cysts, without necessitating endoscopic angulation. We also found that the arms moved less robotically during the stages of the experiment than they did during the manual experiments, and that they generally moved more slowly. Qualitatively, the presence of a second, dexterous tool completely changed the surgical approach. In particular, the ability to apply tension, retraction, and use the arms cooperatively allowed the surgeon to utilize more complex surgical maneuvers to manipulate the cyst, instead of tilting the endoscope as they would during the manual experiment.

Further refinements of the robotic system are necessary for this system to reach its full potential. Many of these refinements are related to the fidelity of the surgeon interface, but also the design of the tubes, and handling the challenges of visualization through the endoscope. It is likely that the concept of having bimanual, dexterous manipulators through a rigid endoscope will prove useful in several other endoscopic neurosurgical applications, and, here, we have used the colloid cyst as the first experimental evaluation of this robotic system. Future studies should include a larger number of experiments and perhaps several surgeon users to draw wider conclusions about the performance of the robotic system versus the manual, conventional approach.

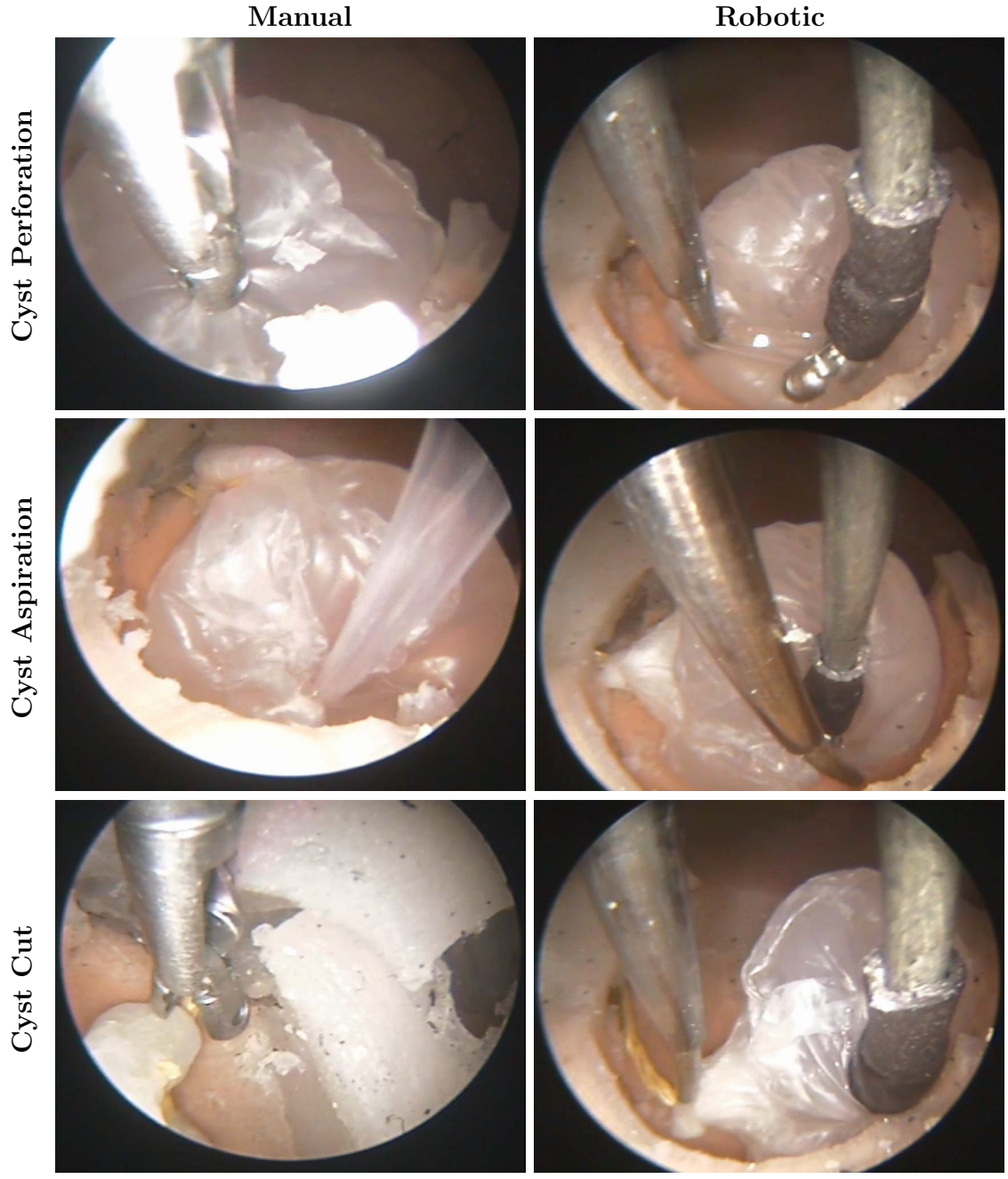

Figure 5.38: (Top Row) Manual: The cyst is perforated by grabbing the membrane and pulling/twisting. Robotic: The left and right arm provide tension to open the cyst. (Middle Row) Manual: The cyst is poked with the aspiration tube until it is debulked. Robotic: The right arm is used to move the cyst off of the floor so that the left arm can aspirate the cyst contents beneath it. (Bottom Row) Manual: The entire endoscope is moved substantially (see Figure 5.33 - Top, and notice the shifted endoscopic view) so that the forceps can grasp the string. Robotic: The right arm moves the cyst towards the left arm which reaches to touch the string.

CHAPTER 6

CONCLUSIONS AND FUTURE WORK

This dissertation has provided several contributions for the design of transendoscopic continuum robots and modeling of elastic stability. Controlling miniature, continuum manipulators through an endoscope presents several unique challenges and opportunities, which have just begun to be explored. The following sections outline future opportunities for contributions in this area.

6.1 Future Work: Hand-Held Endoscopic Robot Design

Hand-held surgical robots may be the ideal compromise between the capabilities that a large robotic system provides and the simplicity that a hand-held manual tool provides. The user interface remains a challenge in the design of these systems. Future user studies taking into account human factors and comparatively quantifying the performance of several user interfaces could prove to be the key to these devices reaching their potential. These future studies may include investigating the option of switched control, where the hand-held device can be grossly, manually positioned, and the manipulators can be controlled, but not simultaneously. This approach would allow for more conventional user interface designs that do not require the hands to be rigidly locked to the device. Within the HoLEP application, future work needs to be done to quantify the improvement in HoLEP this robotic system provides, in comparison to a conventional, manual HoLEP.

6.2 Future Work: Elastic Stability

While the elastic stability measure defined in this dissertation defines exactly when a snap will occur, we have yet to determine a physical meaning of this measure when it is greater than zero. Without this physical intuition, it is difficult to understand what the relative stability of the system means from a safety standpoint. Understanding this could be very important for enhanced safety of high curvature concentric tube robots. In addition, there have yet to be any studies on preventing elastic instability via a sensing technique. It may be possible to predict a snap before it happens based on a sensory approach, or a machine learning approach. This type of algorithm, if robust enough, could provide a safety guarantee for these flexible manipulators and be used as a risk mitigation strategy in an eventual clinical system.

6.3 Future Work: Redundancy Resolution in Concentric Tube Robots

In this dissertation, a redundancy resolution approach was used to maximize or minimize the most compliant direction of a flexible manipulator. There may be times when the surgeon would like to adjust the stiffness of the tool in a particular direction of task space, and this could be conveyed via the user interface. Exactly how this information is communicated from the surgeon to the system (i.e. via a joystick, haptic device, touchscreen, etc.) is an interesting question which could be approached in future work.

The robustness of the instability avoidance control law and the limits of the manipulator designs that are useful with this controller deserves further investigation. The robustness of this control law should be investigated during teleoperation scenarios, when the desired manipulator velocities are arbitrary. Future work should push the curvature limits experimentally of a manipulator design to see how far the design can be pushed and still remain useful.

6.4 Future Work: Robotic Neuroendoscopy

The neuroendoscopy application presented in this dissertation has laid the groundwork for several more interesting endoscopic neurosurgical applications using this same system. We hypothesize that there may be neurosurgical applications that would not only be easier to complete with this robotic system, but that may actually be enabled because of the capabilities provided by this system. There remain design opportunities to investigate automated methods for tool changes, since saving this time during brain surgery could potentially prevent catastrophic outcomes, during bleeding scenarios, for example. Ultimately, this system should be investigated in a more clinically realistic scenario, like in a cadaver or animal model.

6.5 Conclusions

This dissertation has presented four main contributions. In Chapter 2, the first ever hand-held robotic surgical device with multiple manipulators was achieved and validated experimentally in laser prostate surgery phantom and cadaver experiments. Chapter 3 defined an algorithm which exactly tests if a concentric tube robot design could exhibit elastic instability, a measure of relative stability, and a technique to determine where in joint space elastic instability will occur. Chapter 4 applied redundancy resolution techniques to concentric tube robots for the first time for stiffness optimization and instability avoidance. The instability avoidance technique is the first control technique for concentric tube robots which integrates the stability measure in real time, enables previously off-limit designs, and could even potentially enable new surgical applications. The main contribution of Chapter 5 is a quantitative experimental comparison of robotic versus manual endoscopic neurosurgery to begin to quantify the value that the transendoscopic continuum manipulators provide during neuroendoscopy.

Ultimately, the goal of this work was to equip surgeons with tools to solve the most challenging minimally invasive surgery problems, particularly when working through rigid endoscopes. The aforementioned contributions provide the foundation for future research towards this goal, and, once this occurs, the work described in this dissertation promises to ultimately benefit both patients and surgeons.

BIBLIOGRAPHY

[1] 2016. The Oxford Dictionary, Accessed Online.

[2] A. Gawande. Two hundred years of surgery. *New England Journal of Medicine*, 366(18):1716–1723, 2012.

[3] T. Wortrich. Laparoscopic instruments and methods, October 17 1995. US Patent 5,458,608.

[4] `http://www.ethicon.com/healthcare-professionals/products/other/lap-hand/laparoscopic-hand-instruments`, 2016. Ethicon Laparoscopic Tool, Accessed Online.

[5] J. H. Dreyfuss. Fewer complications, similar analgesia with paravertebral vs. thoracic epidural block for thoracotomy. `http://www.mdalert.com/article/fewer-complications-similar-analgesia-with-paravertebral-vs-thoracic-epidural-block-for-thoracotomy`, 2016. Video Assisted Thoracoscopy, Accessed Online.

[6] Aesculap, Inc. Launches MINOP InVent: The Future of Neuroendoscopy. `http://news.cision.com/aesculap/r/aesculap--inc--launches-minop--invent--the-future-of-neuroendoscopy,c9397646`, 2016. Minop Invent Rigid Neuroendoscope, Accessed Online.

[7] Aesculap, inc. launches minop invent: The future of neuroendoscopy. http://finance.yahoo.com/news/aesculap-inc-launches-minop-r-204136281.html, 2016. Minop Invent Rigid Neuroendoscope, Distal Tip, Accessed Online.

[8] http://www.intuitivesurgical.com/company/media/images/xi/, 2016. Intuitive Surgical da Vinci Xi, Accessed Online.

[9] M. Zimmermann, R. Krishnan, A. Raabe, and V. Seifert. Robot-assisted navigated endoscopic ventriculostomy: implementation of a new technology and first clinical results. *Acta neurochirurgica*, 146(7):697–704, 2004.

[10] M. J. Lum, D. C. Friedman, G. Sankaranarayanan, H. King, K. Fodero, R. Leuschke, B. Hannaford, J. Rosen, and M. N. Sinanan. The raven: Design and validation of a telesurgery system. *The International Journal of Robotics Research*, 28(9):1183–1197, 2009.

[11] R. J. Webster and B. A. Jones. Design and kinematic modeling of constant curvature continuum robots: A review. *The International Journal of Robotics Research*, 2010.

[12] J. Burgner-Kahrs, D. C. Rucker, and H. Choset. Continuum robots for medical applications: A survey. *IEEE Transactions on Robotics*, 31(6):1261–1280, 2015.

[13] J. Ding, R. E. Goldman, K. Xu, P. K. Allen, D. L. Fowler, and N. Simaan. Design and coordination kinematics of an insertable robotic effectors platform for single-port access surgery. *IEEE/ASME Transactions on Mechatronics*, 18(5):1612–1624, 2013.

[14] J. Shang, C. J. Payne, J. Clark, D. P. Noonan, K. Kwok, A. Darzi, and G. Yang. Design of a multitasking robotic platform with flexible arms and articulated

head for minimally invasive surgery. *IEEE/RSJ International Conference on Intelligent Robots and Systems*, pages 1988–1993, 2012.

[15] R. J. Webster III, A. Okamura, and N. J. Cowan. Toward Active Cannulas: Miniature Snake-Like Surgical Robots. *IEEE/RSJ International Conference on Intelligent Robots and Systems*, pages 2857–2863, 2006.

[16] P. Sears and P. Dupont. A Steerable Needle Technology Using Curved Concentric Tubes. *IEEE/RSJ International Conference on Intelligent Robots and Systems*, pages 2850–2856, 2006.

[17] R. H. Taylor and D. Stoianovici. Medical robotics in computer-integrated surgery. *IEEE Transactions on Robotics and Automation*, 19(5):765–781, 2003.

[18] D. B. Camarillo, T. M. Krummel, and J. K. Salisbury Jr. Robotic technology in surgery: Past, present, and future. *The American Journal of Surgery*, 188(4):2–15, 2004.

[19] F. Rodriguez y Baena and B. Davies. Robotic surgery: From autonomous systems to intelligent tools. *Robotica*, 28:163–170, 2010.

[20] H. Yamashita, N. Hata, M. Hashizume, and T. Dohi. Handheld laparoscopic forceps manipulator using multi-slider linkage mechanisms. *Medical Image Computing and Computer-Assisted Intervention*, pages 121–128, 2004.

[21] F. Focacci, M. Piccigallo, O. Tonet, G. Megali, A. Pietrabissa, and P. Dario. Lightweight hand-held robot for laparoscopic surgery. *IEEE International Conference on Robotics and Automation*, pages 599–604, 2007.

[22] S. Okazawa, R. Ebrahimi, J. Chuang, S. E. Salcudean, and R. Rohling. Hand-held steerable needle device. *IEEE/ASME Transactions on Mechatronics*, 10(3):285–296, 2005.

[23] J. Shang, D. P. Noonan, C. Payne, J. Clark, M. H. Sodergren, A. Darzi, and G. Z. Yang. An articulated universal joint based flexible access robot for minimally invasive surgery. *IEEE International Conference on Robotics and Automation*, pages 1147–1152, 2011.

[24] W. Wei, R. E. Goldman, H. F. Fine, S. Chang, and N. Simaan. Performance evaluation for multi-arm manipulation of hollow suspended organs. *IEEE Transactions on Robotics*, 25(1):147–157, 2009.

[25] E. J. Butler, R. Hammond-Oakley, S. Chawarski, A. H. Gosline, P. Codd, T. Anor, J. R. Madsen, P. E. Dupont, and J. Lock. Robotic neuro-endoscope with concentric tube augmentation. *IEEE/RSJ International Conference on Intelligent Robots and Systems*, pages 2941–2946, 2012.

[26] S. S. Antman. *Nonlinear Problems of Elasticity.* Springer-Verlag, 2nd edition, 2005.

[27] R. J. Webster III, J. M. Romano, and N. J. Cowan. Mechanics of precurved-tube continuum robots. *IEEE Transactions on Robotics*, 25:67–78, 2009.

[28] D. C. Rucker, B. A. Jones, and R. J. Webster, III. A geometrically exact model for externally loaded concentric tube continuum robots. *IEEE Transactions on Robotics*, 26:769–780, 2010.

[29] P. E. Dupont, J. Lock, B. Itkowitz, and E. Butler. Design and control of concentric-tube robots. *IEEE Transactions on Robotics*, 26(2):209–225, 2010.

[30] J. Kim, D. Lee, K. Kim, S. Kang, and K. Cho. Toward a solution to the snapping problem in a concentric-tube continuum robot: Grooved tubes with anisotropy. *IEEE International Conference on Robotics and Automation*, pages 5871–5876, 2014.

[31] H. Azimian, P. Francis, T. Looi, and J. Drake. Structurally-redesigned concentric-tube manipulators with improved stability. *IEEE/RSJ International Conference on Intelligent Robots and Systems*, pages 2030–2035, 2014.

[32] J. Ha and P. E. Dupont. Designing stable concentric tube robots using piecewise straight tubes. *IEEE Robotics and Automation Letters*, 2(1):298–304, 2017.

[33] R. J. Hendrick, H. B. Gilbert, and R. J. Webster III. Designing snap-free concentric tube robots: A local bifurcation approach. In *IEEE International Conference on Robotics and Automation*, pages 2256–2263, 2015.

[34] J. Ha, F. Park, and P. Dupont. Achieving elastic stability of concentric tube robots through optimization of tube precurvature. *IEEE/RSJ International Conference on Intelligent Robots and Systems*, pages 864–870, 2014.

[35] R. Xu, S. F. Atashzar, and R. V. Patel. Kinematic instability in concentric-tube robots: Modeling and analysis. *IEEE International Conference on Biomedical Robotics and Biomechatronics*, pages 163–168, 2014.

[36] J. Ha, F. C. Park, and P. E. Dupont. Optimizing tube precurvature to enhance the elastic stability of concentric tube robots. *IEEE Transactions on Robotics*, 2016.

[37] H. B. Gilbert, R. J. Hendrick, and R. J. Webster III. Elastic stability of concentric tube robots: A stability measure and design test. *IEEE Transactions on Robotics*, 32(1):20–35, 2016.

[38] J. Ha, F. C. Park, and P. E. Dupont. Elastic stability of concentric tube robots subject to external loads. *IEEE Transactions on Biomedical Engineering*, 63(6):1116–1128, 2016.

[39] C. Bergeles, A. H. Gosline, N. V. Vasilyev, P. J. Codd, J. Pedro, and P. E. Dupont. Concentric tube robot design and optimization based on task and anatomical constraints. *IEEE Transactions on Robotics*, 31(1):67–84, 2015.

[40] N. Simaan. Snake-like units using flexible backbones and actuation redundancy for enhanced miniaturization. In *International Conference on Robotics and Automation*, pages 3012–3017. IEEE, 2005.

[41] G. S. Chirikjian and J. W. Burdick. A modal approach to hyper-redundant manipulator kinematics. *IEEE Transactions on Robotics and Automation*, 10(3):343–354, 1994.

[42] G. S. Chirikjian and J. W. Burdick. The kinematics of hyper-redundant robot locomotion. *IEEE Transactions on Robotics and Automation*, 11(6):781–793, 1995.

[43] D. B. Camarillo, C. F. Milne, C. R. Carlson, M. R. Zinn, and J. K. Salisbury. Mechanics modeling of tendon-driven continuum manipulators. *IEEE Transactions on Robotics*, 24(6):1262–1273, 2008.

[44] J. Edelmann, A. J. Petruska, and B. J. Nelson. Magnetic control of continuum devices. *The International Journal of Robotics Research*, 36(1):68–85, 2017.

[45] V. P. Bodani, H. Azimian, T. Looi, and J. M. Drake. Design and evaluation of a concentric tube robot for minimally-invasive endoscopic pediatric neurosurgery. *Neurosurgery*, 61:192, 2014.

[46] V. Bodani, H. Azimian, T. Looi, and J. Drake. Design and evaluation of a concentric tube robot for minimally-invasive endoscopic paediatric neurosurgery. In *The Hamlyn Symposium on Medical Robotics*, volume 1, pages 25–26, 2014.

[47] H. Azimian, T. Looi, and J. Drake. A dual-arm robotic neuroendoscope: Early results. In *The Hamlyn Symposium on Medical Robotics*, volume 1, pages 34–35, 2016.

[48] M. Hess, K. Eastwood, B. Linder, V. Bodani, A. Lasso, T. Looi, G. Fichtinger, and J. Drake. Visual design and verification tool for collision-free dexterous patient specific neurosurgical instruments. In *SPIE Medical Imaging*, pages 97861M–97861M. International Society for Optics and Photonics, 2016.

[49] S. Manjila, M. Mencattelli, B. Rosa, K. Price, G. Fagogenis, and P. E. Dupont. A multiport MR-compatible neuroendoscope: spanning the gap between rigid and flexible scopes. *Neurosurgical Focus*, 41(3):E13, 2016.

[50] M. Mencattelli, S. Manjila, B. Rosa, K. Price, G. Fagogenis, and P. E. Dupont. Multi-port neuroendoscope for robotic intraventricular procedures. In *The Hamlyn Symposium on Medical Robotics*, volume 1, pages 32–33, 2016.

[51] T. Vrielink, D. Khan, H. J. Marcus, A. Darzi, and G. P. Mylonas. Neurocyclops: A novel system for endoscopic neurosurgery. In *The Hamlyn Symposium on Medical Robotics*, volume 1, pages 36–37, 2016.

[52] R. J. Hendrick, C. R. Mitchell, S. D. Herrell, and R. J. Webster. Hand-held transendoscopic robotic manipulators: A transurethral laser prostate surgery case study. *The International Journal of Robotics Research*, 34(13):1559–1572, 2015.

[53] R. J. Hendrick, S. D. Herrell, and R. J. Webster III. A Multi-Arm Hand-Held Robotic System for Transurethral Laser Prostate Surgery. *IEEE International Conference on Robotics and Automation*, pages 2850–2855, 2014.

[54] R. J. Hendrick, C. R. Mitchell, S. D. Herrell, and R. J. Webster III. Concentric Tube Robots for Transurethral Prostate Surgery: Matching the Workspace to

the Endoscopic Field of View. *The Hamlyn Symposium on Medical Robotics*, 2014.

[55] R. J. Hendrick, S. D. Herrell, C. R. Mitchell, and R. J. Webster III. Experiments on the simultaneous hand-held control of rigid endoscopes and robots passing through them. In *Experimental Robotics*, pages 73–87. Springer, 2016.

[56] C. R. Mitchell, R. J. Hendrick, R. J. Webster III, and S. D. Herrell. Toward improving transurethral prostate surgery: Development and initial experiments with a prototype concentric tube robotic platform. *Journal of Endourology*, 30(6):692–696, 2016.

[57] T. Vos, A. D. Flaxman, M. Naghavi, R. Lozano, C. Michaud, M. Ezzati, K. Shibuya, J. A. Salomon, S. Abdalla, V. Aboyans, et al. Years lived with disability (ylds) for 1160 sequelae of 289 diseases and injuries 1990–2010: a systematic analysis for the global burden of disease study 2010. *The Lancet*, 380(9859):2163–2196, 2013.

[58] M. M. Issa, T. C. Fenter, L. Black, A. L. Grogg, and E. J. Kruep. An Assessment of the Diagnosed Prevalence of Diseases in Men 50 Years of Age or Older. *The American Journal of Managed Care*, 12(4):83–89, 2006.

[59] N. Bhojani, G. Gandaglia, and A. Sood *et al.* Morbidity and mortality after benign prostatic hyperplasia surgery: data from the American College of Surgeons national surgical quality improvement program. *Journal of Endourology*, 28(7):831–840, 2014.

[60] A. El-Hakim and M. Elhilali. Holmium laser enucleation of the prostate can be taught: the first learning experience. *BJU International*, 90(9):863–869, 2002.

[61] M. Kim, H.-E. Lee, and S.-J. Oh. Technical aspects of holmium laser enucleation of the prostate for benign prostatic hyperplasia. *Korean Journal of Urology*, 54(9):570–579, 2013.

[62] J. Placer, A. Gelabert-Mas, F. Vallmanya, J. M. Manresa, V. Menéndez, R. Cortadellas, and O. Arango. Holmium laser enucleation of prostate: outcome and complications of self-taught learning curve. *Urology*, 73(5):1042–1048, 2009.

[63] N. Seki, O. Mochida, N. Kinukawa, K. Sagiyama, and S. Naito. Holmium laser enucleation for prostatic adenoma: analysis of learning curve over the course of 70 consecutive cases. *The Journal of Urology*, 170(5):1847–1850, 2003.

[64] H. N. Shah, A. P. Mahajan, H. S. Sodha, S. Hegde, P. D. Mohile, and M. B. Bansal. Prospective evaluation of the learning curve for holmium laser enucleation of the prostate. *The Journal of Urology*, 177(4):1468–1474, 2007.

[65] R. L. Kuo, R. F. Paterson, S. C. Kim, T. M. Siqueira Jr, M. M. Elhilali, and J. E. Lingeman. Holmium Laser Enucleation of the Prostate (HoLEP): A Technical Update. *World Journal of Surgical Oncology*, 1(1):6, June 2003.

[66] M. Cynk. Holmium laser enucleation of the prostate: a review of the clinical trial evidence. *Therapeutic Advances in Urology*, pages 62–73, 2013.

[67] P. J. Gilling, L. C. Wilson, C. J. King, A. M. Westenberg, C. M. Frampton, and M. R. Fraundorfer. Long-term results of a randomized trial comparing holmium laser enucleation of the prostate and transurethral resection of the prostate: results at 7 years. *BJU International*, 109(3):408–411, 2012.

[68] N. Gupta, R. Kumar, P. N. Dogra, A. Seth, et al. Comparison of standard transurethral resection, transurethral vapour resection and holmium laser enucleation of the prostate for managing benign prostatic hyperplasia of > 40 g. *BJU International*, 97(1):85–89, 2006.

[69] R. M. Kuntz, S. Ahyai, K. Lehrich, and A. Fayad. Transurethral holmium laser enucleation of the prostate versus transurethral electrocautery resection of the prostate: a randomized prospective trial in 200 patients. *The Journal of Urology*, 172(3):1012–1016, 2004.

[70] F. Montorsi, R. Naspro, A. Salonia, N. Suardi, A. Briganti, M. Zanoni, S. Valenti, I. Vavassori, and P. Rigatti. Holmium laser enucleation versus transurethral resection of the prostate: results from a 2-center, prospective, randomized trial in patients with obstructive benign prostatic hyperplasia. *The Journal of Urology*, 172(5):1926–1929, 2004.

[71] S. A. Ahyai, K. Lehrich, and R. M. Kuntz. Holmium Laser Enucleation versus Transurethral Resection of the Prostate: 3-Year Follow-Up Results of a Randomized Clinical Trial. *European Urology*, 52(5):1456–63, 2007.

[72] E. Anthes. Save blood, save lives. *Nature*, 520(7545):24, 2015.

[73] S. van Rij and P. J. Gilling. In 2013, holmium laser enucleation of the prostate (holep) may be the new gold standard. *Current Urology Reports*, 13(6):427–432, 2012.

[74] T. F. Aho. Holmium laser enucleation of the prostate: a paradigm shift in benign prostatic hyperplasia surgery. *Therapeutic Advances in Urology*, 5(5):245–253, 2013.

[75] J. Michalak, D. Tzou, and J. Funk. HoLEP: the gold standard for the surgical management of BPH in the 21st century. *American Journal of Clinical and Experimental Urology*, 3(1):36–42, 2015.

[76] D. C. Rucker, B. A. Jones, and R. J. Webster III. A Geometrically Exact Model for Externally Loaded Concentric-Tube Continuum Robots. *IEEE Transactions on Robotics*, 26(5):769–780, 2010.

[77] P. E. Dupont, J. Lock, B. Itkowitz, and E. Butler. Design and Control of Concentric-Tube Robots. *IEEE Transactions on Robotics*, 26(2):209–225, 2010.

[78] J. Burgner, D. C. Rucker, H. B. Gilbert, P. J. Swaney, P. T. Russell, K. D. Weaver, and R. J. Webster III. A Telerobotic System for Transnasal Surgery. *IEEE/ASME Transactions on Mechatronics*, 19(3):996–1006, 2014.

[79] R. Xu and R. V. Patel. A fast torsionally compliant kinematic model of concentric-tube robots. *International Conference of the IEEE Engineering in Medicine and Biology Society*, pages 904–907, 2012.

[80] M. Piccigallo, U. Scarfogliero, C. Quaglia, G. Petroni, P. Valdastri, A. Menciassi, and P. Dario. Design of a novel bimanual robotic system for single-port laparoscopy. *IEEE/ASME Transactions on Mechatronics*, 15(6):871–878, 2010.

[81] A. C. Lehman, N. A. Wood, S. Farritor, M. R. Goede, and D. Oleynikov. Dexterous miniature robot for advanced minimally invasive surgery. *Surgical Endoscopy*, 25(1):119–123, 2011.

[82] S. J. Phee, S. C. Low, Z. L. Sun, K. Y. Ho, W. M. Huang, and Z. M. Thant. Robotic system for no-scar gastrointestinal surgery. *The International Journal of Medical Robotics and Computer Assisted Surgery*, 4(1):15–22, 2008.

[83] D. J. Abbott, C. Becke, R. I. Rothstein, and W. J. Peine. Design of an endoluminal notes robotic system. *IEEE/RSJ International Conference on Intelligent Robots and Systems*, pages 410–416, 2007.

[84] B. L. Davies, R. D. Hibberd, W. S. Ng, A. G. Timoney, and J. E. A. Wickham. The development of a surgeon robot for prostatectomies. *Proceedings of the Institution of Mechanical Engineers, Part H : Journal of Engineering in Medicine*, 205:35–38, 1991.

[85] B. Davies. Medical robotics - a bright future. *Lancet*, 368:S53–S54, 2006.

[86] G. Ho, W. S. Ng, M. Y. Teo, C. K. Kwoh, and W. S. C. Cheng. Experimental study of transurethral robotic laser resection of the prostate using the LaserTrode lightguide. *Journal of Biomedical Optics*, pages 244–251, 2001.

[87] E. S. de Badajoz, A. J. Garrido, F. G. Vacas, V. F. M. Martinez, J. G. de Gabriel, J. F. Lozano, and A. G. Cerezo. New master arm for transurethral resection with a robot. *Archivos Espanoles de Urologia*, 55:1.247–1.250, 1998.

[88] R. Hashimoto, D. Kim, N. Hata, and T. Dohi. A Tubular Organ Resection Manipulator for Transurethral Resection of the Prostate. *IEEE/RSJ International Conference on Intelligent Robots and Systems*, pages 3954–3959, 2004.

[89] R. E. Goldman, A. Bajo, L. S. MacLachlan, R. Pickens, S. D. Herrell, and N. Simaan. Design and Performance Evaluation of a Minimally Invasive Telerobotic Platform for Transurethral Surveillance and Intervention. *IEEE Transactions on Biomedical Engineering*, 60(4):918–25, 2013.

[90] J. Burgner, H. B. Gilbert, and R. J. Webster III. On the computational design of concentric tube robots: Incorporating volume-based objectives. *IEEE International Conference on Robotics and Automation*, pages 1185–1190, 2013.

[91] C. Bedell, J. Lock, A. Gosline, and P. E. Dupont. Design optimization of concentric tube robots based on task and anatomical constraints. *IEEE International Conference on Robotics and Automation*, pages 398–403, 2011.

[92] R. M. Murray, Z. Li, and S. S. Sastry. *A Mathematical Introduction to Robotic Manipulation*. CRC Press, Boca Raton, FL, 1994.

[93] R. J. Webster III and B. A. Jones. Design and kinematic modeling of constant curvature continuum robots: A review. *The International Journal of Robotics Research*, 2010.

[94] C. W. Wampler II. Manipulator inverse kinematic solutions based on vector formulations and damped least-squares methods. *IEEE Transactions on Systems, Man, and Cybernetics*, 16(1):93–101, 1986.

[95] S. Chiaverini. Singularity-robust task-priority redundancy resolution for real-time kinematic control of robot manipulators. *IEEE Transactions on Robotics and Automation*, 13(3):398–410, 1997.

[96] J. L. Leenstra, B. J. Davis, T. M. Wilson, L. A. Mynderse, M. G. Herman, D. Hillman, K. Allen, J. Cheville, D. Holmes, and B. King. Prostate Dimensions and Volume in 700 Patients Undergoing Primary Surgical or Radiotherapeutic Management of Localized Adenocarcinoma: Implications for Design of Minimally Invasive Prostate Cancer Devices. *International Journal of Radiation Oncology*, 69(3):S380–S381, 2007.

[97] L. Swanstrom and B. Zheng. Spatial orientation and off-axis challenges for notes. *Gastrointestinal Endoscopy Clinics of North America*, 18(2):315–324, 2008.

[98] W. Wei and N. Simaan. Modeling, force sensing, and control of flexible cannulas for microstent delivery. *ASME Journal Dyn. Sys. Meas. Control*, 134(4):041004–1–041004–12, 2012.

[99] N. V. Vasilyev, A. H. Gosline, A. Veeramani, G. P. Wu, M. T. Schmitz, R. T. Chen, A. Veaceslav, P. J. del Nido, and P. E. Dupont. Tissue removal inside the beating heart using a robotically delivered metal mems tool. *International Journal of Robotics Research*, 34(2):236–247, 2015.

[100] J. Burgner, D. C. Rucker, H. B. Gilbert, P. J. Swaney, P. T. Russell III, K. D. Weaver, and R. J. Webster III. A telerobotic system for transnasal surgery. *IEEE/ASME Transactions on Mechatronics*, 19(3):996–1006, 2014.

[101] L. Torres, R. J. Webster III, and R. Alterovitz. Task-oriented design of concentric tube robots using mechanics-based models. In *IEEE/RSJ International Conference on Intelligent Robots and Systems*, pages 4449–4455, 2012.

[102] K. Leibrandt, C. Bergeles, and G.-Z. Yang. Implicit active constraints for safe and effective guidance of unstable concentric tube robots. In *IEEE/RSJ International Conference on Intelligent Robots and Systems*, pages 1157–1163. IEEE, 2016.

[103] K. Leibrandt, C. Bergeles, and G.-Z. Yang. On-line collision-free inverse kinematics with frictional active constraints for effective control of unstable concentric tube robots. In *IEEE/RSJ International Conference on Intelligent Robots and Systems*, pages 3797–3804. IEEE, 2015.

[104] K. Hoffman and R. Manning. An extended conjugate point theory with application to the stability of planar buckling of an elastic rod subject to a repulsive self-potential. *SIAM Mathematical Analysis*, 41:465–494, 2009.

[105] R. S. Manning. Conjugate points revisited and neumann-neumann problems. *SIAM review*, 51(1):193–212, 2009.

[106] S. V. Levyakov and V. V. Kuznetsov. Stability analysis of planar equilibrium configurations of elastic rods subjected to end loads. *Acta Mechanica*, 211(10):73–87, 2009.

[107] T. Bretl and Z. McCarthy. Quasi-static manipulation of a kirchoff elastic rod based on a geometric analysis of equilibrium configurations. *International Journal of Robotics Research*, 33(1):48–68.

[108] D. C. Rucker, R. J. Webster III, G. S. Chirikjian, and N. J. Cowan. Equilibrium conformations of concentric-tube continuum robots. *International Journal of Robotics Research*, 29(10):1263–1280, 2010.

[109] R. M. Murray, Z. Li, and S. S. Sastry. *A Mathematical Introduction to Rootic Manipulation*. CRC Press, 1994.

[110] H. I. Dwyer and A. Zettl. Eigenvalue computations for regular matrix sturm-liouville problems. *Electronic Journal of Differential Equations*, (5):1–13, 1995.

[111] I. M. Gelfand and S. V. Fomin. *Calculus of Variations*. Dover Publications, Mineola, NY, 2000.

[112] J. Lock and P. E. Dupont. Friction modeling in concentric tube robots. In *IEEE International Conference on Robotics abd Automation*, pages 1139–1146. IEEE, 2011.

[113] A. R. Pelton, N. Rebel, T. W. Duerig, and A. Wick. Experimental and FEM analysis of the bending behavior of superelastic tubing. In *Proceedings of the First International Conference on Shape Memory and Superelastic Technologies*, pages 353–358, 1994.

[114] H. B. Gilbert, D. C. Rucker, and R. J. Webster III. Concentric tube robots: The state of the art and future directions. In *Robotics Research*, pages 253–269. Springer, 2016.

[115] J. Till and D. C. Rucker. Elastic stability of cosserat rods and parallel continuum robots. *IEEE Transactions on Robotics*, 2017.

[116] D. E. Whitney. Resolved motion rate control of manipulators and human prostheses. *IEEE Transactions on man-machine systems*, 1969.

[117] T. F. Chan and R. V. Dubey. A weighted least-norm solution based scheme for avoiding joint limits for redundant joint manipulators. *IEEE Transactions on Robotics and Automation*, 11(2):286–292, 1995.

[118] J. Peirs, J. Clijnen, D. Reynaerts, H. Van Brussel, P. Herijgers, B. Corteville, and S. Boone. A micro optical force sensor for force feedback during minimally invasive robotic surgery. *Sensors and Actuators A: Physical*, 115(2):447–455, 2004.

[119] R. J. Andrews and J. R. Bringas. A review of brain retraction and recommendations for minimizing intraoperative brain injury. *Neurosurgery*, 33(6):1052–1064, 1993.

[120] A. G. Osborn and M. T. Preece. Intracranial cysts: radiologic-pathologic correlation and imaging approach. *Radiology*, 239(3):650–664, 2006.

[121] G. A. Waggenspack and F. C. Guinto. MR and CT of masses of the anterosuperior third ventricle. *American journal of neuroradiology*, 10(1):105–110, 1989.

[122] V. N. Kornienko and I. N. Pronin. Diagnostic neuroradiology, 2006.

[123] A. I. Lewis, K. R. Crone, J. Taha, H. R. van Loveren, H.-S. Yeh, and J. M. Tew Jr. Surgical resection of third ventricle colloid cysts: preliminary results comparing transcallosal microsurgery with endoscopy. *Journal of neurosurgery*, 81(2):174–178, 1994.

[124] E. M. Horn and R. F. Spetzler. Treatment options for third ventricular colloid cysts: comparison of open microsurgical versus endoscopic resection. *Neurosurgery*, 62(6):E1384, 2008.

[125] J. D. Greenlee, C. Teo, A. Ghahreman, and B. Kwok. Purely endoscopic resection of colloid cysts. *Neurosurgery*, 62(3):51–56, 2008.

[126] N. M. El-Ghandour. Endoscopic cyst fenestration in the treatment of uniloculated hydrocephalus in children: Clinical article. *Journal of Neurosurgery: Pediatrics*, 11(4):402–409, 2013.

[127] N. Nathoo, M. C. Çavusoglu, M. A. Vogelbaum, and G. H. Barnett. In touch with robotics: neurosurgery for the future. *Neurosurgery*, 56(3):421–433, 2005.

[128] A. Benabid, P. Cinquin, S. Lavalle, J. Le Bas, J. Demongeot, and J. De Rougemont. Computer-driven robot for stereotactic surgery connected to ct scan and magnetic resonance imaging. *Stereotactic and Functional Neurosurgery*, 50(1-6):153–154, 1988.

[129] A. Benabid, D. Hoffmann, S. Lavallee, P. Cinquin, J. Demongeot, J. Le Bas, and F. Danel. Is there any future for robots in neurosurgery? In *Advances and technical standards in Neurosurgery*, pages 3–45. Springer, 1991.

[130] A. Benabid, S. Lavallee, D. Hoffmann, P. Cinquin, J. Demongeot, and F. Danel. Potential use of robots in endoscopic neurosurgery. In *Minimally Invasive Neurosurgery I*, pages 93–97. Springer, 1992.

[131] B. Davies, S. Starkie, S. J. Harris, E. Agterhuis, V. Paul, and L. M. Auer. Neurobot: A special-purpose robot for neurosurgery. In *IEEE International Conference on Robotics and Automation*, volume 4, pages 4103–4108. IEEE, 2000.

[132] H. Takasuna, T. Goto, Y. Kakizawa, T. Miyahara, J. Koyama, Y. Tanaka, T. Kawai, and K. Hongo. Use of a micromanipulator system (neurobot) in endoscopic neurosurgery. *Journal of Clinical Neuroscience*, 19(11):1553–1557, 2012.

[133] T. Anor, J. R. Madsen, and P. Dupont. Algorithms for design of continuum robots using the concentric tubes approach: A neurosurgical example. In *IEEE International Conference on Robotics and Automation*, pages 667–673. IEEE, 2011.

[134] C. Baykal, L. G. Torres, and R. Alterovitz. Optimizing design parameters for sets of concentric tube robots using sampling-based motion planning. In *IEEE/RSJ International Conference on Intelligent Robots and Systems*, pages 4381–4387. IEEE, 2015.

[135] D. C. Rucker and R. J. Webster III. Computing Jacobians and compliance matrices for externally loaded continuum robots. *IEEE International Conference on Robotics and Automation*, pages 945–950, 2011.

[136] `https://www.aesculapusa.com/products/neurosurgery/neuroendoscopy/intraventricular/minop-invent`, 2017. Aesculap Minop Invent Images, Accessed Online.

[137] T. W. Duerig, A. R. Pelton, and D. Stöckel. Superelastic nitinol for medical devices. *Medical Plastic and Biomaterials*, 4:30–43, 1997.

[138] F.-Y. Lin, C. Bergeles, and G.-Z. Yang. Biometry-based concentric tubes robot for vitreoretinal surgery. In *International Conference of the IEEE Engineering in Medicine and Biology Society*, pages 5280–5284. IEEE, 2015.

[139] T. Yoshikawa. Manipulability of robotic mechanisms. *The International Journal of Robotics Research*, 4(2):3–9, 1985.

[140] J.-O. Kim and K. Khosla. Dexterity measures for design and control of manipulators. In *IEEE/RSJ International Conference on Intelligent Robots and Systems*, pages 758–763. IEEE, 1991.

[141] J. Angeles and C. Gosselin. A global performance index for the kinematic optimization of robotic manipulators. *Journal of Mechanical Design*, 113(3):220–226, 1991.

[142] G. E. Breimer, V. Bodani, T. Looi, and J. M. Drake. Design and evaluation of a new synthetic brain simulator for endoscopic third ventriculostomy. *Journal of Neurosurgery: Pediatrics*, 15(1):82–88, 2015.

[143] J. M. Fitzpatrick, D. L. G. Hill, and C. R. Maurer. *Image Registration, Chapter 8, Handbook of Medical Imaging, Volume 2, Medical Image Processing and Analysis*. 2000.

[144] A. Zettl. *Sturm-Liouville Theory*. American Mathematical Society, 2005.

[145] J. H. Maddocks. Restricted quadratic forms and their application to bifurcation and stability in constrianed variational principles. *SIAM J. Math. Anal.*, 16(1), 1985.

[146] P. B. Bailey, W. N. Everitt, J. Weidmann, and A. Zettl. Regular approximations of singular sturm-liouville problems. In *Results in Mathematics*, pages 3–22, 1993.

APPENDICES

APPENDIX A

The Second Variation, Chapter 3

These appendices were included in the journal publication "Elastic Stability of Concentric Tube Robots: A Stability Measure and Design Test," which was published in *IEEE Transactions on Robotics*[1].

In the calculus of variations, it is well-known that Euler's equation is a necessary but not sufficient condition for a minimum, and it is equivalent to the first variation functional being equal to zero,

$$\delta E[\boldsymbol{h}] = \int_{\mathcal{D}} [F_{\boldsymbol{x}}\boldsymbol{h} + F_{\boldsymbol{x}'}\boldsymbol{h}']\, d\sigma = 0$$

for all admissible variations $\boldsymbol{h}$ for which $\boldsymbol{x}_0 + \boldsymbol{h}$ satisfies the boundary conditions of the problem. The quantities $F_{\boldsymbol{x}}$ and $F_{\boldsymbol{x}'}$ are evaluated along the extremal curve $\boldsymbol{x}_0$ for which Euler's equation is satisfied. The expression $F_{\boldsymbol{x}}\boldsymbol{h}$ is interpreted as a row vector multiplied by a column vector.

It is also well-known that for $\boldsymbol{x}_0$ to be a weak minimum of the energy functional, the second variation $\delta^2 E[\boldsymbol{h}]$ must be strictly positive for all nonzero admissible variations $\boldsymbol{h}$. The second variation is given by

$$\delta^2 E[\boldsymbol{h}] = \frac{1}{2}\int_{\mathcal{D}} (F_{\boldsymbol{x}\boldsymbol{x}}\boldsymbol{h}, \boldsymbol{h}) + 2(F_{\boldsymbol{x}\boldsymbol{x}'}\boldsymbol{h}', \boldsymbol{h}) + (F_{\boldsymbol{x}'\boldsymbol{x}'}\boldsymbol{h}', \boldsymbol{h}')\, d\sigma \tag{A.0.1}$$

where $F_{\boldsymbol{x}\boldsymbol{x}}$, $F_{\boldsymbol{x}\boldsymbol{x}'}$, and $F_{\boldsymbol{x}'\boldsymbol{x}'}$ are the matrices of second partial derivatives, evaluated

[1] © 2015 IEEE. Reprinted, with permission, from Hunter B. Gilbert, Richard J. Hendrick, and Robert J. Webster III, Elastic Stability of Concentric Tube Robots: A Stability Measure and Design Test, IEEE Transactions on Robotics, December 2015.

as before along the extremal curve $\boldsymbol{x}_0$, and the parentheses denote the scalar product $(a, b) = \sum a_i b_i$.

For the problems generated by the concentric tube robot problem, we have that the mixed partial derivatives $F_{\boldsymbol{x}\boldsymbol{x}'} = 0$. An integration by parts reveals that (A.0.1) is equivalent to

$$\delta^2 E[\boldsymbol{h}] = \langle \boldsymbol{\mathcal{S}}\boldsymbol{h}, \boldsymbol{h} \rangle = \int_D (\boldsymbol{\mathcal{S}}\boldsymbol{h}, \boldsymbol{h}) \ d\sigma \tag{A.0.2}$$

which is an inner product on the underlying Hilbert space of admissible variations. Then, the spectral theorem for self-adjoint operators on Hilbert spaces shows that the second variation is strictly positive only when all eigenvalues of the second variation operator $\boldsymbol{\mathcal{S}}$, defined by

$$\boldsymbol{\mathcal{S}}\boldsymbol{h} = -\left(F_{\boldsymbol{x}'\boldsymbol{x}'}\boldsymbol{h}'\right)' + F_{\boldsymbol{x}\boldsymbol{x}}\boldsymbol{h} \ ,$$

are positive.[2] It is a prerequisite for the condition $\delta^2 E[\boldsymbol{h}] > 0$ to be transformed into the condition on the eigenvalues of $\boldsymbol{\mathcal{S}}$ that the eigenvectors of $\boldsymbol{\mathcal{S}}$ form a complete orthonormal set for the underlying Hilbert space. For the operators generated by the concentric tube robot model, the eigenvectors of $\boldsymbol{\mathcal{S}}$ do form such a basis, as guaranteed by Theorem 1 of Dwyer and Zettl, which says that $\boldsymbol{\mathcal{S}}$ is a self-adjoint operator [110]. The eigenvalue equation $\boldsymbol{\mathcal{S}}\boldsymbol{\psi} = \rho\boldsymbol{\psi}$ is a Sturm-Liouville eigenvalue problem, which has a countably infinite number of orthonormal eigenvectors with eigenvalues that are all real and bounded below. Because there are an infinite number of eigenvalues, a direct computation will not suffice for a feasible numerical test of stability.

Fortunately, continuous changes in $F_{\boldsymbol{x}\boldsymbol{x}}$, $F_{\boldsymbol{x}'\boldsymbol{x}'}$ and the endpoints of the interval $\mathcal{D}$ cause continuous changes in the spectrum of $\boldsymbol{\mathcal{S}}$ [144]. The basic idea for a numerical test is the following: if one can show that $\boldsymbol{\mathcal{S}}$ has positive eigenvalues on some shortened domain which is a subset $J \subset \mathcal{D}$, then the endpoints of J can be continuously varied

[2] A technical note is that we consider only admissible variations such that each component of $(F_{\boldsymbol{x}'\boldsymbol{x}'}\boldsymbol{h}')'$ is absolutely continuous. For the concentric tube robot kinematics, $\boldsymbol{h}$ represents a variation in the rotational angles of the tubes, the variation in moment is differentiable and has a continuous derivative.

to the endpoints of $\mathcal{D}$ while watching for zero-crossings in the eigenvalues of $\boldsymbol{\mathcal{S}}$ [105]. If $\boldsymbol{\mathcal{S}}$ has a zero eigenvalue for some choice of J, then we have an equation $\boldsymbol{\mathcal{S}}\boldsymbol{h} = 0$ on that domain with boundary conditions on $\boldsymbol{h}$ also satisfied at the endpoints of J.

If the problem has Dirichlet boundary conditions, it is well known that stability is determined by looking for conjugate points [111], and the conjugate point formulation and the eigenvalue characterization have been shown to be equivalent [105, 145]. For concentric tube robots, the boundary conditions are not Dirichlet, and therefore the conjugate point condition must be modified. We must first verify that all eigenvalues of $\boldsymbol{\mathcal{S}}$ are positive when the operator is taken to act on a shorter domain. For concentric tube robots, this means a shorter robot. Second, we look for conjugate points, which occur when $\boldsymbol{\mathcal{S}}\boldsymbol{h} = \mathbf{0}$ is solved for an admissible variation $\boldsymbol{h}$, which is precisely when $\boldsymbol{\mathcal{S}}$ has an eigenvalue at zero. This two-part modification is explained in detail by Hoffman et al. [104].

We are no longer guaranteed that a conjugate point results in an increase in the number of negative eigenvalues [105], because the Neumann boundary condition, in general, prevents the eigenvalues from being strictly decreasing functions of the domain length. Nevertheless, we can still conclude that the absence of a conjugate point implies positive eigenvalues, making it a sufficient condition.

APPENDIX B

Proof Of Result 3, Chapter 3

We define the family of related eigenvalue problems

$$\boldsymbol{\mathcal{S}}\phi = \rho\phi,\ \phi(\beta) = 0,\ \phi'(a) = 0 \tag{B.0.1}$$

for the variable endpoint a, with $\beta < a \leq 1$. It is known that the eigenvalues ρ_i, $i = 1, 2, ...,$ move continuously with respect to continuous changes in a [105, 144]. The basic idea of the test is that if there is a small enough a where all eigenvalues are positive, then for an eigenvalue of the problem (B.0.1), with $a = 1$, to be negative, it must cross zero as a varies between β and 1. This condition can be checked with a simple test.

To look for an eigenvalue at zero in any of the related problems (B.0.1), we assume that zero is an eigenvalue, with eigenvector h, by setting $\boldsymbol{\mathcal{S}}h = 0$, i.e. we set $-h'' + \lambda\cos(\theta)h = 0$. It follows that there exists a length σ for which $\boldsymbol{\mathcal{S}}h = 0$, $h(\beta) = 0$, and $h'(\sigma) = 0$. Since we do not know σ, we begin at the proximal boundary, where we know that $h(\beta) = 0$. Because $\boldsymbol{\mathcal{S}}$ is linear, the eigenvectors have arbitrary scale, so that if h is an eigenvector, $h'(\beta)$ may be arbitrarily chosen by scaling (h must be non-trivial). We choose $h'(\beta) = 1$, and integrate the differential equation forward. In doing this, we have enforced both the differential form and the proximal boundary of the entire family of operators (B.0.1). If the distal boundary condition $h'(\sigma) = 0$ is not satisfied for any σ, then zero is not an eigenvalue for any of the operators of the family (B.0.1), contradicting the assumption of an eigenvalue at zero.

Since zero is not an eigenvalue for any of the problems, and if the problem has no negative eigenvalues for a sufficiently small value of a, it is not possible that the

boundary value problem on the whole interval has a negative eigenvalue by continuity of the spectrum with changes in the interval endpoint a.

To see that no eigenvalues are negative for small a, note that $\boldsymbol{\mathcal{S}}$ can be decomposed into $\boldsymbol{\mathcal{S}} = \mathcal{T} + \mathcal{Q}$, with $\mathcal{T}h = -h''$ and $\mathcal{Q}h = \lambda \cos(\theta) h$. As a becomes smaller, it is known that the eigenvalues of $\mathcal{T}$ become larger. The operator $\mathcal{Q}$ can be seen as a perturbation of $\mathcal{T}$, and when the eigenvalues of $\mathcal{T}$ are made sufficiently large by choosing a sufficiently small, the perturbation $\mathcal{Q}$, being bounded in magnitude, is incapable of moving an eigenvalue negative. The argument of this paragraph is made rigorously by Hoffman and Manning in [104].

APPENDIX C

Proof Of Result 5, Chapter 3

We begin by showing that the eigenvalues of the problem are positive when the boundary conditions at L are moved to be close to the boundary conditions at β. Here the allowable variation h_i belongs to the space $\mathcal{D}_i([\beta_i, a_i]) = \{f, (k_{it}f') \in AC([\beta_i, a_i]) : f(\beta_i) = 0, (k_{it}f')(a_i) = 0\}$, and the collection $\boldsymbol{h}$ belongs to the Cartesian product $\mathcal{D}(\boldsymbol{\mathcal{S}}) = \mathcal{D}_1 \times ... \times \mathcal{D}_n$. Consider the eigenvalue problem in which $a_i = \beta_i + \epsilon$ for some small ϵ. Then, we still have the decomposition of $\boldsymbol{\mathcal{S}}$ as in the proof of Result 3 as $\boldsymbol{\mathcal{S}} = \boldsymbol{\mathcal{T}} + \boldsymbol{\mathcal{Q}}$. The operator $\boldsymbol{\mathcal{T}}$ acts diagonally on the h_i, and so the eigenvalues γ of $\boldsymbol{\mathcal{T}}\boldsymbol{h} = \gamma\boldsymbol{h}$ may be found as the eigenvalues of n independent problems. The eigenvalues are positive and the smallest eigenvalue can be made arbitrarily large by the choice of ϵ. Consider the extension of h_i to the whole interval $[\beta, L]$, where it must be that $h(\beta) = h(\beta_i)$ and $h'(L) = h'(\beta_i + L_i)$ since the two-point extension of (3.6) simulates the tubes as having infinite torsional stiffness and zero bending stiffness in the regions $[\beta, \beta_i]$ and $[\beta_i + L_i, L]$. The operator $\boldsymbol{\mathcal{Q}}$ is identically the zero operator over the interval $[\beta, \beta_{max}]$ due to the restriction of equation (3.8) and the form of $\mathbf{F}_{\psi\psi}$. The extended domain of the operator will be called $\mathcal{D}_{[\beta,L]}(\boldsymbol{\mathcal{S}})$. We will refer to $\boldsymbol{h}$ as the extension, since any solution on the domain $\mathcal{D}(\boldsymbol{\mathcal{S}})$ can be extended to a solution on the domain $\mathcal{D}_{[\beta,L]}(\boldsymbol{\mathcal{S}})$. The eigenvalues of $\boldsymbol{\mathcal{S}}$ do not change during the extension to the left when all β_i are moved to the left to β. The eigenvalues may change as all a_i which are less than β_{max} are increased to β_{max}, but all remain strictly greater than zero since the equations are decoupled and still of the form $\boldsymbol{\mathcal{T}}\boldsymbol{h} = \gamma\boldsymbol{h}$. Finally, the eigenvalues may change by a bounded amount as the a_i are increased to $\beta_{\max} + \epsilon$, but by choice of ϵ we can guarantee that this change will not cause the eigenvalues to become negative. Thus, there is some domain for which the eigenvalues are all

positive. As a_i are then increased together, $a_i = a \to L$, if an eigenvalue crosses zero we have a sub-problem on the interval $[\beta, a]$ for which $\boldsymbol{\mathcal{S}}\boldsymbol{h} = 0$ has a non-trivial solution $\boldsymbol{h}$, which is to say that there is a choice of constants $\boldsymbol{c}$ with $\boldsymbol{c} \neq \mathbf{0}$ so that $\mathbf{H}_{22}(a)\boldsymbol{c} = 0$, and therefore $\boldsymbol{h}(s) = \mathbf{H}_{12}\boldsymbol{c}$ is an eigenvector with eigenvalue zero. If, on the other hand, we do not have $\det \mathbf{H}_{22}(a) = 0$ for any a, then it must be that if zero is not an eigenvalue of $\boldsymbol{\mathcal{S}}\boldsymbol{h} = 0$ on any interval $[\beta, a]$, and since the spectrum changes continuously with a, $\det \mathbf{H}_{22} > 0$ on the whole interval thus guarantees that $\boldsymbol{\mathcal{S}}$ has only positive eigenvalues on the whole domain $[\beta, L]$.

The proof tacitly assumes that the eigenvalues move continuously with changes in the endpoint of the interval on which $\boldsymbol{\mathcal{S}}$ is defined, which is known to be true for the scalar Sturm-Liouville problem [144]. It is reasonable to assume this remains true for the matrix problem due to the fact that the resolvent operators of $\boldsymbol{\mathcal{S}}$ on different domains with "close" endpoints are close in a precise sense. For a discussion of resolvent convergence in the context of Sturm-Liouville problems, see for example [146].

APPENDIX D

Computation of the State Transition Matrix $e^{L\mathbf{\Gamma}_e}$, Chapter 3

First, assume that $\mathbf{\Gamma}_e$ is constant over some length L. Additionally, assume that all tubes are present in this section. Then, use the change of coordinates $\boldsymbol{y} = \mathbf{T}^{-1}\boldsymbol{x}$, to yield

$$\boldsymbol{y}' = \mathbf{T}^{-1}\mathbf{\Gamma}_e\mathbf{T}\boldsymbol{y} = \mathbf{Q}\mathbf{y} \tag{D.0.1}$$

where

$$\mathbf{Q} = \begin{bmatrix} \mathbf{0} & \mathbf{V}^{-1}\mathbf{K}_t^{-1}\mathbf{K}_t\mathbf{V} \\ \mathbf{V}^{-1}\mathbf{K}_t^{-1}\mathbf{A}_e\mathbf{V} & \mathbf{0} \end{bmatrix} = \begin{bmatrix} \mathbf{0} & \mathbf{I} \\ \mathbf{\Lambda} & \mathbf{0} \end{bmatrix} \tag{D.0.2}$$

Compute the flow of the differential equation (D.0.1) over a length L as

$$\boldsymbol{y}(L) = e^{L\mathbf{Q}}\boldsymbol{y}(0) \tag{D.0.3}$$

The matrix exponential $e^{L\mathbf{Q}}$ is given by

$$e^{L\mathbf{Q}} = \mathbf{G} = \begin{bmatrix} \cosh(L\sqrt{\mathbf{\Lambda}}) & \sqrt{\mathbf{\Lambda}}^{-1}\sinh(L\sqrt{\mathbf{\Lambda}}) \\ \sqrt{\mathbf{\Lambda}}\sinh(L\sqrt{\mathbf{\Lambda}}) & \cosh(L\sqrt{\mathbf{\Lambda}}) \end{bmatrix}, \tag{D.0.4}$$

where we define the hyperbolic trigonometric functions and the square roots to operate only on the diagonal elements of the matrix arguments. This equivalence can be shown by comparing the Taylor series expansions of $e^{L\mathbf{Q}}$ and the Taylor series expansions of the entries in $\mathbf{G}$. Then, in the original coordinates we have

$$\boldsymbol{x}(L) = \mathbf{T}\mathbf{G}\mathbf{T}^{-1}\boldsymbol{x}(0) \tag{D.0.5}$$

as claimed.